Multi-scale statistical analysis of the deformation processes and residual stresses in nickel-base superalloys



Jingwei Chen

Linacre College

University of Oxford

Supervised by

Professor Alexander M. Korsunsky

A thesis submitted for the degree of

Doctor of Philosophy

Trinity 2022

Abstract

The deformation of polycrystalline metallic materials is highly heterogeneous, originating from the anisotropic elastic and plastic properties of individual grains. Plastic deformation is often localized into slip bands or sub-grain shear bands. Recent advances in experimental measurements and numerical simulations, such as focused ion beam-digital image correlation (FIB-DIC), synchrotron X-ray diffraction (XRD), and crystal plasticity finite element modelling (CPFEM) contribute to shifting the research focus in solid mechanics from macroscopic scale toward the assessment and analysis of the strains and stresses within individual grain or grain groups. Nevertheless, very few research studies report precise, quantitative and reliable evaluation of the relationship between the microscopic (Type II+III) strains and stresses, and the apparent macro-scale (Type I) stresses and the overall mechanical behaviour.

The principal objective of the present study is to evaluate the multi-scale distributions of internal strains and stresses in aerospace nickel-base superalloys subjected to thermal and mechanical loading. The report begins with the numerical investigation of the deformation process in polycrystals using statistical distributions. To this end, the carefully calibrated CPFEM simulations of stresses and strains at different scales were conducted, and statistical distributions were extracted. A specially constructed series of numerical experiments was performed to investigate the effect of discretization methods in CPFEM.

As the nature of stress and strain inhomogeneities at different scales were revealed, it was found that the dispersion of local stress and strain distributions is much larger than the

those of the macroscopic average. Notably, it is argued based on theoretical analysis and observations that the elastic strain accumulation represents an additive process, whereas the plastic strain accumulation is a multiplicative process. Hence, the statistical distributions of these quantities differ and are normal and lognormal, respectively.

Another important achievement presented in this Thesis connects the macroscopic stress-strain behaviour to the Yield Volume Fraction (YVF) function using lognormal distribution and extreme value (Gumbel) distribution. The incorporation of statistical information in the simulation of complex deformation histories improves the reliability and robustness of predictions.

Finally, the effect of the microstructure and micro-scale properties on the macroscopic deformation resistance was investigated. Two case studies devoted to the quantitative evaluation of the deformation and stresses at the micro-scale using FIB-DIC and synchrotron XRD were conducted for welded and pre-crept samples, respectively. The experimental findings validate and further extend the applicability of the simulation framework that incorporates the modelling of complex thermomechanical processes. Experimental studies in combination with microstructure-based simulations capture the grain interaction scenarios during deformation for polycrystalline (super)alloys and allow the development of improved predictive design methods for enhanced structural integrity.

Acknowledgements

First and foremost, I would like to express my deepest gratitude to my supervisor Prof. Alexander M. Korsunsky, who inspired my passion for the research conducted in this thesis. He is always supportive and ready to help when I meet difficulties in my research and life. His brilliant ideas guided me throughout my DPhil study at Oxford and encouraged me to push the limit beyond my expectation. It has been a pleasure working with him. I hope we will have other opportunities to work together in the future.

I appreciate the help from my colleagues over the past four years. Many thanks to the former and current AMK group members: Zifan Wang, Cyril Besnard, Enrico Salvati, Chryssa Papadaki, Tom Moxham, Joris Everaerts, Fatih Uzun, Sisini Sasidharan, Simone Moriconi, Benjamin de Jager and Eugene S. Statnik. My special thanks to researchers at the Diamond Light Source, especially Igor Dolbnya and Oxana V. Magdysyuk, for helping my experiment. I would like to thank Kalin Dragnevski and Marzena Tkaczyk for their experimental help at LIMA. A special mention goes to my college supervisor Cathy Ye, who continually supports my life at Oxford.

I would further express my gratitude to my parents, my sister and my friends at Linacre college and the university. They have been incredibly supportive, and we have had lots of memorable moments. Their understanding and help supported me to go through tough times over the past four years.

Finally, I would like to thank my examiners for taking the time to read and preparing to examine my thesis – I look forward to discussing my work with you.

Selected Publications

The following papers have been either published or in preparation based on this thesis:

1. **Chen, J**., Salvati, E., Uzun, F., Papadaki, C., Wang, Z., Everaerts, J. and Korsunsky, A.M., 2020. An experimental and numerical analysis of residual stresses in a TIG weldment of a single crystal nickel-base superalloy. *Journal of Manufacturing Processes*, 53, pp.190-200.

2. **Chen, J**. and Korsunsky, A.M., 2021. Why is local stress statistics normal, and strain lognormal? *Materials & Design*, 198, p.109319.

3. **Chen, J**., Wang, Z. and Korsunsky, A.M., 2022. Multiscale stress and strain statistics in the deformation of polycrystalline alloys. *International Journal of Plasticity*, 152, p.103260.

4. **Chen, J.**, and Korsunsky, A.M., 2022. The Yield Volume Fraction approach to the description of the stress-strain curve of a nickel-base superalloy. *arXiv preprint arXiv:2206.12658*.

5. **Chen, J**., Wang, Z. Papadaki, C. and Korsunsky, A.M. The creep deformation of a new nickel-base alloy-by-design studied using synchrotron X-ray diffraction (submitted).

6. **Chen, J**., Wang, Z. and Korsunsky, A.M. A numerical study of the effect of discretization methods on the crystal plasticity finite element method (submited).

Below are other co-authored publications which are related to the subject of the thesis but are not a direct result of the thesis.

1. Wang, Z., **Chen, J**., Besnard, C., Kunčická, L., Kocich, R. and Korsunsky, A.M., 2021. In situ neutron diffraction investigation of texture-dependent Shape Memory Effect in a near equiatomic NiTi alloy. *Acta Materialia*, 202, pp.135-148.

2. Wang, Z., **Chen, J**., Besnard, C. and Korsunsky, A.M., 2020. Microstructure evolution in a severely cold-worked NiTi wire during ageing treatment: An in situ neutron diffraction study. *Materials Letters*, 281, p.128676.

3. Uzun, F., Salimon, A.I., Statnik, E.S., Besnard, C., **Chen, J**., Moxham, T., Salvati, E., Wang, Z. and Korsunsky, A.M., 2020. Polar transformation of 2D X-ray diffraction patterns and the experimental validation of the hDIC technique. *Measurement*, 151, p.107193.

4. Statnik, E.S., Salimon, A.I., Besnard, C., **Chen, J**., Wang, Z., Moxham, T., Dolbnya, I.P. and Korsunsky, A.M., 2020. Ovine Bone Morphology and Deformation Analysis Using Synchrotron X-ray Imaging and Scattering. *Quantum Beam Science*, 4(3), p.29.

5. De Jager, B., Moxham, T., Besnard, C., Salvati, E., **Chen, J**., Dolbnya, I.P. and Korsunsky, A.M., 2020. Synchrotron X-ray Scattering Analysis of Nylon-12 Crystallisation Variation Depending on 3D Printing Conditions. *Polymers*, 12(5), p.1169.

6. Wang, Z., **Chen, J**., Magdysyuk, O.V., Uzun, F. and Korsunsky, A.M., 2022. Ultra-fast quantification of polycrystalline texture via single shot synchrotron X-ray or neutron diffraction. *Materials Characterization*, 186, p.111827.

7. Wang, Z., **Chen, J**., Kocich, R., Tardif, S., Dolbnya, I.P., Kunčická, L., Micha, J.S., Liogas, K., Magdysyuk, O.V., Szurman, I. and Korsunsky, A.M., 2022. Grain Structure Engineering of NiTi Shape Memory Alloys by Intensive Plastic Deformation. *ACS Applied Materials & Interfaces*, 14(27), pp.31396-31410.

Table of Contents

1. Introduction 1
1.1 General background 1
1.2 Aims and strategies 3
1.3 Thesis scope 5
2. Literature review and methodology 9
2.1 Use of nickel-based superalloys 9
2.2 Strengthening mechanisms in nickel alloys 12
2.2.1 Work hardening 12
2.2.2 Solid solution strengthening 13
2.2.3 Precipitation hardening 13
2.2.4 Grain boundary strengthening 15
2.3 The nature of creep deformation 15
2.4 Residual stress 17
2.5 Residual stress evaluation techniques 19
2.5.1 Diffraction based methods 20
2.5.2 FIB-DIC ring-core method 24
2.6 Crystal Plasticity Finite Element Method 27
2.6.1 Crystal slip 30
2.6.2 Schmid's rule 31
2.7 The importance of multiscale and statistical analysis 32
2.8 Summary 33
3. Multiscale stress and strain statistics in the deformation of polycrystalline alloys 34
3.1 Introduction 34
3.2 Methodology 38
3.2.1 Rate-independent crystal plasticity formulation 38
3.2.2 Implementation of the CPFE model 40
3.2.3 Statistical distributions 44
3.3 Macroscopic response of RVE 45
3.3.1 The fitting of crystal plasticity model parameters 45
3.3.2 The effect of crystal orientation permutation on the statistical variation of overall stress 48

3.3.3 The effect of grain morphologies on the fluctuation of overall stresses 52
3.3.4 The effect of grain sizes on the fluctuation of overall stresses 60
3.3.5 Discretization and statistical induced size effect 65
3.4 The mesoscopic response of RVE 70
3.5 The microscopic response of RVE 72
3.6 The multi-scale investigation of mechanical response in two extreme realizations . 85
3.7 Analysis and conclusion 93
4. A numerical study of the effect of discretization on the crystal plasticity finite element simulation results 97
4.1 Introduction 97
4.2 Modelling methodology 99
4.2.1 Crystal plasticity formulation and hardening law 99
4.2.2 Microstructure generation procedures 100
4.2.3 Loading and boundary conditions 102
4.2.4 Model calibration and material parameters 103
4.3 Simulation results and discussion 104
4.3.1 The effect of discretization methods 104
4.3.2 The effect of discretization methods with various grain numbers 108
4.3.3 CPU time 115
4.4 Discussion 116
4.5 Conclusion 118
5. The statistical description of deformation process 120
5.1 Why is local stress statistics normal, and strain lognormal? 120
5.1.1 Introduction 120
5.1.2 Results and discussion 121
5.1.3 Conclusion 126
5.2 The Yield Volume Fraction approach to the description of the stress-strain curve of a nickel-base superalloy 126
5.2.1 Introduction 126
5.2.2 Methodology 128
5.2.3 Results and discussion 135
5.2.4 Conclusions 139
6. An experimental and numerical analysis of residual stresses in a TIG weldment of single crystal nickel-base superalloy 140

6.1 Introduction 140
6.2 Specimen and microstructure 144
6.2.1 Material and specimen 144
6.2.2 Microstructure and texture analysis 146
6.3 Residual stress evaluation and numerical simulation 148
6.3.1 FIB-DIC micro-ring-core milling for residual stress evaluation 148
6.3.2 FEM simulation 153
6.4 Result evaluation 160
6.4.1 Radial Residual Stresses 160
6.4.2 Hoop residual stress 161
6.5 Discussion 163
6.6 Conclusion 165
7. The creep deformation of a new nickel-base alloy-by-design studied using synchrotron X-ray diffraction 167
7.1 Introduction 167
7.2 Experimental procedure 170
7.2.1 Materials and creep tests 170
7.2.2 Synchrotron XRD experiment 172
7.3 Results and discussion 175
7.3.1 Material characterization 175
7.3.2 Lattice misfit 180
7.3.3 Phase fraction 182
7.3.4 Microstrain 183
7.3.5 Lattice parameter distributions 186
7.3.6 The statistical distribution of lattice parameter variation 191
7.4 Conclusion 193
8. Conclusions and Future work 195
8.1 Conclusions 195
8.1.1 Multiscale stress and strain statistics in the deformation of polycrystalline alloys 195
8.1.2 The effect of discretization methods on CPFEM 196
8.1.3 The statistical description of deformation process 197
8.1.4 Residual stresses and internal strains evaluation at multiscale 198

8.2 Future work 201
Appendix A 204
References 207

Nomenclature

FIB	Focus Ion Beam
DIC	Digital Image Correlation
XRD	X-Ray Diffraction
CPFEM	Crystal Plasticity Finite Element Method
RS	Residual Stress
FEM	Finite Element Method
SEM	Scanning Electron Microscopy
STEM	Scanning Transmission Electron Microscopy
EBSD	Electron Backscatter Diffraction
YVF	Yield Volume Fraction
FCC	Face-Centred Cubic
AM	Additive Manufacturing
APB	Anti-Phase Boundaries
LCF	Low Cycle Fatigue
KB	Kirkpatrick-Baez
XRPD	Synchrotron X-Ray Powder Diffraction
SE	Secondary Electron
BSE	Back-Scattered Electron
CCD	Charge-Coupled Device
FE	Finite Element
SC	Self-Consistent
CPFE	Crystal Plasticity Finite Element
CRSS	Critical Resolved Shear Stress
HAZ	Heat Affected Zone

EDM	Electrical Discharge Machining
TIG	Tungsten Inert Gas
PWHT	Post Weld Heat Treatment
ETMT	Electro-Thermo-Mechanical Testing
PID	Proportional Integral Derivative
DLS	Diamond Light Source
GSAS	General Structure Analysis System
SFE	Stacking Fault Energy
RVE	Representative Volume Element
FEDPP	Finite Element Diffraction Post-Processing
PBC	Periodic Boundary Conditions
MRD	Multiples of Random Distribution
ODF	Orientation Distribution Function
FIP	Fatigue Indicator Parameter
R-O	Ramberg-Osgood
CDF	Cumulative Distribution Function
PDF	Probability Density Function
IP	Integration Point
EPSC	Elasto-Plastic Self-Consistent

1. Introduction

1.1 General background

When gas turbine engines operate in service conditions, they experience extremely aggressive thermo-mechanical loading. To meet the demand for increased gas turbine performance, high-performance alloys should be developed to withstand higher stresses at working temperatures. Nickel-based superalloys are extensively used in the manufacturing of gas turbine blades and vanes for several decades due to their high-temperature strength and excellent oxidation resistance. The need to increase the efficiency of aeroengines requires elevated turbine inlet temperature. Over the last few decades, the working limit temperature has increased from 650 ℃ to 750 ℃ for powder metallurgy Ni-based superalloys. Figure 1.1 illustrates the usage of nickel-based superalloys in different sections of a jet engine.

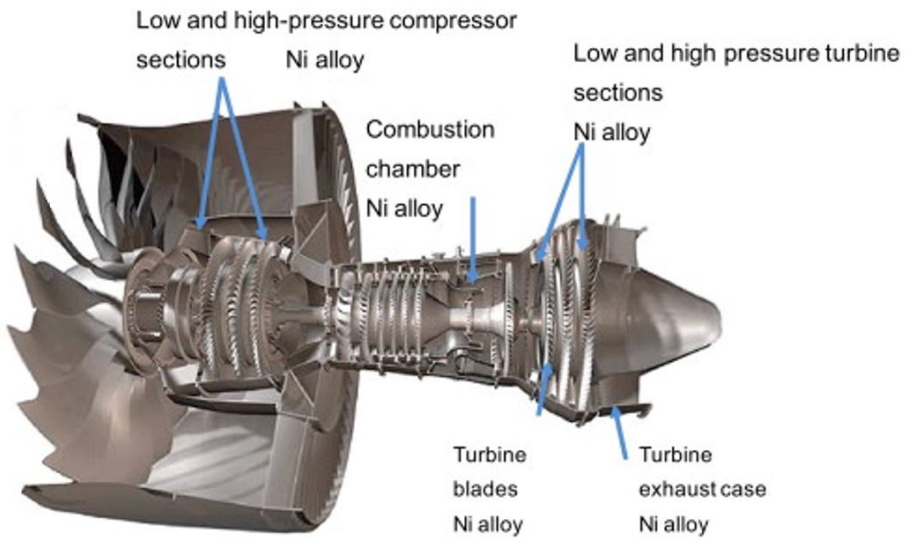


Figure 1.1. Nickel-based superalloys used in gas turbine engines [1].

The stress in gas engines varies during a typical flight cycle which includes taking off, cruising and landing stages. It can be simplified into three main parts: first, there is a stress increase at a constant rate, followed by stress holds at the maximum value, and finally an unloading part. The temperature profile and stress states that accompany this loading are complex and non-proportional so that both high stress/high temperature and high stress/low temperature combinations are encountered. During subsequent cooling, the surface layers of the material experience temperature reduction and shrinkage, which leads to tensile stress accompanied by creep that may lead to damage.

Most of the metallic materials in use are polygranular, which means that they consist of distinct domains of materials (grains), in terms of crystal orientation, phase composition and lattice structure, etc. In polycrystalline materials such as nickel-base superalloy, both the elastic and plastic deformation are highly inhomogeneous. Consequently, engineering failures often originate from localized regions even when the macroscopic strain is small. A typical fatigue fracture surface tomography in a turbo-engine compressor blade is presented in Figure 1.2. It is well accepted that fatigue crack initiation starts mainly at surface or subsurface defects, such as pores or inclusions. Up to now, the lifetime evaluation of aerospace components is still mainly based on *macroscopic* properties, safety factors and continuous examination of component defects, although it is *localized* strain and stress field that determines the failure of components. It is therefore essential to find the relationship between micro-scale deformation processes and macro-scale response.

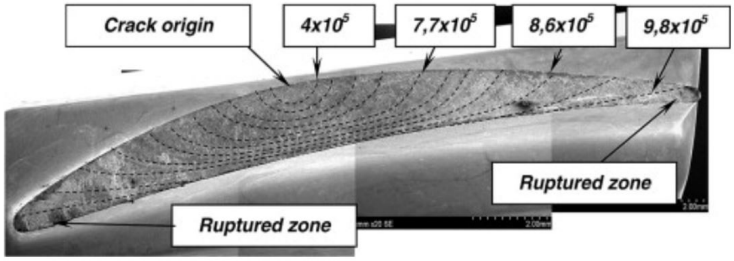


Figure 1.2. View of a damaged compressor blade in fatigue test [2].

1.2 Aims and strategies

A considerable amount of research work has been conducted on the thermo-mechanical processing in nickel superalloys over the past twenty years. However, very limited data is available in terms of the accompanying residual stress states down to the grain level i.e. intergranular and intragranular Residual Stress (RS). Investigating the deformation behaviour of nickel superalloys requires insights not only into the structural and mechanical property changes but also into the RS that exert significant influence on structural integrity. The presence of residual stresses can increase the likelihood of time-dependent failure by contributing to the driving force for crack initiation and propagation. In polycrystalline material, elastic and plastic deformation depends on the crystal lattice orientation and can be highly anisotropic. Hence, depending on their crystallographic orientation with respect to the loading axis, grains experience different magnitudes of stress during deformation and yield at different remote applied stress, giving rise to heterogeneous stress fields between adjacent grains and within individual grains. Therefore, the critical assessment of RS at both macro-scale (Type I) and grain level (Type II and III) is important for the correct prediction of mechanical failure. This thesis is concerned with the multiscale deformation behaviours

of polycrystalline materials before failure occurs, especially when the loading point shows strong strain localization.

The present research project evaluates multi-scale internal strains and stresses in nickel-base superalloys subjected to thermal and mechanical loading. As highlighted in the introduction, the relationship between local deformation processes and the global response is an area of particular interest. The ultimate objective is to improve the material processing and provide a more reliable component life prediction.

The research employs both experimental work and simulation to study the local deformation during loading and after unloading. The global response of superalloy can be readily extracted from the overall mechanical behaviour of simulation and experimental data. The local strains and stresses are evaluated by FIB-DIC, synchrotron XRD, continuum and crystal plasticity finite element method (FEM). The project begins with the investigation of describe the deformation process in polycrystals using statistical distribution by modelling method. To this end, the statistical distribution of stresses and strains at different scales was studied by CPFEM simulations. The most notable finding reveals that local elastic strain, as well as stress, were found to obey a normal distribution, whereas the statistics of local plastic strain conforms to a lognormal distribution. This part of the research also includes the Yield Volume Fraction approach to the description of the stress-strain curve of a nickel-base superalloy using lognormal distribution and extreme value distribution. The incorporation of statistical information in the simulation of complex deformation histories improves the reliability and robustness of predictions. Additionally, a numerical study was performed to investigate the effect of discretization method in

CPFEM.

Another objective of this project is to evaluate the residual stresses and internal strains at multiscale using experimental technique. Two case studies are presented in this part of the project. In the first case, the microscale properties and residual stresses in a weldment were investigated using FIB-DIC and continuum FEM. This is followed by quantitative evaluation of material properties, including lattice parameters, misfit, phase volume fraction and microstrain in crept samples using scanning electron microscopy (SEM), scanning transmission electron microscopy (STEM), electron backscatter diffraction (EBSD) and synchrotron XRD. The experimental finding validates and further extends the applicability of the simulation results from only mechanical loading conditions to thermomechanical processes.

1.3 Thesis scope

In this thesis, a series of advanced experimental and simulation techniques have been used to evaluate the magnitude and statistical distribution of multiscale strains and stresses within deforming polycrystalline superalloys. A summary of the thesis is outlined below.

Chapter 2 – Literature review

Chapter 2 provides a detailed review of the literature relating to the usage and peculiar properties of nickel-base superalloy. The chapter subsequently explores the latest progress regarding the experimental evaluation of residual strain and simulation method for polycrystalline materials.

Chapter 3 – Multiscale stress and strain statistics in the deformation of polycrystalline alloys

In Chapter 3, crystal plasticity FEM was employed to investigate the statistical distribution of deformations at macro-, meso- and micro-scale. The strains and stresses were found to behave distinctly differently at different scales. The findings revealed the nature of stress and strain inhomogeneity at multiple scales and emphasized the fact that the dispersion of local stress and strain is much larger than that of the macroscopic average. The statistical analysis of stress and strain distribution at multiple scales provides rich insights into the connection between microstructure and mechanical properties.

Chapter 4 – A numerical study of the effect of discretization methods on the crystal plasticity finite element method

In Chapter 4, a large number of simulations with static and grain-based mesh were performed to investigate the discretization deviations in CPFEM. Static mesh tends to smooth the stress/strain profile at the grain boundary, and more stress/strain discontinuities exist in grain-based mesh compared to static mesh. It is then suggested that static mesh is more desirable when investigating the *macroscopic* behaviour of the materials and grain-based mesh is recommended to study the *local* response using CPFEM.

Chapter 5 – The statistical description of deformation process

In the first part of Chapter 5, The origins of local strain and stress statistics were given fundamental consideration. Local elastic strains, as well as stresses, were found to obey a normal distribution, whereas the statistics of local plastic strain was found to conform to a

lognormal distribution. The results reveal the nature of strain inhomogeneity at the microscale and emphasize the fact that elastic strain accumulation represents an additive process, whereas plastic deformation is a multiplicative process. In the second part of Chapter 5, a new approach is developed to describe the tensile stress-strain curve based on the Yield Volume Fraction (YVF) function. The most important finding is that the YVF model can achieve excellent agreement with observations when the lognormal and extreme value distributions are employed to express the cumulative and incremental YVF. The results in this chapter highlight the potential for more extensive use of statistical methods in the description of material deformation response

Chapter 6 – An experimental and numerical analysis of residual stresses in a TIG weldment of single crystal nickel-base superalloy

In Chapter 6, the FIB-DIC micro-ring-core technique and a sequentially coupled thermo-mechanical finite element model were employed to assess the residual stress state near a weldment surface in the radial and hoop directions. Good agreement was obtained between experimentally evaluated residual stresses and refined numerical predictions. These findings were discussed in conjunction with the temperature history and residual stress self-equilibration.

Chapter 7 – The creep deformation of a new nickel-base alloy-by-design studied using synchrotron X-ray diffraction

In Chapter 7, the creep behaviour of a newly designed superalloy at 750℃/400MPa and 700 ℃/800MPa was systematically investigated using SEM, STEM, EBSD and

synchrotron X-ray diffraction. Spatially resolved measurements were performed to evaluate lattice parameters, misfit, phase volume fraction and microstrain in the reference and crept samples. STEM characterization of deformed materials reveals that multiple deformation mechanisms and defects could be identified in crept samples. The most important finding is that creep deformation is localized due to a symmetrical bell-shaped temperature profile along the sample.

Chapter 8 – Conclusions & future work

Chapter 8 summarises the key points of the thesis and discusses the direction of the remaining research questions.

2. Literature review and methodology

2.1 Use of nickel-based superalloys

Nickel-base superalloys exhibit high strength and creep resistance at elevated temperatures. These properties, together with their fatigue performance, microstructural stability, and high-temperature corrosion resistance have made them the materials of choice for the hot section of gas turbines, such as blades, discs, vanes, and combustion casings. On the other hand, the need for greater efficiency of engines caused an increase in the turbine inlet temperature and thus required the development of stronger, microstructurally and compositionally more complex, and more creep and oxidation-resistant superalloys [3,4].

The first wrought nickel-base superalloy used for turbine blades was introduced in the early 1940s. Increased operating temperature requires the addition of aluminium and titanium to obtain better creep resistance and higher strength through the formation of γ' phase with ordered FCC $L1_2$ structure [5]. In addition to alloy development, the introduction of vacuum melting and casting technology in the mid-1950s opened the way for the production of components made from high-performance alloys. Haynes 282 alloy is a wrought superalloy developed for critical gas turbine applications, such as exhaust sections, combustors, and nozzle components. It can be easily fabricated compared with currently available commercial superalloys and it possesses a unique combination of creep resistance, weldability, and thermal stability. Haynes 282 was used in the thesis to build virtual microstructure in simulation method.

The conventional casting process is suitable for producing nickel-base superalloys

with only a small amount of strengthening elements (Cr, Al, Ti, and Nb), since a large number of additional elements can cause segregation during the casting process. Therefore, powder metallurgy is developed to overcome the problem in casting superalloys. Compared with conventional cast and wrought superalloys, powder metallurgy superalloys have excellent properties, such as uniform microstructure, fine grains and no segregation, which make powder superalloy the preferred material for manufacturing aeroengine turbine disk. From a historical perspective, first generation powder metallurgy superalloys were designed to have high volume fractions of gamma prime and fine grain size to achieve better tensile strength at low and intermediate temperatures. Second generation powder metallurgy superalloys, like FGH96, were developed with lower gamma prime volume fractions and intermediate grain sizes to improve fatigue crack resistance. Third generation alloys powder metallurgy are focussed on high gamma prime volume fractions and intermediate grain sizes. Superalloys used for rotor discs for modern gas turbine engines are expected to operate at temperatures above 700℃, or even 800℃ for long periods of time. The operating temperature for most of the commercial superalloys ranges between 700℃ and 750℃. Above this temperature range, the yield strength of these alloys has been found to be insufficient for rotor discs in gas turbine engines. Alloy 11 is a newly developed powder metallurgy superalloy that are particularly suitable for producing gas turbine rotor discs at higher operating temperature (generally between 700℃ and 800℃). It is also relatively lightweight, resistant to environmental degradation, inexpensive and suitable for low cost manufacturing techniques. In this thesis, the creep mechanism for alloy 11 between 700℃ and 800℃ was examined for the first time.

In the subsequent turbine blade developments, more attention was concentrated on process optimisation and the control of grain orientation. Since grain boundary sliding is an important deformation mechanism during creep, grain boundaries can become a source of weakness under high stress and high temperature [6]. Directional solidification produces large, columnar grains and essentially eliminates transverse grain boundaries, thus providing further potential for the exploitation of nickel-base superalloys. Single crystal technology was soon developed to achieve total elimination of grain boundaries. In comparison with conventional casting and directional solidification polycrystalline superalloys, single-crystal blades exhibit excellent thermo-mechanical properties, particularly in respect of creep and fatigue resistance, and are therefore increasingly used in turbine blade and bane fabrication. Figure 2.1 illustrates three choices in grain structure in the development of nickel-base superalloy turbine blades. The single crystal superalloys are often classified into first, second and third generation alloys based on the content of rhenium. The addition of rhenium can improve the creep strength and fatigue resistance of single crystal superalloys. There is no rhenium in the first generation single crystal superalloys, while the second and third generations contain about 3% and 6% of rhenium, respectively. CMSX-4 is a second generation single crystalline superalloy containing 70% volume gamma prime. It is capable of higher stress/temperature operation of at least 1150℃. In this thesis, the weldability of CMSX-4 was studied by FIB-DIC micro-ring-core technique and a sequentially coupled thermo-mechanical finite element model.

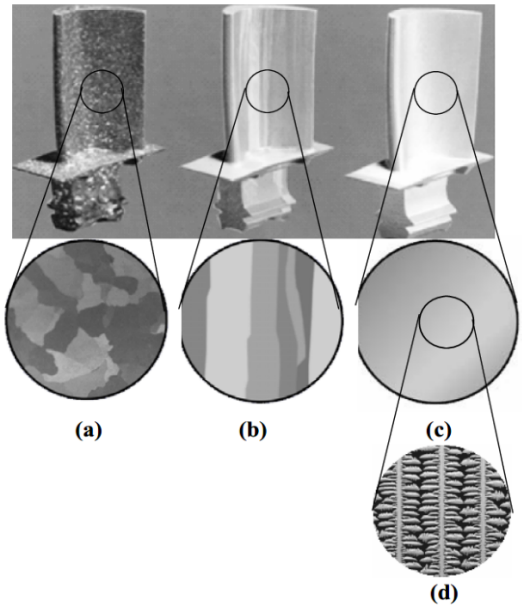


Figure 2.1. Advances in nickel-base superalloy turbine blades. (a) conventional casting, (b) columnar grains, (c) single crystal, and (d) a detailed view showing a dendritic structure in the single crystal blade [7].

2.2 Strengthening mechanisms in nickel alloys

2.2.1 Work hardening

In metallic crystals, a dislocation is defined as a linear crystallographic defect or irregularity within a crystal structure. Plastic deformation of a material usually occurs on a microscopic scale by the movement of dislocations, which correspond to an irregularity within a crystal structure in the form of a line defect of edge or screw character. As dislocation generation and movement within crystals occur, these interact to form ‘forest’, ‘pile-up’, ‘lock’ and ‘ladder’ structures that lead to increasing saturation of crystal volume with dislocations that prevent their further generation and movement. Hence, further plastic deformation is impeded, leading to macroscopically observed strengthening.

2.2.2 Solid solution strengthening

This strengthening mechanism allows increasing the strength of Ni alloys through the addition of alloying elements to form solid solutions. The solute atoms generate lattice distortions and local stress fields that impede dislocation motion, causing apparent strengthening. The difference in the volume and bonding between solute atoms and the matrix further contribute to the elastic interaction. Some other effects, including decreases in stacking-fault energy and impeding recovery rate, may also play a role [8,9].

2.2.3 Precipitation hardening

The peculiar thermo-mechanical performance of nickel-based superalloys mainly arises from the presence of an intermetallic phase, γ' precipitates $Ni_3(Ti, Al)$, which have an ordered FCC $L1_2$ structure. Figure 2.2 illustrates the crystal structure of γ and γ' phases in nickel-base superalloy. The γ matrix phase contains a disordered face-centred cubic (FCC) crystal lattice structure, while the γ' precipitate has an ordered FCC crystal lattice structure, having Al atoms at the corners of the unit cell and Ni atoms at the face centre.

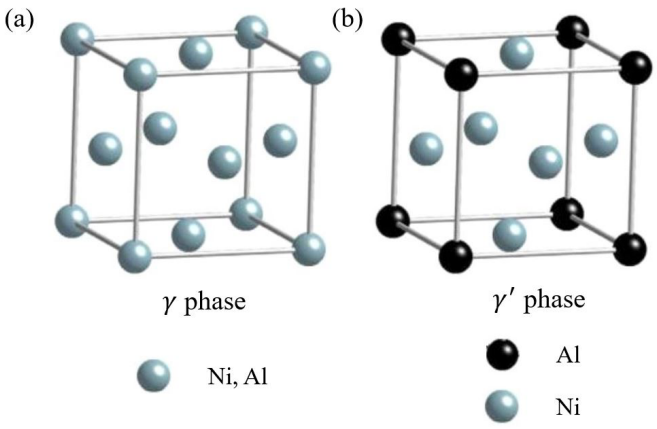


Figure 2.2. Crystal structure of (a) disordered γ matrix and (b) ordered γ' precipitate.

When dislocations travelling through the matrix encounter γ' particles, they are prevented from further easy glide and must undergo bowing, climb, splitting, and formation of anti-phase boundaries (APB) for further deformation to occur. Dislocation interacts with obstacles in one of three ways: particle cutting, particle bowing and climbing around particles. Many factors, such as stress, temperature, volume fraction, size and spacing of the particles, may affect the type of bypass mechanisms occurred. Particle cutting and bowing are most important at high stresses and low temperatures, but during creep where the stresses are relatively lower and the temperatures are greater than half of the melting point, diffusional and time-dependent dislocation climb becomes the most predominant precipitation hardening method. In addition, the changes of γ' phase size and morphology during service conditions will affect the particle/dislocation interaction mechanism. For small particles, it is easier for dislocations to cut through γ' phase, creating APB. For large particles, dislocations tend to bow or loop around particles. Figure 2.3 shows that there is a critical size of precipitates at which maximum strengthening occurs. This critical size is typically 5-30nm in modern nickel-base superalloys.

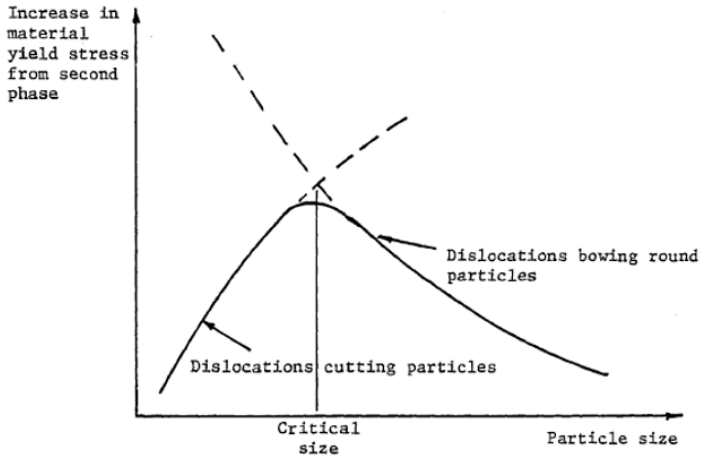


Figure 2.3. The relationship between particle size and strengthening [10].

2.2.4 Grain boundary strengthening

In polycrystalline metals, one grain usually has a different crystallographic orientation from its neighbouring grains. Dislocations must penetrate the grain boundary that presents an obstacle due to the discontinuity of slip planes between grains that impedes the movement of dislocations into adjacent grains [11]. Dislocations must also change their motion direction due to the different orientations of adjacent grains. Therefore, grain size can affect the number of dislocations piled up at the grain boundary and yield strength of the material. In general, yield stress increases with decreasing grain size, which is known as the Hall-Petch relationship that can be observed in most polycrystalline metals.

2.3 The nature of creep deformation

The temperature profile and stress states that accompany gas turbine blade and discs service conditions are complex and non-proportional so that both high stress/high temperature and high stress/low temperature combinations are encountered, causing detrimental creep deformation of nickel superalloys. Creep is the time-dependent deformation of a material when subjected to constant load or stress. The plot of creep strain versus time, which is demonstrated in Figure 2.4, can be divided into three categories: primary creep, secondary or steady-state creep, and tertiary creep. Primary creep has a continuously decelerating creep rate, implying that the material is experiencing an increase in creep resistance due to work hardening. During secondary creep, there is a constant strain rate because of the balance between strain hardening and recovery. Tertiary creep is a region of accelerating creep rate leading to ultimate rupture. The failure is on account of

both necking and grain boundary voids.

The mechanisms of creep in service are usually affected by changing conditions of stress, temperature and microstructure. Diffusion creep is a mechanism involving the diffusion of atoms or material transport. It tends to dominate at low stresses and relatively high temperatures. There are mainly two types of diffusion creep, depending on whether diffusion occurs through grain boundaries, termed Coble creep (activated at a lower temperature) or through the main body of the grains, known as Nabarro-Herring creep (favoured at high temperatures). Dislocation creep occurs by the motion of dislocations through crystal lattices. Dislocations can glide along slip planes and this requires little thermal activation. It becomes favourable at high stresses and relatively low temperatures.

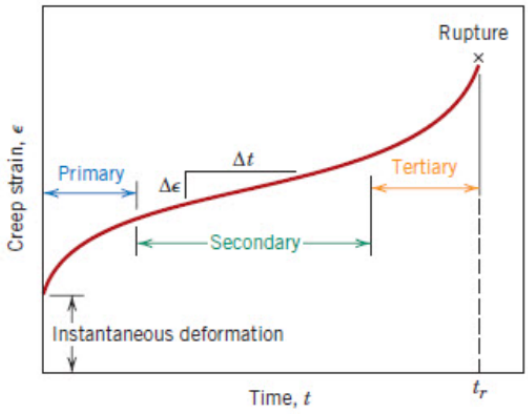


Figure 2.4. A typical creep curve [12].

Nevertheless, the creep curve of nickel-base superalloys usually shows a continuously increasing creep rate and lack of steady-state stages. This can be explained by the transition of the creep mechanism and microstructure. The main creep mechanisms of nickel-based superalloys are coarsening of γ/γ' microstructure, loss of interface coherency, growth of crystallographic pores and stacking fault [13]. The dominant creep mechanism at low

temperature is the shearing of γ' precipitates or cutting through γ and γ' phase by stacking fault, while at high temperature, the favourable creep mechanisms change to rafting of γ/γ' microstructure, dislocation climbing and loss of interfacial coherency [14]. The above creep mechanisms deteriorate the mechanical properties such as Low Cycle Fatigue (LCF) life and creep lifetime, which can be decreased by a factor up to 10 [13]. Larson and Miller suggest that the creep rupture time, stress and temperature could be described by the following empirical formulas [15]

$$(\sigma) = (20 + \log t_r)\ T/1000 \tag{2.1}$$

Where t_r is rupture time in hours and T is the absolute temperature. The Larson-Miller parameter, $P(\sigma)$, is an empirical function of applied stress.

2.4 Residual stress

Residual stress is that which presents within the material body without external loading and is self-balanced with its surroundings. It can be introduced into engineering components during manufacture e.g., casting, bending and welding processes, as a result of forces and thermal loading history. Consider welding as an example, only a localised zone undergoes melting during welding. The total volume of the molten metal trend to shrinkage during solidification, while the adjacent base metal provides a constraint for the volume changes. Residual stresses arise from the expansion/shrinkage and contraction between the weld metal and surrounding base metal during welding process. Apart from residual stress, the weldment may contain internal defects and microstructural changes that further deteriorate the mechanical properties of the component. Consequently, post-weld heat treatment is commonly used to alleviate residual stresses and reduce the risk of

cracking.

With the development of modern analytical and computational techniques, it is often feasible to evaluate the components lifetime in service conditions. However, this life prediction approach itself is not sufficient to obtain a reliable estimation of component performance due to the presence of residual stress. Residual stresses may be beneficial or deleterious for component performance. In many cases, the pre-existing sub-surface tensile residual stress can be detrimental to the performance of materials and lead to unexpected failure. On the other hand, compressive residual stress near the surface may be beneficial to fatigue life as they prevent crack initiation and propagation [16]. Therefore, many techniques, such as shot peening and laser peening, have been developed to introduce compressive residual stresses in the final products.

Normally, residual stresses may be categorized into three types based on length scale, namely type I, II and III stresses. Type I stresses are nearly homogeneous across macroscopic dimensions. Such stresses can be evaluated using continuum finite element methods (FEM) without consideration of grain-level behaviours. This is in contrast to type II or intergranular stresses which exist across grains due to the anisotropy of different grains or grain families and the constraints to deformation that occur between them. Type III stresses, on the other hand, are produced at the atomic level as a result of defects, dislocation motion/interaction and precipitates in materials and balance with a grain. The separation of stresses into these three types can be written in additive form, namely:

$$\sigma^{total} = \sigma^{I} + \sigma^{II} + \sigma^{III} \tag{2.2}$$

Figure 2.5 illustrates the distribution of residual stresses in polycrystals at different scales.

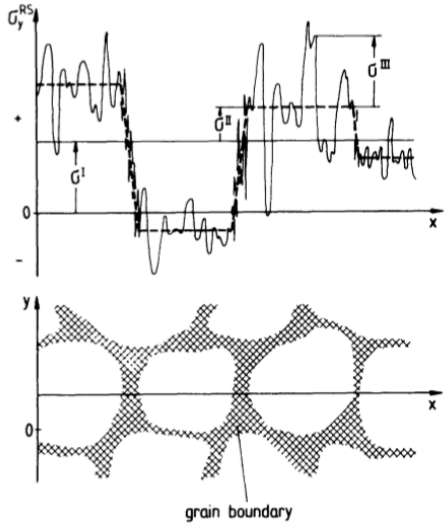


Figure 2.5. Multi-scale residual stress distribution in polycrystals [17].

2.5 Residual stress evaluation techniques

The evaluation of macro-scale residual stress has seen several decades of development, while grain-level stress assessment has only become available progressively in more recent years. The residual stress evaluation techniques can be classified into three principal approaches:

(1) *Destructive*. The contour method and sectioning technique are commonly used destructive approaches to determine RS by full destruction of the specimen being measured. They have been widely used in industry because of their practicability and cheap cost. The contour method determines residual stress by cutting a specimen into two pieces and measuring surface height maps along the free plane created by the cut. Combined with numerical modelling, it enables the evaluation of a 2D residual stress map normal to the measurement plane [18].

(2) *Semi-destructive*. Semi-destructive (minimally disturbing) methods are based on material removal and strain relief measurement. The structure integrity remains

well as only a small amount of material is removed compared to the destructive approach. The traditional semi-destructive techniques, such as deep hole drilling and centre hole drilling, can achieve ~1mm lateral resolution and ~0.03mm deep resolution. The need for probing residual stresses at microscale accelerates the development of material removal techniques at a finer scale. With help of a focused ion beam and scanning electron microscope, the FIB-DIC micro-ring-core method has been developed to evaluate RS on the scale from a few microns to sub-micron (Type II and Type III) [19].

(3) *Non-destructive*. Non-destructive methods allow RS evaluation based on measuring the effects of relationships between RS and small variations in physical parameters such as crystal lattice spacing by diffraction. Examples of non-destructive techniques include high-resolution electron backscattered diffraction (HR-EBSD), neutron diffraction and X-ray diffraction.

2.5.1 Diffraction based methods

X-ray diffraction is one of the most powerful residual stress analysis methods that can achieve sub-micron resolution with the help of synchrotron X-ray beams. These diffraction based methods, including X-ray and neutron diffraction, evaluate residual stresses by changes in material atomic lattice spacing. Diffraction based methods can achieve higher resolution and precision without destructing or removing material. Back in 1912, Max von Laue and colleagues came up with the idea to use a beam of X-rays to penetrate through a copper sulphate crystal and record the results on photographic plates. Multiple diffraction

spots were observed in their experiment. Laue's experiment first reveals that diffraction occurs when X-rays impinge on the repeating arrangement of atoms within the crystal. A regular array of scatterers produces a regular array of spherical waves. These waves collide and cancel out each other in most directions by destructive interference, while some waves collide in a few specific directions by constructive interference according to Bragg's law:

$$n\lambda = 2d\sin\theta \tag{2.3}$$

Here n is any integer, λ is the wavelength of the wave, d is the spacing between diffracting planes, and θ is the incident angle. As illustrated in Figure 2.6, Bragg's law provides a concise mathematical description of the relationship between lattice spacing, scattering angle and incident beam wavelength. With the development of instruments, the scatter angle can be precisely measured, and hence, for known incident beam wavelength, the lattice spacing can be determined by Bragg's law. Therefore, lattice strain can be determined using the relative change in lattice spacing.

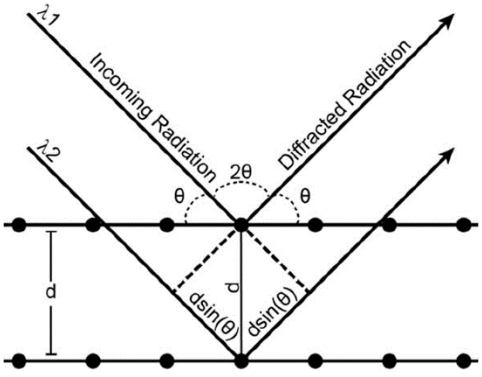


Figure 2.6. Schematic representation of Bragg's law conditions [20].

While early work involving XRD strain analysis can be performed using laboratory X-ray sources, they offer limited photon flux and less penetration depth. With the development of synchrotron radiation sources, extremely powerful X-rays (~100keV) can

be generated to investigate the bulk characteristics of the specimen. (Sub-)micron resolution can be achieved by further focusing the incident beam by optical methods, such as Kirkpatrick-Baez (KB) mirrors. Synchrotron X-ray powder diffraction (XRPD) is widely used for strain evaluation, texture analysis and phase identification in crystalline materials. XRPD typically employed a monochromator to generate a monochromatic beam which is characterised by a single constant wavelength with small bandwidth. The selection of wavelength is highly dependent on the sample thickness, X-ray absorption property of the material and beamline characteristics. XRPD operates under the assumption that the sample is untextured i.e. grains are randomly orientated. The beam size for XRPD should be significantly larger than the averaged crystalline size so that a statistically significant number of grains are within the illumination volume. When X-ray interacts with a sufficient number of crystallites, the Bragg condition will be achieved for random azimuthal angle and many crystallites will be in the proper orientation to diffract the X-rays. Consequently, Debye-Scherrer cones are formed for different half of the scattering angle θ, as illustrated in Figure 2.7. The diffraction pattern can then be collected using an area detector.

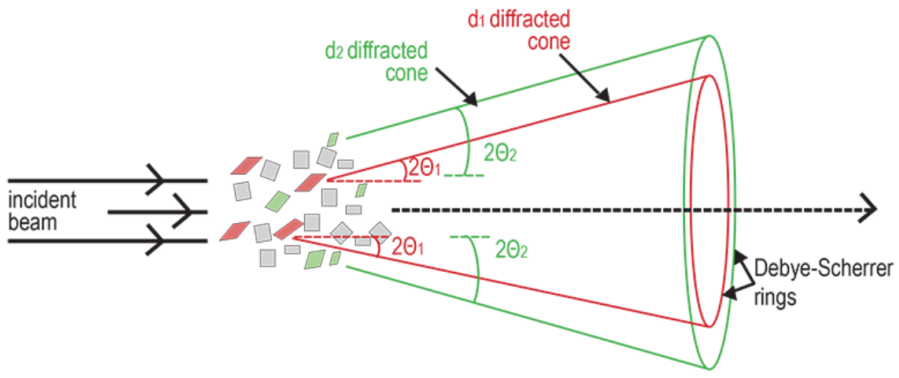


Figure 2.7. Schematic illustration of Debye-Scherrer rings obtained from XRPD [21].

XRPD can be carried out using transmission mode or reflection mode. Figure 2.8 gives an example of a typical diffraction pattern, which is characterized by beam intensity versus scattering angle. Based on the analysis of peak position, height and half-width change, quantitative description of lattice parameter/composition change, atom density and permanent deformation can be made. Diffraction patterns from calibration samples are needed in each experiment to generate well-known Debye-Scherrer rings from which sample-to-detector distance can be determined using fitting software such as DAWN [22]. The crystal structure can be refined using the full pattern analysis technique called Rietveld refinement. Diffraction peaks are typically described by a combination of Gaussian and Lorentzian functions.

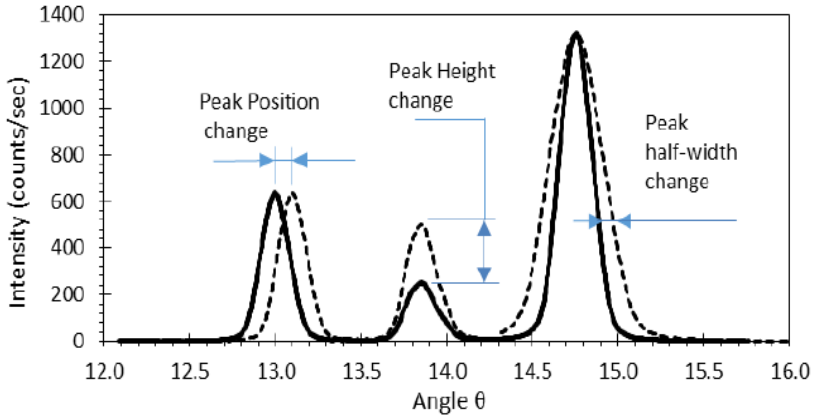


Figure 2.8. A typical diffraction pattern [23].

EBSD stress evaluation technique relies on the inverse problem of eigenstrain (caused by any inelastic process), and it enables sub-micron reconstruction of residual stress by using the residual elastic strain data on a free surface. Nevertheless, its accuracy is also limited by the reliability of a reference and it is rather time-consuming and expensive [24].

However, there are mainly two limitations to these diffraction-based methods. These

techniques rely on the comparison of relative changes in the measured parameters with stress-free lattice parameters. This means that their accuracy is limited by the reliability of a reference. Another limitation is that these approaches are only applied to crystalline or polycrystalline materials, not suitable for amorphous materials [25].

2.5.2 FIB-DIC ring-core method

Another promising residual stress measurement method that can overcome these shortcomings is based on material removal and strain relief measurement. When a cut is performed on the material surface, strain relief will take place on the subsurface, which provides quantitative information on the residual stress state before cutting. With the development of material characterization tools, such as Focused Ion Beam (FIB) and Scanning Electron Microscopy (SEM), it becomes feasible to perform this semi-destructive method from macroscale to microscale, or even nanoscale. At microscopic scale, the strain relief is usually tracked using Digital Image Correlation (DIC) technique. Generally, this semi-destructive method can be categorized according to the milled material geometry, for example, H-bar [26], slot cutting [27], hole drilling [28] and ring-core milling [23, 25, 29].

In the last decade, the FIB-DIC micro-ring-core method has been well developed on account of increasing accessibility of SEM and FIB systems, as well as improved DIC software. In this method, FIB is employed to mill incrementally a circular trench or micropillar in the material surface. A contrasting pattern is deposited by Pt or Au on the micropillar top surface. It is then possible to measure the strain relief using DIC software

in successive SEM images [30]. As the milling depth increases with the FIB milling process, the strain relief first increases and then saturates, as shown in Figure 2.9. Finite element simulation shows that the residual stress is completely relieved when the micropillar depth becomes comparable with its diameter [31].

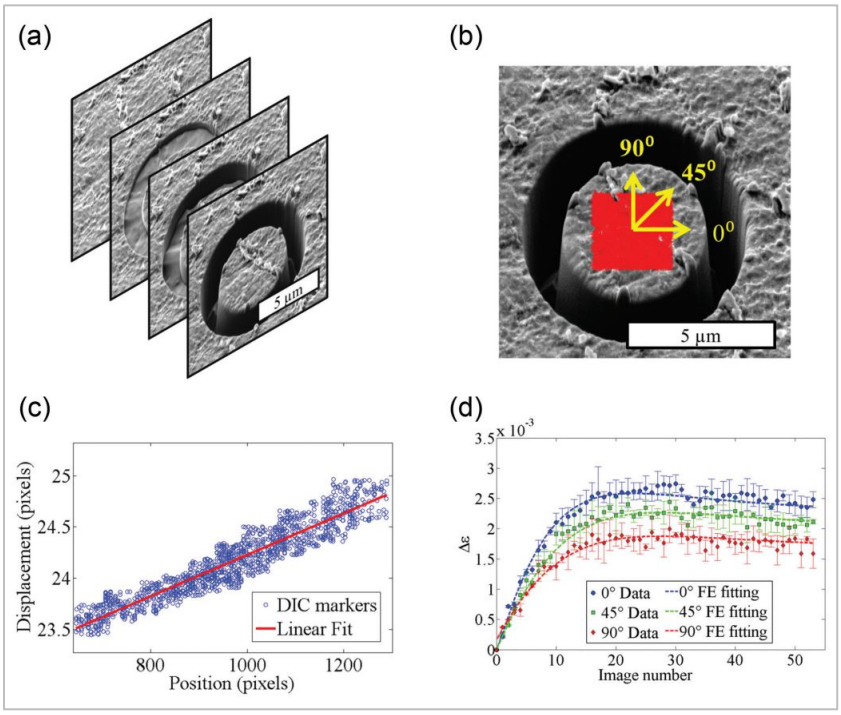


Figure 2.9. (a) An illustration for the incremental acquisition of SEM images obtained during FIB milling. (b) DIC marker tracking on the central core region. (c) Gradients of the displacement against position plots provide strain estimates at each milling depth. (d) Strain relief analysis is performed in three directions (0°, 45° and 90°) [31].

A fitting function derived from finite element modelling is employed to determine the complete elastic strain relief value. Accordingly, together with the knowledge of material elastic properties, the pre-existing local residual stress can be reconstructed from the strain relief using Hooke's law:

$$\sigma_{xx} = \frac{E}{(1-v^2)}\left[\varepsilon_{xx} + v\varepsilon_{yy}\right] \tag{2.4}$$

$$\sigma_{yy} = \frac{E}{(1-v^2)}\left[\varepsilon_{yy} + v\varepsilon_{xx}\right] \tag{2.5}$$

In the above equations, E is Young's modulus, v is Poisson's ratio, and ε_{xx} and ε_{yy} are the components of residual elastic strain in the corresponding directions. Multiple FIB-DIC measurements can be performed at different locations to obtain the desired stress profile. For polycrystalline materials, FIB-DIC enables probing Type I and Type II residual stresses by varying the ring-core diameter. Figure 2.10 represents two possible cases when choosing FIB-DIC ring-core geometries. When the ring-core diameter is in the same order of magnitude as the average grain size, only one or two grains are included in the gauge volume. Therefore, the measurement, in this case, is sensitive to Type II. On the other hand, when the ring-core diameter is twice the order of magnitude as grain size, several grains are included in the gauge volume. As a result, the contribution from Type II will be averaged out in this case, and the measured residual stress is closer to Type I (macroscopic).

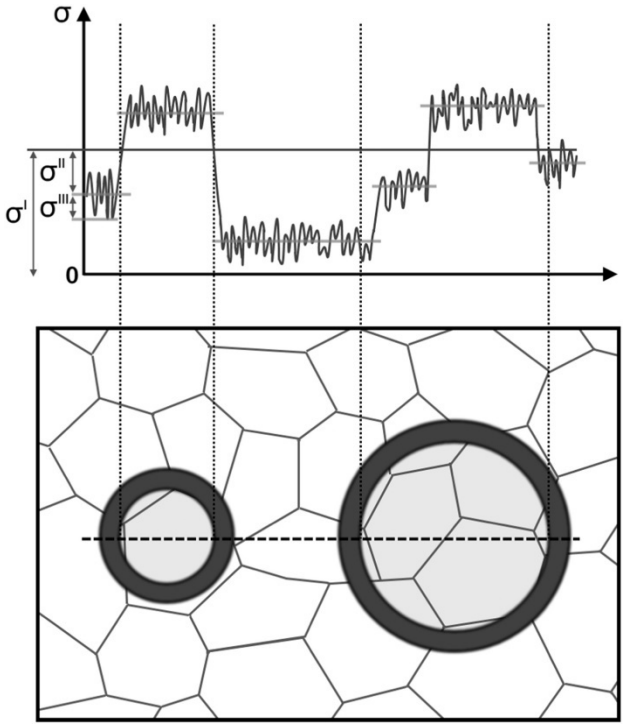


Figure 2.10 Illustration of Type I, Type II and Type III stress profile along a line, and the relation between ring-core diameter and averaged grain size [32].

In comparison to other non-destructive through-thickness averaging methods (e.g. neutron and synchrotron X-ray diffraction techniques), FIB-DIC method does not require the knowledge of stress-free lattice parameters, thus providing absolute residual stress value. Also, the applicability of this method is much wider, and it can evaluate residual stress in non-crystalline materials. In addition to in-plane RS evaluation, FIB-DIC can be employed to reconstruct depth profiles of RS in the case of equi-biaxial RS states [33] and even non-equi-biaxial RS states [25]. So far, despite extensive previous work, the application of this novel method has merely focused on the strain relief of the interior micropillar and has been limited only to the case of RS at the final state. However, in many cases during strain-controlled loading, the stress state is time-dependent rather than constant. Further research should concentrate on the strain relief of exterior cutting part than the interior micropillar. Since the strain relief of exterior part changes correspondingly with external stresses, it is then possible to evaluate the time-dependent RS by using exterior FIB-DIC micro-ring core technique.

2.6 Crystal Plasticity Finite Element Method

Until the early 1980s, the modelling of elastoplastic deformation mainly relied on phenomenological formulations at the macroscopic level. Continuum level models neglect the microstructural representation of the heterogeneous nature of the materials, and hence are incapable of providing a reliable prediction of the deformation process when the relevant length scale is down to microns. Since then, many studies were carried out to establish the foundation of computational plasticity frameworks based on crystal slip [34, 35]. At that

time, the vast majority of crystal plasticity simulations were applied to simulate the anisotropic deformation behaviour of single crystals or bicrystals, due to the limitation of computing power. The modelling of polycrystals has become possible and increasingly popular with the development of high-performance computing. Over the past 20 years, researchers have proposed various methods to improve the formulation and implementation of polycrystal plasticity theory [36-40]. The most widely used modelling approaches among them are self-consistent (SC) and finite element (FE) based methodologies that include empirically or physically based elastoplastic crystal slip constitutive equations and a detailed representation of microstructure. The elastoplastic SC approach was developed by Hill [41] based on Eshelby's research [42] and first implemented by Hutchinson [43]. The implementation of the SC model is based on a population of ellipsoidal grains chosen with a distribution of orientations and volume fractions that match the measured texture. It provides a particularly elegant and efficient way to account for some principal aspects of material microstructure. However, some limitations of this approach have been reported in many studies. SC method can give a fair prediction but is only limited to a very specific morphology of the components, and also does not provide information on the statistics of strain and stress within grain groups. Additionally, the effect of grain boundaries cannot be captured well by the self-consistent model, and hence, strain localization might be underestimated by neglecting the effect of neighbouring grains [44, 45]. For these reasons, finite element methods have gained ever greater momentum alongside self-consistent models in the field of computational mechanics. The implementation of crystal plasticity formulations within the FE framework is referred to as crystal plasticity finite-element

(CPFE) methods. Compared with self-consistent methods, the CPFE approach provides a more effective way to model the deformation kinematics of materials with complicated geometries subjected to mixed boundary conditions.

CPFE method can be employed at microscopic and macroscopic scales. Microscopically, it is widely used to simulate the inter- and intra-grain mechanical behaviour where the contact and boundary conditions are difficult to control or monitor in the experiment. On the macroscopic side, CPFE method is mostly utilized in the fields of large-scale forming and texture simulations, where appropriate homogenization schemes are required to represent the phase and texture of the materials under study. This can be achieved by employing the concept of a representative volume element (RVE). The present model in this thesis was implemented using the rate-independent constitutive equations following Manonukul & Dunne [46]. It was further modified and extended to account for elastic anisotropy, and to allow three-dimensional analysis for materials with various crystal structures. Dini, Korsunsky & Dunne introduced the diffraction post-processing interpretation to simulate the intragranular strains that can be directly comparable with the results of diffraction measurements [47]. Multiscale modelling can be achieved with the help of RVE and diffraction post-processing interpretation. The macroscopic and microscopic stress/strain can be readily collected from the overall response of the whole RVE and each integration point, respectively. At the mesoscopic scale, the inhomogeneous deformation is characterized by the anisotropic response that originates from different grain families, which can be captured via the use of diffraction post-processing of finite element simulation results. The aim of the usage of multiscale modelling approach is to find the

relationship between local deformation processes and global response, and the it is then possible to provide more reliable deformation prediction and to optimise thermomechanical processing.

2.6.1 Crystal slip

There are mainly two types of deformation in micromechanics, namely crystal slip and twinning. Twinning is often concerned for commercially pure metals rather than superalloys. Therefore, crystal slip is the only mode of plastic deformation considered in this thesis.

The origin of plasticity in crystalline materials is crystal slip. Metal atoms have a periodic arrangement and repeated microstructure, known as a crystal. Plastic deformation, such as slip in nickel-base superalloy, can be defined as the sliding of blocks of crystal relative to one other. Crystal slip can be easily seen in single crystal uniaxial loading test. Figure 2.11 illustrates the slip of a single crystal micro pillar specimen under compression loading. The breaking and re-combining of bonds contribute to dislocation movement, leading to slip planes shown in Figure 2.11. Millions of dislocations move at the same time, causing a large displacement.

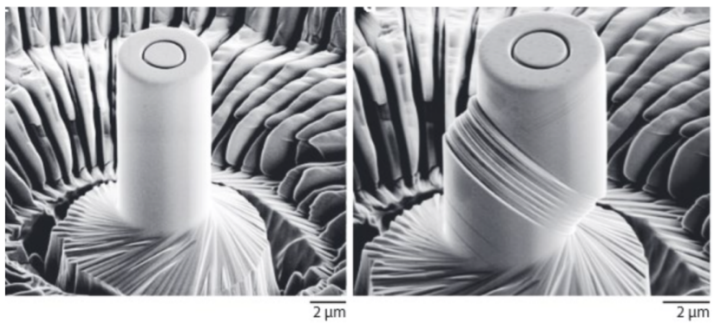


Figure 2.11. SEM image of single crystal micro pillar specimen under compression [48].

Slips in metal often occur in the highest atomic density direction with the shortest lattice vector. The combination of a slip plane and a slip direction is called a slip system. The crystal structure of the nickel-base superalloys researched in this project is face-centred cubic (FCC), and it has 12 $\langle 1\bar{1}0\rangle\{111\}$ slip systems as shown in Figure 2.12.

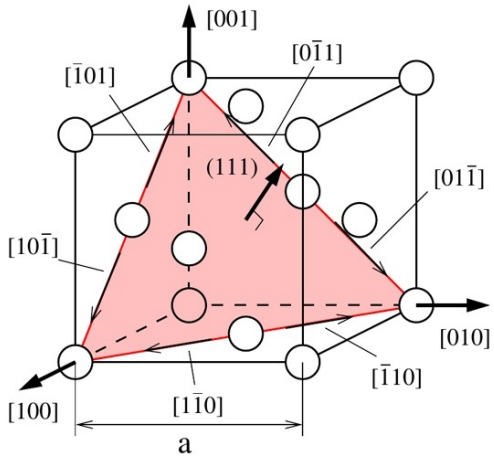


Figure 2.12. Slip systems in FCC structure [49].

2.6.2 Schmid's rule

Critical resolved shear stress (CRSS) is the component of shear stress resolved on a crystal slip system, it is the necessary stress to initiate slip in a grain. According to Schmid's rule, crystal slip will start when the shear stress resolved in the slip direction is greater than CRSS.

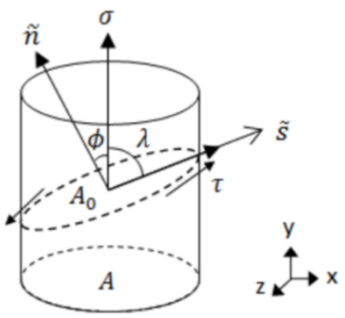


Figure 2.13. A single crystal bar with a slip system.

Figure 2.13 is a schematic diagram to show the calculation of resolved shear stress using Schmid's rule. In the picture, $\boldsymbol{n}$ is the slip plane normal, $\boldsymbol{s}$ represents the slip direction, $\boldsymbol{\sigma}$ is the tensile stress applied to the single crystal rod. The tensile stress $\boldsymbol{\sigma}$ causes shear stress on the slip plane. The area of the slip plane is: $A_0 = A/cos\ \emptyset$. The force component in the slip direction can be calculated as $A{\cdot}\sigma{\cdot}\cos\ \lambda$. Where A is the area of cross section, ϕ is the angle between tensile stress and slip plane normal, λ is the angle between tensile stress and slip direction. Therefore, the shear stress applied on the slip plane is the force component in the slip direction divided by the area of the slip plane:

$$\tau = \boldsymbol{\sigma} cos\lambda cos\emptyset = \boldsymbol{\sigma}(\boldsymbol{t}\cdot\boldsymbol{n})(\boldsymbol{t}\cdot\boldsymbol{s}) \tag{2.6}$$

Where $\boldsymbol{t}$ is the unit vector in tensile stress direction and $\boldsymbol{s}$ is the slip direction vector. Researchers often use the Schmid factor to describe the relative crystal slip orientation. The smaller Schmid factor values are called "hard" orientation, while the larger values correspond to "soft" orientation.

2.7 The importance of multiscale and statistical analysis

The deformation of polycrystalline materials is highly heterogeneous. In many cases, the macroscopic stresses (type I) are zero, while the magnitude of intergranular (Type II) and intragranular (Type III) RS may be comparable to the material yield point, leading to earlier component failure. While a considerable number of studies have concentrated on the convergence of the macroscopic average properties, comparatively less attention has been paid to the *statistical distributions* of the local mechanical behaviour within a small volume of interest. Furthermore, failure in polycrystalline alloys under cyclic loading frequently

originates in highly localized fields where intergranular and intragranular strain and stress dominate. Most failure criteria are extremely sensitive to the existence of stress concentration owing to inclusions or triple points that often have a much smaller influence on the homogenized response. Consequently, investigating the residual stresses at different scales, especially Type II and III, is critical for understanding the performance of engineering components in service, as it allows the development of improved design methods for enhanced structural integrity. A pointwise residual stresses simulation and experimental evaluation with material microstructure remain rather costly and time-consuming, whereas a statistical description of strains and stresses may improve the understanding of the deformation process.

2.8 Summary

This chapter reviews the current literature on the experimental and numerical evaluation of strains and stresses at multiscale. A thorough review suggests that multiscale statistical analysis of stress and strain evaluation requires significant further development in order to provide more reliable deformation prediction. The focus of the Chapter 3 and 4 is to study the relationship between microscopic deformation processes and macroscopic response using CPFEM simulation. Chapter 5 provides a statistical description of deformation process, and Chapter 6 and 7 present two further experimental case studies of residual stress and internal strain evaluation.

3. Multiscale stress and strain statistics in the deformation of polycrystalline alloys

3.1 Introduction

In polycrystalline metallic materials such as nickel-base superalloys, the deformation response in both elastic and plastic regimes is highly anisotropic. Depending on their crystallographic orientation with respect to the loading axis, and also depending on the immediate neighbourhood, grains deform to different extents to carry disparate magnitudes of stress under different applied loads, giving rise to heterogeneous stress fields between adjacent grains and within individual grains. Alongside the anisotropy of stiffness and yield resistance of single crystals, the polycrystal grain morphology (grain shapes and sizes) are also important constitutive aspects of the microstructure of polycrystalline aggregates [50]. In order to conduct rational and reliable experimental and numerical investigations of the behaviour of polycrystalline materials with complex microstructure, it is essential to obtain statistical descriptions of the crystallographic orientation and grain morphology within the material body, and establish their effects on the overall mechanical response of the material.

The implementation of crystal plasticity formulations within the FE framework is referred to as crystal plasticity finite-element (CPFE) methods. RVE is a powerful tool for modelling the effect of micro- and mesoscale heterogeneities on the overall mechanical response of components at the macroscopic level. So far, several definitions and determination methods of RVE have been proposed for different proposes. One of the most commonly used definitions in the literature introduced by Hill states that an RVE must

include a sufficient number of micro-heterogeneities (grains, inclusions, voids, etc.) to obtain the effective properties of heterogeneous materials [41]. The meaning of this statement is twofold: (a) all possible microstructural configurations must be statistically described and (b) the mechanical behaviour of RVE should be correct independently of the boundary condition type. A more explicit definition was proposed by Drugan & Willis who define RVE as the smallest material volume within components that provides a sufficiently accurate representation of the **mean** constitutive response [51]. This approach is based on the idea of homogenization for an infinite medium and does not consider the fluctuations of the effective properties over finite domains. Kanit et al. added statistical consideration to the concept of RVE [52]. Based on Kanit's definition, one single RVE is not enough to get an accurate estimation of effective properties, while a sufficient number of realizations should be simulated to obtain a desired precision for the estimation. This appears to be the first approach that uses multiple realizations and adopts a statistical procedure to analyse the results.

The above review of various definitions of RVE suggests that there has been no systematic quantitative criterion proposed so far for the determination of RVE. As a consequence, the element size used by one author may not be suitable for the research performed by another, leading to some confusion when determining the size of RVE. Although there is a large diversity of criteria used by different researchers, some common considerations are well accepted. The RVE size should be large enough to contain sufficient information about material microstructure to be considered as representative, on the other hand, and it should be computationally efficient and hence small enough with regard to the

macroscopic dimensions [53]. While considering the process of RVE determination, the question of stability is always of interest and importance. The mechanical response of RVE can be influenced by statistical size effects caused by uncertainty arising from a poor choice of samples. Such effects can be controlled by increasing the number of realizations to reduce statistical uncertainty. Accordingly, statistical–numerical RVE determination techniques were proposed over the past 15 years. Kanit et al. created a general framework for RVE determination based on the correlation of numbers of realizations and relative error for linear elastic properties [52]. Gitman, Askes & employed the same RVE determination procedure to deal with non-linear material behaviour [54], but was still based on a very small number of realizations that cannot be statistically representative in the case of highly non-linear mechanical responses such as plastic slip. Furthermore, this approach does not quantitatively reproduce how effective properties vary between different realizations. To the best of the authors' knowledge, there is no report providing a mathematical description of the distribution of effective properties among a sufficient number of nominally identical RVEs. While a considerable number of studies have concentrated on the convergence of the macroscopic average properties (e.g. homogenized response), comparatively less attention has been paid to the *statistical distributions* of the local mechanical behaviour within RVE. Failures in polycrystalline alloys under cyclic loading frequently originates in highly localized fields where intergranular and intragranular strain and stress dominate. Most failure criteria are extremely sensitive to the existence of stress concentration owing to inclusions or triple points that often have a much smaller influence on the homogenized response, as previously discussed for several heterogeneous systems [55-57]. Local plastic

slip distributions have been widely studied and it is well known that they follow an exponential distribution within the RVE, and an extreme value distribution when comparing the maxima of several RVEs [58, 59]. Therefore, the frameworks for RVE determination based only on the macroscopic average properties are usually not valid, hence more attempts should be made to investigate the mechanical behaviour at the mesoscopic and microscopic scales along with the attendant statistics.

The inhomogeneous nature of strain and stress distribution has led to the concept of three types of stresses which describe the spatial variation over different length scales. Type I stresses are nearly homogeneous across macroscopic dimensions. Such stresses can be evaluated using the average effects over many grains of RVE without consideration of the behaviour of individual grain. This is in contrast to Type II or mesoscopic stresses which equilibrate over grain scale. It can be calculated from orientation-dependent lattice strain via X-ray diffraction [4] and neutron diffraction [60] measurement. Type III stresses, on the other hand, vary at the sub-grain and down to atomic dimensions and balance within a grain. Analogous to stress, strain can also be categized into three types based on different length scales. In many cases, the macroscopic stresses and strains (Type I) have specific values under a given applied load, while the magnitude of mesoscopic (Type II) and microscopic (Type III) stresses and strains may vary significantly through the body and be responsible for controlling the onset of failure. Consequently, investigating the stresses and strains at different scales, especially at the mesoscale and microscale, is crucial for understanding the performance of engineering components in service, as it allows the development of improved design methods for enhanced structural integrity.

The objective of the present research in Chapter 3 is to study the nature and the statistical distribution of the fluctuation of stresses and strains in polycrystalline alloys using different realizations of RVE with various microstructures. In this chapter, a microstructurally flexible CPFE model was employed to simulate the mechanical properties of a polycrystalline alloy at the macro-, meso- and micro-scale. The model describes the macroscopic response to monotonic and cyclic loading for a range of RVE implementations. Material properties and grain orientations were assigned at integration points, with each grain containing dozens of integration points. The stress and strain magnitudes in each integration point were extracted, thus providing for the data for the quantification of microscopic deformation heterogeneity within grains. Additionally, via the use of finite element diffraction post-processing (FEDPP), the stress and strain field history were interpreted in terms of crystallographic orientation such that the mesoscopic properties (e.g. grain-orientation averages) could be extracted. The reproduced behaviour for average grain family elastic strains was then validated by matching the results of experimental neutron diffraction measurements.

3.2 Methodology

3.2.1 Rate-independent crystal plasticity formulation

The formulation is based on the multiplicative decomposition of the deformation gradient $\boldsymbol{F}$ into elastic and plastic parts

$$\boldsymbol{F} = \boldsymbol{F}^E \boldsymbol{F}^P \tag{3.1}$$

The material undergoes plastic slip γ^α on the slip system α, through the undeformed

crystal lattice, expressed as

$$\boldsymbol{F}^{P} = \boldsymbol{I} + (\boldsymbol{s}^{\alpha}\boldsymbol{n}^{\alpha T})\gamma^{\alpha} \tag{3.2}$$

Here $\boldsymbol{I}$ is the identity tensor, $\boldsymbol{s}^{\alpha}$ and $\boldsymbol{n}^{\alpha}$ are two mutually orthogonal vectors describing the slip direction and normal, respectively. The term $\boldsymbol{F}^{E}$ represents elastic stretching and rigid-body rotations. The stress rate at arbitrary points within a grain during the deformation process is given by

$$\dot{\boldsymbol{\sigma}} = \boldsymbol{C}:\boldsymbol{D} - \boldsymbol{\sigma} tr(\boldsymbol{D}) - \boldsymbol{\Omega\sigma} + \boldsymbol{\sigma\Omega} - \sum_{\alpha=1}^{N}(\boldsymbol{C}:\boldsymbol{P}^{\alpha} + \beta^{\alpha})\dot{\gamma}^{\alpha} \tag{3.3}$$

Here $\boldsymbol{C}$ is the elastic moduli tensor, $\beta^{\alpha} = \boldsymbol{W}^{\alpha}\boldsymbol{\sigma} - \boldsymbol{\sigma}\boldsymbol{W}^{\alpha}$, $\boldsymbol{W}^{\alpha}$ being the skew part of the velocity gradient, and $\boldsymbol{P}^{\alpha}$ the symmetric part of the velocity gradient. $\boldsymbol{D}$ describes the deformation rate, and $\boldsymbol{\Omega}$ denotes the spin tensor. All active slip systems will contribute to the overall plastic strain rate. The constitutive model uses a critical resolved shear stress, τ_c^{α}, as a state variable for the determination of plastic flow on each slip system α. When the resolved shear stress on the αth slip system, τ^{α}, exceeds the current critical resolved shear stress τ_c^{α}, that slip system is considered to become active. The critical resolved shear stress reflects the resistance of a slip system, and is allowed to evolve as a consequence of the current dislocation density and substructure. The yield surface has a polygonal shape in the stress space. The conditions under which a slip system is active are based on the yield and loading-unloading criteria. In order to calculate the Cauchy stress rate, the shearing rate $\dot{\gamma}^{\alpha}$ on the α th active slip system should be determined. The magnitude of $\dot{\gamma}^{\alpha}$ can be determined using the constitutive equation for plastic slip on each slip system,

$$\dot{\tau}_c^{\alpha} = \sum_{\alpha=1}^{N} \boldsymbol{h}_{\alpha\beta}\, \dot{\gamma}^{\alpha} \tag{3.4}$$

Where τ_c^{α} is the current critical resolved shear stress. The hardening modulus $\boldsymbol{h}_{\alpha\beta}$

represents the hardening on slip system α due to shearing on slip system β. The rate of change of the resolved shear stress is given by

$$\dot{\tau}^{\alpha} = \boldsymbol{P}^{\alpha}: \left(\boldsymbol{C}: \boldsymbol{D} - \boldsymbol{C}: \sum_{\alpha=1}^{N} \boldsymbol{P}^{\alpha}\, \dot{\gamma}^{\alpha} - \boldsymbol{\sigma}\mathrm{tr}(\boldsymbol{D})\right) + \beta^{\alpha}: (\boldsymbol{D} - \sum_{\alpha=1}^{N} \boldsymbol{P}^{\alpha}\, \dot{\gamma}^{\alpha}) \tag{3.5}$$

To satisfy the consistency condition during plastic slip,

$$\dot{\tau}^{\alpha} = \dot{\tau}_{c}^{\alpha} \tag{3.6}$$

And hence, from Equations (3.4) and (3.5)

$$\sum_{\alpha=1}^{N} \boldsymbol{h}_{\alpha\beta}\, \dot{\gamma}^{\alpha} = \boldsymbol{P}^{\alpha}: \left(\boldsymbol{C}: \boldsymbol{D} - \boldsymbol{C}: \sum_{\alpha=1}^{N} \boldsymbol{P}^{\alpha}\, \dot{\gamma}^{\alpha} - \boldsymbol{\sigma}\mathrm{tr}(\boldsymbol{D})\right) + \beta^{\alpha}: (\boldsymbol{D} - \sum_{\alpha=1}^{N} \boldsymbol{P}^{\alpha}\, \dot{\gamma}^{\alpha}) \tag{3.7}$$

Equation (3.7) can be rewritten in the form

$$\sum_{\alpha=1}^{N} \boldsymbol{A}_{\alpha\beta}\, \dot{\gamma}^{\alpha} = b^{\alpha} \tag{3.8}$$

When the matrix $A_{\alpha\beta}$ is singular, the above equation has non-unique solutions. This problem can be overcome by using a singular-value decomposition to obtain a pseudo-inverse of the matrix $A_{\alpha\beta}$ [46], and it is adopted here. The hardening modulus matrix can be simply described as

$$\boldsymbol{h}_{\alpha\beta} = \left[q + (1-q)\boldsymbol{\delta}_{\alpha\beta}\right]h. \tag{3.9}$$

Here h is the self-hardening rate and q denotes the latent-hardening ratio, with values in the range $1 < q < 1.4$. Hence, four material parameters need to be set in this model: the initial critical resolved shear stress τ_{c}^{α}, two hardening parameters, and the elastic moduli matrix.

3.2.2 Implementation of the CPFE model

There are mainly three types of RVE meshing homogenization methods for polycrystalline materials that are based on crystal plasticity theory: the voxel RVE model,

truncated octahedron-based model and grain-based RVE model. The voxel model consists of cubic finite elements and each element corresponds to an individual grain. It is an efficient and effective way to model the collective behaviours of RVE, while this mesh method cannot be used to capture the grain shape or the heterogeneous intragranular deformation. The grain morphology in the truncated octahedron-based RVE model is more realistic represented than the voxel and grain-based model. Nevertheless, the required computation time of truncated octahedron-based RVE is much higher compared with the voxel and the grain-based model. Some research suggests that the detailed features of grain morphology have a relatively small influence on the collective behaviours of RVE [55]. Besides, the improvement of simulation accuracy achieved by octahedron-based RVE is not equivalent to the simulation time consumed [61]. Therefore, the grain-based RVE model is employed in current research. In the grain-based RVE model, each grain consists of many cubic elements, so it can effectively capture more details about grain morphologies and sizes distribution in polycrystalline materials. Such RVE model has been extensively used nowadays to investigate the grain scale tensile deformation [61], fatigue indicator parameters [62, 63] and texture evolution [64] in different types of polycrystalline alloy.

Some published examples of RVEs used in the polycrystalline CPFE model, total numbers of grains and averaged number of elements with a single grain are listed in Table 3.1. According to the published data, 20-100 elements per grain is sufficient to perform grain level deformation analysis. Thus, for the purposes of the present study we select a grain-based RVE with 30x30x30 elements and 600 grains that are accurate for the investigation of grain level stress and strain.

Table 3.1. Examples of grain-based RVEs used in previous CPFE studies.

Material	Total numbers of grains	Total numbers of element	Average number of elements/grain	Reference
Cu	125	8000	64	[65]
Ti-6Al-4V	263	13824	52	[62]
Al	1000	64000	64	[66]
Steel	151	12800	85	[67]
Al	3181	125000	39	[68]
Al	1000	27000	27	[69]

The crystal plasticity constitutive equations are implemented in the form of a user-defined material subroutine UMAT within the nonlinear finite element analysis package ABAQUS. Grain-based RVE models with periodic microstructure are generated using the DREAM.3D software [70]. Lognormal grain size distribution and random grain orientation are used to construct the RVEs. Texture can be described by the choice of grain orientation distribution function (ODF). In this thesis, a set of RVE together with the assigned initial crystal orientations are referred to as a *microstructural realization*. It can be used to investigate statistical material response induced by a number of realizations once the deformation model is validated by one realization. $30 \times 30 \times 30$ finite element meshes were introduced to the RVEs by using eight-node continuum elements (C3D8) of ABAQUS. The RVE used for validation contains 600 randomly oriented grains is shown in Figure 3.1. The objective of this chapter was to use a simple but powerful numerical model to capture

the multiscale nature of stress and strain distributions in polycrystalline materials. Each implementation of an advanced CPFE model for computational polycrystalline plasticity is predominantly considered as an instance for statistical purposes. However, the point-to-point and grain-to-grain variations contain rich information about real physical phenomena.

Some researchers have investigated the influence of crystal plasticity hardening framework on the deformation behaviour of polycrystalline materials. Lim et al. found that slip-based hardening constitutive equations can accurately reproduce the single and polycrystal response of dislocation density-based hardening [55]. Additionally, slip-based hardening law shows smaller relative error and smaller mesh sensitivity compared to dislocation density-based constitutive equations. Their finding provides a firm basis for the selection of phenomenological constitutive equation (slip-based) hardening law in this research. To make the statistics result in this research widely applicable, a simple phenomenological constitutive equation is employed, and general conclusions are drawn.

Good results in terms of macroscopic (stress-strain curve) and mesoscopic (diffraction validation) response of materials can be achieved via using the grain-based RVE model with 600 grains. Figure 3.1 illustrates the initial configuration of the RVE with periodic microstructure subjected to Periodic Boundary Conditions (PBC). In polycrystalline materials, the deformation of RVE can be non-uniform even if a uniform external loading is applied. It is well-known that PBC leads to smaller RVE sizes than a homogeneous boundary. PBC is implemented by coupling the displacements of the nodes of each pair of opposites faces of the RVE. Any over-constraint should be avoided when coupling nodes in eight vertices and twelve edges. The constraint equation is set by using the open-source

ABAQUS plugin tool EasyPBC [71]. In this study, 8373 constraint equations are generated for the constructed RVE model. After setting the periodic boundary, displacement constraints are applied at RVE vertexes and a displacement-controlled loading is applied at the dummy node that constrains the relative displacement between the front and back surface in the third direction. The RVE has a cubic shape with a total volume of $1\times1\times1 mm^3$. All the simulations were performed at room temperature.

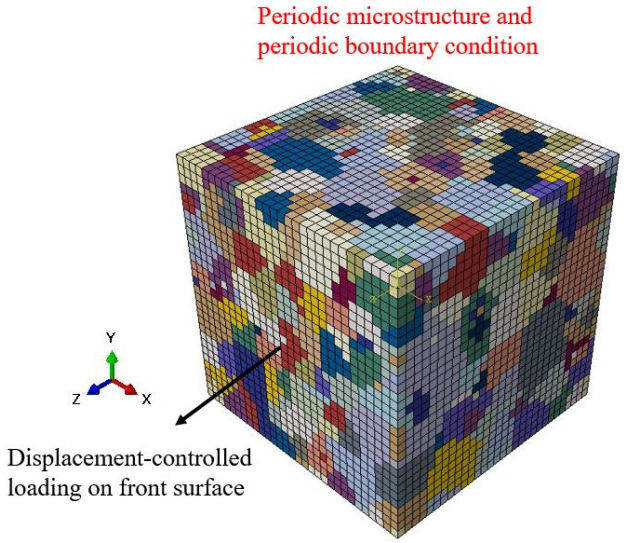


Figure 3.1. The RVE model was subjected to periodic boundary conditions. Note: different colours represent different grains.

3.2.3 Statistical distributions

Statistical analysis was carried out of the grain morphology and deformation characteristics of RVE polycrystalline assemblies. In this chapter, the spatial position of grains was randomly distributed, and the grain diameter was spatially non-correlated. Statistical distributions of size and stress-strain values during deformation were found to evolve towards continuous Gaussian (normal) and lognormal distributions. The normal probability density function is given by

$$f(x|\mu,\sigma) = \frac{1}{\sigma\sqrt{2\pi}} \exp\left\{\frac{-(x-\mu)^2}{2\sigma^2}\right\} \quad (3.10)$$

where μ and σ are the mean and standard deviation of the variable x, respectively.

The lognormal distribution is expressed by the function

$$f(x|M,S) = \frac{1}{xS\sqrt{2\pi}} \exp\left\{\frac{-(\ln x-M)^2}{2S^2}\right\} \quad (3.11)$$

where M and S are respectively the mean value and standard deviation of the variable $\ln x$.

3.3 Macroscopic response of RVE

3.3.1 The fitting of crystal plasticity model parameters

To calibrate the elastic and hardening parameters, the macroscopic response of RVE was first fitted to the monotonic stress-strain curve for Haynes 282 alloy (a nickel-based superalloy). The crystal structure of this alloy is face-centred cubic (FCC), and it has 12 $\langle 1\bar{1}0\rangle\{111\}$ slip systems. Figure 3.2 shows the grain morphology and orientation within one RVE realization. A set of discrete grain orientations was generated to get random texture described by the Euler angles using Bunge's notation (shown in Figure 3.2 (b)). The randomness of orientation can be further described by the multiples of random distribution (MRD) illustrated in Figure 3.2 (c). The MRD value is the normalized probability density of a given orientation. It describes the factor by which specific orientations of crystallites are over-represented compared with the random condition. A higher number of MRD means a stronger texture, while a lower number represents a weaker texture. Under ideal conditions, an MRD value of 1 means perfectly random orientation. The values in Figure 3.2 (c) are quite close to 1, indicating the set of orientations are randomly distributed and the grains are

not textured. It is important to note that the same ODF is employed throughout the chapter.

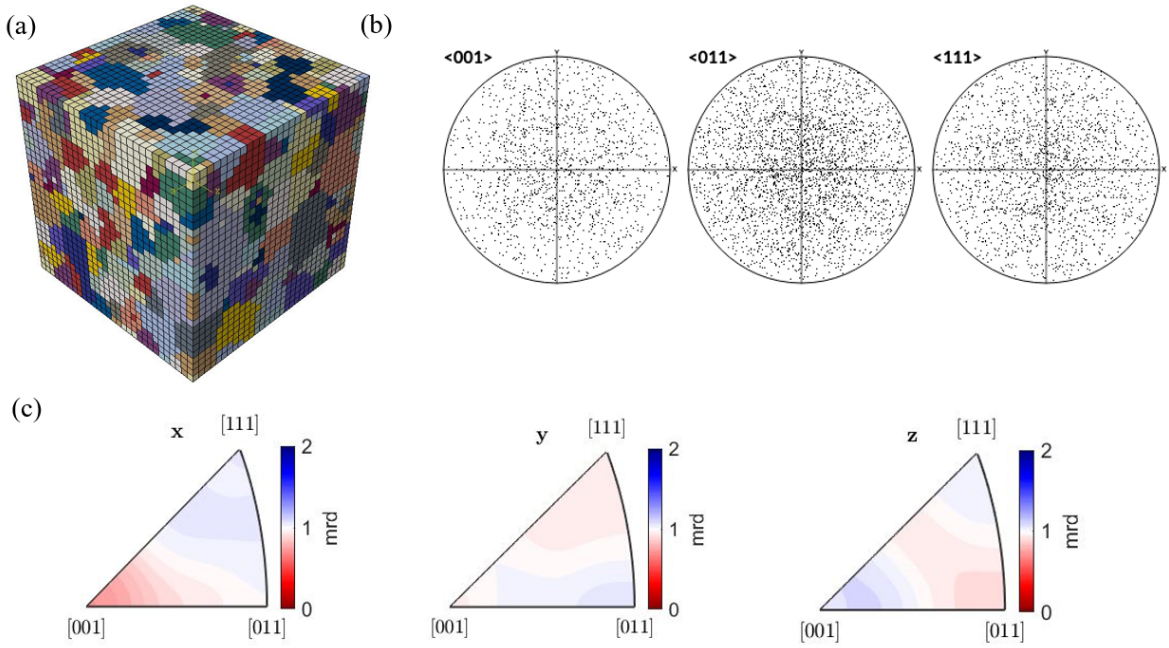


Figure 3.2. The microstructure of RVE used for material parameters fitting. (a) microstructure (b) pole figures in three directions (c) multiples of random distribution for the used orientation.

Macroscopic stress and strain can be obtained from the overall response of the whole RVE. The material parameters that need to be fitted in this model are single-crystal elastic moduli, critical resolved shear stress and hardening parameters. In order to get a reliable evaluation of the above parameters, it is essential to reproduce both the macroscopic behaviours by fitting the macroscopic stress-strain curve and the mesoscopic property by matching the simulation result with neutron diffraction measurements. Optimal values of crystal stiffnesses can be determined by fitting the mesoscopic response of RVE obtained from finite element diffraction post-processing in the elastic region to neutron diffraction measurement of orientation-specific elastic strains. A detailed description of diffraction post-processing can be found later in this chapter. The macroscopic stress-strain curve can then be employed to evaluate the critical resolved shear stresses and hardening parameters.

The macroscopic tensile stress-strain response obtained from the simulation is shown in Figure 3.3, together with the experimental data [72]. An excellent agreement has been achieved between CPFE reproduction and experimental observation. The corresponding elastic modulus matrix parameters, the critical resolved shear stress and hardening parameters are listed in Table 3.2. Here, we are interested in statistical analysis of the multiscale deformation behaviours of polycrystalline materials before failure occurs, especially when the loading point shows strong strain localization. Failures often originate from localized regions even when the macroscopic strain is small. When the global strain is 1.55%, the maximum plastic slip locally is ~6-7% in our model. Finally, it should be noted that at the chosen total strain level the contributions from elastic and plastic are of approximately similar magnitude. This represents the most difficult condition for description compared to cases when either elastic or plastic deformations dominate.

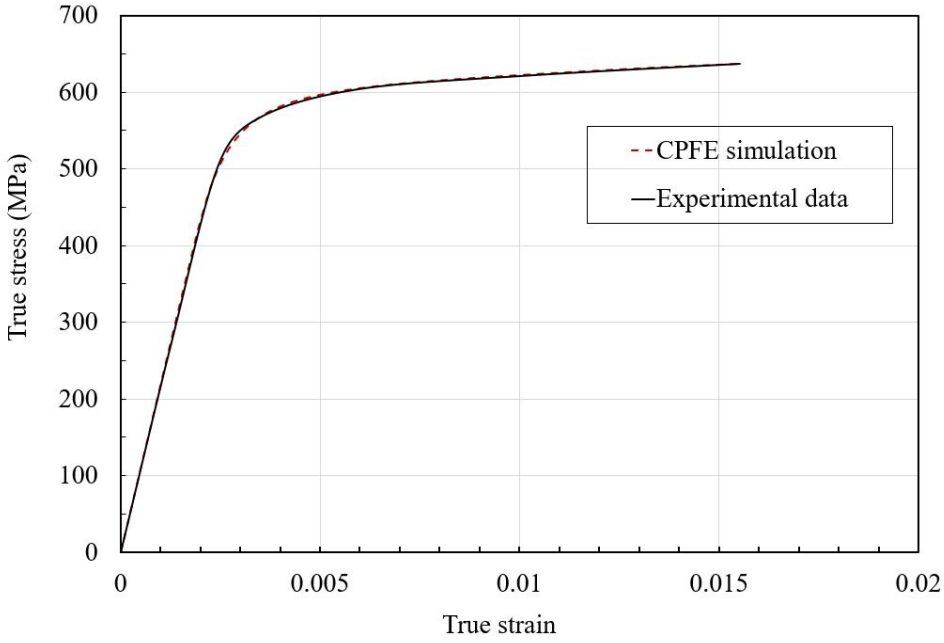


Figure 3.3. Illustration of the macroscopic stress-strain curves under monotonic loading obtained from CPFE reproduction and experiment.

Table 3.2. Material parameters used in the simulation.

Stiffnesses (GPa)			CRSS		
C11	C12	C44	(MPa)	h	q
250	160	118	257	$h = h_F\left[1 + (h_R - 1)\exp(-100 h_{exp}\,\varepsilon)\right]^*$	1.01

$^*h_F = 950, h_R = 14, h_{exp} = 4.$

3.3.2 The effect of crystal orientation permutation on the statistical variation of overall stress

In the first part of the chapter, we focused our attention on the effect of *crystal orientation permutation*. We introduced this term to describe the variation of orientation assignment to grain seeds, and hence grains, without changing any of the individual grain shapes. The equivalent of this mathematical contrivance is not possible experimentally but is extremely useful in that it allows separating the influence of grain orientation from that of grain size and shape.

The RVE model calibrated against experimental data was run with 48 realizations that used identical grain shapes, but randomly re-assigned orientations, to study the influence of orientation permutation on the material response statistics. In each of the 48 realizations, the grain morphologies are identical to each other, while the numbered list of crystal orientations is permuted randomly. Therefore, these realizations possess the same grain morphology and orientation distribution function, but correspond to different orientation permutations. In such a way, it is possible to eliminate the effect of grain morphology and to study the sensitivity of the mechanical response to one particular aspect i.e. crystal

orientation.

The macroscopic stress-strain curves for all 48 realizations were obtained, and statistical analysis was performed to obtain the deviation between each curve and the average of them. The tensile loading was displacement-controlled, and all simulations were stopped when RVE reached 1.55% total strain. The overall stress $\sigma_{1.55\%}$ in each realization was collected. Figure 3.4 illustrates the averaged stress-strain curves using a group of 12, 24, 36 and 48 realizations. As expected, the averaged curves gradually approach a certain 'true' average when the number of realizations increases, implying that the 3D cube considered is an effective RVE. The overall stresses in all realizations were averaged, and the difference from the mean value was calculated. As the dataset was too large to represent in one graph, the difference from the mean of 16 randomly chosen realizations is illustrated in Figure 3.5. There is an apparent increase in scattering at the elastic-plastic transition region. The difference from mean first changes approximately linearly as the strain increases within the elastic region, and then shows a largely nonlinear relationship once the material begins to deform plastically. Analogous results could be obtained from the standard deviation of all 48 realizations. Once again, an apparent separation between the elastic and plastic regions can be recognised in the standard deviation curve depicted in Figure 3.6.

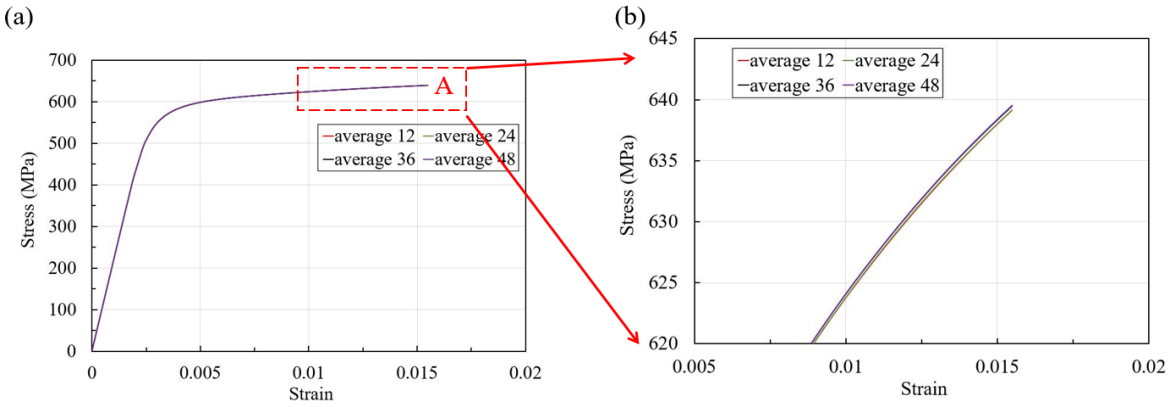


Figure 3.4 (a) The averaged uniaxial stress-strain curves using 12, 24, 36 and 48 realizations. (b) An enlarged view of the rectangular area A.

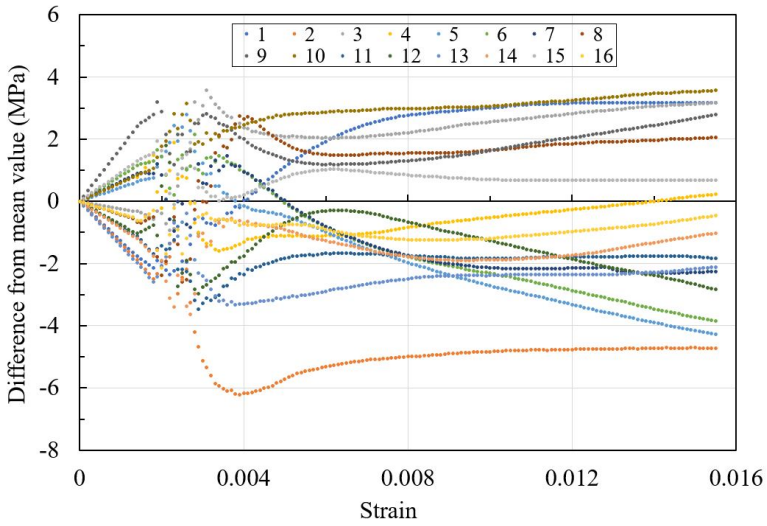


Figure 3.5. The difference from the mean obtained from 16 realizations.

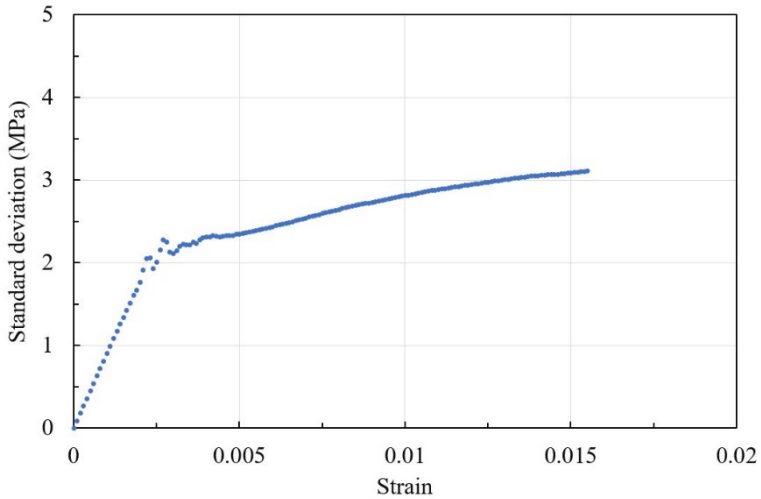


Figure 3.6. The standard deviation of 48 realizations obtained during the loading process.

To describe the statistics and to visualize the distribution of the simulation output, a histogram of overall stresses across 48 simulations was built and is shown in Figure 3.7. Interestingly, the fluctuation of overall stresses at 1.55% total strain obtained from 48 simulations appears to follow a normal distribution. The Gaussian function fit to the histogram is shown by the continuous curve. The goodness of fit did not show significant improvement when the total number of realizations was increased above ~48. It was concluded that a further increase in the number of realizations was not warranted, as it would only raise the effort in terms of CPU time and hard drive space required without evident accuracy return. Despite some minor deviations between the fitting curve and points of the histogram, the fitting was reliable and allowed concluding that the overall stresses across all simulations follow a normal distribution.

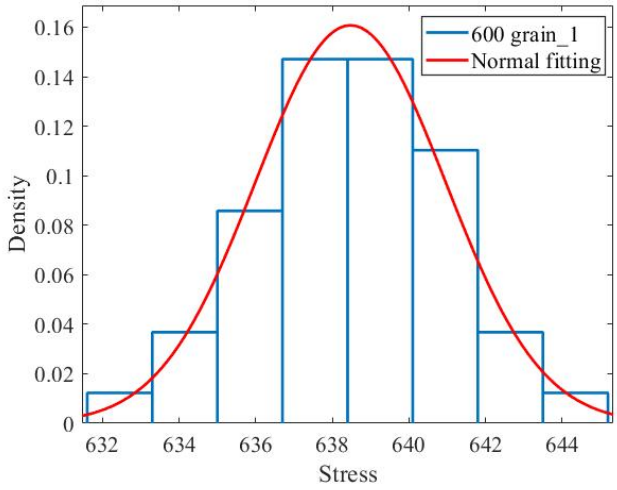


Figure 3.7. Gaussian fitting to the histogram of overall stresses at 1.55% total strain across 48 realizations.

The above finding leads to some challenging questions that deserve further study: Will the gaussian distribution remain the same for all realizations with different microstructures?

What determines the width and height of the distribution? Up to now, only the effect of orientation permutation statistics was investigated. It is a well-known fact that the mechanical properties of polycrystalline alloys are tightly related to their microstructure that includes both grain morphologies and orientation. In the next section, more realizations will be considered and the influence of grain size and morphology on the variation of overall stresses will be studied.

3.3.3 The effect of grain morphologies on the fluctuation of overall stresses

A medium number of 600 grains was chosen in this part of the chapter. Seven more statistical ensembles with different grain morphologies were generated, each ensemble containing 48 realizations. The same numbered list of crystal orientations as used in the first set were used for the seven additional sets of realizations. Accordingly, the effect of grain orientation selection was moderated, and the mechanical response was compared between different ensembles. Table 3.3 lists the realization numbers with the assigned grain orientation and morphology. The microstructures of the eight ensembles with different grain morphologies are illustrated in Figure 3.8. The grain size statistics of all ensembles obey the same lognormal probability density function as shown in Figure 3.9. This particular distribution has been often reported in both experimental observations and simulations for grain size statistics in polycrystalline alloys [73-76]. Thus, the morphology of each ensemble was nominally the same from a statistical point of view, but different locally.

Table 3.3. Sets of realizations generated in this study.

Realization	No. of grains in RVE	Grain morphology	Average grain diameter (μm)	Grain orientation
1-48	600	1	147.1	Orientation permutation, same ODF
49-96	600	2	147.1	The same as corresponding realization 1-48
97-144	600	3	147.1	The same as corresponding realization 1-48
145-192	600	4	147.1	The same as corresponding realization 1-48
193-240	600	5	147.1	The same as corresponding realization 1-48
241-288	600	6	147.1	The same as corresponding realization 1-48
289-336	600	7	147.1	The same as corresponding realization 1-48
337-384	600	8	147.1	The same as corresponding realization 1-48
385-432	22		442.8	Orientation permutation, same ODF

433-480	99	268.2	Orientation permutation, same ODF
481-528	345	176.9	Orientation permutation, same ODF
529-576	1208	116.5	Orientation permutation, same ODF
577-624	2005	98.4	Orientation permutation, same ODF

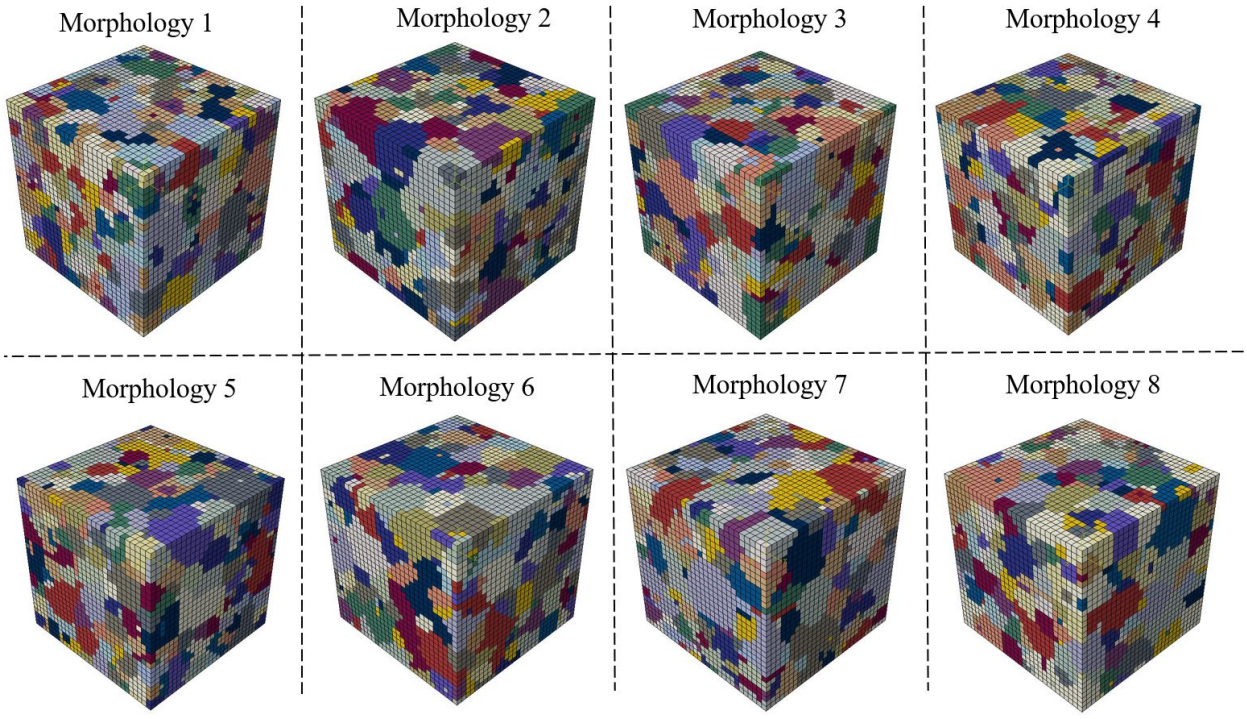


Figure 3.8. An illustration of the microstructure of the eight ensembles with distinct grain morphologies.

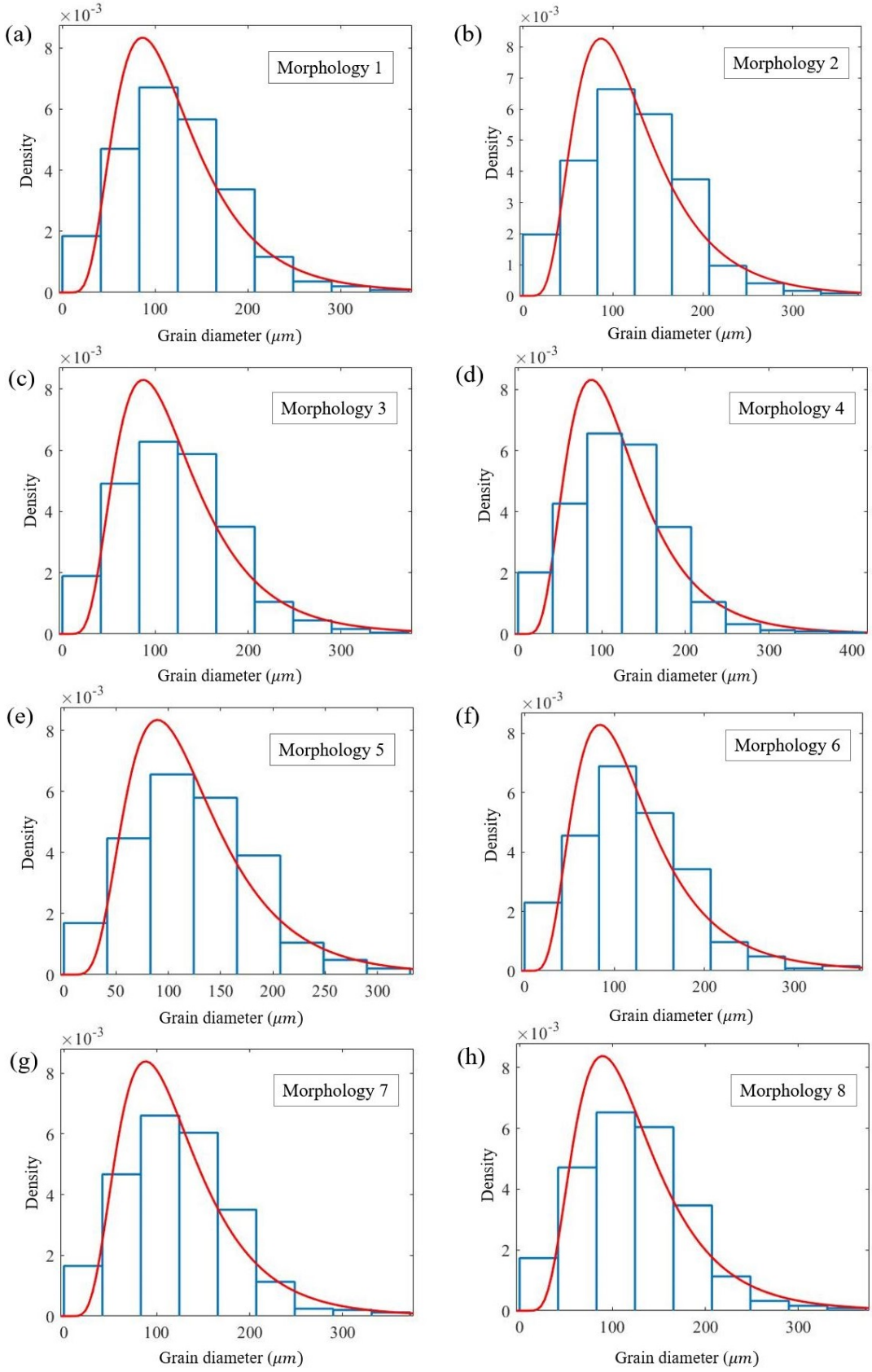
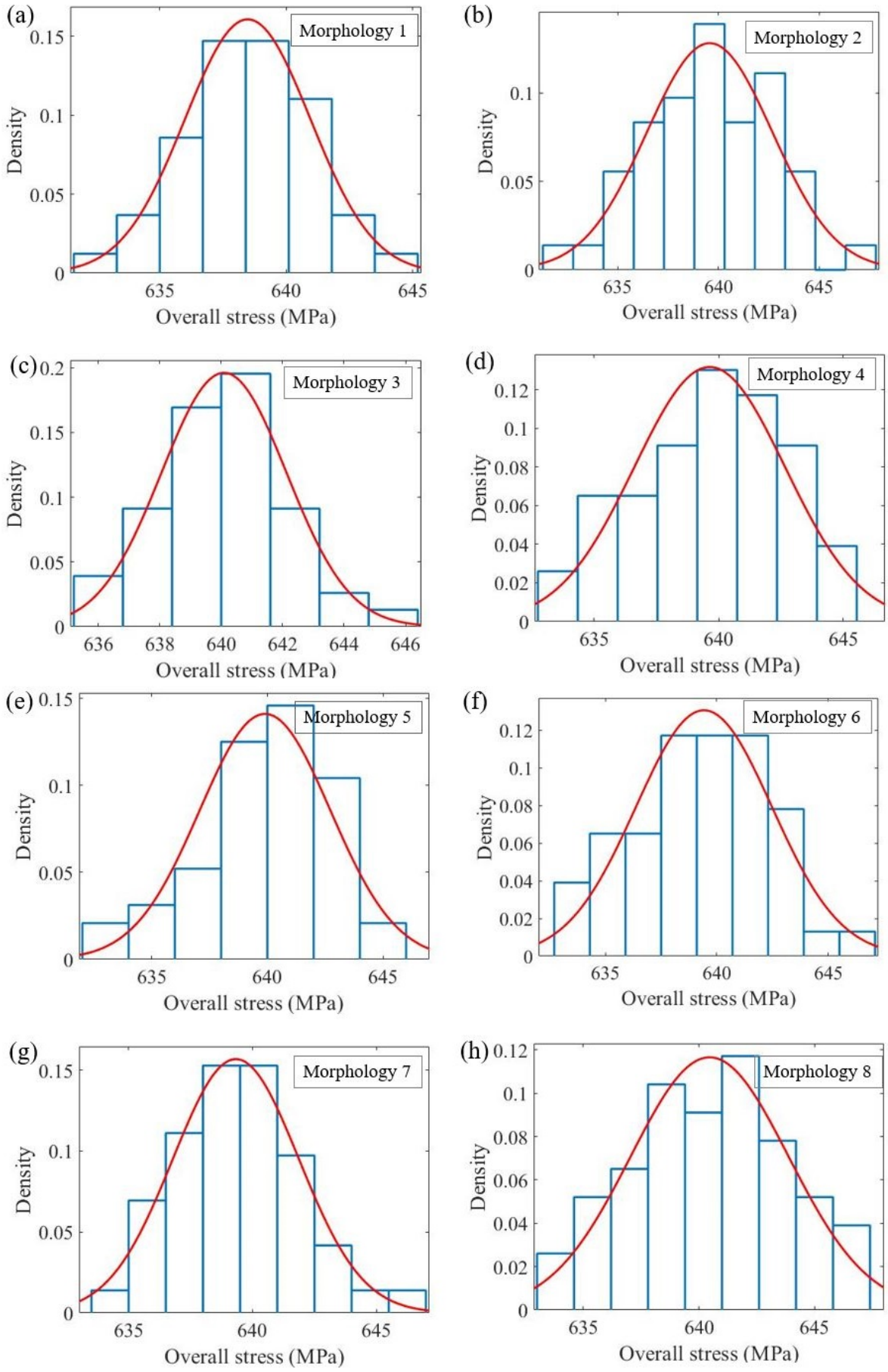


Figure 3.9. (a-h) The grain size distribution fitted by a single common lognormal distribution for different grain morphologies.

Displacement-controlled uniaxial tensile loading was performed for all RVE ensembles to 1.55% total strain, and macroscopic stress data were collected. Figure 3.10 (a-h) represents the histograms of the stress reached during deformation for ensembles with different grain morphologies, with Gaussian fitting applied to each. It is apparent that the distributions of overall stresses in the ensembles with eight grain morphologies were significantly different, although the mean value of stress for all ensembles was close to 639 MPa for all grain morphologies. Morphology 8 shows the widest stress distribution, while Morphology 3 presents the narrowest distribution. The macro-stress statistical distribution widths for other Morphologies fall in between those for Morphologies 3 and 8. The majority of macrostress values fall within the range 637 to 641 MPa indicated by the red arrows in Figure 3.10 (j).


(a)
Morphology 1
Density
Overall stress (MPa)
(b)
Morphology 2
Density
Overall stress (MPa)
(c)
Morphology 3
Density
Overall stress (MPa)
(d)
Morphology 4
Density
Overall stress (MPa)
(e)
Morphology 5
Density
Overall stress (MPa)
(f)
Morphology 6
Density
Overall stress (MPa)
(g)
Morphology 7
Density
Overall stress (MPa)
(h)
Morphology 8
Density
Overall stress (MPa)

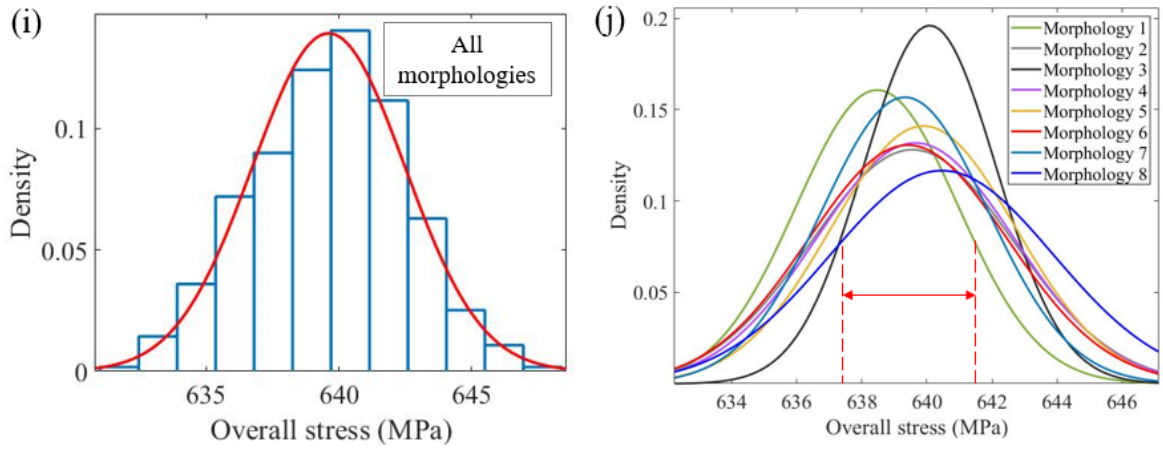


Figure 3.10. Histograms and Gaussian fitting of overall stresses obtained from each set of morphology (a-h) and all morphologies (i). (j) Probability density of macroscopic stress distribution for eight sets of realizations.

Since the same ODF was assigned to all sets of realizations, the variation of the overall stress distribution is affected by the difference in the grain morphologies, or, more specifically by the combination of grain shape and orientation. Although the eight sets of grain morphologies were generated by the same algorithm and parameters, since only a finite number (600) grains were generated, some difference was present among various realizations in terms of the *discrete* distribution of grain size. The fitting parameters for overall stress normal distribution and grain size lognormal distribution in different sets of realizations are listed in Table 3.4. In this chapter, we found that not only the mean grain size plays a role but also grain size dispersion has an impact on the overall yield stress and hardening behaviour in this simple yet powerful phenomenological crystal plasticity model. Since the discrepancy of grain size distribution is minor among different morphologies, it seems problematic to obtain a quantitative description of the correlation. Yet the overall trend of the correlation can be confidently determined as there is an apparent correlation

between the standard distribution of average stress in an ensemble of RVEs with the grain size distribution in the RVE. It is interesting to find that the morphology with a larger grain size dispersion (larger S) will result in fewer overall stress discrepancies (smaller σ). This finding is consistent with previous simulation results in the literature [77]. As opposed to grain Morphology 8, Morphology 3 has a widely dispersive grain size distribution and corresponds to the narrowest overall stress distribution. The correlation between the grain size distribution parameter (standard deviation S) and the overall stress distribution parameter (standard deviation σ) is illustrated in Figure 3.11. The physical explanation of the phenomenon highlighted here is that broad grain size dispersions tend to reduce the grain size dependence whereas the individual grain behaviour is grain-size dependent according to the discretization induced size effect addressed in the following section.

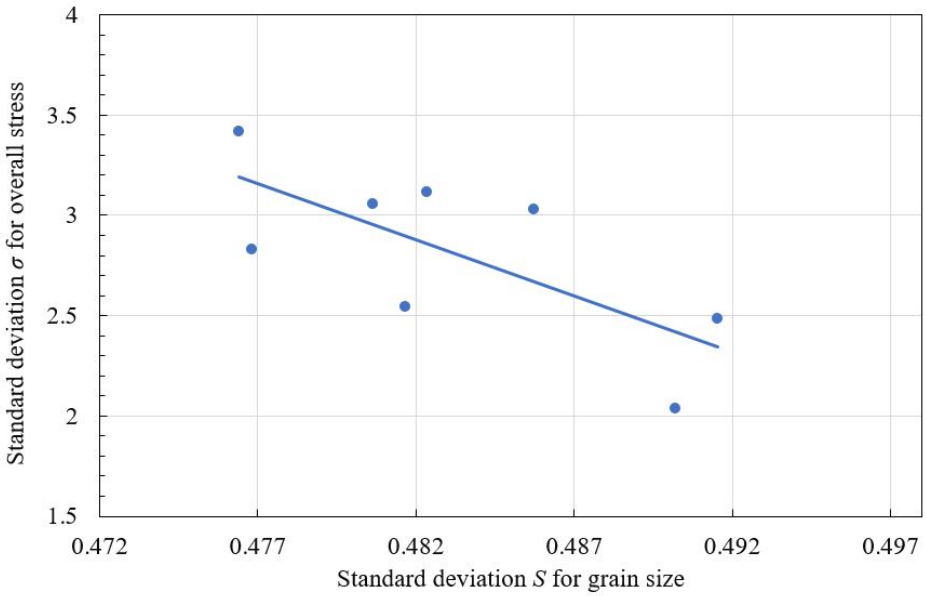


Figure 3.11. The correlation between lognormal grain size distribution fitting parameter S and normal overall stress distribution fitting parameter σ.

Table 3.4. Normal fitting parameters of the overall stress and lognormal fitting parameters of grain size distribution.

Morphology	Grain size fitting parameters		Overall stress fitting parameters	
	M	S	μ	σ
1	4.699	0.492	638.476	2.482
2	4.706	0.482	639.561	3.115
3	4.706	0.490	640.090	2.035
4	4.710	0.486	639.646	3.027
5	4.721	0.477	639.898	2.828
6	4.685	0.481	639.420	3.054
7	4.709	0.482	639.327	2.544
8	4.718	0.476	640.462	3.420

3.3.4 The effect of grain sizes on the fluctuation of overall stresses

To quantify the influence of grain size on the overall effective response, six more statistical ensembles (sets of realizations) with different mean grain sizes (grain numbers) were generated, and each ensemble contains 48 realizations. The same random ODF was used for all ensembles and the realizations in each ensemble have different grain orientation permutations. Accordingly, the effect of grain orientation selection was moderated, and the mechanical response was compared between different ensembles.

As illustrated in Figure 3.12, each ensemble contains different grain numbers, i.e., 22, 99, 345, 600, 1208 and 2005 grains. Each RVE has the same volume, therefore, RVEs with

larger grain numbers correspond to smaller average grain sizes. The grain size within an RVE follows a lognormal distribution. The overall stress is the maximum stress value when loading is stopped. The magnitude of overall macroscopic stress $\sigma_{1.55\%}$ and the yield stress $\sigma_{0.2\%}$ in each realization were collected when the total strain reached 1.55%. Figure 3.13 and Figure 3.14 show that the distribution of $\sigma_{1.55\%}$ in each ensemble follows a normal distribution. The width of the distribution decrease with increased grain number. In engineering design, components with a narrower property discrepancy are expected to be more reliable for the purposes of structural integrity. This study shows that the RVE with a larger number of grains is more reliable in the statistical respect.

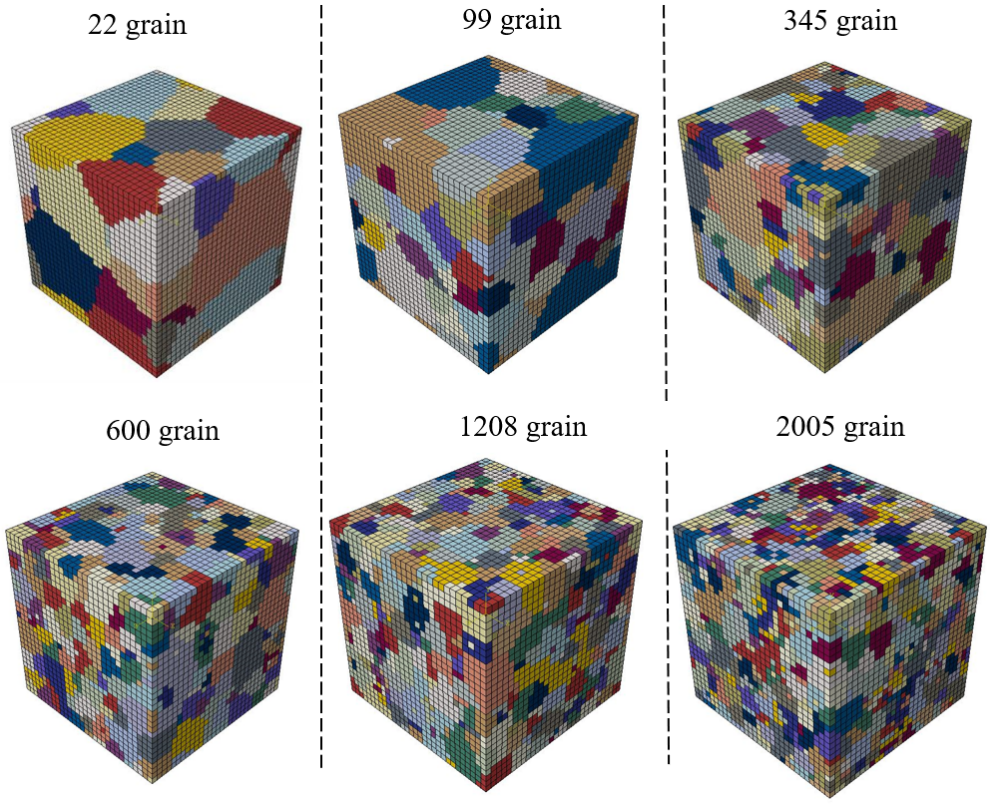


Figure 3.12. RVE realizations with different grain sizes in which different colours indicate different grains.

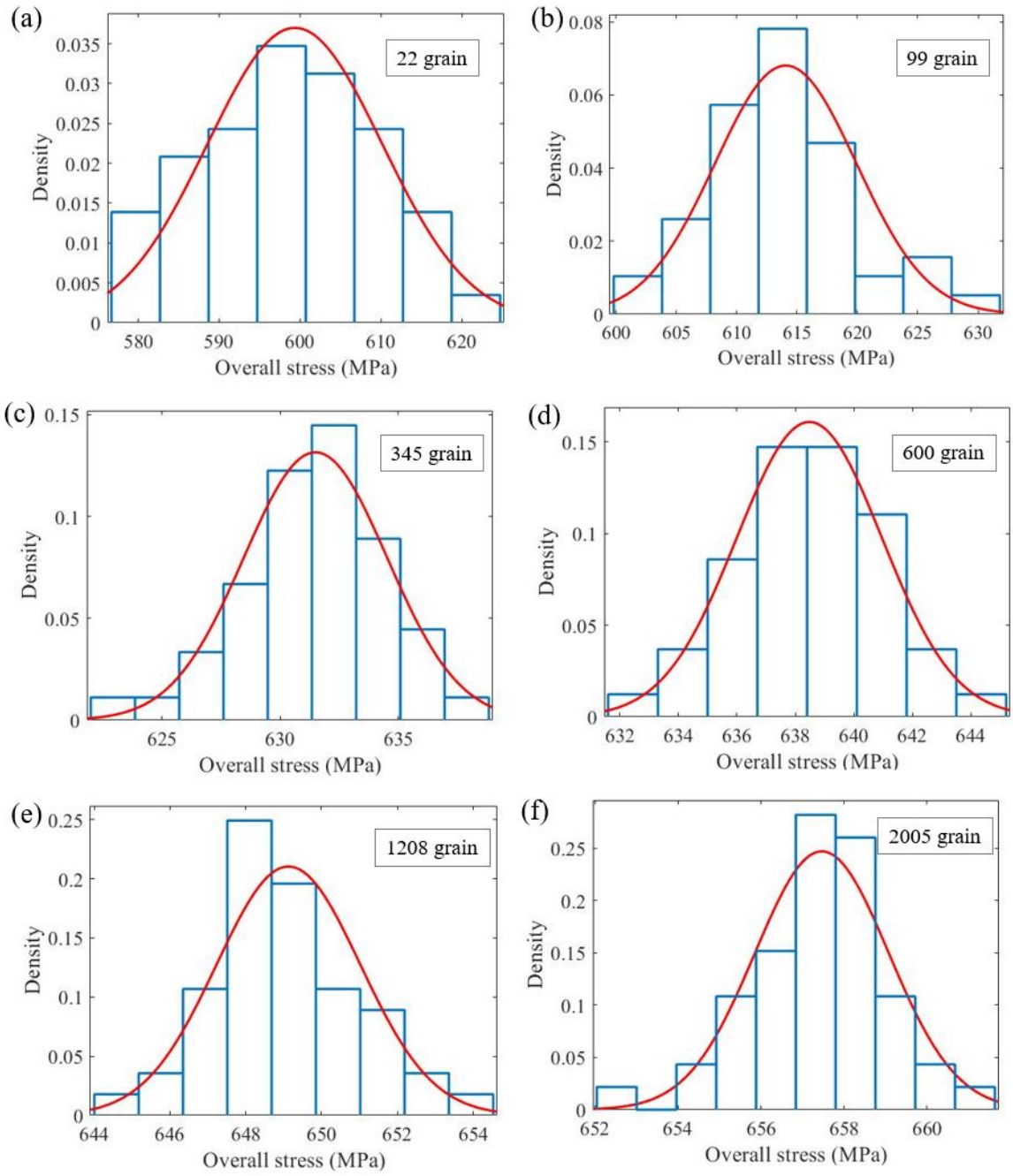


Figure 3.13. Histograms and Gaussian fitting of overall stresses $\sigma_{1.55\%}$ obtained from each ensemble with different mean grain sizes.

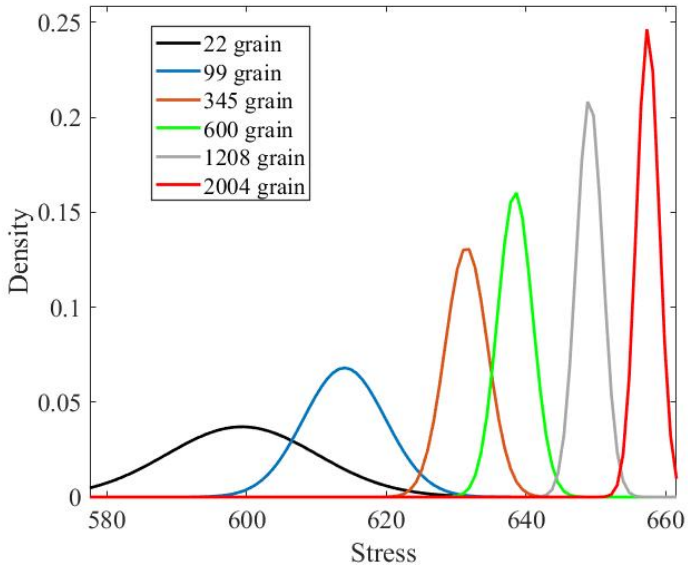


Figure 3.14. Probability density of macroscopic stress $\sigma_{1.55\%}$ distribution for six sets of realizations

As shown in Figure 3.15, the mean of the stress distribution increases with increasing grain number, indicating that smaller grain size strengthens this polycrystal alloy. The average yield stress $\sigma_{0.2\%}$ and the flow stresses $\sigma_{1.55\%}$ against the reciprocal square root of the grain size are plotted in Figure 3.16. Straight trendlines are fitted by the least square method. Please note that both the error bars and confidence intervals are very small because of the excellent fitting of the data. Since internal length scales are not considered in the constitutive formulation, they remain the same simulations and there is no Hall-Petch relationship. The Hall-Petch like correlation in Figure 3.16 might come from discretization and statistics induced size effect or one of them. Some researchers suggest that long-range *intragranular* correlations will induce a slower decay of the fluctuations of strain and stress [78]. We are here mainly focusing on the long-range *intergranular* correlations of size effect and no decay was shown in our research.

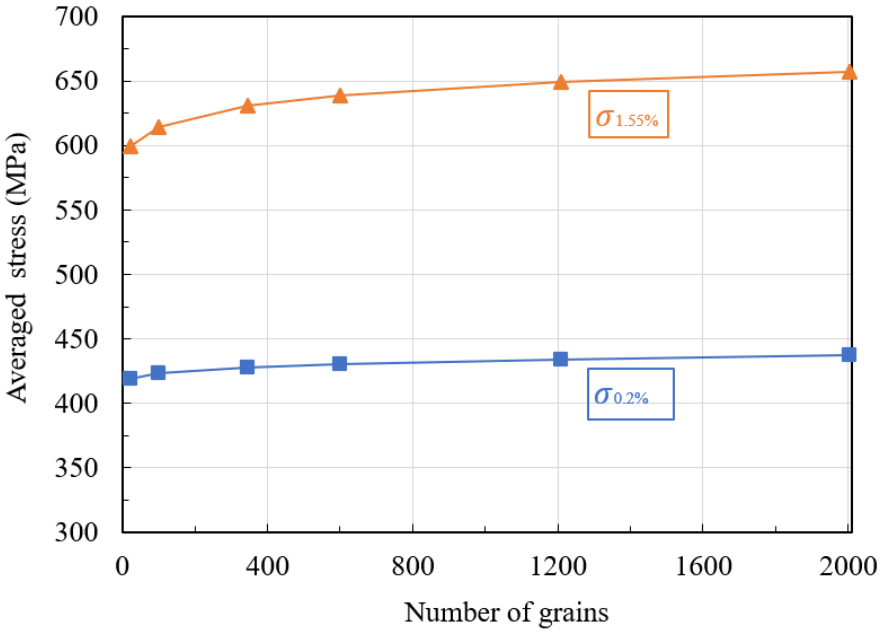


Figure 3.15. Comparison of the averaged overall stress in each ensemble when total strain equals 0.2% and 1.55% versus the number of grains.

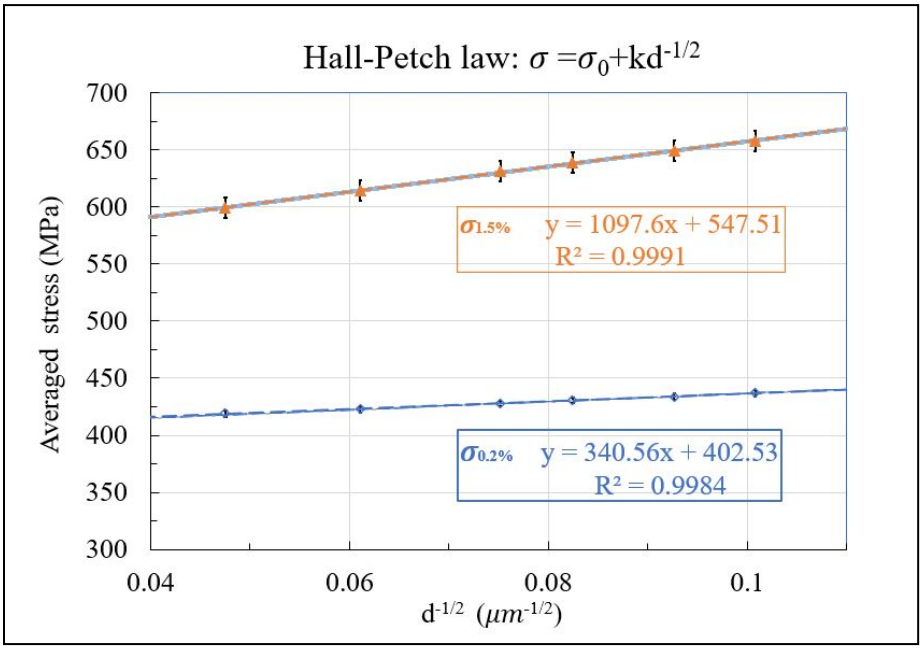


Figure 3.16. Illustration of the Hall–Petch like relationship captured by the simulation.

3.3.5 Discretization and statistical induced size effect

The size effect in the current study can be classified as discretization induced size effect and statistical induced size effect. The former is caused by the discretization of grain (the number of elements per grain), while the latter statistical effect arises from different numbers of grains in the RVE. It is important to separate these two effects when performing a systematic study of the size scaling of stress fluctuations. If the grain size, RVE size and element size are changed proportionally, the simulation results will be the same as the original configuration. The above statement provides the foundation for the following study of size fluctuation.

To evaluate the discretization induced size effect, four more RVE ensembles with different mesh discretization (as shown in Figure 3.17) were generated, and each ensemble contains 10 realizations. RVEs in each ensemble have 600 grains and the same element size, while the grain size and RVE size were increased proportionally. The grain microstructure was changed proportionally compared to the corresponding RVE in other ensembles. In this case, the number of grains in the RVE is fixed, it will not have a statistical induced size effect. But the number of elements per grain increases, hence only the discretization induced size effect will be investigated. Table 3.5 summarizes these RVE parameters.

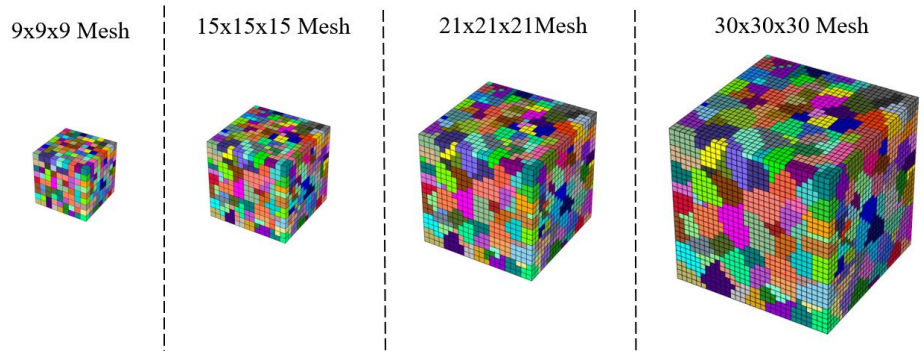


Figure 3.17. RVE realizations with different mesh discretization in which different colours indicate different grains

Table 3.5. RVE size, grain numbers and mesh variation parameters.

Realization	No. of grains in RVE	RVE volume (μm^3)	Total numbers of element	Average number of elements/grain
625-634	600	300^3	9^3	1
635-644	600	500^3	15^3	6
645-654	600	700^3	21^3	15
655-664	600	1000^3	30^3	45
665-712	22	1000^3	10^3	45
713-760	75	1000^3	15^3	45
761-808	178	1000^3	20^3	45
809-856	307	1000^3	24^3	45
857-904	600	1000^3	30^3	45
905-952	1422	1000^3	40^3	45
953-1000	2163	1000^3	46^3	45
1001-1048	2778	1000^3	50^3	45
1049-1096	3499	1000^3	54^3	45
1097-1144	4800	1000^3	60^3	45

The average yield stress $\sigma_{0.2\%}$ and the flow stresses $\sigma_{0.3\%}$, $\sigma_{1.55\%}$ obtained from these four ensembles against the reciprocal square root of the grain size are plotted in Figure 3.18. It is interesting to find that discretization effect will introduce a Hall-Petch like relationship in polycrystalline materials. Since internal length scales are not considered in the constitutive law, it is not a real Hall-Petch relationship but is only called Hall-Petch like behaviour. Here we demonstrate that discretization can lead to a Hall-Petch like relationship when the number of elements per grain ranges from 1.2 to 45 on average per RVE. To the best of the author's knowledge, no known relevant literature regarding discretization and Hall-Petch like relationship has been published yet.

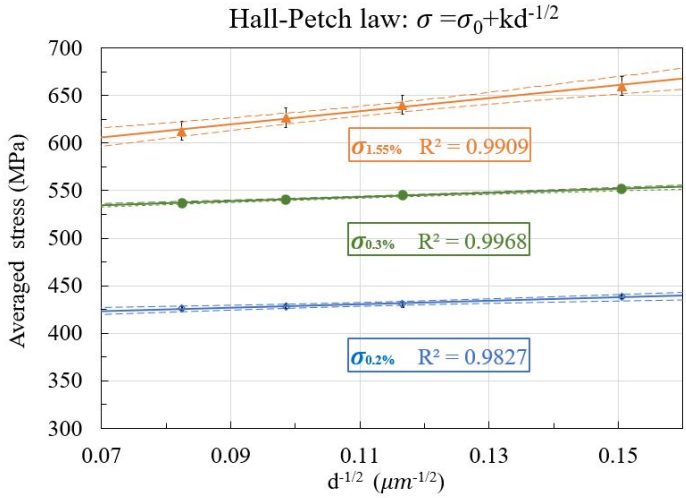


Figure 3.18. Illustration of the discretization induced size effect (Hall-Petch like effect).

To quantify the statistical induced effect on the overall effective response, ten ensembles with fixed RVE size (as shown in Figure 3.19) were generated, and each ensemble contains 48 realizations. Again, the same random ODF was used for all ensembles and the realizations in each ensemble have different grain orientation permutations. RVEs in each ensemble have a volume of 1mm^3, while the grain size and the element size were changed

proportionally to keep the same number of elements per grain among different RVE ensembles. Therefore, discretization effects on the grain scale that arise from the pixellation of the grain morphologies by the cubic elements do not change, and only the statistical induced size effect was studied.

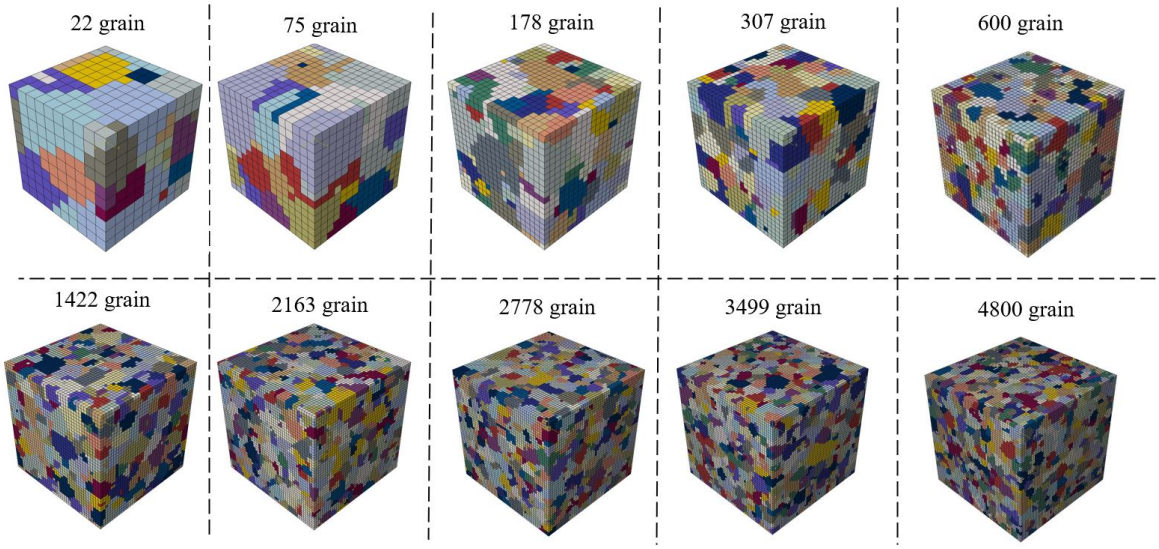


Figure 3.19. RVE realizations with different grain numbers and element sizes.

As illustrated in Figure 3.20, the distribution of $\sigma_{1.55\%}$ in each ensemble follows a normal distribution. The mean of a normal distribution is not observed to obey any particular correlation with the number of grains in the RVE, while the standard deviation of the distribution decreases significantly with increased numbers of grains as shown in Figure 3.21. This explains the reason why RVEs with more grains are preferred in engineering design, as they can provide more reliable predictions with less deviation. The correlation between the standard deviation of overall stress $\sigma_{1.55\%}$ and the grain numbers can be well described by a power law function. Further investigation reveals that the standard deviation of both yield stress and flow stress decreases with the increased grain numbers and they all

have a power law relationship, as illustrated in Figure 3.22. The standard deviation of yield stress is smaller than that of the flow stress, especially when the number of grains is larger than 1000. Since there is no observed statistical induced size effect in this research, it is then reasonable to conclude that the Hall-Petch like behaviour reported in Section 3.3.4 arises from the discretization induced size effect. This study also suggests that RVEs with more grains are preferred for engineering design in the statistical respect.

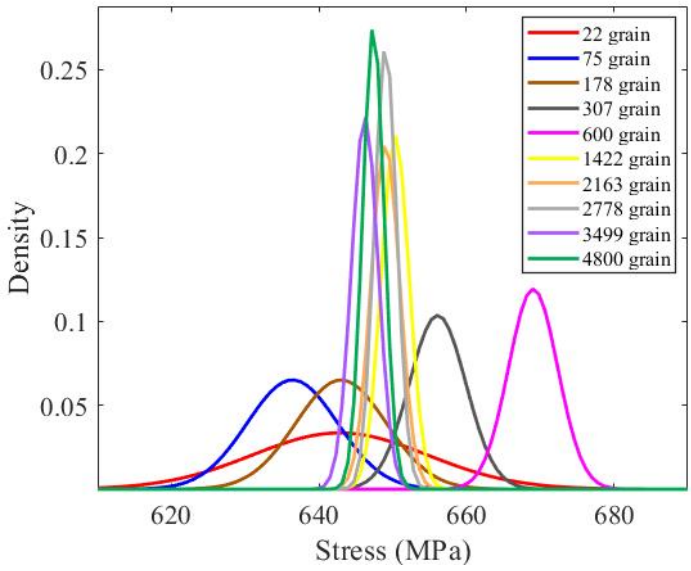


Figure 3.20. Probability density of macroscopic stress $\sigma_{1.55\%}$ distribution for ten sets of realizations

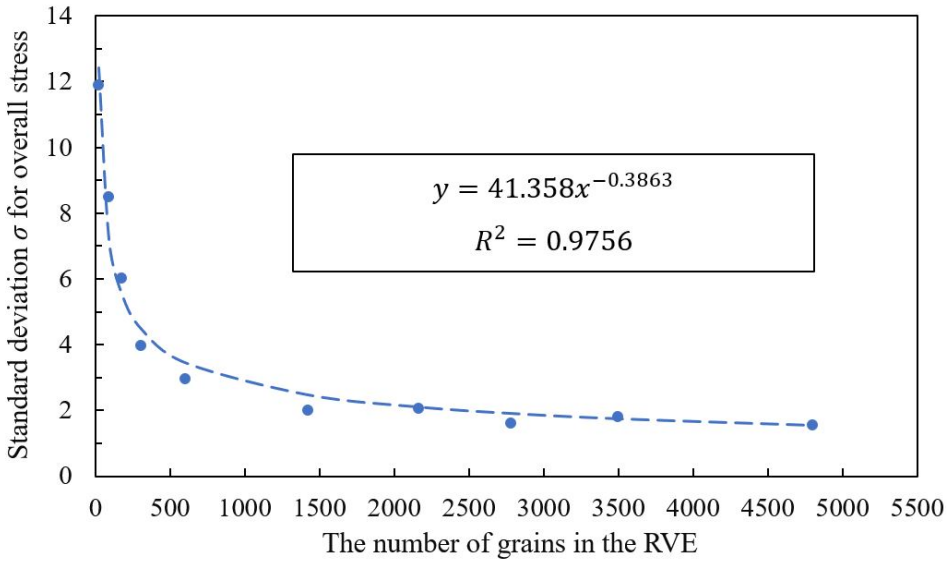


Figure 3.21. An illustration showing the decreased standard deviation for overall stress with an increased number of grains in the RVE.

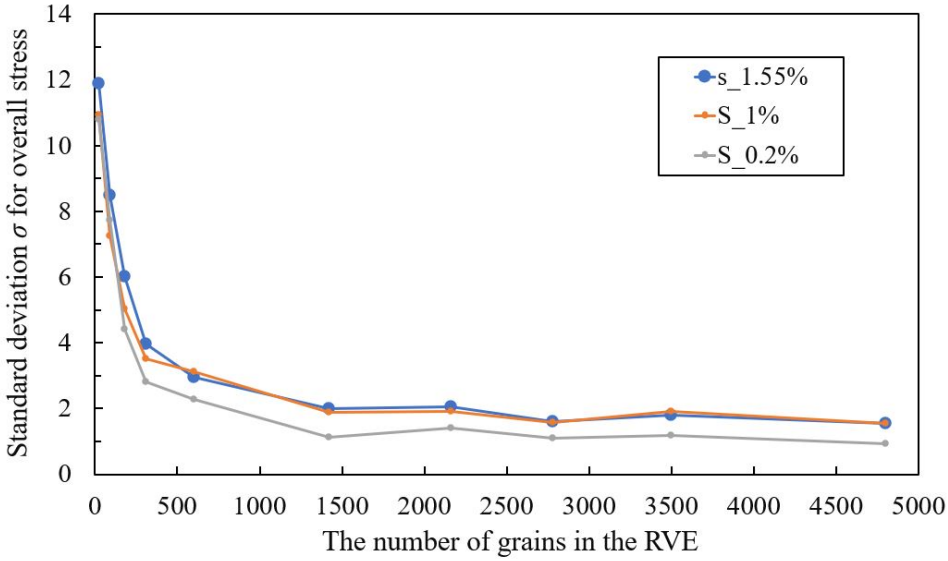


Figure 3.22. The curves showing the correlation between the standard deviation of $\sigma_{0.2\%}, \sigma_{1\%}, \sigma_{1.55\%}$ and the number of grains in the RVE.

3.4 The mesoscopic response of RVE

One of the main challenges of CPFE model validation arises from the fact that the uniaxial stress-strain curves only provide an incomplete description of plastic flow as they reduce a six-dimensional yield surface to a one-dimensional yield curve. It means that

acceptable agreement with the monotonic stress-strain curve can be obtained using different combinations of material parameters, such as single-crystal elastic moduli, critical resolved shear stress, hardening parameters, etc. In order to get a reliable evaluation of the above parameters, it is essential to reproduce both the macroscopic and mesoscopic behaviours of RVE and fit the result with experimental measurements. With the help of diffraction post-processing, optimal values of crystal stiffnesses can be determined by fitting the mesoscopic response of RVE obtained from different grain groups in the elastic regime to diffraction measurement of orientation-dependent elastic strains. The post-yielding behaviour can then be employed to evaluate the critical resolved shear stresses and hardening parameters.

The optimal material parameters for mesoscale fitting are listed in Table 3.2, and the simulation results from diffraction post-processing are depicted in Figure 3.23, together with the neutron diffraction data of Haynes 282 alloy [72]. Jaladurgam et al. employed in-situ neutron diffraction experiments to evaluate the elastic lattice strains in different reflection groups [72]. The result for Haynes 282 alloy with coarse gramme prime in their research was used to validate our model. The error bar in Figure 3.23 is from experiment data. Good agreement has been achieved, considering the fact that a relatively small number of grains (600) were used in this model. This model can well reproduce the anisotropic elastic-plastic behaviour for all grain groups, especially for the 111, 220 and 311 families, and somewhat less precisely for the 200 grain family. Considering the goodness of fitting shown in Figure 3.3 and 3.23, it is suggested that both macroscopic and mesoscopic behaviour of elastic strains are adequately captured by the current model.

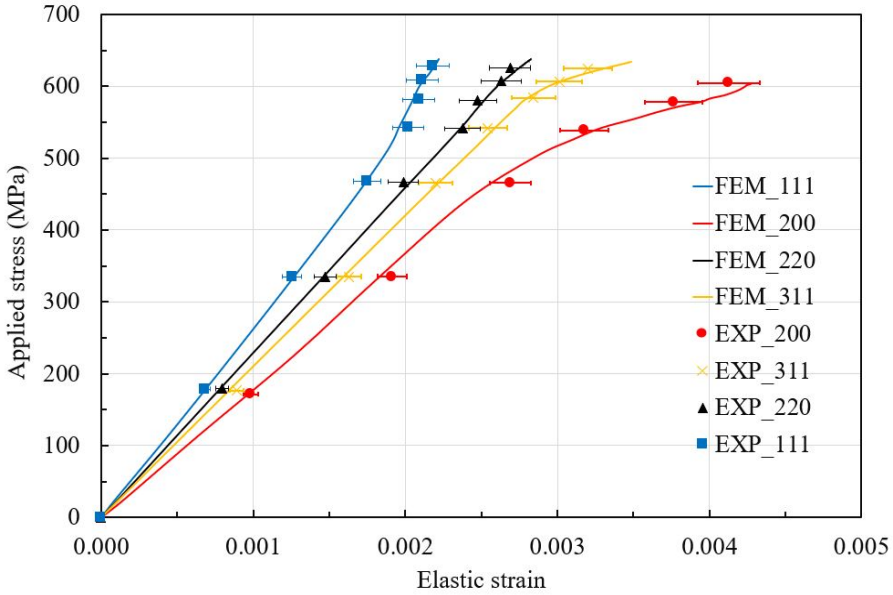


Figure 3.23. Comparison between CPFE diffraction post-processing reproduction and experimental diffraction data for Haynes 282 under monotonic loading.

3.5 The microscopic response of RVE

In Section 3.3, the macroscopic stresses under monotonic loading obtained from multiple realizations were found to follow a normal distribution. The macroscopic overall stresses of the RVEs are relatively stable, lying within a 2% difference band for the eight grain morphology ensembles used. It is important to note, however, that failure is governed by local stress and strain values that may show a greater degree of variation. It is therefore interesting to directly investigate the distribution of local stresses and strains within RVEs. For each realization, approximately 300000 IPs are used in one RVE with 600 grains, suggesting that each grain contained around 500 IPs on average. Diard et al. examined the relationship between IP numbers and grain numbers that are sufficient for adequate deformation description [40]. According to their results, it is found that 25 IPs per grain could be sufficient to provide adequate reproduction in the case of small deformation. It

should be pointed out that a detailed representation of intragranular stresses and strains was not attempted in the current study. The aim is to develop a computationally efficient model that captures the macro-meso-microscopic behaviour of RVE and to analyse the model reproduction statistically.

As the loading was applied in the z direction, the local stress, elastic and plastic strain components of interest are termed σ_{zz}, ε_{zz}^{el} and ε_{zz}^{pl}, respectively. At each integration point, the local stress and strain values can be readily collected. After the total strain reaches 1.55%, the distributions of stresses and strains at IPs were examined for several realizations. They were found to show the same type of distribution, therefore the results from only one randomly selected realization are illustrated here in Figure 3.24. In Figure 3.24 (a), it is evident that local stress σ_{zz} follows a normal distribution, and the range of fluctuation is as large as 639 ± 400 MPa. In contrast, the histogram in Figure 3.7 shows that the overall macroscopic stresses at the chosen strain level (1.55%) across 48 realizations follow a much narrower normal distribution within 639 ± 6 MPa. It is worth mentioning that stress is directly related to *elastic* strain through generalised Hooke's law, implying the distribution of local elastic strain should also have a normal profile, as illustrated in Figure 3.24 (b). The local plastic strain distribution is observed to follow a lognormal distribution, as shown in Figure 3.24 (c). The lognormal profile shape suggests that plastic strain accumulation is a multiplicative process, and it does not increase uniformly as deformation proceeds – it becomes progressively localized and the local regions of large strains make a significant contribution to the overall average strain increase. When the total deformation is large, the plastic strain becomes dominant, and hence the total strain appears to follow a lognormal

distribution that has been reported in the literature [79]. The overall strain of the whole RVE reaches precisely 1.55%, whereas the value of local elastic and plastic strain vary significantly within the RVE. The above finding is statistically significant, as it represents the fact that the variation of microscopic response is much broader than the macroscopic average. More importantly, local elastic strain, as well as stress, were found to obey a normal distribution, whereas the statistics of local plastic strain conforms to a lognormal distribution. The results reveal the nature of strain inhomogeneity at the microscale and emphasize the fact that elastic strain accumulation represents an additive process, whereas plastic deformation is a multiplicative process. For the causes of this phenomenon, readers can refer to Chapter 5.

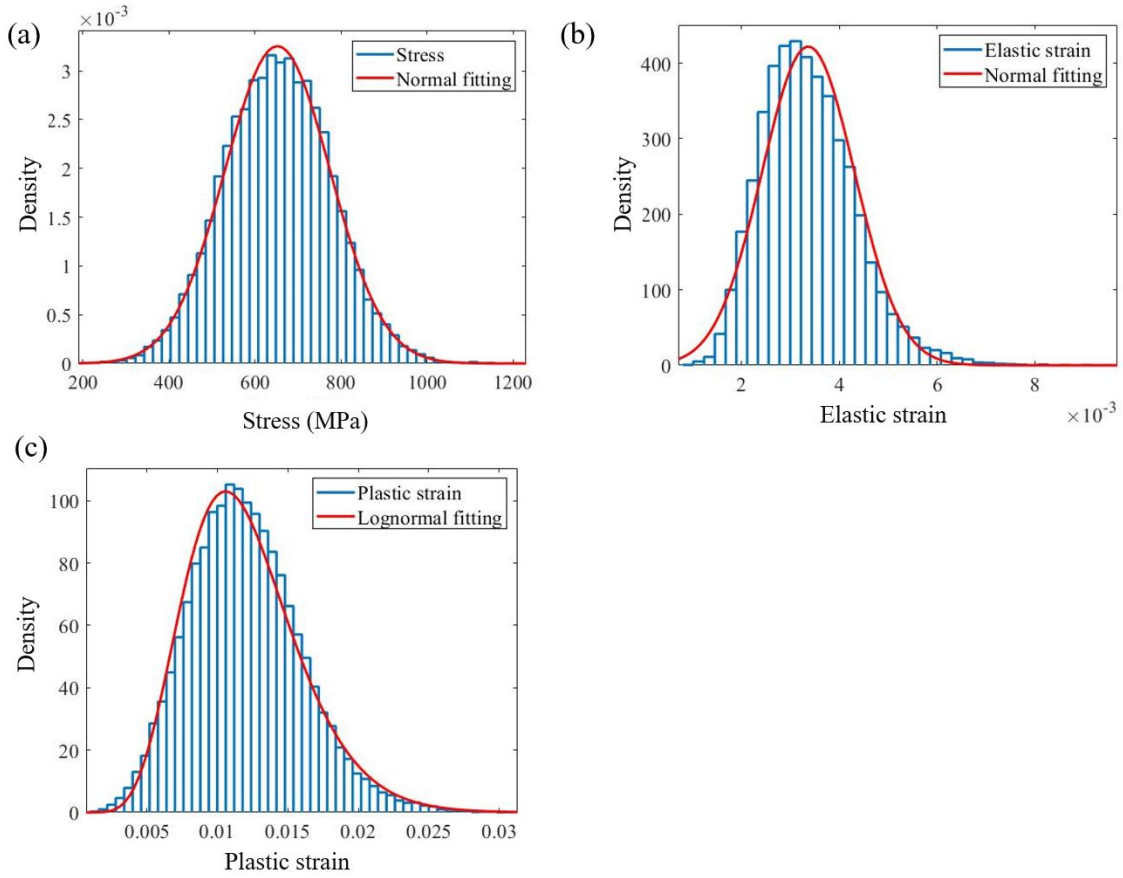


Figure 3.24. The distribution and fitting of local σ_{zz} (a), ε_{zz}^{el} (b) and ε_{zz}^{pl} (c) across all IPs in one randomly selected realization.

Equiaxed grains were employed in all the realizations. It is also found that the fitting for normal and lognormal distribution will be more accurate when the RVE contains sufficient grains (at least ~200 grains) and enough small mesh sizes (at least 8x8x8). It is then reasonable to assume that the statistical results of local stress and strain are convincing based on sufficient equiaxed grains and small mesh sizes. Nevertheless, it is believed that our finding has significantly broader applicability for grain morphologies. Figure 3.25 (a) illustrates an RVE with a rolled grain morphology. The averaged long semi-axis of the equivalent ellipsoid is 10 times larger than the averaged short semi-axis. Uniaxial loading was applied to the RVE and the loading is stopped when the magnitude of total strain reached 1.55%. Analogous to the results obtained from equiaxed grains, the normal and lognormal strain distribution assumption appears to remain valid for RVEs with a rolled grain morphology, as shown in Figure 3.25 (b) and (c).

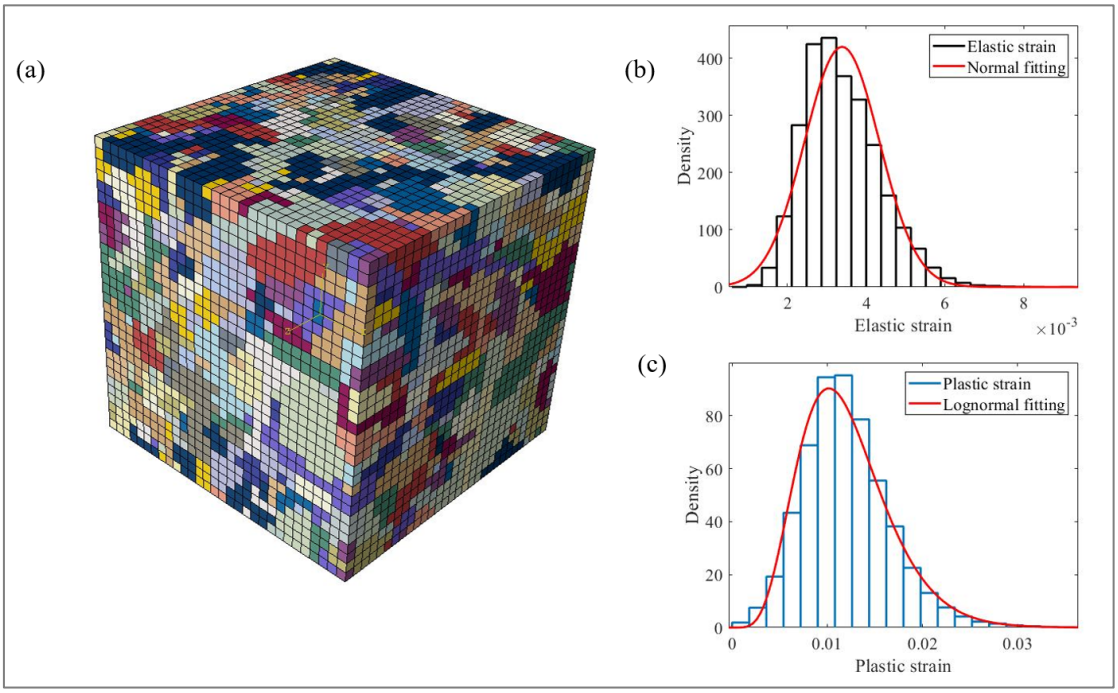


Figure 3.25. (a) an RVE model with a rolled grain morphology. (b-c) normal and lognormal fitting for elastic and plastic strain, respectively, when the total strain reached 1.55%.

Our statistical results of local stress and strain are convincing when global strain ranges from 0-10%. Significant strain localization occurs when the global strain is above 5% and corresponds to the long 'tail' in the lognormal strain distribution. Figure 3.26 depicts the local elastic and plastic distribution when the total strain is 20% and 30%. Further investigation suggests that the distributions of local elastic and plastic strain obtained from the current model can still be described by normal and lognormal distributions to some extent even when the global strain is larger than 20%. However, the fitting quality for strains larger than 20% is not as good as that for smaller strains less than 10%, especially in the case of elastic strain and normal distribution. Such behaviours can be explained by the fact that a *small strain kinematic formulation* was implemented in the current study and the crystal orientations remain static throughout the FEM calculation. Grain rotation will be significant when investigating large deformation. As discussed in the previous section, large deformation that more than 20% lies beyond the scope of our current paper. A global strain of 1.55% was chosen because it represents the most difficult condition for description compared to cases when either elastic or plastic deformations dominate.

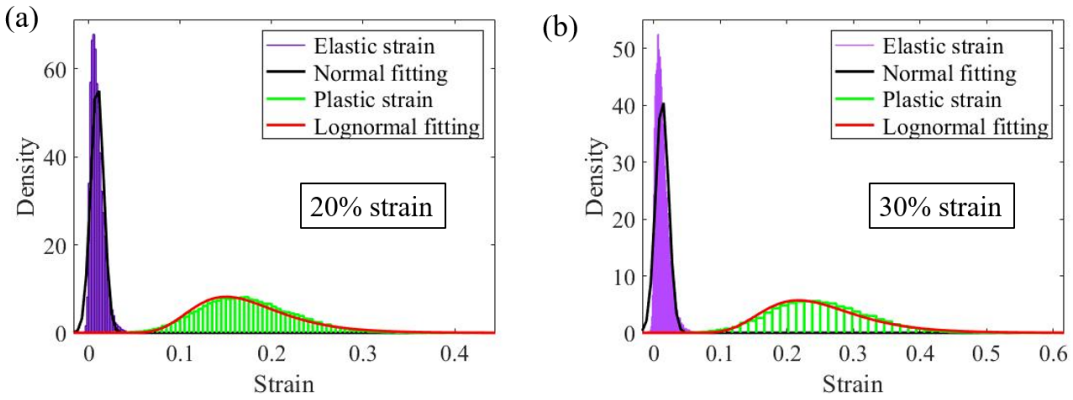


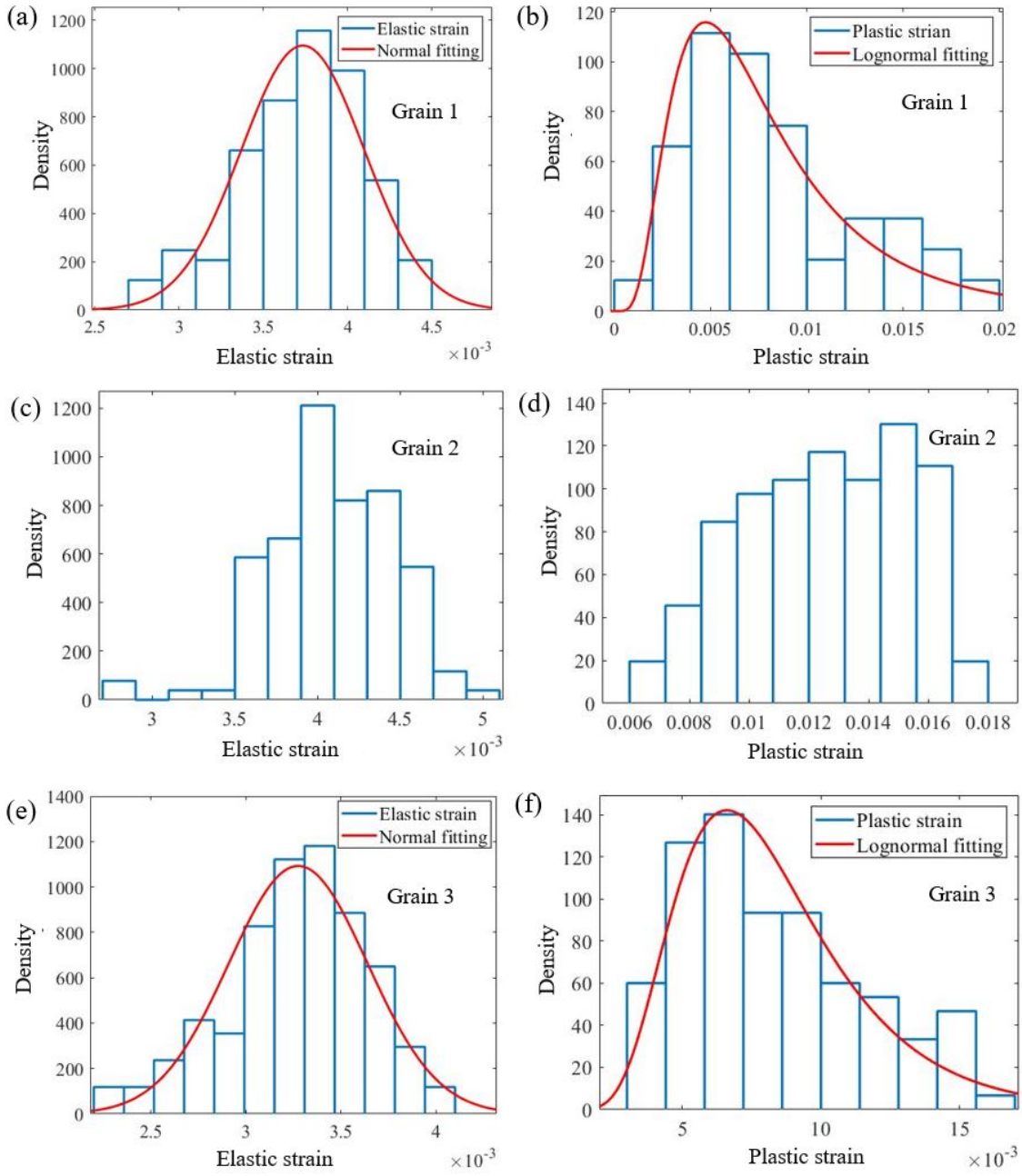
Figure 3.26. The distribution of local elastic and plastic strain when the total strain reached 20% and 30%.

The normal elastic strain and lognormal plastic strain distribution laws are conditional upon the macroscopic homogeneity of deformation within the volume of interest. A large deviation can be expected to be observed when investigating the statistical distribution of strains and stresses within individual grains. The dislocation introduced stress/strain fields were studied by Groma and Bako [80], and Kapetanou et al. [78] on the level of dislocation simulations. Groma and Bako found the stress field generated by the dislocations can be approximated as the sum of a stochastic and a slowly varying component. However, their model only had a few hundred parallel edge dislocations and the volume of interest is nanoscale. They mainly focus on the probability distribution of shear stress, not the strain and stress in the loading direction as in our research. Kapetanou et al. employed a 3D discrete dislocation model with a volume of only $3\mu m^3$ and their simulation suggests that the fluctuations of strain and stress decay are in inverse proportion with the increase of the averaging volume [78], which is consistent with our simulation results that the fluctuation of smaller scale local stress (639 ± 400 MPa) is much larger than overall macroscopic average stresses at the chosen strain level (1.55%) across 48 RVE realizations (639 ± 6 MPa). Figure 3.27 depicts the probability density distribution of elastic and plastic strains within 6 large grains, each containing a large number of 1000-1500 IPs. Due to the low number of values in each data set, the quality of discrete statistical distribution is moderate. Nevertheless, the normal and lognormal strain distribution assumptions remain valid for grains 1, 3, 4 and 6. However, for the other grains, the elastic and plastic strain statistics do not follow a distinct distribution. It is interesting to find that if the elastic strain in one grain conforms to a normal distribution, then the plastic strain obeys a lognormal distribution in

the same grain. We speculate that these two particular types of statistical distribution are coupled within the same volume of interest. Table 3.6 lists the grain number and its corresponding reflection group with respect to the loading direction. According to the diffraction postprocessing data illustrated in Figure 3.23, the 220, 311, 331 and 531 planes show higher linearity compared to 111 and 200 planes. Strain heterogeneities increase when local behaviour becomes strongly non-linear. In this chapter, we state that local elastic strain (stress) and plastic strain universally within the whole RVE follow a normal distribution and lognormal probability distribution, respectively. It is not expected nor claimed that the *local* elastic and plastic strains within *each* grain follow these particular distributions. Further investigation suggests that 233 out of 600 grains show this kind of distribution characterization. Among these 233 grains, 99 out of 102 grains are from 220, 311, 331 and 531 related reflection groups. It is therefore hypothesized that the strains within grains (Type III or microscale) that belongs to the high linearity reflection group (Type II or mesoscale) will show normal or lognormal distribution characterization.

Table 3.6. Grain and its corresponding reflection group.

Grain ID	1	2	3	4	5	6
Reflection	311	200	331	-	200	531


(a)
Elastic strain
Normal fitting
Grain 1
Density
Elastic strain
×10^-3
(b)
Plastic strian
Lognormal fitting
Grain 1
Density
Plastic strain
(c)
Grain 2
Density
Elastic strain
×10^-3
(d)
Grain 2
Density
Plastic strain
(e)
Elastic strain
Normal fitting
Grain 3
Density
Elastic strain
×10^-3
(f)
Plastic strain
Lognormal fitting
Grain 3
Density
Plastic strain
×10^-3

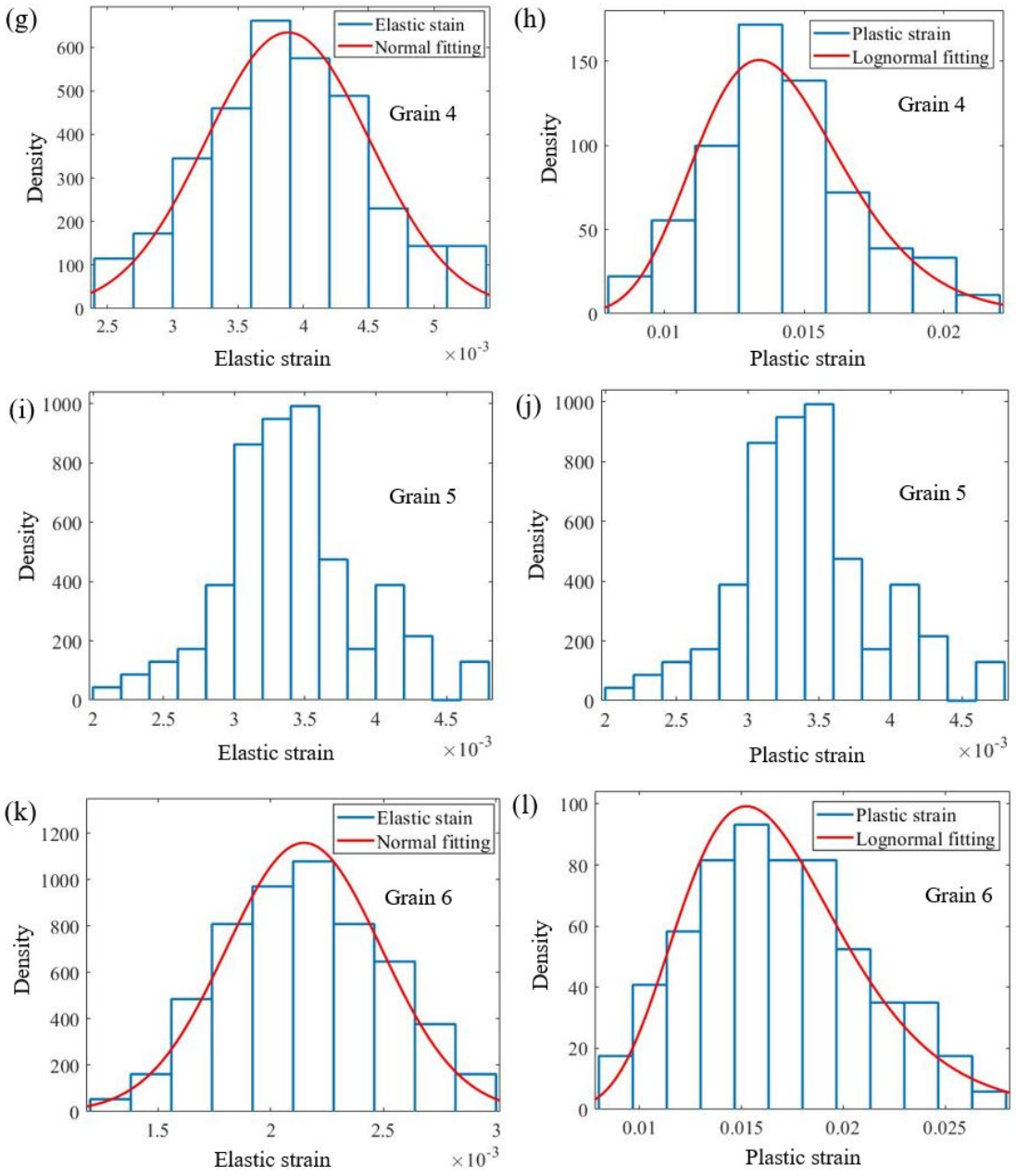


Figure 3.27. The probability density distribution of elastic and plastic strains in 6 large grains.

Local stress and strain deviation from the macroscopic average (Type I) can be further classified into Type II (grain level) and Type III (intragranular deviation from grain average) that is highly inhomogeneous due to the difference in crystal orientation and intra-grain strain localization due to plastic slip. We notice that stresses within polycrystals are multi-

scale, and the separation of stresses into these three types can be written in additive form, namely:

$$\sigma^{total} = \sigma^{I} + \sigma^{II} + \sigma^{III} \tag{3.12}$$

At each IP, the total stress (Types I+II+III) in the loading direction can be directly collected from the simulation result. Type I stresses are those which exist over the scale of the dimension of sample or component. They are continuous over large distances and can be obtained from the macroscopic stress curve. Types II stresses are those which exist across grains due to the anisotropy of different grains or grain families and the constraints to deformation that occur between them. They are not the grain average stress here, but the fluctuation of stresses in different grains. Type III stresses are produced at the atomic level as a result of defects, dislocation motion/interaction and precipitates in materials. It can be evaluated by the fluctuation of stress in different IPs. With the knowledge of total stress, Type I and II stress, Type III stress (intragranular fluctuation) can be then calculated from the Equation (3.12). Figure 3.28 represents the probability density distribution of elastic strain in 10 grains and overall RVE. The corresponding normal fitting parameters are listed in Table 3.7. Considering the overall RVE contains a large number of grains, it is not surprising to find that the normal profile shapes of individual grains are much higher and narrower than that of the overall RVE, suggesting that the standard deviation of local elastic strain within one grain (Type III) is much smaller than that within the whole RVE (Type I). Additionally, the deviation and mean value of the strain distribution in different grains (Type II) vary significantly (up to 100% difference) from each other.

Table 3.7. Gaussian fitting parameters of the elastic strain statistics in individual grains and overall RVE.

Elastic strain statistics	μ	σ
Grain 1	3.73E-3	3.64E-4
Grain 3	3.27E-3	3.65E-4
Grain 4	3.88E-3	6.29E-4
Grain 6	2.15E-3	3.44E-4
Grain 7	4.09E-3	3.80E-4
Grain 8	3.12E-3	3.21E-4
Grain 9	3.18E-3	5.09E-4
Grain 10	1.93E-3	2.16E-4
Grain 11	4.02E-3	2.48E-4
Grain 12	3.48E-3	4.69E-4
Overall RVE	3.37E-3	9.46E-4

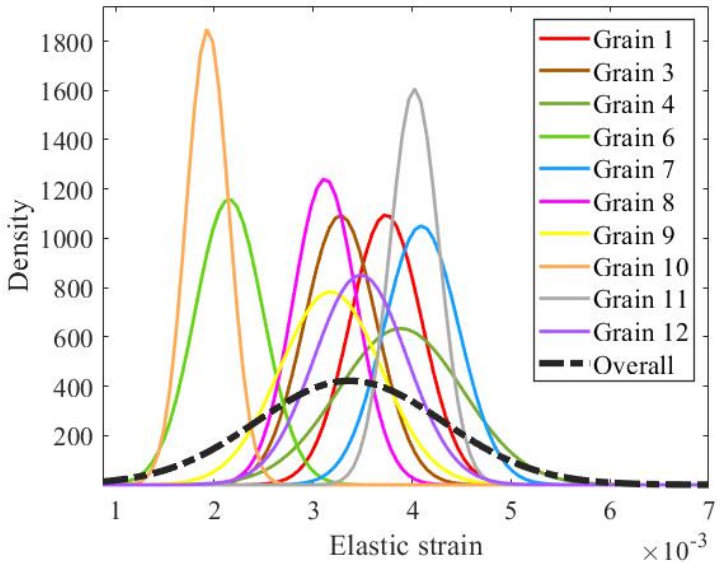


Figure 3.28. A comparison of the probability density distribution of elastic strain in 10 grains and overall RVE.

Figure 3.29 illustrates the multi-scale nature of stresses within the RVE by considering the stress component in the loading direction. The RVE shown in Figure 3.29 (a) was cut in half by a horizontal plane indicated by the black dashed lines. The lower half of the RVE is shown in Figure 3.29 (b), with path AB created at the cut surface. The total stress profiles (Types I+II+III) in the loading direction along the path are represented by coloured dotted lines, with the colours of dots set to be identical to that of their corresponding grains according to the colour key of IPF. The coloured short solid lines are the grain level average of stresses (Type I+II) that vary between different grains, while Type I stresses are constant along the entire path. In this chapter, a significant variation of stress magnitudes within one grain and among different grains is observed. Type II and III stresses are often neglected when investigating the mechanical response of engineering components having a characteristic length of millimetres. However, mechanical failures often originate at the grain level, where intragranular and intergranular stresses are critically important. For these

reasons, critical assessment of stresses and strains at both macro-scale (Type I) and grain level (Type II and III) has the potential to improve the design methods for enhanced structural integrity. From the practical point of view, a detailed representation of Type II and III stresses within material microstructure remains rather computationally expensive. On the other hand, employing a statistical approach to study multi-scale stresses may allow reliable uncertainty quantification in terms of the onset and development of failure processes. It should be mentioned that the current model is not able to capture the fine-scale fluctuation of Type III stresses within the grain, as the mesh was not refined sufficiently to allow performing efficient statistical analysis of a large number of realizations.

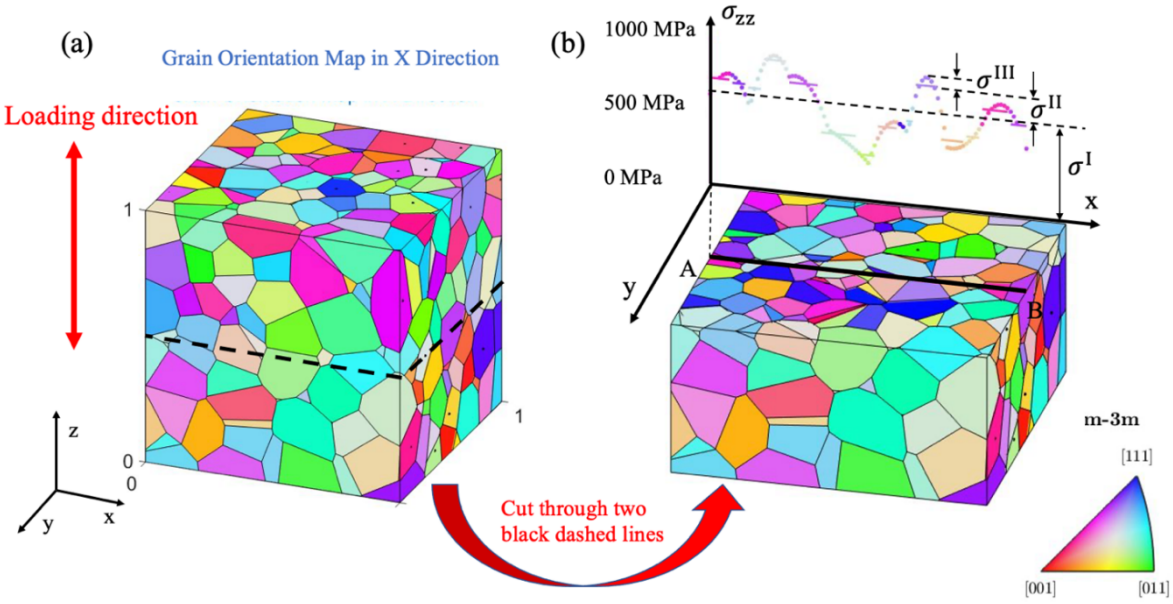


Figure 3.29. Illustration of the multi-scale nature of stresses in the RVE and the separation into Types I, II and III.

3.6 The multi-scale investigation of mechanical response in two extreme realizations

Failures in structural components are often governed by extreme cases according to the weakest link principle. Therefore, it is of great importance and interest to explore the difference in macro-meso-microscopic stress and strain response for extreme realizations. Based on the stress histogram depicted in Figure 3.7, two realizations No. 35 and 46 were found to behave distinctly different in terms of overall stresses at 1.55% strain. Figure 3.30 represents the macroscopic stress-strain curve under uniaxial loading for realizations No. 35 and 46. Realization 35 has the highest overall stress and can be seen as the upper limit within the statistical distribution. On the other hand, Realization 46 shows the lowest overall stresses and can be looked as the lower limit. These two realizations have identical grain morphology, but different orientation permutations. Thereby, it can reasonably be assumed that the difference in overall stresses between Realizations 35 and 46 may originate from the anisotropic behaviour of different grain groups.

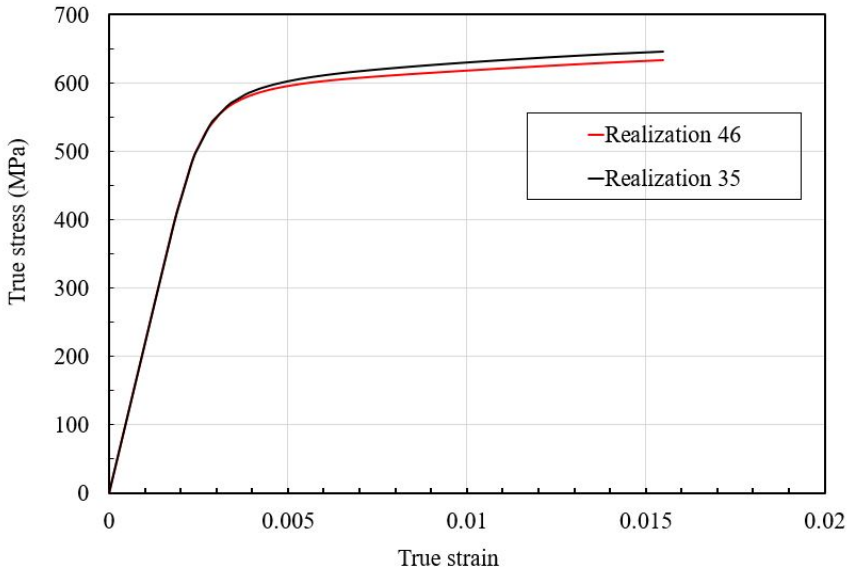


Figure 3.30. Macroscopic stress-strain curves obtained from Realizations 6 and 53.

Figure 3.31 shows the orientation-specific elastic lattice strain obtained from CPFEM diffraction post-processing for the two realizations. Analogous to their macroscopic stress-strain behaviour, the applied stress vs. elastic lattice strain curve of different grain groups (except group 331) in Realization 35 is higher than the corresponding grain groups in Realization 46. The deviation of the curves in the elastic region between these two realizations is smaller than in the near-yield region for all diffracting grain groups, indicating that the major difference in mesoscopic mechanical response comes from the anisotropic plastic deformation in different grain families. In both realizations, the applied stress and the elastic lattice strain for the 311, 220, 531 and 331 diffracting grain groups show a relatively linear correlation, while lower linearity is observed for the 111 and 200 planes. The 220 and 311 planes show less orientation dependence in the elastic region than other planes, while the highest orientation dependence is observed for 111 planes.

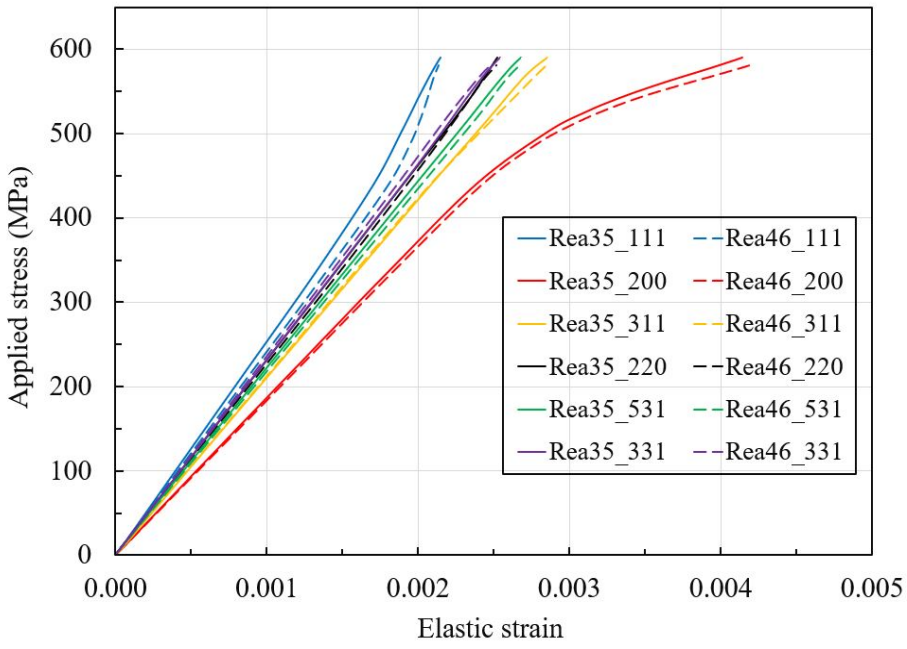


Figure 3.31. Illustration of the orientation-dependent elastic lattice strain reproduced by the finite element method using Realizations 35 and 46.

To capture the microscopic response of all diffracting grain groups, the distribution of elastic lattice strain in Realizations 35 and 46 across IPs that belong to different grain groups when the total strain reached near yield region (0.4% strain) are illustrated in Figures 3.32 and 3.33, respectively. The distributions of the elastic strain for all grain groups in both realizations appear to follow a normal distribution, albeit with some asymmetry. Nevertheless, the elastic strain distributions for 111 and 200 planes could not be fitted particularly well with the normal distribution. There are mainly two explanations for the difference of local elastic strain distribution in various diffracting grain families. First, larger numbers of IPs were found to correspond to the 220, 311, 331 and 531 scattering vector orientations compared to 111 and 200 orientations. Larger data sets would result in better statistical distributions. Additionally, according to the FEDPP data illustrated in Figure 3.31, the 220, 311, 331 and 531 planes show higher linearity compared to 111 and 200 planes. Strain heterogeneities increase when local behaviour becomes strongly non-linear, and when strong interaction between plastic deformation and elastic strain is observed. The lattice strain distribution is likely to be scattered and irregular if more non-linearity is apparent. The non-linearity of 111 and 200 planes suggests that strong elastic-plastic interaction occurs in grains with these two orientations. When the total strain reaches 0.4%, the material deformation undergoes the transition from elastically dominated to plastically dominated deformation, and more plastic deformation effects accumulated in 111 and 200 grain families than in the other orientations. It is therefore argued that the elastic strain distribution is greatly sensitive to the accumulated plastic slip in the elastic-plastic transition region.

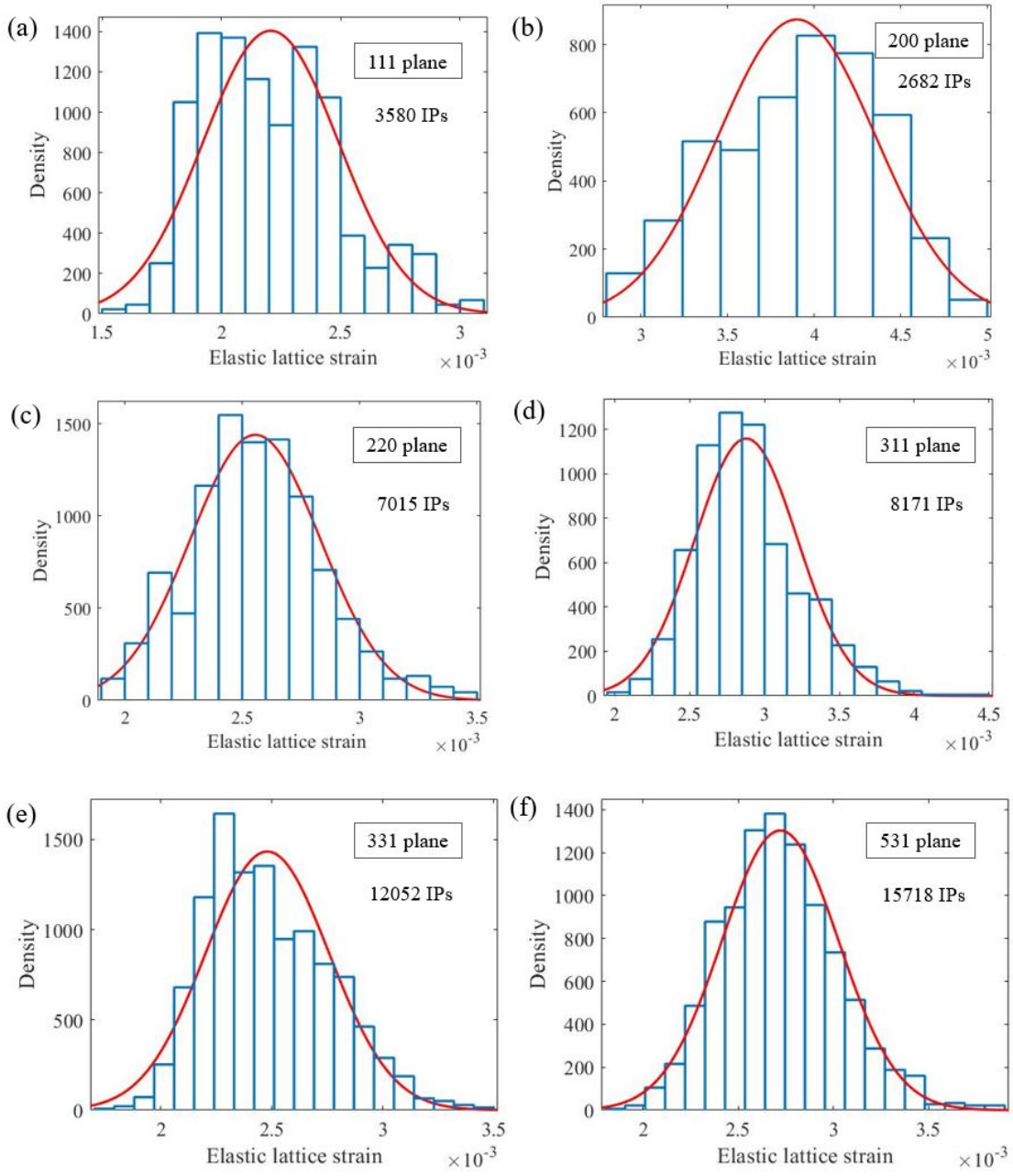


Figure 3.32. The distribution of elastic strain in Realization 35 across the IPs that contribute to different diffraction planes at the total strain level of 0.4%.

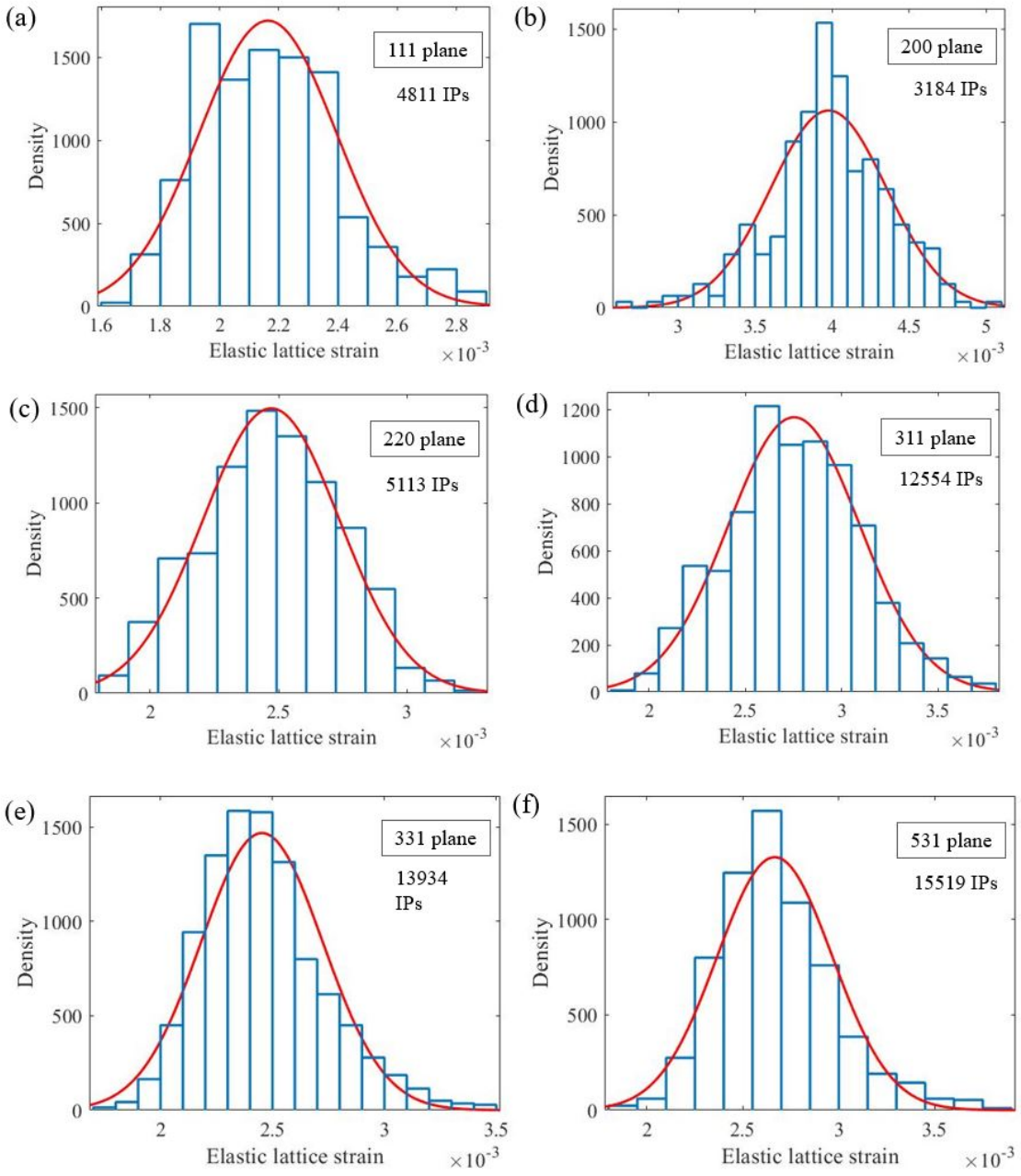


Figure 3.33. The distribution of elastic strain in realization 46 across the IPs that contribute to different diffraction planes with a total strain level of 0.4%.

Fatigue indicator parameters (FIPs) including accumulated plastic slip and dissipation energy are widely used two types of damage accumulation and fracture initiation criteria in the literature. Computable FIPs are introduced to facilitate the studies of the influence of microstructure on fatigue crack formation. It is commonly accepted that these FIPs can serve

as a quantitative evaluation of the cyclic driving force for the formation and early growth of cracks within grains. High values of FIPs often correspond to localized "hot spots" of slip. FIPs can be well associated with experimentally observed fatigue crack sites in polycrystals [81, 82]. For accumulated plastic slip, Dunne et al. found that a microstructurally sensitive crystal plasticity model can well predict the crack nucleation site based on the accumulated slip [83]. It is also suggested by some researchers that dissipated energy could be used as a FIP to determine the damage accumulation [84, 85]. The multi-scale stress and elastic strain distributions described above provide a statistical description of the inhomogeneity of deformation in two distinctly different realizations. Ductile fracture often occurs in the region with highly localized plasticity, and this suggests the importance of physically-based initiation criteria at the microscopic level when evaluating the durability of components and structures. The plastic strain ε_f to failure in uniaxial tensile loading can be calculated using the path integral

$$\varepsilon_f = \int \sqrt{\frac{2}{3} d\varepsilon_{ij}^p d\varepsilon_{ij}^p} \tag{3.13}$$

Figure 3.34 represents the distribution of accumulated plastic slip across all IPs in Realizations 35 and 46 at the total uniaxial tensile strain of 1.55%. The macroscopic strain in both realizations is expected to be the same, whereas the localized plastic strain has apparently different distributions. The maximum plastic strain in Realization 46 is 5.74%, which is slightly larger than the peak plastic strain of 5.68% in Realization 35. This implies that more localized damage is introduced in Realization 46 under uniaxial tensile loading based on the accumulated plastic slip criterion.

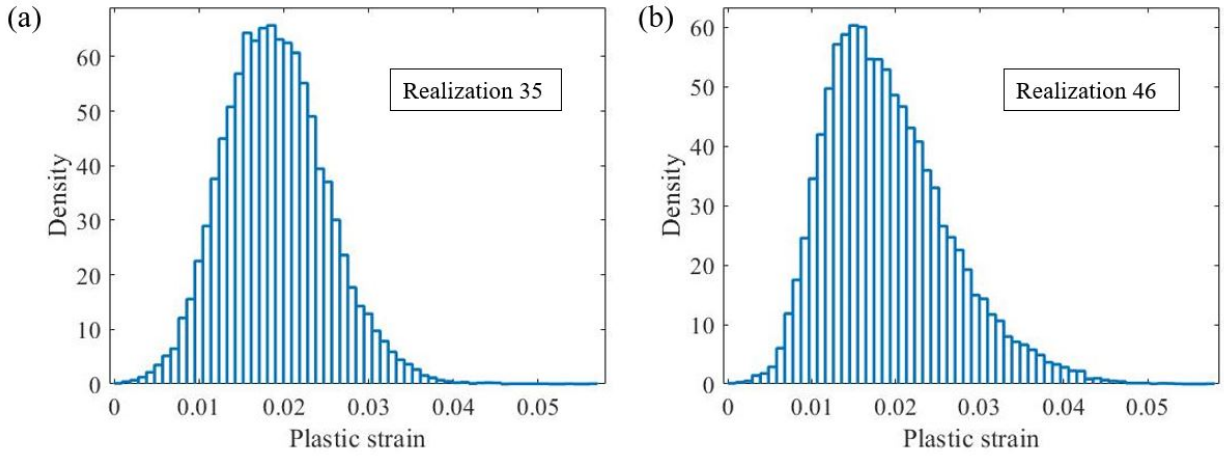


Figure 3.34. The distribution of accumulated plastic slip across all IPs in two extreme realizations at a total strain of 1.55%.

Energy-based criteria, such as the net dissipated energy, are often used to analyse the fatigue damage caused by cyclic loading. The increment of dissipated energy at each load increment can be expressed as

$$dW(x) = \sum_{\alpha=1}^{n} \tau_c^{\alpha} \dot{\gamma}^{\alpha} dt \tag{3.14}$$

Here x is the location of the integration point, and dt refers to the duration of load increment. The dissipated energy at each IP can be calculated by integrating Equation (3.14) and summing over all increments during loading. Cyclic simulation has been carried out at room temperature on Realizations 35 and 46 for fully reversed strain-controlled loading with zero mean stain. The maximum strain was chosen to be 0.8% so that the plastic deformation was not greatly dominant, corresponding to low to intermediate cycle fatigue regime. The cyclic stress-strain response of the two realizations is depicted in Figure 3.35. At the end of one cycle of loading, the local dissipation energy value across all the IPs was collected and analysed statistically. The distribution of the dissipated energy across all IPs in two realizations is illustrated in Figure 3.36. Realization 35 has a larger averaged

dissipated energy (13.0 mJ) after cyclic loading compared to Realization 46 (8.1 mJ), which can be explained by the fact that Realization 35 has a higher overall stress response than Realization 46 at the same strain level. The maximum dissipation energy in Realization 46 (25.3 mJ) is much smaller than that in Realization 35 (31.6 mJ). This suggests that localized failure is more likely to occur in Realization 35 under cyclic loading based on the dissipated energy criterion.

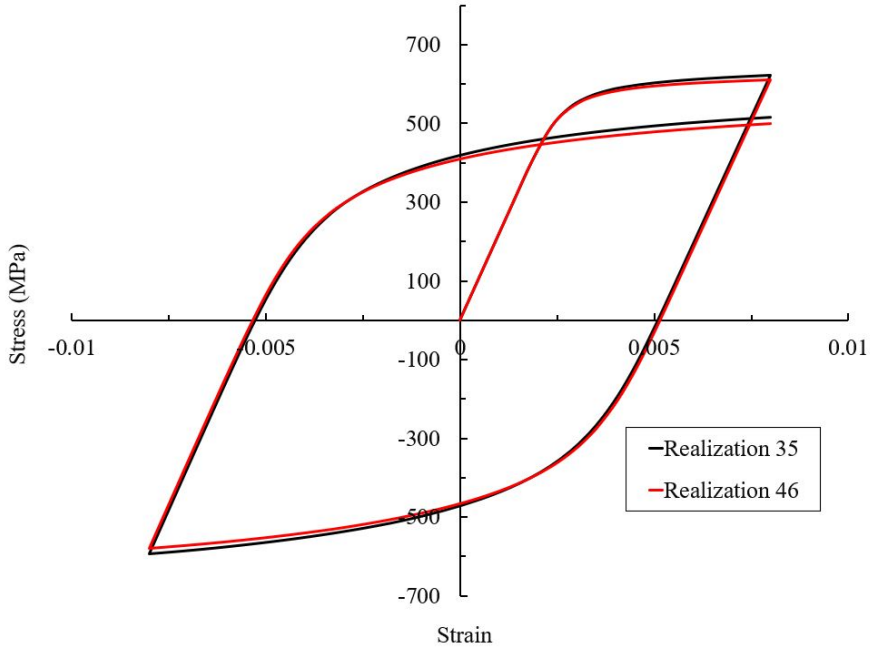


Figure 3.35. The cyclic stress-strain response of realization 35 and 46 (maximum strain 0.8%)

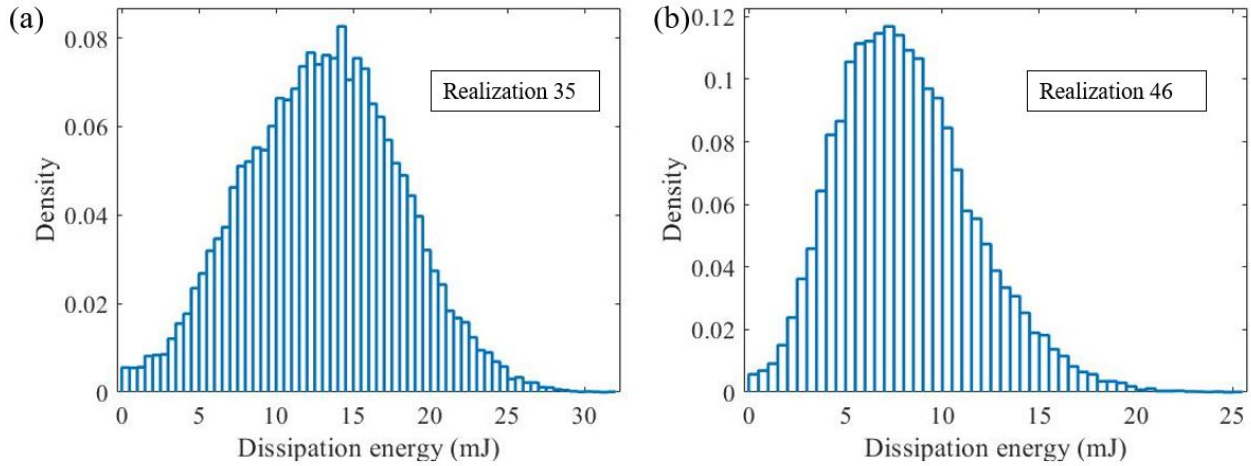


Figure 3.36. Distribution of dissipation energy across all IPs in two extreme realizations at the end of cyclic loading.

3.7 Analysis and conclusion

Stress and deformation in polycrystalline materials are often heterogeneous, and they can be classified into three types according to their characteristic length scale and controlling microstructure: Type I macroscale (different RVEs), Type II mesoscale (grains and grain groups), and Type III microscale (integration points). In this chapter, a rate-independent formulation is implemented within a crystal plasticity framework utilizing representative volume elements. To perform a multiscale analysis of the distributions of strain, stress and other mechanical responses, many RVE realizations with different grain morphologies and orientation permutations were generated. The material properties and crystallographic orientation for polycrystalline alloy Haynes 282 were assigned to each integration point within an RVE such that the mesoscopic response of diffraction grain groups and microscopic behaviour across IPs could be readily captured.

At the macroscale, the strain and stress differences emerge between different RVEs

with various microstructures. Statistical analysis was performed on the macroscopic stress-strain responses of RVEs. An apparent discontinuity between elastic and plastic regimes was found in the standard deviation curve for the first set of RVEs (No. 1-48) with the same grain morphology. By changing the grain orientation permutation, the overall stresses that correspond to 1.55% strain among different RVEs were found to follow a normal distribution. The width and height of the normal distribution were affected by the parameters that described the lognormal grain size distribution. Interestingly, the morphology with a larger grain size dispersion was found to lead to smaller overall stress discrepancies. The investigation between ensembles with different grain sizes suggests that discretization can introduce Hall–Petch like size effect in polycrystalline materials. The overall stresses of Morphologies 3 and 8 show two distinctly different normal distribution shapes. In engineering design, the reproducibility of the mechanical behaviour of mass-produced components remains a critical question. Components with a narrower stress distribution (such as Morphology 3) are expected to be more reliable for the purposes of structural integrity, whereas parts that show a wider stress distribution (like Morphology 8) will possibly introduce a larger uncertainty for structural integrity lifing procedures.

At the mesoscopic scale, the inhomogeneous deformation is characterized by the anisotropic response that originates from different grain families. This chapter evaluates the grain-orientation average of elastic lattice strain via the use of diffraction post-processing of FE simulation results. The orientation-specific elastic strains reproduced by CPFEM are validated by comparison with the neutron diffraction data of a polycrystalline Haynes 282 alloy.

At the microscale, deformation is controlled by the crystal structure, defect distribution and dislocation motion/interaction, which are discrete in nature. Consequently, the stress and strain can only be obtained by averaging atomic-scale properties over a certain region (i.e. integration points in this study). When the total strain reaches 1.55%, the elastic strain (and stress) accumulation is found to be additive leading to a normal distribution, whereas plastic strain can be well described by a lognormal distribution and obeys a multiplicative accumulation process. As opposed to the distribution of local properties, the macroscopic overall stresses of different RVEs follow a much narrower normal distribution. Relatively stable macroscopic stress responses of the RVEs with various grain orientation permutations and morphologies are all found to be within 2% difference bounds. The separation of stresses into these three types is illustrated using one randomly selected realization, and a significant variation of stress magnitudes within one grain (Type III) and among different grains (Type II) is observed. The above finding reveals the nature of stress and strain inhomogeneity at different scales and highlights the fact that the dispersion of local stress and strain distribution is much larger than the macroscopic average. We hypothesize that this finding is valid when the volume of interest is above a minimum representative volume that accounts for the macroscopic homogeneity of deformation.

A multiscale investigation of mechanical response is performed on two extreme realizations. Realization 35 and 46 have identical grain morphology but different orientation permutation. Realization 35 has the highest macroscopic stress-strain curve, whist Realization 46 represents the weakest strain hardening and hence the lowest macroscopic curve. Similar to their macroscopic response, elastic lattice strains of different grain families

(except the 331 group) in Realization 35 are higher than the corresponding grain families in Realization 46 at the same applied stress. The mechanical response of the 111 plane family shows the largest discrepancy between these two realizations, therefore, it is reasonable to expect the 111 plane family response to be highly orientation dependent. Microscopically, the elastic lattice strains at IPs that contribute to the 220, 311, 331 and 531 grain groups (with higher mesoscopic linearity) appear to follow more closely a Gaussian distribution in both realizations. The distributions of local plastic slip and dissipation energy suggest that pure macroscopic response is not sufficient to perform a reliable calculation for lifing analysis, as failures often originate from localized regions where microscopic behaviour with broader histograms is dominant. The above statistical analysis of stress and strain at the local and global level for different RVEs provides a means of developing new insights into the relationship between microstructure and mechanical properties at multiple scales. The results obtained here provide a statistical description of the magnitude of grain level stresses and strains variation that gives guidance to the rational design for structural integrity allowing for reliable uncertainty quantification.

4. A numerical study of the effect of discretization on the crystal plasticity finite element simulation results

4.1 Introduction

Before the 1980s, the prediction of the mechanical field mainly relies on continuum level models, which neglect the inhomogeneous nature of the materials. Such method is not reliable when the characteristic length is down to the micrometre level. For polycrystalline metals such as nickel-based superalloys, the elastic and plastic deformation are highly anisotropic. Plasticity deformation occurs mainly by the movement of dislocation along specific slip planes and directions. Depending on their crystallographic orientation with respect to the loading direction, grains deform to different extents to carry disparate magnitudes of stress under different applied loads, giving rise to heterogeneous deformation fields between adjacent grains and within individual grains.

With the advance in computational mechanics in recent years, crystal plasticity frameworks were established and applied to predict the deformation behaviour of both single crystal and polycrystals. The implementation of crystal plasticity theory within the finite element method is called the crystal plasticity finite element method (CPFEM). CPFEM was first initiated by Peirce et al. [34] and has been extensively used to investigate the heterogeneous deformation response of polycrystals under various boundary conditions [86-90]. The crystal orientation and material state variables are updated in each load increment at every integration point (IP) by solving the crystal plasticity formulation. CPFEM not only predicts the macroscopic stress-strain curve and texture evolution, but also

provides excellent predictions of the local deformation fields and local crystal orientation with the help of appropriate homogenization schemes [91-98], such as a representative volume element (RVE).

Based on the discretization methods, the implementation of CPFEM can be categorized into two types: (i) those considering crystal plasticity constitutive model at the integration point level (called static mesh in this chapter); (ii) those representing the grain morphology at the element level (called grain-based mesh). For static mesh, it is integration point-based and the IPs in the same element can belong to either one grain or different grains. Before 2010s, static mesh is widely used to investigate the microstructure-sensitive material properties, i.e., texture evolution [99, 101], stress concentration [88], phase transformation [100], fatigue criteria [102]. Such discretization method is still employed by some researchers nowadays to study the mechanical properties of various alloys including FeCrAl alloys [103], ultrafine-grained nickel [104] and steel [105]. For grain-based mesh, the minimum discretization unit is an element and the IPs in the same element can only belong to one grain. Over the past decade, the grain-based mesh becomes more popular than the static mesh method due to its advantage in visualization and post-processing [61-64, 66, 69, 106]. A considerable number of researchers employ both static and grain-based mesh in CPFEM, while no published data provide a comprehensive and systematic study of the difference, especially in the mechanical field, that arose from these two discretization methods.

The research in Chapter 4 aims to investigate the effect of discretization methods and grain numbers within an RVE for CPFEM. To represent complex grain interaction scenarios

in realistic microstructures, the present research considers two element types including static and grain-based mesh of various grain numbers that range from 34 to 1250 in predicting the stress and strain field. Material properties and grain orientations were assigned at integration points for static mesh and elements for grain-based mesh. Multiple RVE realizations with different grain numbers were generated by Voronoi tessellation and massive simulations were performed to reveal the effect of discretization methods and grain numbers. Periodic boundary conditions and the same number of elements per grain were employed for all the RVE realizations to minimize any other factor that might affect the simulation results. Comparison of CPFEM predictions in terms of strain/stress fields accuracy and computational efficiency were presented and analyzed in this chapter. It is believed that the main conclusion in this chapter provides further insights into the choice of discretization methods in polycrystalline CPFE modelling.

4.2 Modelling methodology

4.2.1 Crystal plasticity formulation and hardening law

Some researchers have studied the effect of crystal plasticity hardening framework on the mechanical response of polycrystalline alloys. Lim et al. suggested that slip-based hardening law can accurately reproduce the deformation behaviour obtained from dislocation density-based constitutive equations [55]. Additionally, slip-based hardening law shows smaller relative error and smaller mesh sensitivity compared to dislocation density-based law. Therefore, phenomenological constitutive (slip-based) hardening law is chosen in this chapter. The present model was implemented using phenomenological crystal

plasticity constitutive equations following Manonukul & Dunne [46]. It was further extended to account for elastic anisotropy, and to allow three-dimensional modelling for alloys with various crystal structures, i.e. face-centred cubic (FCC), body-centred cubic (BCC) and hexagonal-closest packed (HCP). Here we use the same crystal plasticity equation as present in Chapter 3 and the constitutive equations are implemented using a user-defined material subroutine UMAT within the commercial finite element analysis package ABAQUS.

4.2.2 Microstructure generation procedures

For static mesh, the RVE of the polycrystal is discretized as a fixed hexahedral mesh (C3D8 element) and the material properties are assigned to each **IP**. The open-source software package Neper [107] is utilized to generate the grain origin positions ('seeds') that are associated with the crystal orientation specified at each grain. To reflect the grain growth during the crystallization process, a population of 34 grains is derived from the seeds by 3D Voronoi tessellation. By varying the spatial distribution of the seeds, it is possible to control grain size distribution within RVE. Some published CPFEM studies suggest that 50-100 elements per grain are sufficient to predict microscopic deformation field [65, 66]. Thus, 15x15x15 elements are employed in this study (as shown in Figure 4.1(a)), leading to an average of ~100 elements per grain. In contrast with grain-based meshing, this approach uses a static FE mesh in combination with a dynamic assignment of crystal orientation per IP, allowing a flexible implementation of both grain morphology and orientation, jointly or severally. The use of integration-point-based assignment of grain orientation will improve

the accuracy and efficiency of diffraction post-processing when calculating grain orientation-average elastic strain from CPFEM. The initial crystal orientation is assigned at each IP by inheriting it from the nearest grain seed. Texture can be described by the choice of grain orientation distribution function (ODF). In this chapter, a set of RVE together with the assigned initial crystal orientations are referred to as a microstructural realization. The main advantage of static mesh is that it can be used to investigate statistical material response induced by several realizations without changing the RVE model once the deformation model is validated.

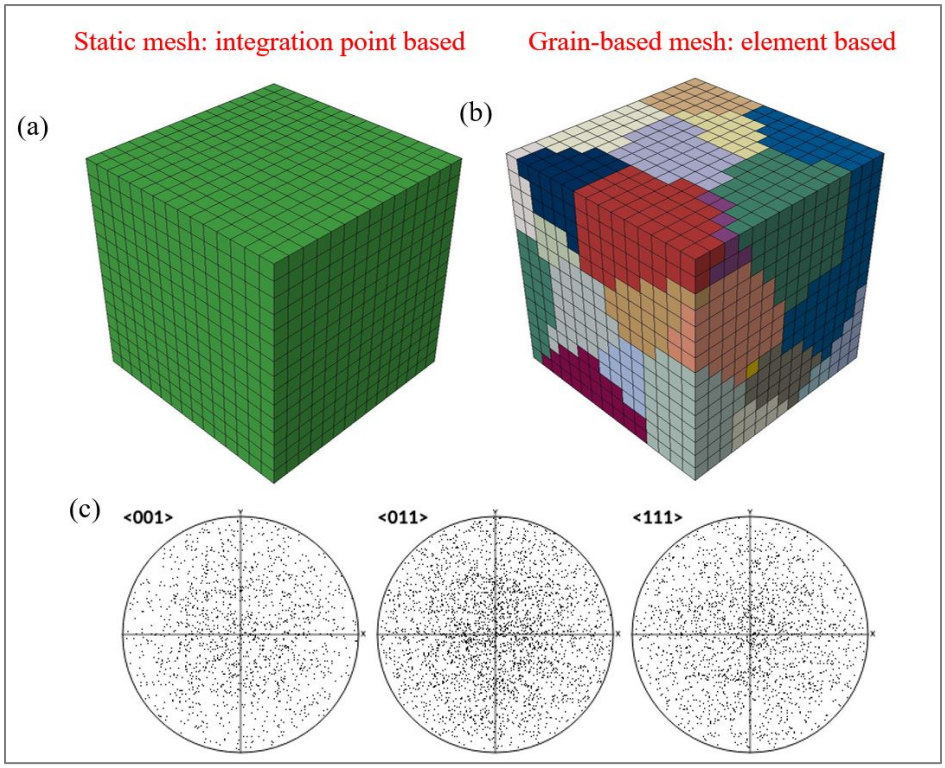


Figure 4.1. The RVE models for (a) static mesh and (b) grain-based mesh. (c) pole figures show random texture in three directions. The same tessellated microstructure is used for both static and grain-based mesh. Different colours represent different grains.

For grain-based mesh, the RVE of the polycrystal is also discretized as C3D8 elements while the material properties are assigned to each **element**. The same set of seeds and

corresponding crystal orientation are employed to generate a grain-based RVE by Neper software, as illustrated in Figure 4.1(b). The set of elements that belong to the same grain is defined in the pre-processing stage, and hence, the RVE model needs to be changed when investigating the mechanical property of different microstructural realizations. It is more convenient to visualize the grain structure for grain-based mesh compared to static mesh. The same lognormal grain size distribution and random ODF (shown in Figure 4.1 (c)) are utilized to construct the RVEs with static mesh and grain-based mesh throughout the study.

4.2.3 Loading and boundary conditions

In polycrystalline alloys, the deformation of RVE is inhomogeneous due to the nature of material anisotropy. To eliminate the effect of the boundary layer, periodic boundary conditions (PBC) instead of homogeneous boundary was applied to the initial configuration of RVE. Figure 4.2 depicts the initial configuration of the RVE subjected to periodic boundary conditions. For one arbitrary node on the surface of RVE, there is a matching node on the opposite RVE boundary. PBC is implemented by coupling the displacements of the nodes of each pair of opposites faces of the RVE. Any over-constraint should be avoided for the nodes that are located on the vertices and edges. The displacement constraint equations were generated by the open-source ABAQUS plugin EasyPBC [71]. After setting the constraint equations, displacement boundary conditions were applied at RVE vertexes. A displacement-controlled loading was applied at the dummy node that constrains the relative displacement between the front and back surfaces in the third direction. Internal length scales are not considered in the study and all the RVEs have the same volume of $1\times1\times1 mm^3$.

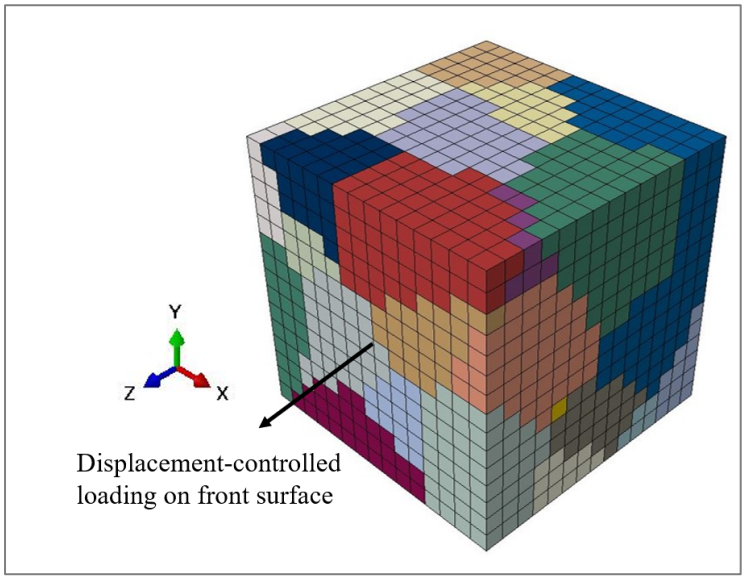


Figure 4.2. The RVE realization is subjected to periodic boundary conditions.

4.2.4 Model calibration and material parameters

Four material parameters need to be calibrated in this model: the initial critical resolved shear stress τ_c^{α}, two hardening parameters, and the elastic moduli matrix. To calibrate these parameters, the overall response of an RVE with 600 grains during tensile loading was fitted to the experimental stress-strain curves for a nickel-based superalloy, Haynes 282. It has an FCC crystal structure with 12 $\langle 1\bar{1}0\rangle\{111\}$ slip systems. Optimal values of materials were determined by fitting the macroscopic and mesoscopic response of RVE to the experimental stress-strain curve and neutron diffraction measurement obtained by Jaladurgam et al. [72]. For a detailed description of the calibration procedure, readers can refer to Chapter 3. Figure 4.3 compares the predicted stress-strain curve with the experiment curve and an excellent agreement has been achieved. The corresponding material parameters are listed in Table 4.1.

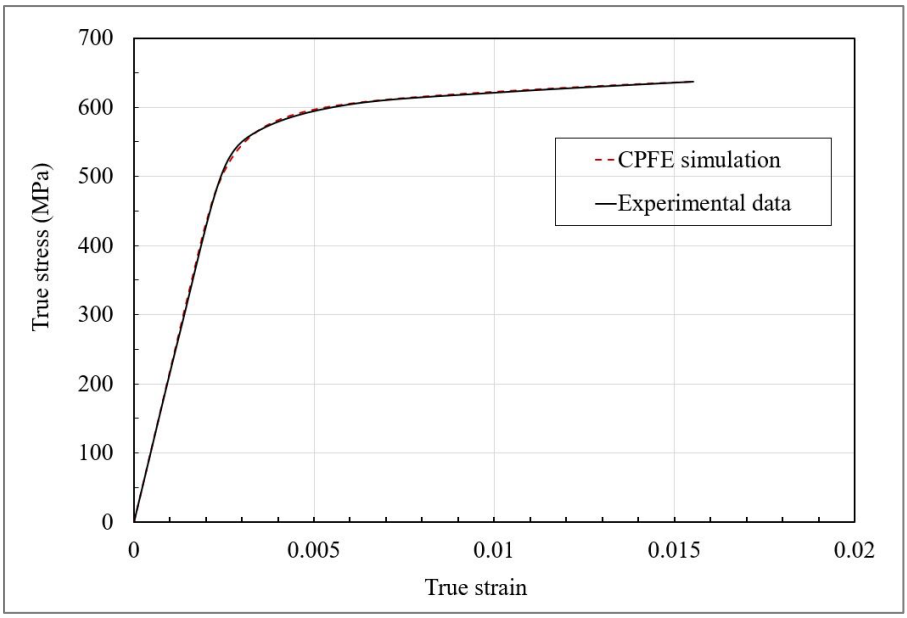


Figure 4.3. The macroscopic stress-strain curves under monotonic loading obtained from CPFE prediction and experiment.

Table 4.1. Material parameters used in the CPFEM simulation

Stiffness (GPa)			CRSS		
C11	C12	C44	(MPa)	h	q
250	160	118	257	h=$h_F[1+(h_R-1)exp(-100h_{exp}\varepsilon)]$ *	1.01

*$h_F = 950, h_R = 14, h_{exp} = 4.$

4.3 Simulation results and discussion

4.3.1 The effect of discretization methods

In the first part of Chapter 4, we concentrate on the difference in mechanical response caused by different discretization methods. Displacement-controlled tensile loading was applied to both RVEs with 34 grains shown in Figure 4.1. The RVEs with the same tessellated microstructure were discretized into the static and grain-based mesh, respectively.

Both simulations were stopped when the total strain reached 1.55% and the overall stress of the whole RVE at 1.55% strain was termed as $\sigma_{1.55\%}$. Figure 4.4 depicts the macroscopic stress-strain curve obtained from RVEs with static and grain-based mesh. The two curves are almost identical with a minor discrepancy in the plastic region, which reveals that different discretization methods introduce little difference in terms of macroscopic response.

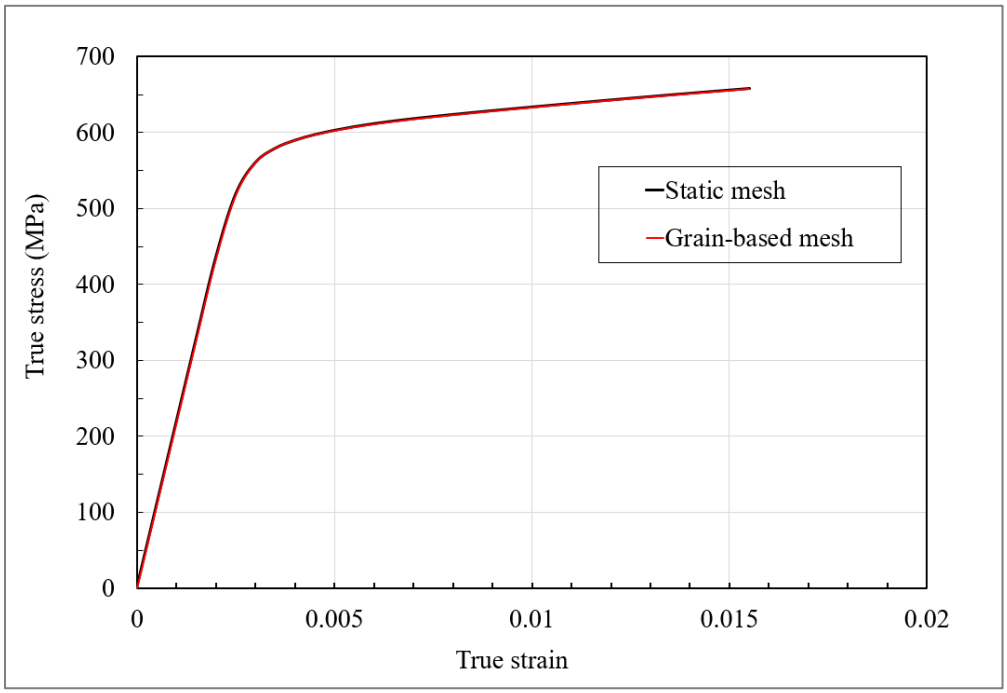


Figure 4.4. Illustration of stress-strain curves predicted from CPFEM with static and grain-based mesh.

Figures 4.5 and 4.6 illustrate the stress in the loading direction σ_{33} and accumulated plastic strain after uniaxial tension to a strain of 1.55%. To further study the internal stress and strain field, the original RVE configuration was cut in half as shown in Figures 4.5 and 4.6. The apparent sensitivity of the models to discretization methods in terms of local (microscopic) mechanical response can be observed. A qualitative comparison of contour maps suggests that the CPFEM models can well predict stress/strain localization points and

weak/cold locations in the polycrystalline materials independent of the two discretization methods investigated in this chapter. However, the predicted stress/strain values show obvious deviations at both inner and surface layers. Further investigation reveals that the largest heterogeneities and strain/stress discontinuities are present in the RVE with grain-based mesh.

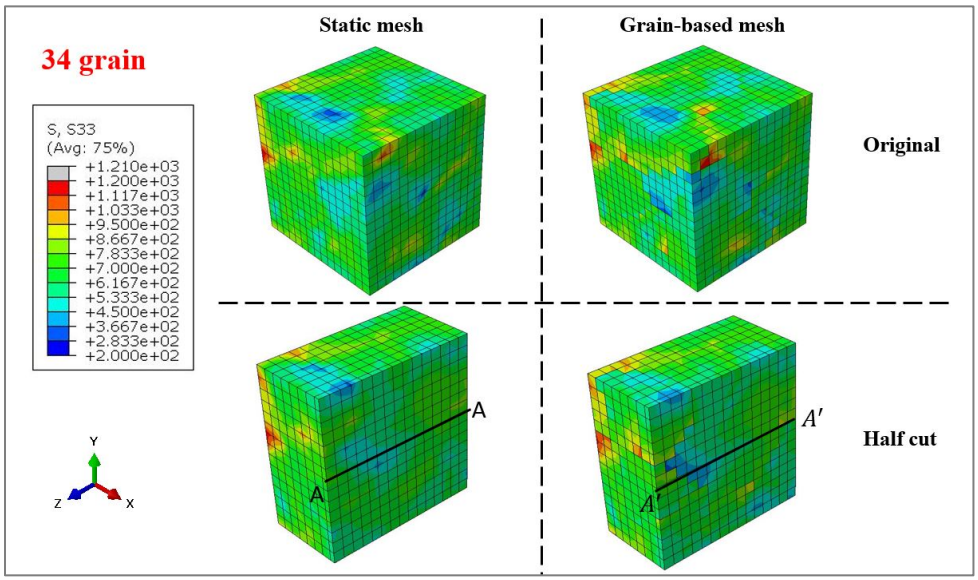


Figure 4.5. Original and half-cut contour maps showing the stress in the loading direction after tension to a total strain of 1.55%.

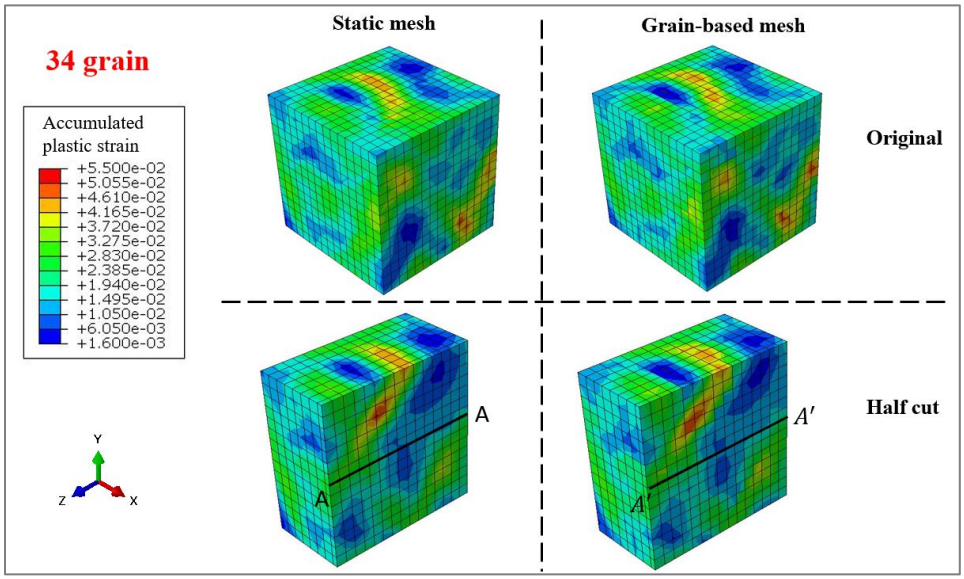


Figure 4.6. Original and half-cut contour maps show the accumulated plastic strain after tension to a total strain of 1.55%.

To investigate the origin of stress and strain discontinuities, path A-A and path A'-A' were drawn at the same location in half-cut RVEs with static and grain-based mesh, respectively. The stress σ_{33} and accumulated plastic strain across the two paths were shown in Figures 4.7 (a) and (b). The strain and stress profiles predicted by static mesh and grain-based mesh show the same trend and comparable magnitude. Stress/strain discontinuities are mainly observed at grain boundaries, and more discontinuities are found for the RVE with grain-based mesh. Two grain boundaries are located at the blue dash-dotted lines in Figure 4.7(a). The stress in the loading direction is continuous for static mesh, while discontinuous for grain-based mesh. Stress discontinuity often origins from material discontinuity. Here, grains with various orientations have different mechanical properties and can sustain different magnitudes of stress due to crystal anisotropy. Further investigation suggests that when the element of interest belongs to a single grain at the material discontinuity or grain boundary, stress discontinuity will occur at that discontinuity location for both static mesh and grain-based mesh. Nevertheless, when one element belongs to two or more grains at the grain boundary for static mesh, the stress discontinuity will be observed at the discontinuity location only for grain-based mesh, not for static mesh. The above finding indicates that static mesh will tend to reduce stress discontinuity and smooth stress profile at the material discontinuous location compared with grain-based mesh.

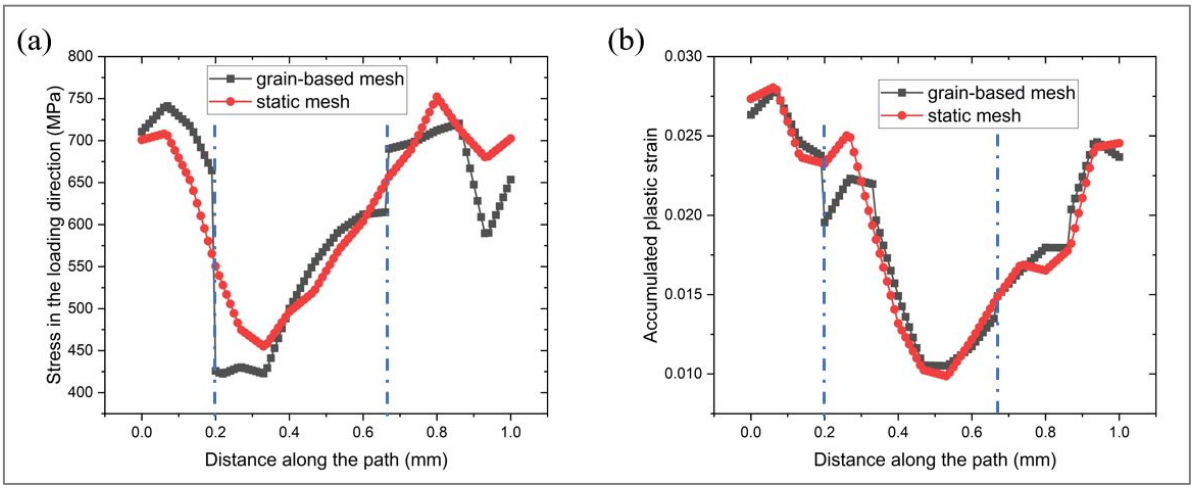


Figure 4.7. The stress in the loading direction and accumulated plastic strain across paths A-A and path A'-A'.

4.3.2 The effect of discretization methods with various grain numbers

The size effect in the CPFEM can be divided into discretization induced size effect and statistical induced size effect. The former effect arises from the discretization of grain (the number of elements per grain), while the latter is caused by different numbers of grains in the RVE. It is important to eliminate the discretization induced size effect when investigating the effect of discretization methods with various grain numbers. Therefore, the number of elements per grain is the same for all RVEs in this chapter. A comprehensive review of the literature shows that most of the CPFEM researches employ ~20-1500 grains in the RVE. As illustrated in Figure 4.8, four sets of RVEs with four grain numbers were generated in this chapter to represent most of the simulations in the literature. Each set of RVEs was discretized into the static mesh and grain-based mesh, and the same random orientation distribution function was used for all sets of RVE. Table 4.2 lists the realization numbers together with the assigned grain numbers and elements.

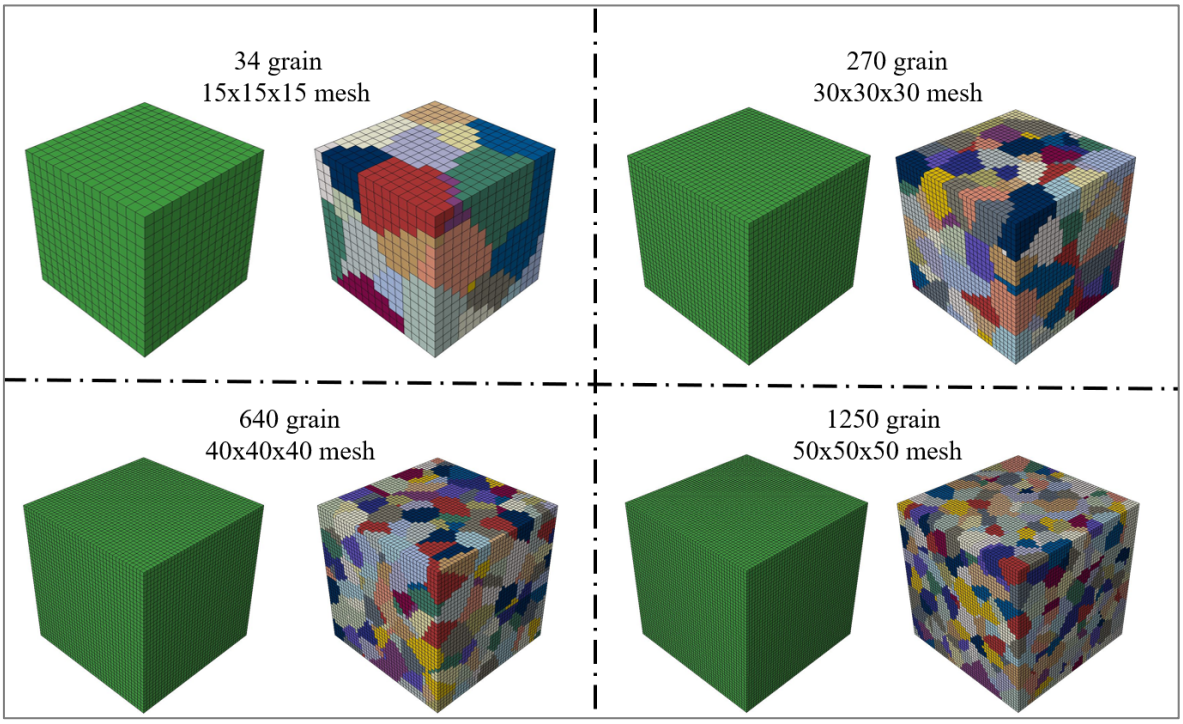


Figure 4.8. Four sets of RVE with different grain numbers and different discretization methods.

Table 4.2. Sets of realizations generated in the current research.

Realization	No. of grains in RVE	Discretization method	Total number of element	The average number of elements/grain
1	34	static	3375	~100
2	34	grain-based	3375	~100
3	270	static	27000	100
4	270	grain-based	27000	100
5	640	static	64000	100
6	640	grain-based	64000	100
7	1250	static	125000	100
8	1250	grain-based	125000	100

The same displacement-controlled loading was applied to all realizations, and the predicted stress-strain curves are shown in Figure 4.9. Similar stress-strain curves are observed independent of discretization methods and grain numbers. An enlarged view in Figure 4.9 (b) suggests that the maximum difference between the curves obtained from static mesh and the corresponding grain-based mesh is less than 0.5%. Figures 4.10-15 illustrate the original and half-cut contour maps for RVE with 270,640 and 1250 grains after tension to a total strain of 1.55%. Analogous to the findings for RVEs with a smaller number of grains as shown in Figures 4.5 and 4.6, the results for RVEs with a larger number of grains also reveal that the CPFEM models can predict stress/strain localization position and weak/cold spots independent of discretization methods. The magnitude of predicted local strain/stress shows apparent deviation and more strain/stress discontinuities are observed in the RVE with grain-based mesh.

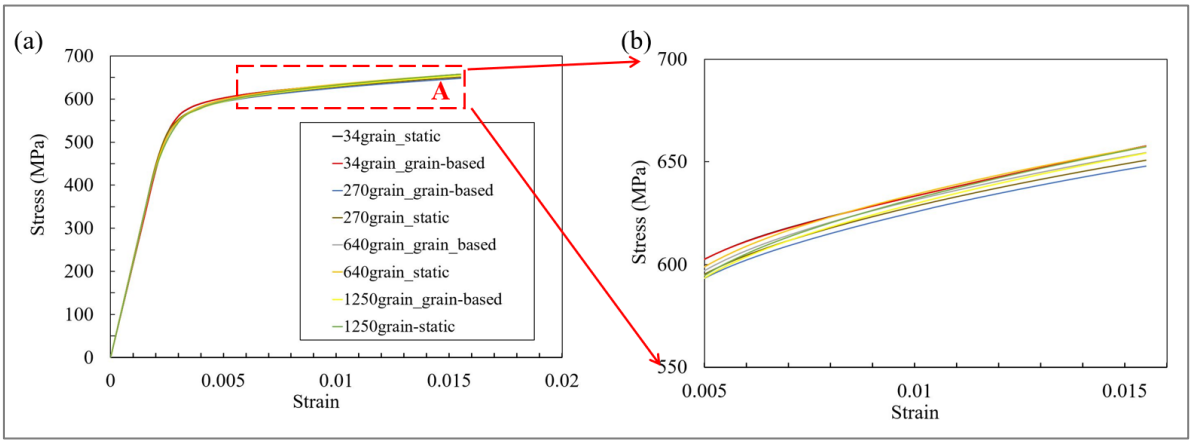


Figure 4.9. (a) The stress-strain curves from different discretization methods and grain numbers. (b) An enlarged view of area A.

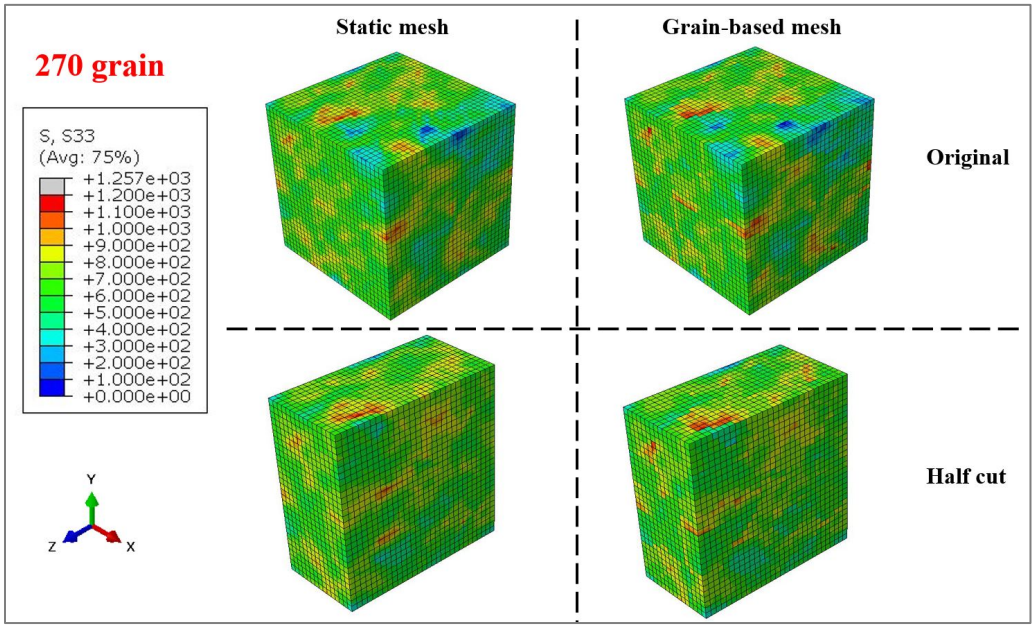


Figure 4.10. Original and half-cut contour maps for RVE with 270 grains show the stress in the loading direction after tension to a total strain of 1.55%.

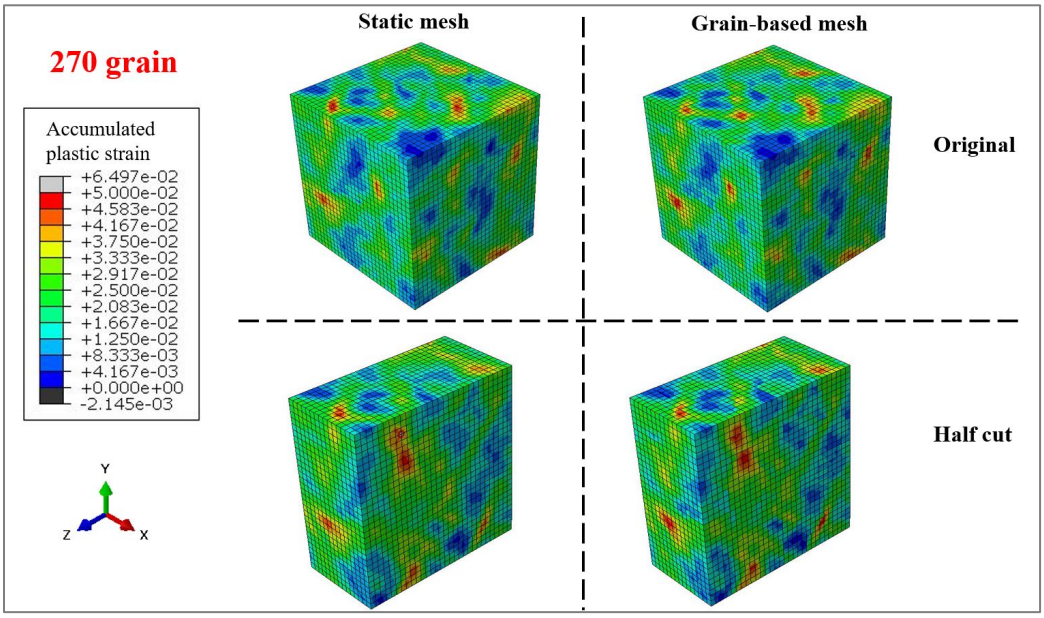


Figure 4.11. Original and half-cut contour maps for RVE with 270 grains show accumulated plastic strain after tension to a total strain of 1.55%.

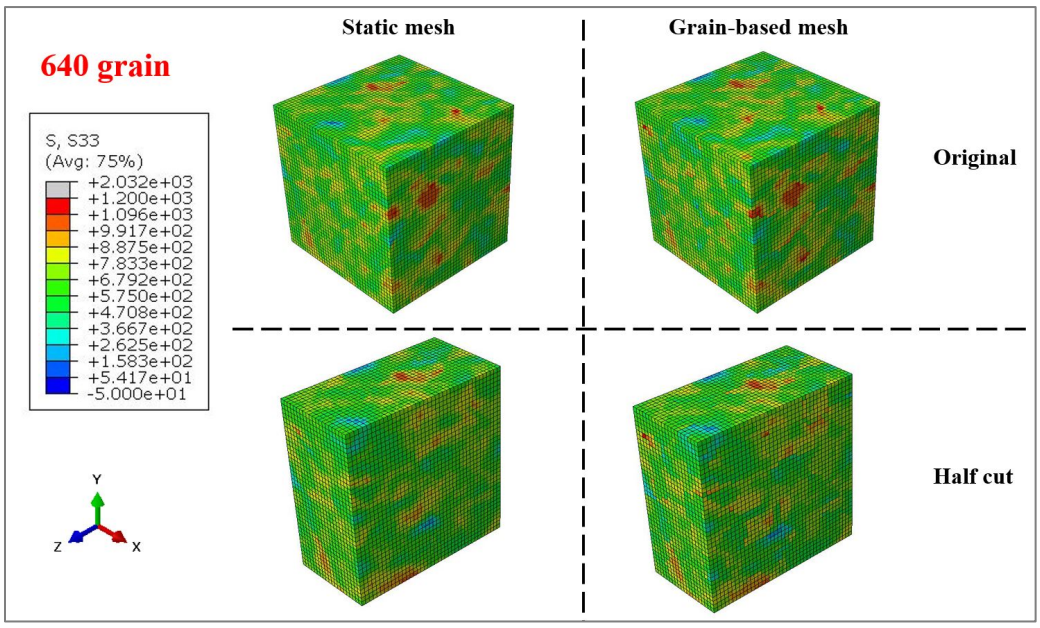


Figure 4.12. Original and half-cut contour maps for RVE with 640 grains show the stress in the loading direction after tension to a total strain of 1.55%.

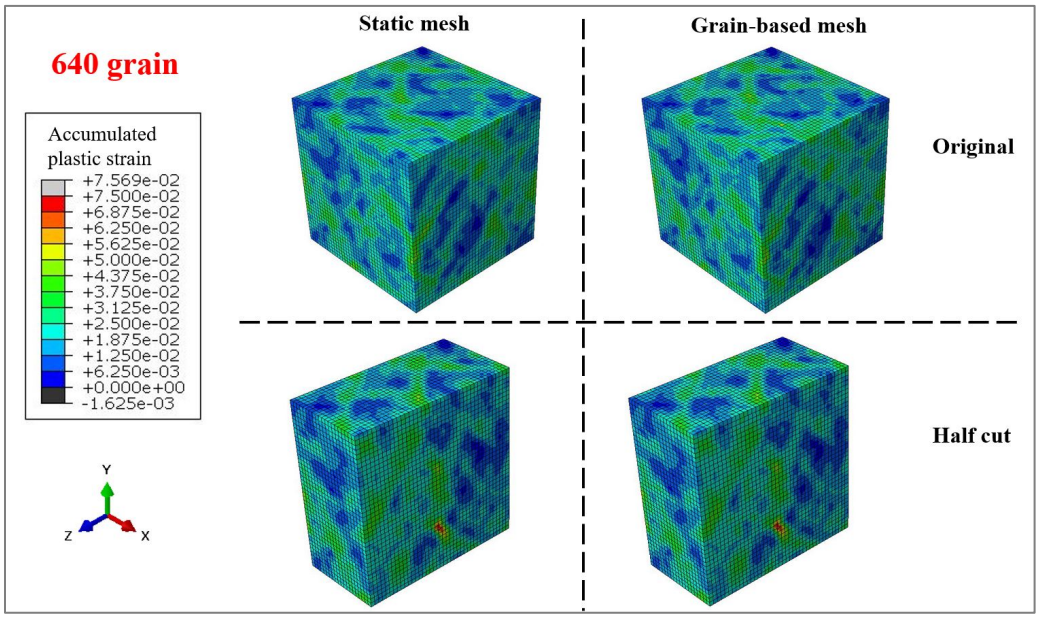


Figure 4.13. Original and half-cut contour maps for RVE with 640 grains show accumulated plastic strain after tension to a total strain of 1.55%.

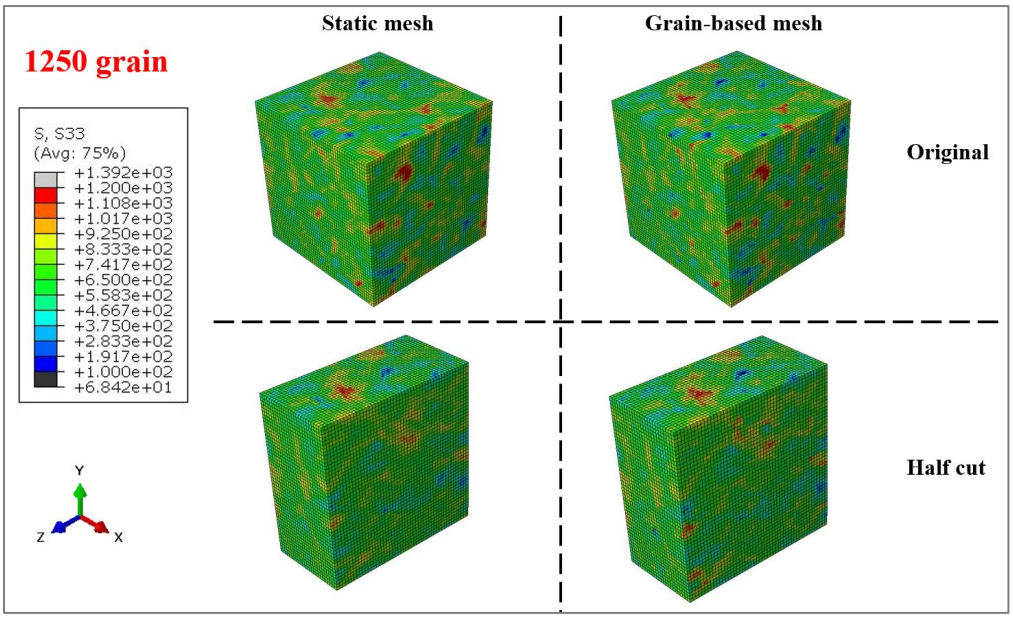


Figure 4.14. Original and half-cut contour maps for RVE with 1250 grains show the stress in the loading direction after tension to a total strain of 1.55%.

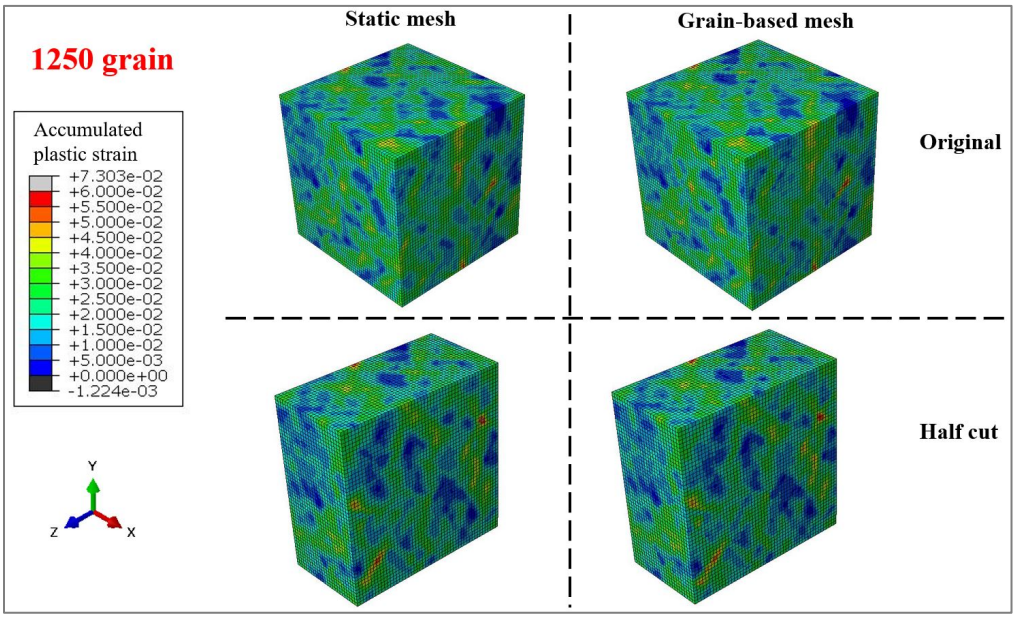


Figure 4.15. Original and half-cut contour maps for RVE with 1250 grains show accumulated plastic strain after tension to a total strain of 1.55%.

To quantitively evaluate the difference arose from these two discretization methods, the deviation is defined as

$$\text{Dev } (\%) = \frac{|\sigma_{static} - \sigma_{grain}|}{\sigma_{static}} \tag{4.1}$$

Where σ_{static} and σ_{grain} are the stress obtained from realizations with static mesh and grain-based mesh, respectively. The deviation can be either macroscopic (global) when σ_{static} and σ_{grain} are the overall response of the RVE, or microscopic (local) when the two stresses are the local stress at the corresponding integration point. As illustrated in Figure 4.16, the macroscopic deviations at 1.55% total strain are relatively small, and they are all within 0.5%. The macroscopic deviations increase significantly when the number of grains within the RVE increases from 34 to 270, and the largest amount of deviation is developed for the RVE with the largest number of grains. A plateau is observed and there is no apparent increase in macroscopic deviations when the grain number further increases above 270.

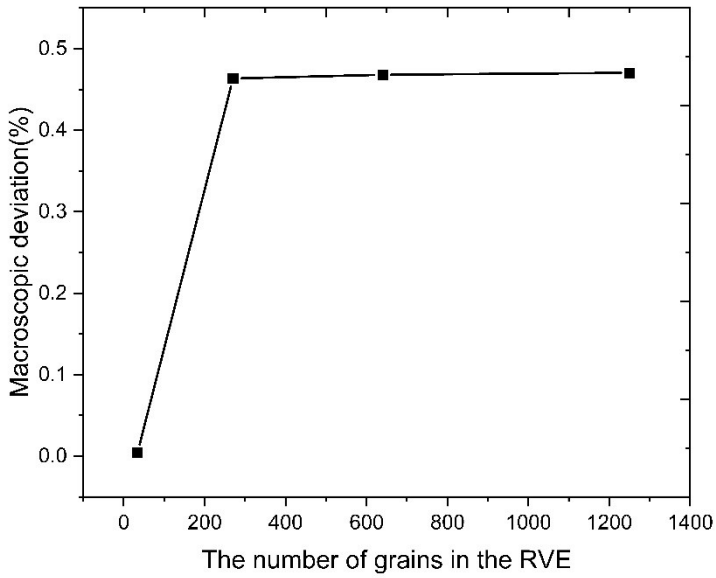


Figure 4.16. The macroscopic deviation after a tensile loading of 1.55% strain.

At each integration point, the microscopic deviation can be evaluated by the local stresses obtained from RVE with static mesh and its corresponding RVE with grain-based mesh. Figure 4.17 compares the probability density of microscopic deviations calculated from RVEs with a different number of grains after 1.55% total strain. Interestingly, no apparent deviation was observed for the distribution of local deviations as the number of grains within an RVE increases. The majority of the microscopic deviations are less than 10%. Compared with macroscopic deviations, the microscopic deviations are more significant, and their value can range between 0-50%.

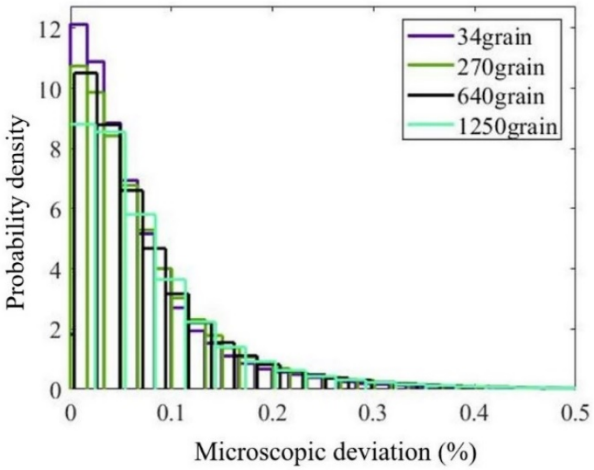


Figure 4.17. The microscopic deviations at all integration points for different numbers of grains within an RVE.

4.3.3 CPU time

To compare the computational efficiency of the CPFEM simulations with static and grain-based mesh, all the simulations were performed using a 48 core Intel Xeon Platinum 8268 computational node. A nonlinear implicit solver was used in Abaqus and the initial step, minimum and maximum step time for all simulations were 0.02s, 0.0001s and 1s, respectively. Table 4.3 lists the number of increments and total CPU time for all the

simulations to achieve 1.55% strain. It is clear from Table 4.3 that static mesh reduces 5%-15% computational time compared to grain-based mesh, which suggests that static mesh shows a faster convergence rate than grain-based mesh. As reported in Section 4.3.1, more strain/stress discontinuities are observed in the RVE with grain-based mesh. More simulation time and increments are needed when there are stress discontinuities, while the static mesh reduces the simulation time by smoothing the discontinuities without introducing any apparent deviation in macroscopic response.

Table 4.3. Total CPU time and the number of increments for all simulations.

Grains per RVE	Total CPU time in hours		The number of increments	
	Static mesh	Grain-based mesh	Static mesh	Grain-based mesh
34	7.2	8.2	347	445
270	129.6	144.5	595	661
640	469.9	547.7	697	806
1250	1710.2	1781.8	938	975

4.4 Discussion

Chapter 4 aims to reveal the macroscopic and microscopic deviations in polycrystalline CPFEM with two discretization methods and different numbers of grains within an RVE. To the best of the author's knowledge, this is the first research quantitatively comparing the simulation accuracy and computational time as a function of discretization methods, i.e.

static mesh and grain-based mesh. This research is essential when predicting the evolutions of local strain and stress fields during plastic deformation, especially while reproducing crack formation and growth. Such phenomena are challenging as the accuracy of these models strongly relies on the explicit meshing of grain structure. Both static mesh and grain-based mesh can well predict the location of strain/stress location and their results are consistent with each other. Although static mesh and grain-based mesh can reproduce almost identical stress-strain curves within a 0.5% difference, the local strain/stress response of the two discretization methods shows a large deviation in magnitude. The microscopic deviations can be as large as 50%, which is a significant and unreliable value for many service conditions.

As for the computational time, static mesh shows faster convergence and reduces 5%-15% computational time compared to grain-based mesh. Another advantage of static mesh is that it can be used to research multiple realizations without changing the RVE model once the model is validated. The only modification needed for static mesh is to provide a different set of seeds position and their corresponding crystal orientation. However, for grain-based mesh, each realization has its unique RVE model, and the element sets for each grain need to be assigned in the pre-processing stage. Because static mesh reduces both pre-processing and simulation time and provides comparable stress-strain curves to grain-based mesh, our results suggest that static mesh is recommended for CPFEM when calibrating the material parameters or when the macroscopic mechanical response is of interest. Nevertheless, the predicted deviations for the microscopic response are much more significant than the macroscopic response. When the local mechanical responses such as fatigue indicator

parameter and accumulated plastic strain, are the main research interest, it is recommended to employ grain-based mesh to get improved solution accuracy as it can explicitly describe the material discontinuity at a proper level (element).

4.5 Conclusion

In this chapter, a large number of crystal plasticity finite element simulations were performed to understand the effect of discretization methods and grain numbers on the solution accuracy of the predicted strain/stress filed. The grain structure in RVEs was discretized into the static mesh and grain-based mesh. Static mesh is integration point-based and the IPs in the same element can belong to multiple grains, while the minimum discretization unit for grain-based mesh is an element and each element can only belong to a single grain. Multiple sets of RVEs were subjected to displacement-controlled loading under periodic boundary conditions and all the simulations were analysed by Abaqus using the UMAT subroutine. RVEs with static and grain-based mesh both can well predict the stress-strain curves and the stress/strain localization points in polycrystalline materials. A qualitative comparison of contour maps and stress profile reveals that more stress discontinuities exist in grain-based mesh compared to static mesh. When one element in static mesh belongs to two or more grains, it tends to smooth the stress profile at the grain boundary. Further investigation suggests that there is a large deviation in terms of the magnitude of local stress/strain predicted by the two discretization methods. The above findings remain the same when the number of grains within an RVE increases. A deviation parameter is defined to evaluate the macroscopic and microscopic differences caused by the

static and grain-based mesh. The macroscopic deviations are relatively small and all within 0.5%, while the microscopic deviations are more significant and range between 0-50%. Static mesh shows faster convergence and reduces CPU time and pre-processing procedure compared to grain-based mesh. It is then suggested that static mesh is recommended when the macroscopic mechanical response is of interest and grain-based mesh is more desirable to choose when the microscopic behaviour of materials is the main research interest. This chapter provides useful guidance for discretization methods in CPFEM and should be applicable to other crystal structures.

5. The statistical description of deformation process

5.1 Why is local stress statistics normal, and strain lognormal?

5.1.1 Introduction

Most polycrystals possess significant elastic and plastic anisotropy, leading to spatial inhomogeneity and pronounced orientation dependence of both elastic and plastic components of the total strain, $\varepsilon^{tot} = \varepsilon^{el} + \varepsilon^{pl}$. In the early stages of deformation far from strain localisation and the attainment of the critical condition (maximum bearing load), the macroscopic strain (Type I) obtained by averaging across multiple grains appears uniform and homogeneous. However, significant variation of local strain arises from the early stages of deformation in polycrystals. Local strain deviation from macroscopic average is further classified into Type II (grain level average) and Type III (intragranular deviation from grain average) that is highly inhomogeneous due to the difference in crystal orientation and intra-grain strain localisation due to plastic slip [108, 109]. Thanks to the development of advanced imaging techniques and crystal plasticity theory it has become possible to investigate strain inhomogeneity both experimentally and numerically [79, 110]. Several studies [79, 110] reported observations that the statistics of *total strain* during deformation follow a lognormal distribution. To the best of the authors' knowledge, there is no statistical study performed **separately** on the distribution of local *elastic and plastic* strains at different loading stages and scales of consideration.

The total strain can be decomposed into elastic and plastic components. In Chapter 3, we discovered that the **elastic** strain obeys a **normal** distribution while plastic strain

conforms to a lognormal distribution. In this chapter, we have been able to identify the universal underlying reason for this observation, namely that due to the respective magnitudes, the elastic strain accumulation represents an additive statistical process, whereas plastic deformation is a multiplicative process. The aim of the current research is to gain a better understanding of strain evolution and progress towards localisation that ultimately leads to failure, thus seeking to improve predictive modelling capability.

5.1.2 Results and discussion

The local elastic and plastic strain distribution during tensile deformation were investigated in a polycrystalline nickel superalloy Haynes 282 using an implementation of crystal plasticity finite element method (CPFEM). A representative volume element (RVE) containing 600 grains and 15000 integration points was employed. Random crystallographic orientation was assigned to the grain ensemble obtained by Delaunay tessellation, and the grain size was found to follow a lognormal distribution. The model was validated macroscopically by matching the experimental stress-strain curve and mesoscopically by matching neutron diffraction data for a polycrystalline Haynes 282 alloy. Figure 5.1(c) illustrates the simulated stress-strain curve of the alloy subjected to uniaxial tensile loading. Two contour plots in Figure 5.1(a) and (b) demonstrate the inhomogeneous elastic and plastic strain fields respectively at 5% total strain. Strong strain localisation was predicted by the model as indicated by the red arrow in Figure 5.1(b), with the maximum value of plastic strain reaching 16%, which is 3 times in excess of the macroscopic average strain (5%). The statistical distributions of the elastic and plastic strain components in the loading

direction at the tensile strain of 5% are depicted in Figure 5.1(g). It is interesting to note that the local elastic strain conforms to a relatively narrow normal distribution, whereas the statistics of local plastic strain was described by a relatively broad lognormal distribution with a pronounced 'tail' at high strains. Failure in polycrystalline alloys frequently originates in highly localised fields where intergranular and intragranular strains and stresses reach large values. Our previous publication [111] highlighted the importance of the emergence of a "tail" of large size defects in defect size statistics during deformation evolution. The appearance of the large size "tail" was proposed as a criterion for the identification of the transition from micromechanical to macromechanical damage regime, i.e. from microcracking to large crack propagation phenomena that ultimately lead to failure. In the current work, we focused our attention on the evolution of *inelastic strain* at the early stage of material deformation process. Strain localization is an important phenomenon for initiation-dominant failure in polycrystals and precedes microcrack formation. Strong strain localisation corresponds to the long 'tail' in the lognormal strain distribution. We proposed that the fitting parameters (mean and standard deviation) of lognormal plastic strain statistics for a particular polycrystal determine the shape of long "tail" that ultimately will allow predicting the microcrack formation and the limit of structural integrity.

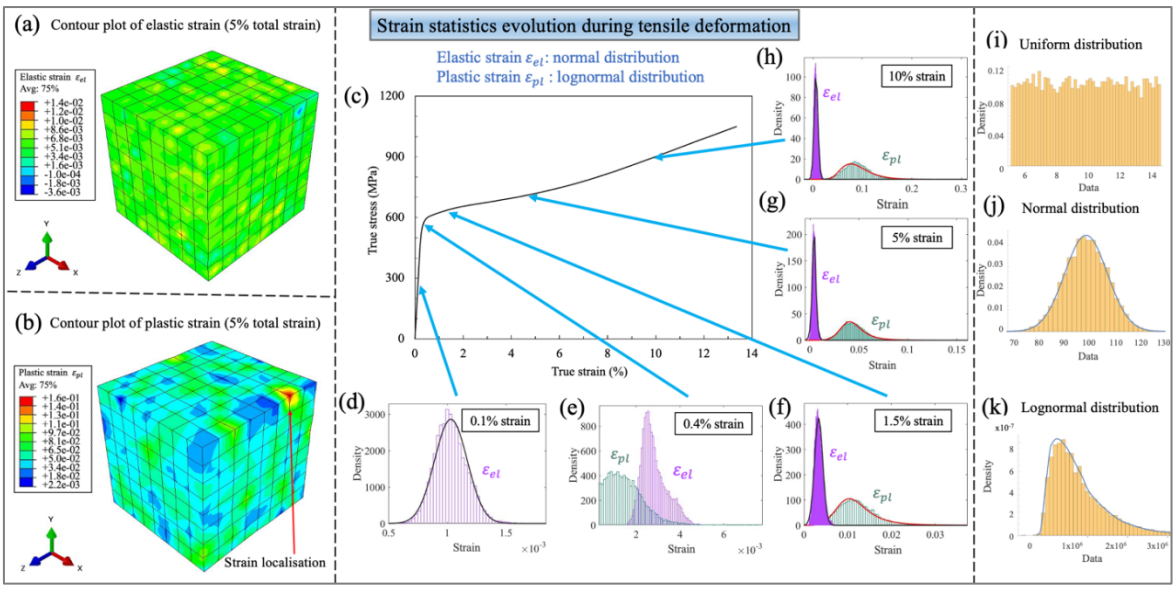


Figure 5.1 Illustration of strain statistics evolution during tensile deformation.

The evolution of elastic and plastic strain histograms at different deformation stages during tensile loading is presented in Figure 5.1(d-h). At a total strain of 0.1% (Figure 5.1(d)), the deformation is purely elastic, and the elastic strain follows a normal distribution. In the elastic-plastic transition region (Figure 5.1(e)), plastic slip gradually accumulates with the progressive activation of crystal slip systems, and the magnitude of plastic strain becomes comparable to that of the elastic strain. It is important to note that in this regime the statistics of elastic strain cannot be fitted by a normal function, indicating the strong interaction between elastic strain and the occurrence of plastic flow. In the plastic strain dominant region, Figure 5.1(f-h), the elastic strain is observed to conform to a normal distribution again, whilst plastic strain follows a lognormal distribution. Additionally, the lognormal distribution curve for plastic strain widens as the deformation occurs. This suggests that strain becomes progressively localised and strain heterogeneity increases as deformation proceeds.

From the statistical point of view, a normal distribution reflects an additive influence of sources of variation [112]. On the contrary, a lognormal distribution emerges due to the multiplicative accumulation of multiple random variables. According to the central limit theorem, the summation of independent random variables tends toward a normal distribution. In the context of incremental deformation processes, a simplifying assumption is that the magnitude of small strain steps can be considered to follow a random distribution (Figure 5.1(i)), then a normal distribution of elastic strain arises after several small increments and is preserved during subsequent deformation (Figure 5.1(j)). When larger plastic strain is considered, the small strain assumption no longer holds and multiplicative accumulation needs to be applied, leading to a lognormal distribution illustrated in Figure 5.1(k). The normal statistics of elastic strain and the lognormal distribution of plastic strain indicate that the elastic strain accumulation process is additive, whereas plastic deformation accumulation is a multiplicative process. When the total deformation is large (8-10%), the plastic strain becomes dominant, and hence the total strain appears to follow a lognormal distribution that has been reported in the literature [79, 110]. This explains the reason why some researchers reported the total strain distribution closely obeying a lognormal distribution. We, therefore, argue that our findings agree with the literature reports, but go much further in explaining the fundamental mechanisms of strain accumulation. It is important to note that stress is directly related to *elastic* strain through generalised Hooke's law, explaining the apparent striking difference between the statistics of strain showing lognormal distribution, while stress follows a normal distribution.

The distribution of elastic strain within crystals is known to be closely associated with diffraction line broadening. The histogram of grain-resolved elastic strains was found to follow a Gaussian shape for polycrystalline copper using X-ray diffraction [113], providing experimental evidence for the finding in this study. Due to the stress-strain relationship obeying generalised Hooke's law, this provides experimental evidence for the total stress also following a normal distribution. In polycrystals, the nature of plastic deformation at the microscale is governed by the generation of dislocations and the movement of existing dislocations. Experimental observation indicates that dislocation density distributions during tensile deformation can be described will with a lognormal function [58]. Furthermore, significant dislocation accumulating in the vicinity of grain boundaries and triple junctions leads to strong strain localisation and pre-determines failure in these regions. It is important to note that plastic strain does not increase uniformly as deformation proceeds. Active slip systems accumulate more plastic strain than other slip systems with the total strain increase – it has been noted that slip activity on a given system leads to softening of other slip systems as reflected in negative lateral hardening [46]. Softening is the mechanism causing strain localisation and multiplicative accumulation resulting in the emergence of lognormal distribution of local plastic strain. The inhomogeneity of plastic deformation becomes progressively exaggerated as deformation proceeds with local areas of large strain continuing to deform significantly [110].

5.1.3 Conclusion

In summary, the considerations presented in this section use statistical analysis of the evolution of strain distributions during tensile deformation using crystal plasticity finite element method, and correlate them with experimental observations of the elastic and plastic strains. The elastic strain (and stress) accumulation is found to be additive leading to a normal distribution, whereas plastic strain can be well described by a lognormal distribution and obeys a multiplicative accumulation process. The origins of local strain and stress statistics have been revealed fundamentally. We hypothesize that this finding is universal for polycrystalline materials with various deformation mechanisms and phase content when the volume of interest is above the minimum size threshold for a representative volume element that reflects the macroscopic homogeneity of deformation. The outcome obtained from this observation is expected to provide useful insight into the relationship between polycrystalline microstructure and mechanical properties.

5.2 The Yield Volume Fraction approach to the description of the stress-strain curve of a nickel-base superalloy

5.2.1 Introduction

Stress-strain curves are a key representation of the material deformation response that allows revealing the relationship between the material structure and its mechanical properties. Important materials properties such as Young's modulus, yield stress and ultimate tensile strength can be determined, along with the detailed hardening response to

plastic deformation. The stress-strain relationships are often represented by fitting suitable mathematical equations to experimental stress-strain data. One of the most popular equations for metallic materials was proposed by Ramberg and Osgood [114] and modified by Hill [115]. The classic Ramberg-Osgood (R-O) relates the engineering strain and stress by the summation of a linear elastic term and a power-law plastic term

$$\varepsilon = \varepsilon_{el} + \varepsilon_{pl} = \frac{\sigma}{E} + \left(\frac{\sigma}{k}\right)^{n} \tag{5.1}$$

Here ε_{el} and ε_{pl} are the elastic and plastic strain, respectively. E, k and n are the elastic modulus, proof stress related parameter, and strain hardening exponent which describes the sharpness of the 'knee' of the stress-strain curve, respectively.

Despite its popularity, the R-O equation is inadequate to represent the full-range stress-strain curves for many alloys. It is well accepted that the Ramberg-Osgood relation can provide an excellent agreement with experimental data for stress below the yield point $\sigma_{0.2}$. For higher stress levels above $\sigma_{0.2}$, R-O predictions may become significantly inaccurate and overestimate the stress [116]. Over the past years, many modified models have been developed based on the classic Ramberg-Osgood expression to account for inaccuracy in stress ranges exceeding $\sigma_{0.2}$ [116-122]. Most of the modified models employ a two-stage or three-stage method to describe the stress-strain curves: one expression for the first stage using Equation (5.1) up to $\sigma_{0.2}$, and one or two separate equations for the stress level above $\sigma_{0.2}$. In the current research, we will examine the limitations of R-O type relations by placing the consideration in the context of yield statistics.

The research in the second part of Chapter 5 introduces a simple yet powerful approach to the analysis of stress-strain curves using a statistical method based on the Yield Volume

Fraction concept. This treatment gives rise to an integrated method that can match well the stress-strain curves of a nickel-base superalloy up to the strain level of 1.55%. In this approach, the stress-strain curves are related to the cumulative yield volume fraction using lognormal distribution and Gumbel distribution. The results obtained from the proposed method are compared with classical R-O description, CPFE simulation and experimental data.

5.2.2 Methodology

5.2.2.1 Experimental stress-strain curve

To develop the proposed method in the present study, the tensile stress-strain curve for a nickel-base superalloy nominated Haynes 282 is employed [72]. The experimental curve is illustrated in Figure 5.2. A total strain ranging up to 1.55% was chosen. We are particularly interested in the regime when the contributions from elastic and plastic strain are of approximately similar magnitude. This represents the most difficult condition for description compared to cases when either elastic or plastic deformations dominate.

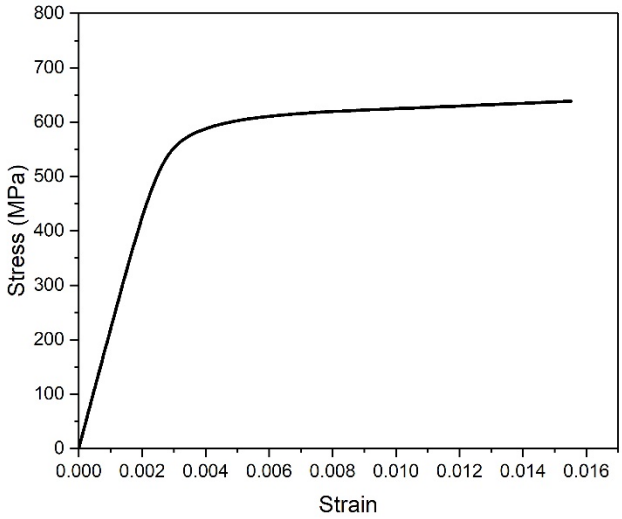


Figure 5.2. The tensile stress-strain curve obtained from the experiment in the literature [72].

5.2.2.2 CPFE simulation

The CPFE model was implemented using phenomenological crystal plasticity constitutive equations described in Chapter 3. To calibrate the material parameters in CPFE, the overall response of a representative volume element (RVE) with 1500 grains during tensile loading was fitted to the experimental stress-strain curve for Haynes 282. Periodic microstructure and periodic boundary were employed in the RVE shown in Figure 5.3 (a). Optimal values of material parameters were determined by fitting the macroscopic and mesoscopic response of RVE to the experimental stress-strain curve and neutron diffraction measurement obtained by Jaladurgam et al. [72]. For a detailed description of the constitutive equations and the calibration procedure, readers can refer to Chapter 3. Figure 5.3(b) compares the predicted stress-strain curve with the experiment curve and shows that excellent agreement was achieved.

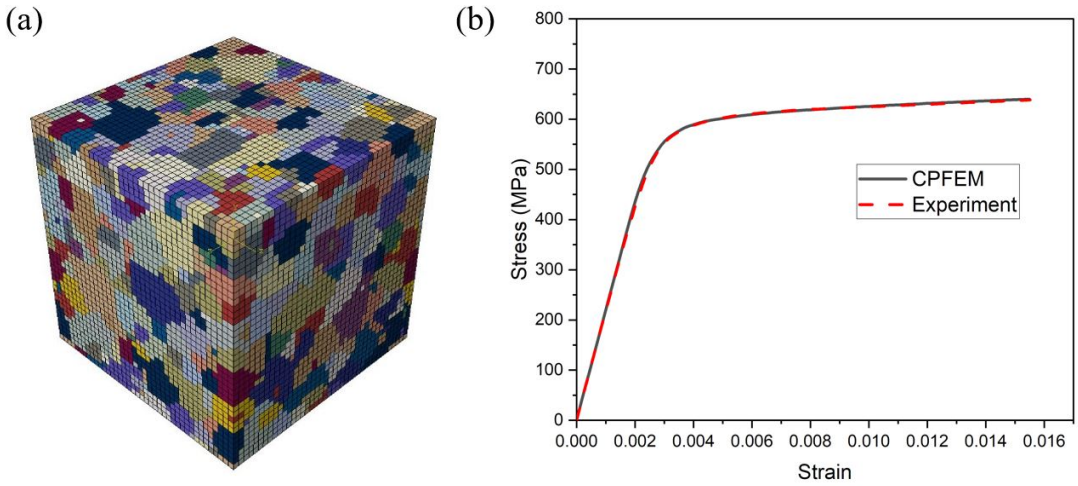


Figure 5.3. (a) The microstructure of the RVE used to calibrate the materials parameters (different colours indicate different grains). (b) The tensile stress-strain curve obtained from CPFE prediction and experimental data.

5.2.2.3 Yield Volume Fraction integrated method

Most of the metallic materials in use are polygranular, which means that they consist of distinct domains of materials (grains), in terms of crystal orientation, phase composition and lattice structure, etc. In polycrystalline materials such as nickel-base superalloy, both the elastic and plastic deformation are highly inhomogeneous. This occurs due to the heterogeneous nature of polycrystalline material caused by the orientation dependence of elastic and plastic properties. As a numerical measure of the extent of disparity between grains of different orientations, the elastic Zener anisotropy factor $A = 2C_{44}/(C_{11} - C_{12})$ can be used that typically takes values close to 2.7 for nickel-base alloys (with unity corresponding to isotropic material)[123]. As far as yield properties are concerned, the ratio of Schmid factors can be used between the most ‘hard’ and ‘soft’ crystal orientations, that shows a milder degree of anisotropy that amounts to about 3% [124].

Depending on the orientation of the underlying lattice structure with respect to the

loading axis (or, more precisely, the local principal stress axes) and also depending on the elastic anisotropy and neighbouring grains, different grains deform to different extents as a function of the remotely applied stress. The onset of yield with polycrystalline materials is a progressive process and it occurs nonlinearly with the increase of macroscopic strain and stress. The progressive yielding is one of the principal causes of macroscopically observed continuous strain hardening in the 'knee' region of the stress-strain curve. Following the concept proposed by Korsunsky [125] and illustrated in Figure 5.4, we introduce here the cumulative Yield Volume Fraction $\beta(\varepsilon)$ under tensile strain ε. Considering the onset and evolution of plasticity within a polycrystal, it may be expected that the YVF function $\beta(\varepsilon)$ be described by a sigmoid curve. When the RVE contains a sufficient number of grains, the $\beta(\varepsilon) - \varepsilon$ curve will be continuous. The strain levels ε_1 and ε_2 represent the starting and ending stages of the progressive yield process, respectively. The polycrystal will behave purely elastically and no yield occurs when the total strain is less than ε_1. Increasing volume of material yields during further loading until the polycrystal is fully yielded at strain ε_2 (this parameter may be assumed to be very large without any loss of generality).

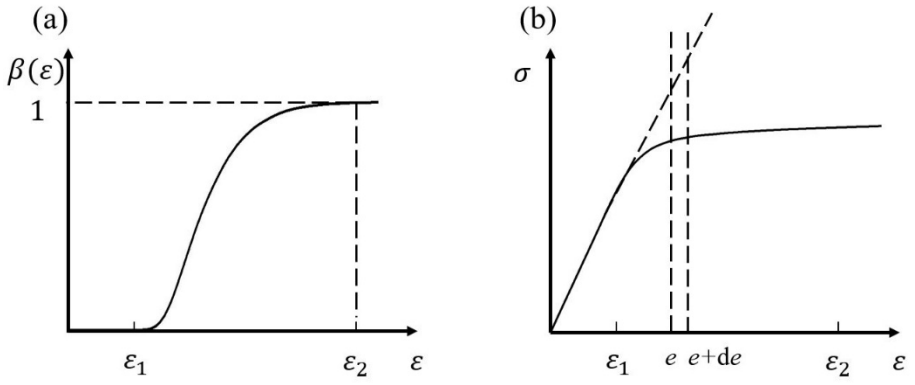


Figure 5.4. (a) Illustration for the cumulative yield volume fraction $\beta(\varepsilon)$ versus strain. (b) The illustration of a stress-strain curve derived from $\beta(\varepsilon)$ [125].

The Yield Volume Fraction description is based on the following relationship between the function $\beta(\varepsilon)$ and the polycrystal stress-strain curve. For simplicity, we shall assume the polycrystal has a sufficient number of grains and has the same Young's modulus *E,* i.e. no elastic anisotropy when we consider the polycrystal as a whole. The stress-strain curve function $\sigma(\varepsilon)$ can be expressed as

$$\sigma(\varepsilon) = \begin{cases} E\varepsilon, & \varepsilon < \varepsilon_1 \\ \sigma_y + \sigma_h, & \varepsilon \geq \varepsilon_1 \end{cases} \tag{5.2}$$

Here σ_y represents the stress that arises as a consequence of the progressive yield process, and σ_h the stress caused by the dislocation strain hardening within crystal grains.

Using Figure 5.4(b) as an illustration for the derivation of stress $\sigma_y(\varepsilon)$ from the Yield Volume Fraction $\beta(\varepsilon)$, we note that when the sample strain increases from *e* to *e*+d*e*, the *additional* yielding volume fraction in this range is $\beta'(e)de$. When the total strain reaches a value ε that is less than ε_1, the polycrystal behaves elastically, and hence, the stress can be calculated by Hooke's law $\sigma(\varepsilon) = E\varepsilon$. After yielding has occurred, it causes a reduction in the load-bearing capacity of the material in the plastic region. The stress reduction caused by the *additional* yielding volume fraction $\beta'(e)de$ between *e* and *e*+d*e* is equal to $E(\varepsilon - e)\beta'(e)de$. The stress σ_y in the yield process can be calculated by the integration:

$$\sigma_y(\varepsilon) = E\varepsilon - E\int_0^{\varepsilon}(\varepsilon - e)\,\beta'(e)de \tag{5.3}$$

Integrating by parts gives:

$$\sigma_y(\varepsilon) = E\varepsilon - ((\varepsilon - \varepsilon)\beta(\varepsilon) - \varepsilon\beta(0)) - E\int_0^{\varepsilon}\beta(\varepsilon)\,de = E\varepsilon - E\int_0^{\varepsilon}\beta(\varepsilon)\,de \tag{5.4}$$

Differentiating both sides with respect to ε yields the following expression:

$$\beta(\varepsilon) = 1 - \frac{1}{E}\frac{d\sigma_y}{d\varepsilon} \tag{5.5}$$

Equation (5.4) expresses the current stress as a function of the Yield Volume Fraction $\beta(\varepsilon)$,

whilst Equation (5.5) represents the inversion of this relationship that expresses $\beta(\varepsilon)$ in terms of $\sigma_y(\varepsilon)$. The additional hardening stress σ_h can be approximated by a simple linear hardening law:

$$\sigma_h(\varepsilon) = E_m \varepsilon \beta(\varepsilon) \tag{5.6}$$

Here E_m is the tangent modulus, and the multiplier $\beta(\varepsilon)$ reflects the fraction of the total volume that contributes to additional hardening.

Once CPFE simulation of deformation is carried out, the cumulative yield volume fraction $\beta(\varepsilon)$ can be obtained from the analysis of the results. It is found (Figures 5.5 and 5.6) that the cumulative Yield Volume Fraction $\beta(\varepsilon)$ can be well described by the cumulative distribution function (CDF) of lognormal or Gumbel extreme value distribution, and the derivative of $\beta(\varepsilon)$ (the incremental Yield Volume Fraction) is in good agreement with the probability density function (PDF) of lognormal or Gumbel distribution. The Yield Volume Fraction method can be developed further based on the above finding. The stress-strain curves function $\sigma(\varepsilon)$ can be then determined from Equation (5.5) and Equation (5.6) by substitution into Equation (5.2).

The probability density function *f(x)* and cumulative distribution function *F(x)* of the lognormal distribution are expressed as:

$$f(x|M,S) = \frac{A_1}{xS\sqrt{2\pi}} \exp\left\{\frac{-(\ln(x)-M)^2}{2S^2}\right\} \tag{5.7}$$

$$F(x|M,S) = A_1 \Phi\left\{\frac{\ln(x)-M}{S}\right\} \tag{5.8}$$

where M and S are respectively the mean and standard deviation of the variable $\ln(x)$, Φ is the CDF of the standard normal distribution.

The probability density function *g(x)* and cumulative distribution function *G(x)* of the

Gumbel distribution are given by:

$$g(x|\mu,\sigma) = A_2 \exp\left[-\exp\left[-\frac{(x-\mu)}{\sigma}\right] - \frac{(x-\mu)}{\sigma}\right] \tag{5.9}$$

$$G(x|\mu,\sigma) = A_2 \int \exp\left[-\exp\left[-\frac{(x-\mu)}{\sigma}\right] - \frac{(x-\mu)}{\sigma}\right] dx \tag{5.10}$$

where μ and σ are the location parameter and scale parameter, respectively.

5.2.2.4 The Ramberg-Osgood relationship and its connection to the proposed method

The Ramberg-Osgood relationship shown in Equation (5.1) is a simple method to reproduce experimental stress-strain curves. First, Young's modulus *E* can be determined from the slope of the elastic region in strain-stress curves. The parameters *K* and *n* are then can be fitted to the following power-law relationship:

$$\varepsilon_{pl} = \varepsilon - \frac{\sigma}{E} = \left(\frac{\sigma}{K}\right)^n \tag{5.11}$$

The incremental form of the Ramberg-Osgood relationship can be calculated as follows:

$$\frac{d\varepsilon}{d\sigma} = \frac{1}{E} + \frac{n\sigma^{n-1}}{K^n} \tag{5.12}$$

Therefore

$$\frac{d\sigma}{d\varepsilon} = \frac{1}{\frac{1}{E}+\frac{n\sigma^{n-1}}{K^n}} \tag{5.13}$$

According to Equation (5.5), the cumulative yield volume fraction function $\beta(\varepsilon)$ for the Ramberg-Osgood relationship is obtained:

$$\beta(\varepsilon) = 1 - \frac{1}{(1+\frac{nE\sigma^{n-1}}{K^n})} \tag{5.14}$$

The incremental Yield Volume Fraction $\gamma(\varepsilon)$ is obtained as the derivative of the Yield Volume Fraction function $\beta(\varepsilon)$ with respect to strain ε for the Ramberg-Osgood relationship in the form:

$$\frac{d^2\sigma}{d\varepsilon^2} = \frac{d}{d\varepsilon}\left(\frac{d\sigma}{d\varepsilon}\right) = \frac{d}{d\sigma}\left(\frac{\mathrm{d}\sigma}{\mathrm{d}\varepsilon}\right)\cdot\frac{\mathrm{d}\sigma}{\mathrm{d}\varepsilon} = \frac{-(n-1)n\sigma^{n-2}}{K^n\left(\frac{1}{E}+\frac{n\sigma^{n-1}}{K^n}\right)^2}\cdot\frac{1}{\frac{1}{E}+\frac{n\sigma^{n-1}}{K^n}} \tag{5.15}$$

$$\gamma(\varepsilon) = \frac{d\beta(\varepsilon)}{d\varepsilon} = -\frac{1}{E}\frac{d^2\sigma}{d\varepsilon^2} = \frac{(n-1)n\sigma^{n-2}}{E\cdot K^n\left(\frac{1}{E}+\frac{n\sigma^{n-1}}{K^n}\right)^3} \tag{5.16}$$

When the parameters K and n are determined by fitting the stress-strain curve, the cumulative and derivative of the Yield Volume Fraction for the Ramberg-Osgood relationship can be then calculated by Equations (5.14) and (5.16), respectively.

5.2.3 Results and discussion

In the current study, the following procedure was followed to calibrate the fitting parameters for the Ramberg-Osgood relationship, lognormal and Gumbel distribution:

(1) CPFE simulation was employed to fit the experimental stress-strain curves shown in Figure 5.2. The crystal plasticity model parameters were optimized by fitting the simulation results to macroscopic experimental stress-strain curves and experimental neutron diffraction measurements, as described in Chapter 3.

(2) Once the best-fit parameters were found for CPFE simulation, the cumulative Yield Volume Fraction $\beta(\varepsilon)$ and the incremental Yield Volume Fraction $\gamma(\varepsilon)$ could be readily obtained from CPFE simulation results.

(3) According to Equations (5.7), (5.9) and (5.16), the PDF for lognormal distribution, Gumbel distribution and Ramberg-Osgood relationship were used to fit the incremental Yield Volume Fraction $\gamma(\varepsilon)$ obtained in CPFE simulation. Least squares optimization was employed to find the best fitting parameters.

(4) Once the best fitting parameters, i.e. M, S and A_1 for lognormal distribution;

μ, σ and A_2 for Gumbel distribution; K and n for the Ramberg-Osgood relationship were determined, and the cumulative yield volume fraction for these three types of methods can be calculated by Equations (5.8), (5.10) and (5.14).

(5) Finally, the stress-strain curves reproduced by a lognormal distribution, Gumbel distribution and R-O relationship can be obtained according to Equations (5.2), (5.5) and (5.6).

The best-fitting parameters for lognormal distribution, Gumbel distribution and R-O relationship are listed in Table 5.1. The tangent modulus for developed plastic flow regime E_m is determined to be 3124 MPa. Figure 5.5 and Figure 5.6 compare the cumulative and incremental Yield Volume Fraction obtained from CPFE simulation, R-O relationship and the presently introduced YVF method. The cumulative and incremental Yield Volume Fraction prediction obtained from lognormal and Gumbel distribution is found to be in excellent agreement with the CPFE simulation result, while a significant difference is observed for the R-O relationship. As illustrated in Figure 5.7, the R-O relationship is capable of predicting the cumulative and derivative yield volume fraction when the total strain is less than 0.23%. However, it significantly underestimates the rate and the cumulative volume of the yield process during further loading above 0.23% strain. A greater volume of material behaves elastically according to the R-O equation, and consequently, R-O tends to overestimate the stress-strain curves and the deviation becomes larger as the total strain increases. The predictions of the proposed Yield Volume Fraction method using both lognormal and Gumbel distribution show significantly better agreement with the CPFE prediction and experimental curves, especially in the elastic-plastic transition regime. The

above comparison reveals the advantage of the proposed method: it can reproduce the experimental stress-strain curves (especially the 'knee' region of the curves) with sufficient accuracy as it employs a statistical method to describe the yield volume fraction in a progressive yield process.

Table 5.1. Material parameters used in R-O relationship and the proposed method.

Methods	R-O relationship			Lognormal distribution			Gumbel distribution		
Parameters	E(MPa)	K	n	A_1	M	S	A_2	μ	σ
Value	220000	1100	11.5	0.956	0.00255	0.23	1860.5	0.00237	0.000524

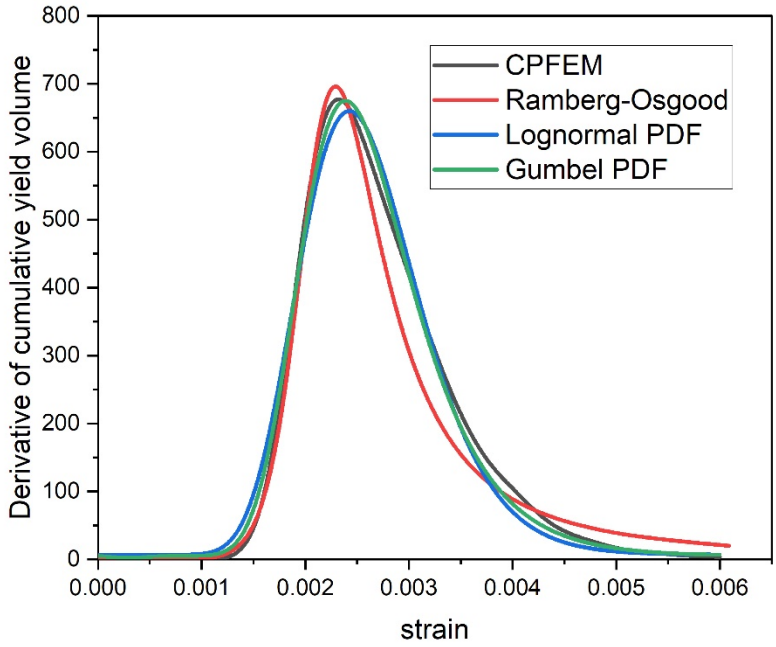


Figure 5.5. The derivative of yield volume fraction obtained from CPFE simulation, R-O relationship and the proposed method.

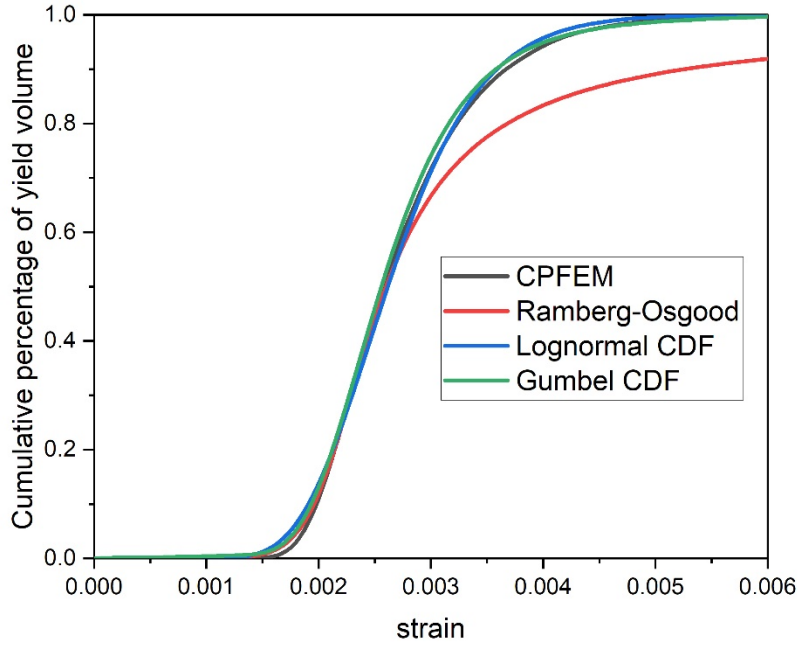


Figure 5.6. The cumulative yield volume fraction obtained from CPFE simulation, R-O relationship and the proposed method.

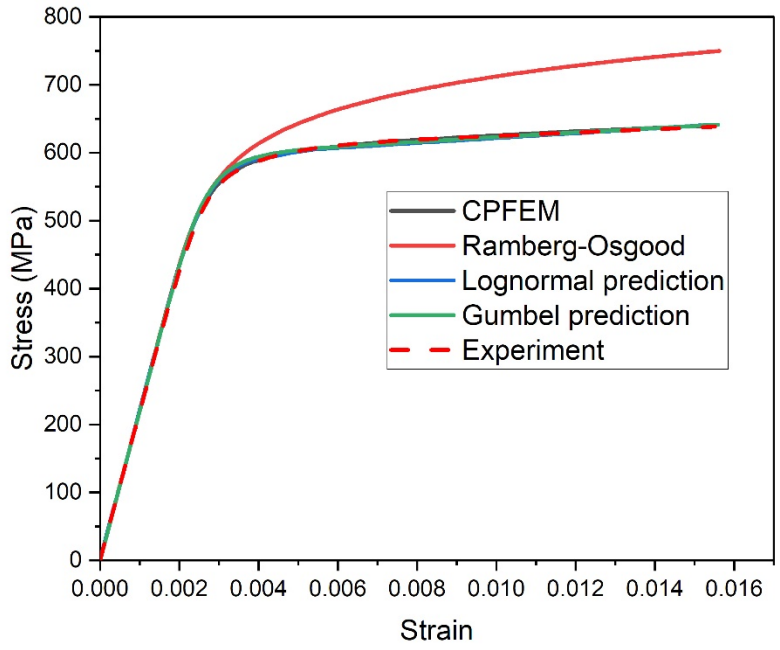


Figure 5.7. Stress-strain curves obtained from the experiment, CPFE simulation, R-O relationship and the proposed YVF method.

5.2.4 Conclusions

It has been well accepted that the Ramberg-Osgood relation can accurately reproduce stress-strain curves of metallic materials up to 0.2% yield stress but is not suitable for higher ranges of stresses. In Section 5.2, the limitation of the Ramberg-Osgood equation was analysed by comparing it with the yield volume fraction integrated method. R-O tends to underestimate the incremental and cumulative Yield Volume Fraction when the strain level is above 0.23% and hence overpredict the stress-strain curves in the 'knee' region of the stress-strain curve.

In section 5.2, a new method was proposed for describing the stress-strain behaviour using the Yield Volume Fraction function. The relationship between stress-strain curves and the Yield Volume Fraction function was derived. Lognormal and Gumbel distribution could provide excellent agreement with the Yield Volume Fraction obtained from the experiment and CPFE simulation. The accuracy of the proposed model was demonstrated by comparing its prediction with CPFE simulation, the Ramberg-Osgood model and experimental observations. It was found that YVF descriptions obtained from lognormal and Gumbel distribution possess the advantage of improved accuracy, especially in the elastic-plastic transition regime.

6. An experimental and numerical analysis of residual stresses in a TIG weldment of single crystal nickel-base superalloy

6.1 Introduction

When gas turbine engines operate in service conditions, they experience extremely aggressive thermo-mechanical loading. In order to meet the demand for increased gas turbine performance, high-performance alloys are being developed to withstand higher stresses at working temperatures. Nickel-based superalloys are extensively used in manufacturing gas turbine blades and vanes for several decades due to their high-temperature strength and excellent oxidation resistance [126]. Traditionally, gas turbine engine manufacturers used polycrystalline nickel superalloys to fabricate turbine blades. However, these polycrystalline superalloys have relatively lower operating temperature compared to highly demanding turbine engines, in which a much higher turbine inlet temperature is required to increase the efficiency of gas turbine engines. In comparison with conventionally cast polycrystalline superalloys, single crystal nickel-based superalloys exhibit increased strength and creep resistance at a higher temperature and, accordingly, are increasingly used in turbine blade and vane fabrication [127].

The stress in gas engines varies during a typical flight cycle which includes taking off, cruising and landing stages. The temperature profile and stress states that accompany this loading are complex and non-proportional, so that both high stress/high temperature and high stress/low temperature combinations are encountered. The complex combination of creep and fatigue represents the most prominent damage mode. Furtado and Le May

reported that superalloys will experience deterioration processes under creep and fatigue loading at high temperatures, and the degradation effects are enhanced by residual stresses [128], especially at the micro-scale (Type II and III residual stress). Consequently, investigating the residual stresses at appropriate scales is critical for understanding the operating conditions of these superalloys, as it allows the development of improved design methods for enhanced structural integrity.

TIG welding is a bonding technique extensively used to join various automobile and aerospace components. It uses a non-consumable tungsten electrode that delivers the current to the welding arc. The electrode and weld area are protected from oxidation and cooled with an inert gas, typically argon or helium, and filler metal is normally used. Residual stress is that which presents within the material body without external loading and is self-balanced with its surroundings [16]. It can be introduced into engineering components during manufacture e.g., forging, bending and welding processes, as a result of forces and thermal loading history. The highly localized temperature profile around the weld zone will cause considerable welding residual stress and possibly, deformation [129]. The presence of residual stresses can increase the likelihood of time-dependent failure by acting as a driving force for crack initiation. To optimize the weld manufacturing process and quantify the effect of welding residual stresses on nickel superalloys performance, it is necessary to research their magnitude and distribution [130].

The residual stress evaluation techniques can be classified into two principal approaches: non-destructive, such as Electron Backscattered Diffraction (EBSD) and X-ray diffraction, and destructive or semi-destructive (minimally disturbing) methods based

on material removal and strain relief measurement [19]. In terms of crystalline materials, X-ray or neutron-based diffraction and EBSD method are widely used to measure residual stress. X-ray diffraction is one of the most powerful residual stress analysis methods that can achieve sub-micron resolution with the help of synchrotron X-ray beams. However, there are mainly two limitations to this synchrotron-based method. One is that access to synchrotron instruments is restricted, the other is that this technique is limited to crystalline materials with high perfection and the X-ray transmission depth is relatively small [29]. EBSD technique can enable sub-micron measurement of residual stress by the examination of Kikuchi patterns. Nevertheless, it is normally confined to free-surface measurement and is rather time-consuming and expensive [131-136]. It is important to note that stress-free lattice parameters of the materials must be first investigated to calculate the residual stress for both XRD and EBSD based methods.

Another promising residual stress measurement method is the recently developed FIB-DIC micro-ring-core milling technique. This semi-destructive method is based on the measurement of localized strain relief through core milling [30]. FIB is employed to mill incrementally a circular trench or micropillar in the material surface. A contrasting pattern is deposited by Pt or Au on the micropillar top surface. It is then possible to measure the strain relief using DIC software in successive SEM images. Finite element simulation shows that the residual stress is completely relieved when the micropillar depth becomes comparable with its diameter [24]. Accordingly, together with the knowledge of material elastic properties, the pre-existing local residual stress can be reconstructed from the strain relief [19]. In principle, with the help of FIB-DIC and eigenstrain modelling, macroscopic

(Type I) and microscopic (Type II+III) residual stresses can be separated [137]. In comparison to other non-destructive through-thickness averaging methods (e.g. neutron and synchrotron X-ray diffraction techniques), the FIB-DIC method does not require the knowledge of stress-free lattice parameters, thus providing absolute residual stress value [137]. In addition, the gauge volume, which is determined by the diameter and depth of the micropillar, is more precisely defined in FIB-DIC. In the last decade, the FIB-DIC method has been well developed on account of increasing accessibility of SEM and FIB systems, as well as improved DIC software [29]. Therefore, FIB-DIC has become increasingly popular and affordable for small and medium-sized facilities to obtain efficient residual stress evaluations.

In this Chapter, FIB-DIC micro-ring-core milling technique and finite element modelling are both employed to assess the residual stress state near a weldment surface along radial and hoop directions. Manual TIG welding is performed on sample components to fill in a hole with filler metal (Ni alloy). The residual stress in the as-welded sample was evaluated by FIB-DIC, followed by simulation of stress distribution by a coupled thermo-mechanical Finite Element Method (FEM) model using ABAQUS. Finally, experimental evaluation and thermal stress simulation results are compared to confirm that a good agreement is achieved.

6.2 Specimen and microstructure

6.2.1 Material and specimen

The as-welded specimens were provided by Rolls-Royce plc. The base material used was a single crystal nickel superalloy CMSX-4. It is a second-generation high-strength single crystal superalloy designed for small gas turbine engines [138]. The solid solution strengthening elements include Rhenium, Chromium, Tungsten, and Tantalum. The addition of Titanium and Aluminum provides further precipitation hardening effect since they are γ′ phase stabilizer [139]. The composition of CMSX-4 is shown in Table 6.1. The central hole of the specimen was filled with Polymet 972 welding wire manufactured by Polymet Corporation. The composition of the welding wire is given in Table 6.2.

Table 6.1. The chemical composition of the CMSX-4 used in this specimen.

Element content, wt.%								
Cr	Co	Mo	Al	Ti	Ta	Hf	Re	Ni
6.5	9.0	0.6	5.6	1.0	6.5	0.1	3.0	~70

Table 6.2. The chemical composition of the Polymet 972 welding wire.

Element content, wt.%								
Ni	Co	Cr	W	Al	Ta	Ti	C	Other
15	~55	20	9	4.4	3	0.2	0.35	1.5

The geometry of the weldment is complex. It is possible to identify the region of parent metal (single crystal CMSX-4) unaffected by welding; the filler metal forms a lozenge-shaped 'plug' that is approximate 3 mm high and 5 mm in diameter, and the fusion and Heat Affected Zone (HAZ) between them. Figure 6.1 illustrates the weld geometry, and a cross-section view through the weldment. The welded hole is indicated by two red arrows. Radial and hoop directions are defined using a polar coordinate system (shown in Figure 6.1) at an arbitrary angle α. In this chapter, α was chosen to be $0°$ during experimental residual stress evaluation to simplify the stress analysis. The real geometry of the base material is relatively complex, but generally, it can be simplified into a cylindrical shape with approximately 11.7mm in diameter and 7mm in thickness. It is a fill-in weldment, and there is a through-hole at the centre of the sample before welding. It is apparent from Figure 6.1 that there exists a hollow area below the filler metal after welding.

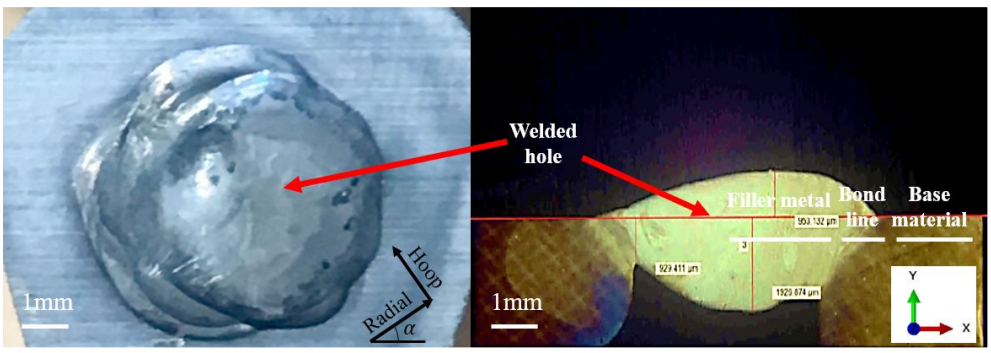


Figure 6.1. The overall geometry of the welded specimen with arrows showing the weld infill (left), and a cross-section view through the weldment (right).

The weldment was sectioned to give an indication of the size of HAZ. The minimum HAZ thickness was 0.44mm, and the maximum depth was 2.26 mm. No welds showed any distortion or cracking. The top bead of the welding area was removed by standard

metallographic grinding, followed by mechanical polishing in a solution containing a suspension of 9 µm, 3 µm and 1 µm diamond particles. The top surface was then electrochemically polished at room temperature with a current density of 0.005 A/mm^2. The electrolyte used contained absolute methanol with 20% vol. sulphuric acid [140]. No further residual stress was introduced by this surface preparation process [141]. The sample height was measured in as-received condition and after polishing, and it was found that materials 0.95 mm below the surface of base metal was machined away during grinding and polishing process.

6.2.2 Microstructure and texture analysis

Prior to FIB milling, a secondary electron (SE) detector was used to examine the microstructure of the welding surface. The accelerating voltage for all SEM images was 10 kV. The microstructure of the as-welded specimen is shown in Figure 6.2. The interface between welding metal and base metal can be clearly distinguished from the secondary electron image in Figures 6.2 (a) and (b). The left region with a coarse surface in Figure 6.2(b) is unaffected base metal CMSX-4, while the right is welding metal Polymet 972. A closer observation of base metal (Figure 6.2(c)), which illustrates the microstructure of single crystal, shows gamma prime phase with very fine secondary gamma prime precipitates in between.

As the sample is nearly axisymmetric, EBSD orientation mapping was performed on a quarter of the specimen, containing a filler metal zone, the bond line, and the base metal. The inverse pole figure in Figure 6.3 illustrates the grain morphology and orientations in

the one-quarter specimen. A clear boundary between the base metal and filler metal is shown since the unaffected base metal is a single crystal nickel superalloy, while the grain size and orientations vary in filler metal. The single crystal orientation was fully determined in terms of the Euler angles, which were 77.4˚, 31.9˚, and 0.8˚ in the Bunge notation. The grains in the fusion zone are narrow and highly elongated in the radial direction with respect to the sample centre. This shape is formed because of the steep temperature gradient during the welding process in the radial direction. The single crystal can be seen as a seed for grains near it, consequently, many grains at the interface exhibit the same orientation as the single crystal superalloy. Since the elongated grains have dimensions that range between 50 and 800 μm in the radial direction that are larger than the diameter of the FIB milling rings (see Figure 6.5), the residual stresses evaluated by FIB-DIC represent the full grain level Type I+II+III residual stress.

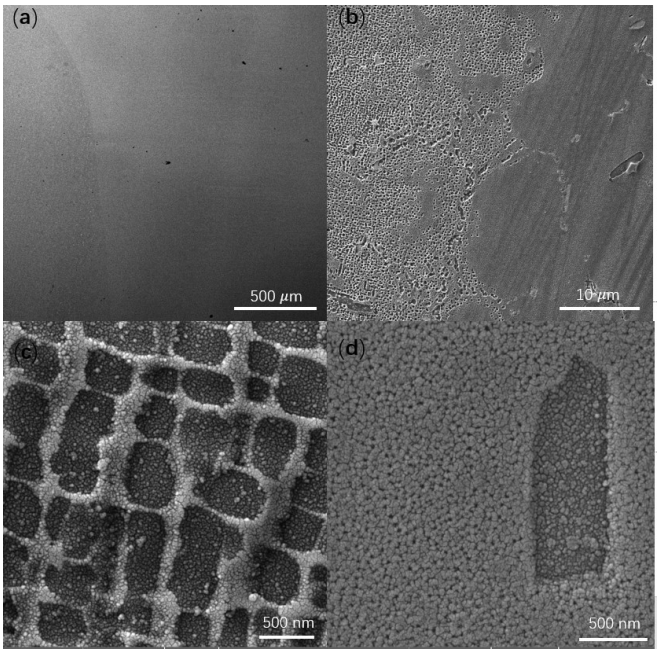


Figure 6.2. Secondary electron images showing the microstructure of the welded specimen at different locations: (a) The interface between welding metal Polymet 972 and unaffected base metal CMSX-4. (b) A close-up image of the interface. (c) The microstructure of single crystal base metal. (d) The microstructure of welding area.

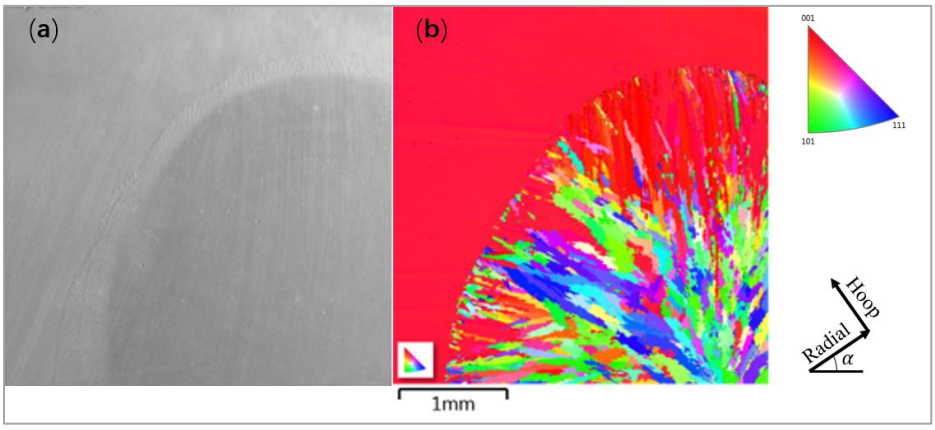


Figure 6.3. (a) SEM image showing the texture in analysis area. (b) Inverse pole figure map for a quarter of the sample (with respect to the hoop direction).

6.3 Residual stress evaluation and numerical simulation

6.3.1 FIB-DIC micro-ring-core milling for residual stress evaluation

All SEM imaging and FIB milling were performed using LYRA3 FIB-SEM system (Tescan, Czech Republic) at MBLEM lab, Oxford. The top surface of the specimen, along with FIB-DIC test positions, are illustrated in Figure 6.4. Grain morphology and orientation were investigated by EBSD using Oxford Instruments NordlysNano detector. Since the strain relief is quantitated by DIC analysis, reasonable contrast is required on the micropillar top surface in order to obtain accurate displacement measurements. Before FIB milling, a thin Pt layer (~5 nm) was deposited on the sample surface so that DIC displacement could be tracked precisely. The random distribution of Pt particles on the surface allowed reliable DIC post-processing. No additional stress was introduced by the deposition of this extremely thin and discontinuous layer [142].

The ion beam energy was set to 30 keV for milling. The inner diameter of micropillar was chosen to be 20 μm, with a 2 μm trench width. The micro-ring-core milling process

was performed in 60 steps, providing a total depth of 7 μm. After each milling step, 10 successive SEM images were recorded with a short dwell time. The displacement of markers containing 12 pixels was calculated, and then the relieved strain changed with milling depth in *x* and *y* directions were determined. The averaging of 10 images minimized the influence of SEM imaging artefacts during the DIC strain analysis. Finally, the obtained displacement field was fitted with a numerical master function to get the in-plane relief strain components [19]. Based on Hooke's law, the residual stresses in *x* and *y* directions were then determined. The above measurement approach provided average values of residual stress within a gauge volume, which is 20 μm in diameter and 7 μm in depth.

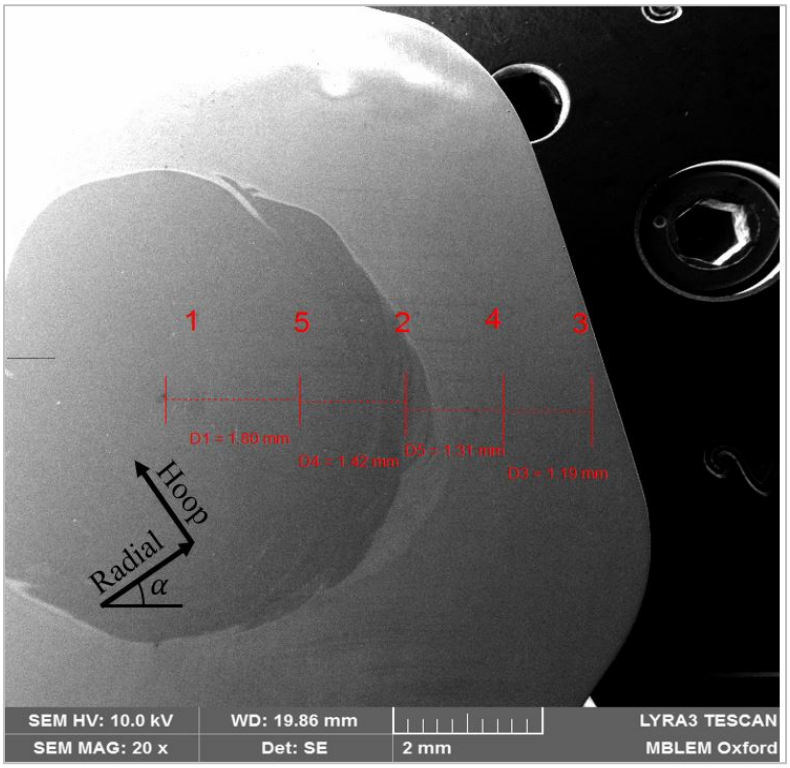


Figure 6.4. The FIB-DIC measurement positions in the sample surface.

In total, FIB-DIC residual stress measurements were performed at 5 and 8 different locations from the sample centre to edge along the radial direction in two samples,

respectively. The average distance between these test locations was ~1.35mm. At each measurement point, 60 incremental milling steps were used, with 10 images taken at each step, providing a sequence of 600 images. The material removal process and the SEM images acquired are illustrated in Figure 6.5 (a). These images were processed using a MATLAB-based DIC software [30], and data from 10 images for each milling increment was averaged. This was followed by a data refinement procedure to detect and remove any outliers. Figure 6.5 (b) shows the strain relief curves in the radial (e_{rr}) and hoop ($e_{\theta\theta}$) directions for one measurement location.

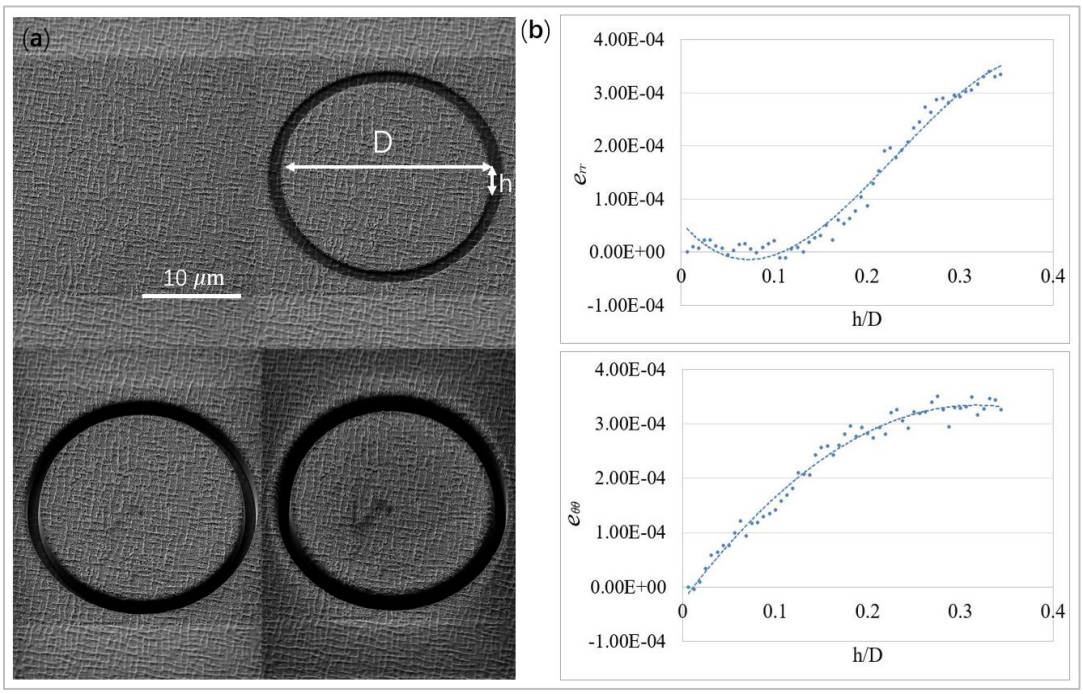


Figure 6.5. (a) An illustration of the FIB milling process. (b) A sample showing strain relief in two referent directions. *D* is the micropillar diameter and *h* is the milling depth.

For the plane stress state, the residual stress profile was then been reconstructed for two orthogonal directions using Hooke's law. The residual stress in the x direction, σ_{xx}, and in the y direction, σ_{yy} can be evaluated from the following equations:

$$\sigma_{xx} = \frac{E}{(1-v^2)}\left[\varepsilon_{xx} + v\varepsilon_{yy}\right] \tag{6.1}$$

$$\sigma_{yy} = \frac{E}{(1-v^2)}\left[\varepsilon_{yy} + v\varepsilon_{xx}\right] \tag{6.2}$$

In the above equations, E is Young's modulus, v is Poisson's ratio, and ε_{xx} and ε_{yy} are the components of residual elastic strain in the corresponding directions. It is worth noting that the strong elastic anisotropy of cubic structure will introduce a further error in residual stress evaluation. The nickel-base superalloys are known to exhibit significantly high anisotropy, and the dimension of each micropillar is smaller than the grain size in both single crystal CMSX-4 and welded area. Accordingly, the crystallographic orientation of each grain within FIB-DIC measurements was considered based on the generalized Hooke's law. Instead of using average Young's modulus, Salvati et al. proposed to evaluate the anisotropic residual stress using the stiffness coefficient matrix calculated based on the Euler angles [143]. The following stiffness matrix was used when calculating residual stress:

$$\begin{pmatrix}\sigma_{11}\\ \sigma_{22}\\ \sigma_{33}\\ \tau_{23}\\ \tau_{31}\\ \tau_{12}\end{pmatrix} = \begin{pmatrix}C_{11} & C_{12} & C_{12} & 0 & 0 & 0\\ C_{12} & C_{11} & C_{12} & 0 & 0 & 0\\ C_{12} & C_{12} & C_{11} & 0 & 0 & 0\\ 0 & 0 & 0 & C_{44} & 0 & 0\\ 0 & 0 & 0 & 0 & C_{44} & 0\\ 0 & 0 & 0 & 0 & 0 & C_{44}\end{pmatrix}\begin{pmatrix}\varepsilon_{11}\\ \varepsilon_{22}\\ \varepsilon_{33}\\ \gamma_{33}\\ \gamma_{31}\\ \gamma_{12}\end{pmatrix}$$

The elastic material properties used in the stress evaluation process are listed in Table 6.3 for both alloys. Figure 6.6 shows the residual stress profile in two samples measured by FIB-DIC. The left sample had 8 measurement points, while the right one had 5 points. It is clear that the magnitude of residual stresses in these two samples was not exactly the same. However, the overall stress profile followed the same trend as the distance from the centre increases. The maximum tensile stresses (around 500-700 MPa) were both observed

near the bond line. In the two specimens, stresses both decreased from the filler hole centre to the bond line, followed by a sudden increase at the bond line. The stresses both decreased from the bond line to the sample edge. To get a numerical description of such residual stress profile, in the next section, a thermal-structural coupled analysis was performed to simulate the residual stress after welding. And because the residual stress profiles in two samples are similar, only one sample (right) was chosen to compare the simulation results with the experiment.

Table 6.3. The elastic properties for CMSX-4 and welding wire Polymet 972 at room temperature.

Material	C_{11}(GPa)	C_{12}(GPa)	C_{44}(GPa)	v
CMSX-4	235.228	142.345	128.808	0.29
Polymet 972	334.852	164.927	84.962	0.33

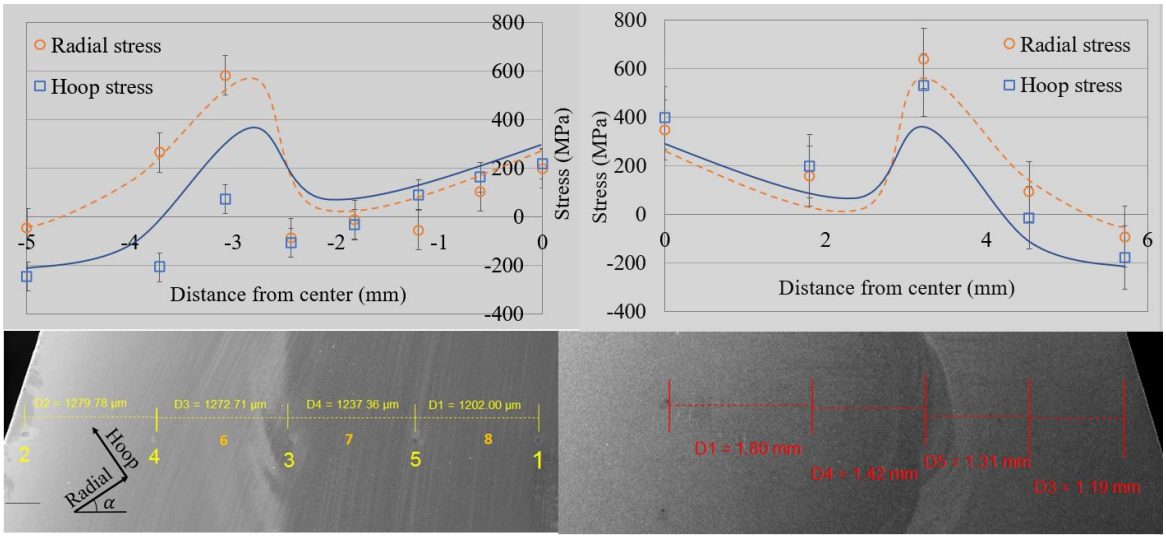


Figure 6.6. Radial stress (σ_{rr}) and hoop stress ($\sigma_{\theta\theta}$) obtained from FIB-DIC measurements with error bars at 95% confidence. The dash guideline curve shows the averaged radial stress with respect to distance from centre, while solid line represents the trend of averaged hoop stress.

6.3.2 FEM simulation

Finite element modelling was performed for the manually welded specimen to calculate the residual stresses in hoop and radial directions using a commercial finite element software ABAQUS. A sequentially coupled thermo-mechanical analysis was introduced in this section. In the past years, many researchers have tried to simulate the distribution of heat flux during the welding process. For instance, a Gaussian heat source was used for simulating the temperature distribution during EDM cutting [144], or more specifically TIG welding process [145, 146]. The body heat flow is distributed as Gaussian distribution from the tip of the electrode. In this chapter, a simplified Gaussian heat source was used to simulate the thermal history during welding, providing a temperature input for subsequent structural analysis.

Since the sample is approximately axisymmetric about its centre line, therefore an axisymmetric model was employed to optimize the computational cost and results accuracy. Figure 6.7 shows the detailed dimensions and mesh of the axisymmetric model. The model represents the material within the cross-section view shown in Figure 6.7 (a). There is an apparent discrepancy in terms of the interface between the filler metal and base metal for different samples. The interface line is not fully axisymmetric even in the same sample. Accordingly, interface sensitivity analysis was performed to evaluate how the residual stress profile changes with interface curvature. Three interface lines (a,b,c in Figure 6.7(b)) were built. Interface a and c indicate the upper and lower limit of interface respectively based on sample geometry measurement, while interface b is optimized to match the experimental residual stress profile in current research. DCAX4 (4-node linear

axisymmetric heat transfer quadrilateral) elements were used from the ABAQUS element library [147] for the thermal model, while CAX4R (4-node bilinear axisymmetric quadrilateral, reduced integration) elements were applied in the subsequent mechanical model. Mesh size was determined through sensitivity analysis in this axisymmetric model. A refined mesh was generated at the filler metal and the bond line where higher stress and larger stress gradient are expected.

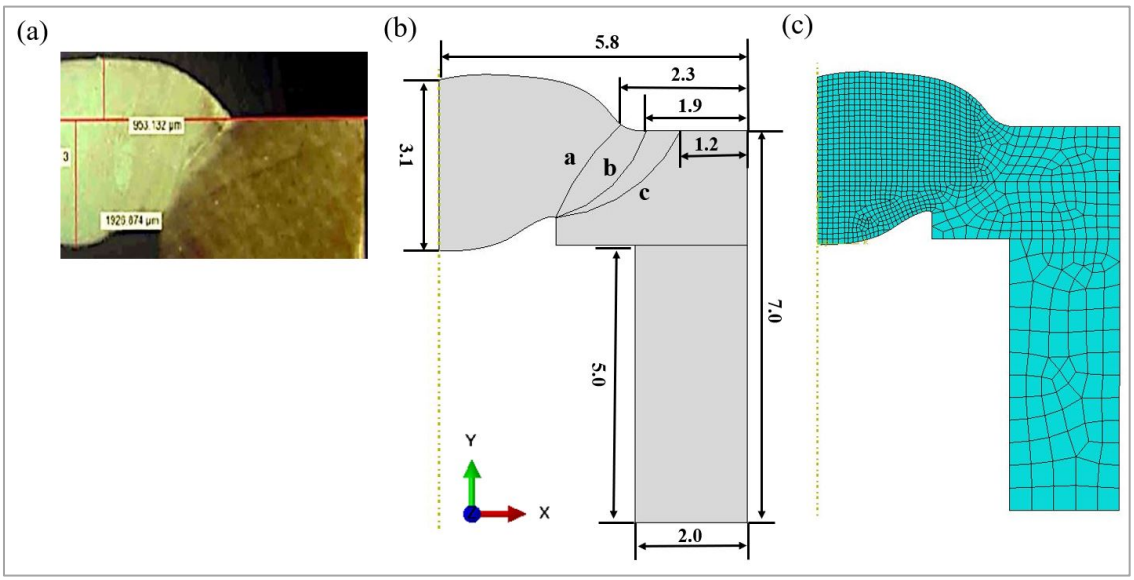


Figure 6.7. (a) The geometry of the sample. (b) The corresponding axisymmetric model with 3 different interface lines. (c) The refined mesh with interface b. The radial direction is along the x coordinate, while the hoop direction is perpendicular to the x-y plane.

Temperature-dependent mechanical properties, which are shown in Figure 6.8, were utilized for materials in different regions. Isotropic hardening and Von Mises yield criterion were employed in this simulation. The temperature-dependent properties for CMSX-4 can be found in the literature [139, 148], while for Polymet 972, the properties of a similar composition Co-Cr-Ni alloy (Elgiloy) [149, 150] were used in this simulation. Other thermal properties are listed in Table 6.4. Thermal and mechanical boundary conditions are

illustrated in Figure 6.9 (b). A thermal heat transfer model with a Gaussian heat source was first simulated. Thermal conduction, convection and radiation were considered during the whole welding process. Thermal conduction was allowed between different zones. Convection and radiation with air were both considered at all the surfaces except the edge overlapped with the axisymmetric axis, having coefficients of 24 mW/(mm^{2}K) and 0.8, respectively. Subsequently, the temperature history calculated by the thermal analysis was input as a predefined field for a mechanical model. Axisymmetric boundary condition is applied at the left edge of the model about y axis. The movement in y direction of the point at the bottom right corner is constrained.

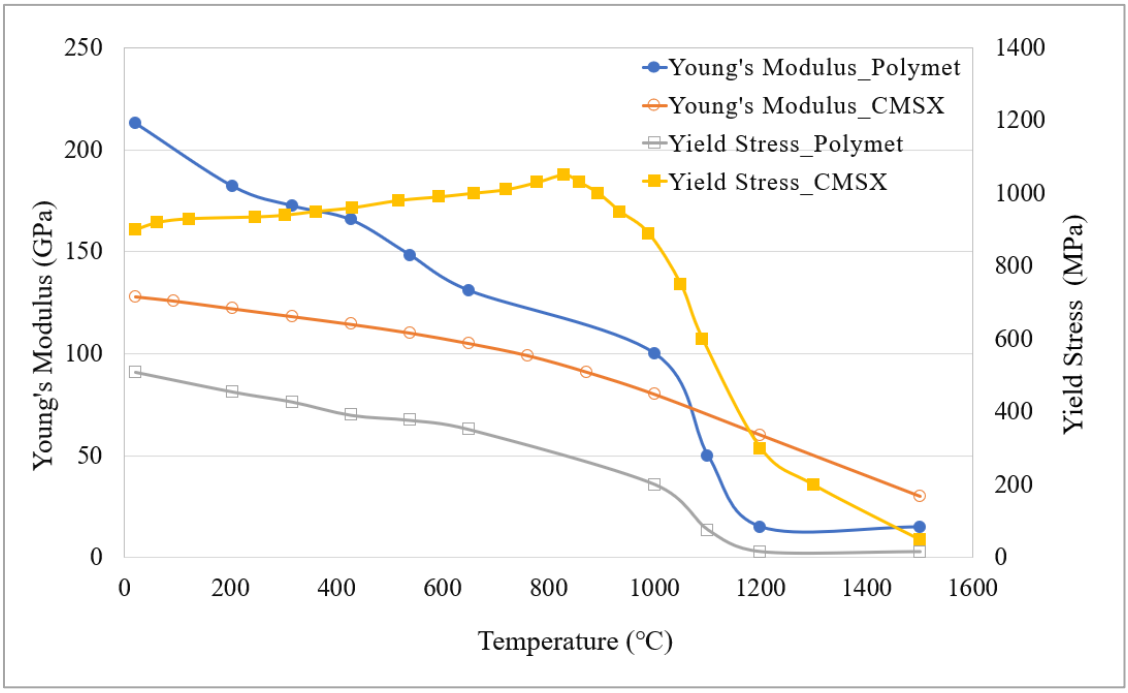


Figure 6.8. Temperature dependent mechanical properties.

Table 6.4. Other material properties used in the finite element model.

Properties	CMSX-4 single crystal	Polymet 972 welding wire
Density (T/mm^3)	8.6E-009	8.3E-009
Coeff. Of Expansion (K^{-1})	1.28E-005	1.27E-005
Conductivity (mW/mm/K)	9	12
Specific Heat (mJ/T/K)	4.29E008	4.30E008

Based on the consideration of the process of infill welding, the principal operative heat source during welding moved in a spiral route from the centre to the bond line (see Figure 6.9 (a)). This heating process can be simplified into 3 steps in the axisymmetric model. (1) Gaussian heat source was first applied in the model centre and held for a period t_0, (2) then the model was cooled for a short time t_1, (3) after which the same heat source was applied near the bond line for t_2 (see Figure 6.9 (b)). The whole model was subsequently cooled to room temperature. As the thermal history during welding was not provided by the manufacturer, trials were performed to find the optimal thermal parameters to achieve residual stresses that match the experimental evaluation. Subsequently, the whole temperature history of heat transfer was input as a predefined field into the mechanical structural analysis.

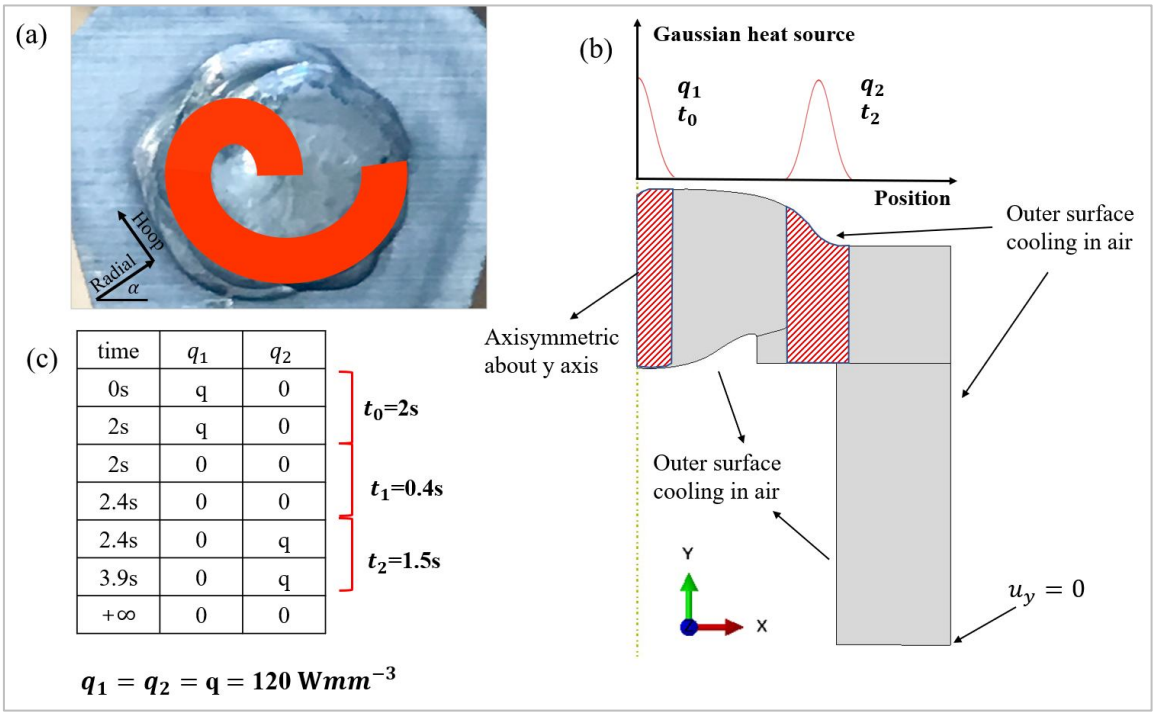


Figure 6.9. (a) The proposed route of heat source from the centre to the edge. (b) An illustration of simplified heat source in the axisymmetric model. (c) The heating parameters used in this simulation.

Figure 6.10 is the contour diagram showing residual stress distribution across the model with optimized interface b right after welding. As the top part of the material (0.95 mm below the surface of base metal) was removed before the residual stress evaluation, the same material removal process was simulated by deactivating the mesh above the A-B path shown in Figure 6.10. Figure 6.11 illustrates the distribution of three components of residual stresses before and after material removal with optimal interface b. It is clear that the maximum magnitude of radial, axial and hoop stress all drop approximately 200 MPa after the cutting process. In addition, the axial stress in the top free surface becomes zero (shown in Figure 6.11(d)) after the material removal process, indicating that the current modelling result is reasonable. As FIB-DIC evaluates the residual stress at the material

surface, to make experimental stress evaluation comparable to the simulation result, radial and hoop stress profiles at the top free surface after cutting (shown in Figure 6.11(b) and (f) respectively) are obtained and plotted using a red line with circular markers in Figure 6.12. The residual stress profiles obtained from the other two models with interface a and c are also illustrated in Figure 6.12. As can be seen in Figure 6.12 that the magnitude of both radial and hoop stress, and the position of stress discontinuity change with different interfaces. However, the overall stress profile in all three cases followed the same trend as the distance from the centre increases. In this simulation, the upper and lower limit of the interface (interface a and c) were first found based on the sample measurement, an optimized interface position (interface b) was then determined in between to match residual stress obtained from FIB-DIC evaluation. It is argued that in such way the residual stress can be accurately simulated without a full 3D description of the interface.

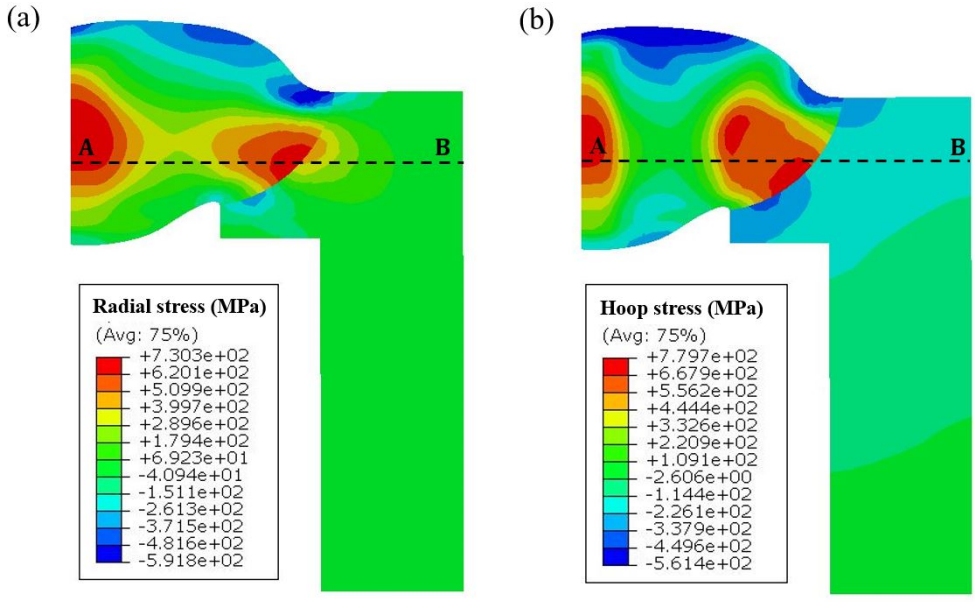


Figure 6.10. The distribution of radial stress (left) and hoop stress (right) right after welding with optimal interface b.

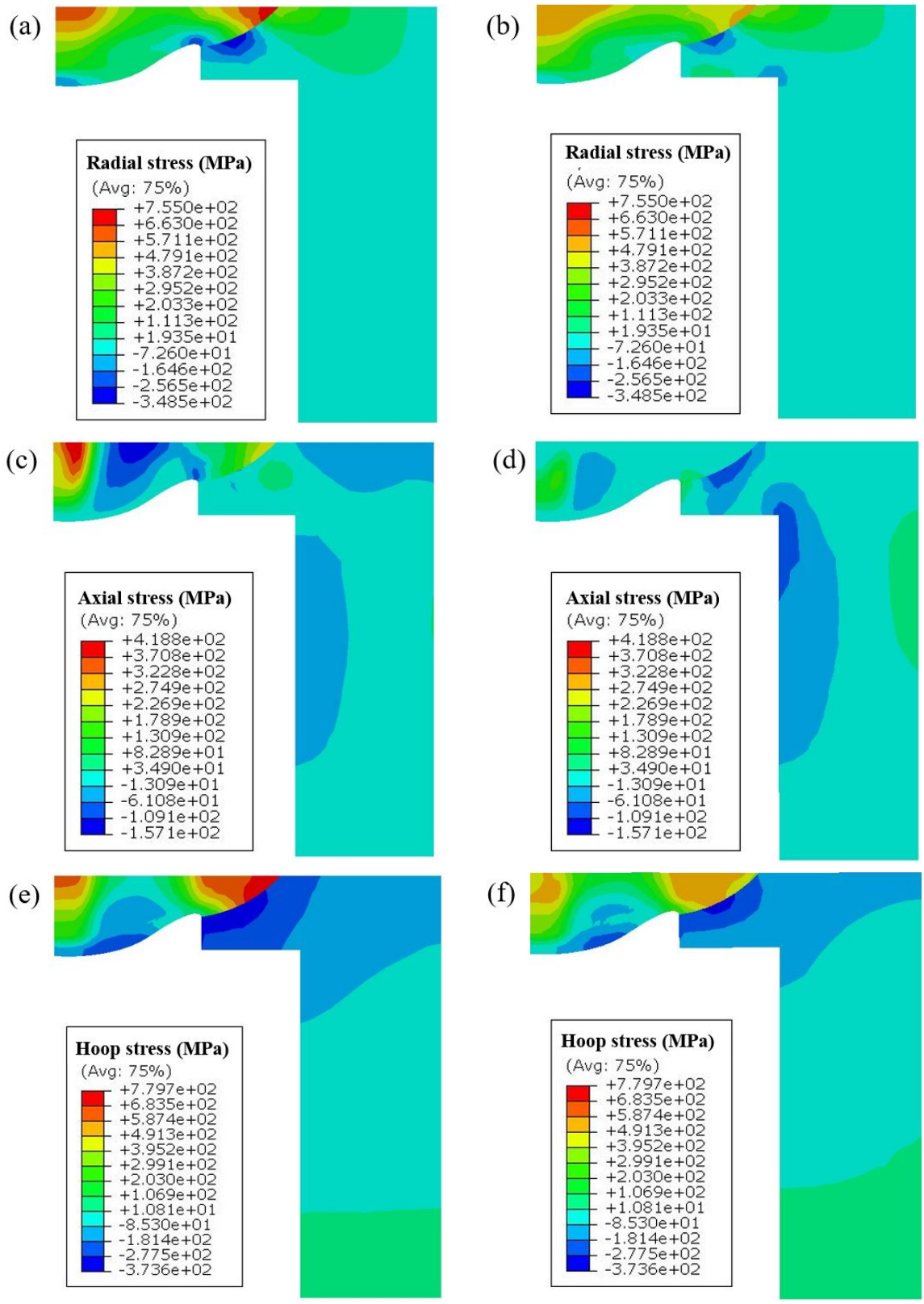


Figure 6.11. Three stress components distribution before ((a), (c), (e)) and after ((b), (d), (f)) material removal with optimal interface b.

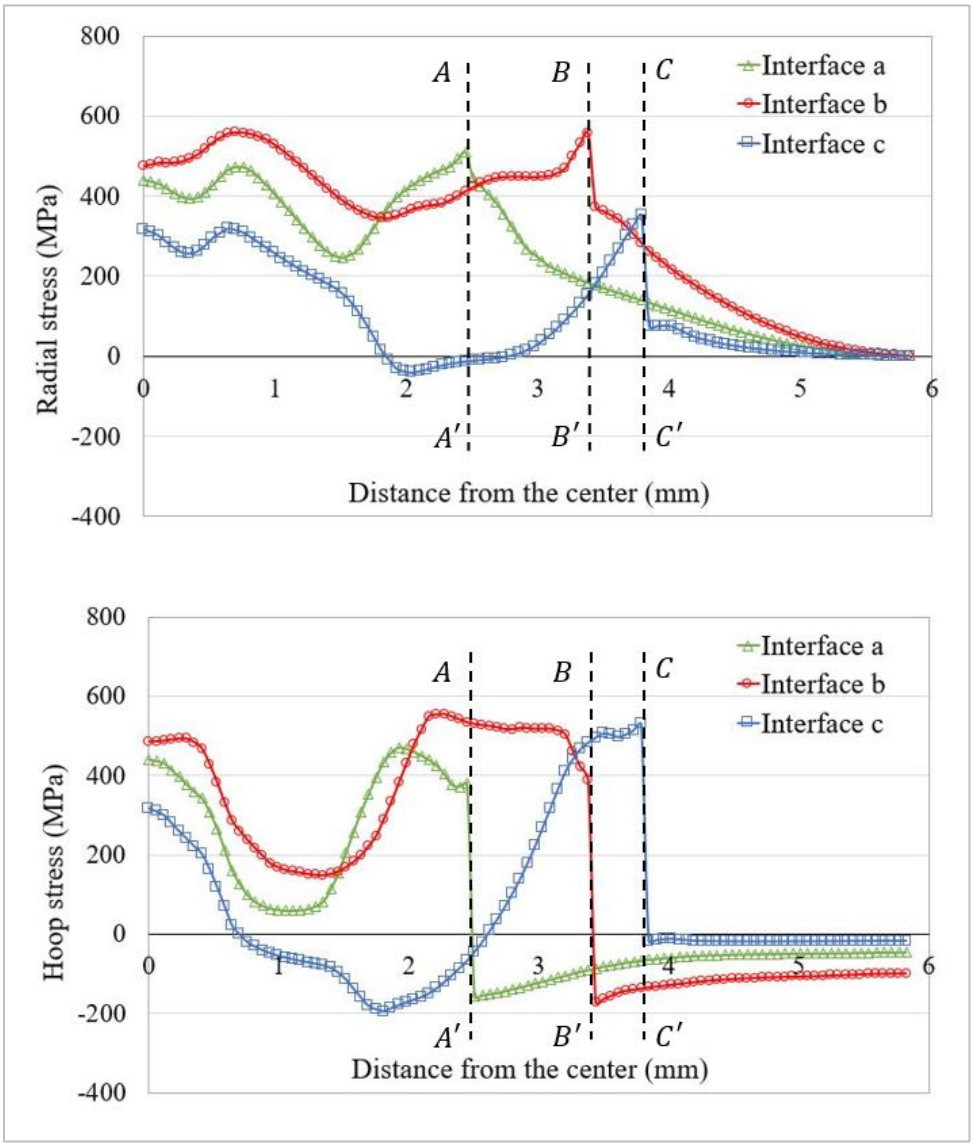


Figure 6.12. Radial (top) and hoop (bottom) residual stress obtained from FEM near the top surface after cutting with three interfaces. Path A-A', B-B' and C-C' indicate the position of interface a, b and c, respectively.

6.4 Result evaluation

6.4.1 Radial Residual Stresses

A stress acting parallel to the radius direction is known as a radial residual stress, denoted σ_{rr} in Figure 6.6. Figure 6.13 (a) depicts the distributions of the radial residual stress σ_{rr} in both FIB-DIC measurements and FE modelling with optimal interface b. The

height of error bars is as much as 200 MPa, and almost all the FEM radial stresses are within the experimental error bar. Radial stress starts at around 450 MPa in the centre, and then it drops slowly to 340 MPa. The largest tensile stress, which is approximately 570 MPa, is observed at the interface between the filler metal and base metal (bond line). This is followed by a decrease to zero as the distance from the centre increases. On account of the highly localized heating, the temperature near the filler metal and bond line changes dramatically with distance from the heat source, namely, the highest temperature is restricted to the heat source, from which temperature decreases in filler metal and parent material. Owing to the non-uniform temperature profile and material properties, the shrinkage varies in different regions during the cooling process and, therefore, the highest tensile stress occurs at the welding bond line. The material discontinuity near the interface between filler and base metal results in a discontinuous stress profile in that region.

6.4.2 Hoop residual stress

A stress acting perpendicular to the radius direction is termed a hoop residual stress, denoted $\sigma_{\theta\theta}$ in Figure 6.6. Figure 6.13 (b) represents the distributions of the hoop residual stress $\sigma_{\theta\theta}$ in both FIB-DIC measurements and FE modelling with optimal interface b. The hoop residual stress develops as a consequence of hoop expansion and shrinkage during the welding process. The highest tensile stress, again, appears near the bone line, followed by a sudden drop and finally becomes compressive as the distance from the centre increases. The hoop stress at the bond line is 580 MPa, approaching the filler metal yield stress. The compressive stresses are formed as a result of weldment self-equilibrium. A

sudden drop in hoop stress was observed by FEM near the bond line. The stress discontinuity is on account of the discontinuous materials (base metal and filler metal) near the bond line.

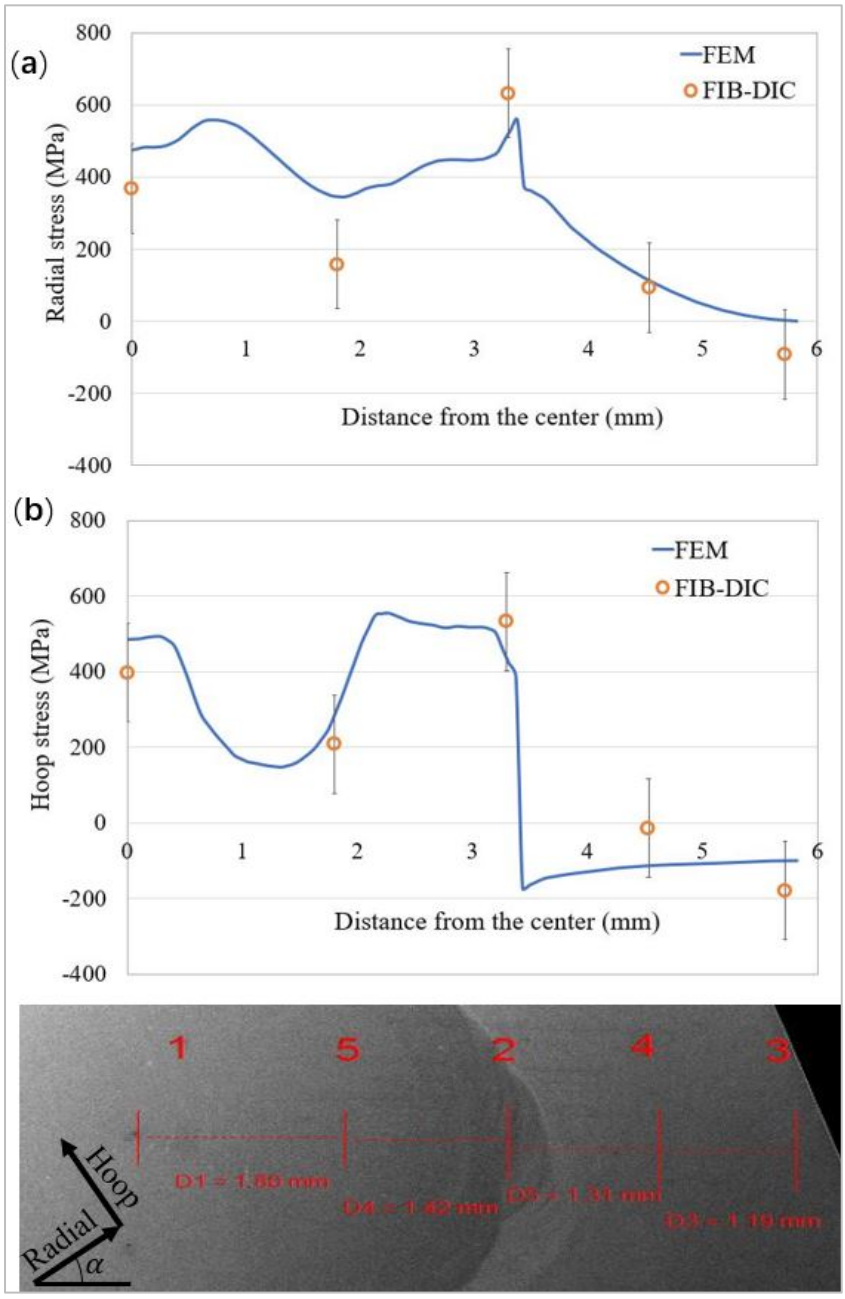


Figure 6.13. Residual stress distribution obtained from FIB-DIC and FEM simulation with interface b. (error bars represent a 95% confidence interval). (a) Component of residual stress in the radial direction. (b) Component of residual stress in the hoop direction.

6.5 Discussion

In this chapter, it is important to point out that the highest tensile hoop and radial stress were both observed to occur in the weld line, and their magnitudes approach the yield strength of filler metal. Consequently, these tensile residual stresses increase the effective mean stress under fatigue loading. The presence of sub-surface tensile residual stress is likely to accelerate the initiation and propagation stages of fatigue cracks, while the compressive residual stress near the surface may be beneficial to fatigue life [151, 152]. Minimizing the magnitude of the tensile stress provides an opportunity to increase the allowable service stress in this region of the component. PWHT can be performed to reduce the tensile residual stress level in the welding joint, or alternatively, shot-peening, autofrettage and other surface treatments can introduce beneficial compressive residual stresses near the surface to increase fatigue life.

Whilst this FIB-DIC measurement and FE modelling provide an initial assessment of the overall stress magnitude, it is a well-known fact in residual stress analysis of welds that the largest stresses invariably arise close to the bond line, in the heat affected zone, for the component aligned with the bond. In this case, this line of reasoning would lead to the anticipation of the largest stresses in the hoop direction, close to the interface between the filler metal and parent material. It is important to consider that the residual stress distribution is different in the two TIG welded samples. Local thermal history during welding needs to be measured to get a more accurate residual stress simulation. Given the inherent variability in manual welding processes, it is not surprising that scatter in the measured residual stress levels was observed.

It is worth noting that there is still a minor mismatch between experiment measurements and FEM prediction, highlighting the axisymmetric model with a simplified heat source is insufficient for obtaining a precise description of the residual stress distribution of welds. Nevertheless, the wide error bars in experiment data indicate a relatively large uncertainty in the FIB-DIC measurements. It is evident that nearly all the experimental data is within the error bar representing a 95% confidence interval, supporting the proposed heat source model. Therefore, as far as residual stress evaluation is concerned, a good agreement can be achieved between experimental evaluation and simulation using a sequentially coupled thermo-mechanical model.

It is important to note that few simplifications were made in the model. For example, a full 3D description and simulation of the thermo-mechanical process could have been able to capture finer details of the residual stress distribution. However, this calculation strategy would have required a substantial computational effort that at this stage of the research we considered not to be appropriate.

Although embedded in our calculation of error propagation in the experimental evaluation, further refinements of the fidelity of the numerical and experimental results can be achieved by accounting for the elastic and plastic anisotropic behaviour. Along with the scatter given by the difficult repeatability of this manual welding process, these considerations provide explanations of the very minor discrepancies found between FEM results and experiment data, but also give insights into further improvement of the model.

6.6 Conclusion

In Chapter 6, both experimental and sequentially coupled thermo-mechanical analyses were performed to study the residual stress state near manual welding surfaces along radial and hoop directions. The highest hoop and radial tensile residual stresses were both observed at the boundary surface between the filler metal and base metal, and a compressive region was found for hoop stress at the edge of the base metal. The magnitude of maximum tensile stress is close to the yield point of filler metal, limiting the allowable service stress of engineering components in service. Such a high magnitude of tensile residual stresses is therefore detrimental as concerns the structural integrity of the manufactured object, particularly for the fatigue life. These evidences lead us to believe that further PWHT or more in general surface treatment are required to obtain better performance.

According to the microstructure shown in EBSD mapping, the grains in filler metal are narrow and highly elongated in the radial direction with respect to the sample centre. This particular grain shape is argued to form because of the steeper temperature gradient during the welding process in the radial direction compared to the hoop direction. Since the temperature changes dramatically only in the radial direction in the current FEM model, the above argument provides strong support in terms of performing welding simulation using an axisymmetric model and a simplified Gaussian heat source. However, it is important to point out that the welding process analysed in this work had been conducted manually, so some variations might be expected from sample to sample. Nevertheless, despite the axisymmetric simplification of the FEM model and variability of results given

by the welding operator, the results obtained in this chapter show a good agreement (experiment vs. simulation), therefore it is possible to confidently say that the underlying residual stress origin has been captured by the model. In turn, this agreement also allows to state that the experimental residual stress profiles are compatible with the geometry and therefore it reinforces the soundness of the findings.

7. The creep deformation of a new nickel-base alloy-by-design studied using synchrotron X-ray diffraction

7.1 Introduction

Nickel-base superalloys exhibit high strength and creep resistance at elevated temperatures. These properties, together with their fatigue performance, microstructural stability, and high-temperature corrosion resistance have made them the materials of choice for the hot section of gas turbines, such as blades, discs, vanes, and combustion casings.

The need for greater efficiency of engines causes an increase in the turbine inlet temperature and thus required the development of stronger, microstructurally and compositionally more complex, and more creep-resistant superalloys [153]. The temperature profile and stress states during a typical flight cycle loading are complex and non-proportional so that both high-stress/high-temperature and high-stress/low-temperature combinations are encountered, causing detrimental creep deformation of nickel superalloys.

The peculiar thermo-mechanical performance of nickel-based superalloys mainly arises from the presence of an intermetallic phase, γ' precipitates $Ni_3(Ti, Al)$, which have $L1_2$ structure (an ordered FCC arrangement). When dislocations travelling through the matrix encounter γ' particles, they are prevented from easy glide and must undergo bowing, climb, splitting, and formation of anti-phase boundaries (APB) for further deformation to occur. Thus, the deformation resistance of an alloy is strongly dependent on the volume fraction of γ' precipitates that can be modified by the thermos-mechanical

treatment history, i.e. the combination of temperature and applied load that has been shown to have a tremendous effect on the creep deformation [154]. A modern generation of superalloys is characterised by a high volume fraction γ' to improve the resistance to plastic deformation (creep).

Creep is the phenomenon of time-dependent deformation of a material when subjected to constant load or stress. A better understanding of creep damage mechanisms improves our understanding of the internal stress and strain interactions during thermos-mechanical loading of polycrystalline alloys. The ultimate purpose of the analysis is to underpin the development of improved material design, including through the optimization of thermomechanical processing routes. A considerable amount of research work has been conducted on the creep deformation in nickel superalloys over the past 50 years. Many creep deformation mechanisms were proposed for different stress and temperature regimes, such as isolated and continuous stacking faults [14, 155, 156], anti-plane boundary (APB) shearing [14, 157-160], dislocation climb [161-164] and microtwinning [165-169]. These mechanisms may operate simultaneously during creep at a given specific combination of stress and temperature. Diffusion creep is a mechanism involving the diffusion of atoms or material transport. At low stress and high temperature loading condition, diffusional and time-dependent dislocation climb are commonly favourable deformation mechanisms. There are mainly two types of diffusion creep, depending on whether diffusion occurs through grain boundaries, termed Coble creep (activated at a lower temperature) or through the main body of the grains, known as Nabarro-Herring creep (favoured at high temperatures). Dislocation creep occurs by the motion of dislocations through crystal

lattices. Dislocations can glide along slip planes and this requires little thermal activation, and hence, dislocation creep becomes favourable at relatively low temperatures. The dominant creep deformation mechanisms at high stress and low temperature are APB shearing and stacking fault [14].

X-ray diffraction (XRD) is one of the most powerful methods for residual strain and stress analysis that can achieve sub-micron resolution, particularly with the help of synchrotron X-ray beams. Particle diffraction-based methods (including neutrons here) [170] evaluate the residual stresses by determining the changes in interplanar lattice spacing. Bragg's law provides a concise mathematical description of the relationship between lattice spacing, scattering angle and incident beam wavelength. In the monochromatic mode, the scattering angle is measured precisely, so that for known incident beam wavelength the changes in lattice spacing can be found using Bragg's law. Figure 2.8 gives an example of a typical diffraction pattern, which is presented as detector counts versus scattering angles. It is illustrated that peak centre position and shape (height, half-width change, integrated intensity), quantitative information can be extracted regarding lattice strain/compositional changes, atomic density and permanent deformation. Synchrotron XRD strain mapping has been widely employed to evaluate the time-independent strain at locations of particular interest, such as near crack tips [136, 171, 172]. However, there appears a dearth of information on the spatially resolved strain distributions after time-dependent creep deformation using this technique. The main advantage of synchrotron XRD is that it can simultaneously and accurately provide a quantitative description of lattice parameters, phase fraction and microstrain in dual-phase

polycrystalline materials.

In Chapter 7, two dog-bone-shaped samples were pre-crept at different temperature/stress combinations and stopped within the secondary creep regime. Ex-situ synchrotron was then performed on one reference sample and two crept samples. The distribution of lattice-parameter changes in γ and γ' phase was studied. The research in this chapter is aimed at investigating the lattice misfit, phase fraction, lattice parameter and microstrain mapping in pre-crept Alloy 11 samples using synchrotron X-ray diffraction.

7.2 Experimental procedure

7.2.1 Materials and creep tests

The materials investigated in this chapter were obtained from a pancake forging of a newly developed nickel-base superalloy-by-design referred to as Alloy 11 [173]. The forging part was manufactured by isothermally forging a powder isostatic pressed cylindrical ingot. Its nominal chemical composition is given in Table 7.1. The material was first given a solution treatment at 1180℃ for 2h and then cooled to room temperature in air. Subsequently, it received a two-step ageing treatment at 850℃ for 2h and air cooled to ambient temperature, followed by ageing at 800℃ for 4h before cooling by air. All the cooling rate was monitored and controlled at 0.7℃/s.

Table 7.1. Chemical composition of Alloy 11 (wt.%)

Ni	Co	Cr	Ta	W	Al	Ti	Mo	Nb	Fe	Mn	Si
Bal	15.06	12.69	4.77	3.22	3.16	2.84	2.14	1.44	0.95	0.48	0.47

Three dog-bone specimens (1.5 mm wide, 1.2 mm thick and 10 mm of gauge length) were machined by an electro-discharge machine from the forging part. The surface of gauge length was carefully polished to avoid any premature failure during thermomechanical loading. Two specimens were crept at 750 ℃/400MPa and 700℃/800MPa, respectively, by the Electro-Thermo-Mechanical Testing (ETMT) system (Instron Ltd., High Wycombe, UK) in an argon atmosphere. The names and the creep conditions for the three samples are listed in Table 7.2. The creep tests were interrupted within the secondary creep regime when the total creep strain reached 0.6%, and the specimens were then cooled to room temperature after removing the constant load. As shown in the creep curves of the two tests in Figure 7.1, it took 35h and 0.26h to achieve a creep strain of 0.6% for 750 ℃/400MPa and 700 ℃/800MPa loading conditions, respectively. The creep rate is much higher in the creep test with a larger constant load.

In the ETMT system, samples were heated by passing electric current. The temperature was controlled by a proportional-integral-derivative controller (PID) and monitored with a thermocouple spot-welded to the centre of the specimen. A symmetrical bell-shaped temperature profile arises, with the temperature in the middle of the sample higher than at the two ends (see Figure B in Appendix A). It was caused by the fact that the ends of the sample were cooled through the relatively massive metallic grips.

Table 7.2. The name and creep conditions for the three samples in this study.

Sample name	Creep conditions
Sample A	Reference sample, no creep
Sample B	750℃/400MPa
Sample C	700℃/800MPa

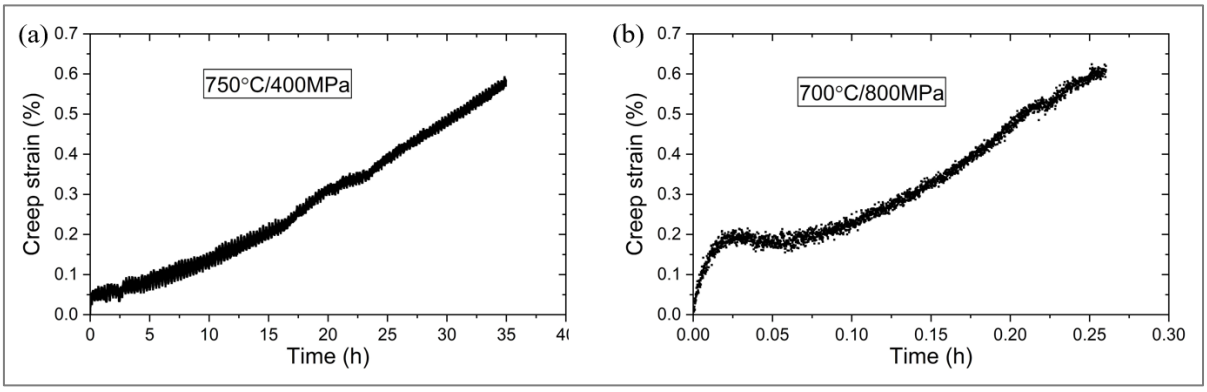


Figure 7.1. The tensile creep curves of Alloy 11 at 750℃/400MPa and 700℃/800MPa loading conditions.

7.2.2 Synchrotron XRD experiment

Synchrotron XRD experiments on one reference sample without creep and two pre-crept samples were performed at the I12 beamline at Diamond Light Source (DLS), UK. As illustrated in Figure 7.2(a), the dog-bone specimens were mounted horizontally with their front vertical surface perpendicular to the incident beam. Debye-Scherrer ring patterns were recorded using a large area diffraction detector Pilatus 2M (1475×1679 pixel and 172μm×172μm pixel size) that was placed behind the sample. Monochromatic beam energy of 93.7 keV was employed with a beam size fixed at 200μm×200μm and a data acquisition rate of 10s per scanning point. The position of the beam was fixed in the

laboratory system, while the sample could be moved horizontally and vertically. Figure 7.3 illustrates the coordinate system and the scanning plan for the three samples. X axis is the horizontal direction and also the loading direction, Y axis is the vertical direction. For each sample, four scanning lines were measured in the 10mm sample gauge region, and four reference points were scanned in the grip region. Each reference measurement point was at the same height that corresponds to each scanning line. The scanning direction for each line was parallel to the loading direction. The distance between the beam centre to the sample edge and the distance between two neighbouring beam centres were $300\mu m$. LaB_6 powder was used for the XRD pattern calibration. Peak indexation and Rietveld refinement (as shown in figure 7.2(b)) were performed using General Structure Analysis System (GSAS-II) [174]. Diffraction data from each reference point were analysed to provide the undeformed lattice parameters for each sample. To determine the phase fraction, lattice misfit, lattice parameters and microstrain (diffraction peak broadening), a series of Rietveld refinements were conducted for diffraction data from each scanning line. Following refinement, the values of residuals were of the order 5% or below, confirming the goodness and reliability of interpretation [175].

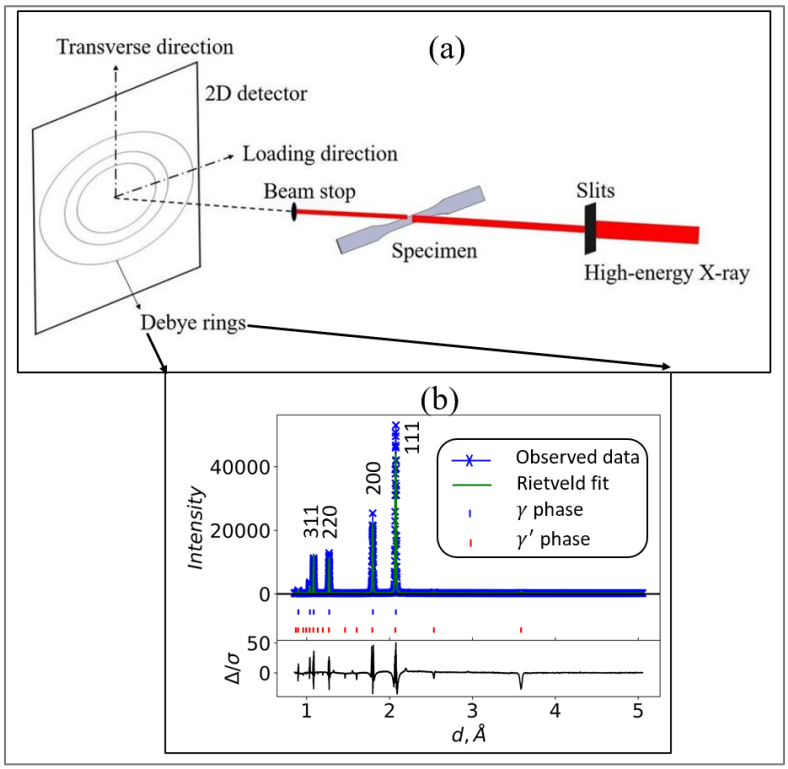


Figure 7.2. (a) Experiment setup of synchrotron X-ray diffraction at I12, DLS. (b) An example of indexed and refined diffraction peak processed by GSAS II software.

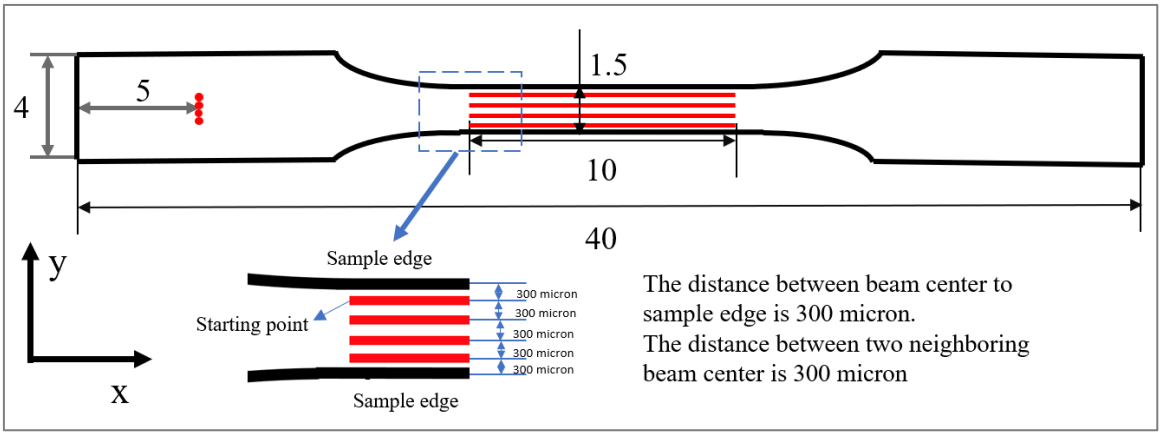


Figure 7.3. An illustration of the scanning routine for the reference sample and pre-crept samples.

7.3 Results and discussion

7.3.1 Material characterization

7.3.1.1 EBSD characterization

After the synchrotron XRD experiment, electron backscatter diffraction (EBSD) characterization was performed using a Tescan LYRA3 FIB-SEM system equipped with a SYMMETRY CMOS EBSD detector from Oxford Instruments. The outer surface of all samples was removed by standard metallographic grinding, followed by mechanical polishing in a solution containing a suspension of diamond particles down to 1 μm. Final polishing was made with 0.25μm colloidal silica. The accelerating voltage for all EBSD mapping was 20 kV and the step size was 0.5μm.

Figure 7.4 (a), (b-c) and (d) illustrate the EBSD measurements of Sample A, B and C, respectively. As shown in Figure 7.4 (a), equiaxed microstructure with twins was observed in the reference sample after a two-step ageing treatment. After thermomechanical creep deformation, no twin was found in the two crept samples. It implies that creep loading conditions at 750 ℃/400 MPa and 700 ℃/800 MPa can introduce detwinning and recrystallization in nickel-base superalloy. Figure 7.4 (b) and (c) depict EBSD mapping from the grip section and gauge region of the sample after creep at 750 ℃/400 MPa, respectively. There was no creep deformation in the grip section, while tensile and creep deformation occurred in the gauge region. The grain size in the gauge region is much smaller than in the grip region. Close observation suggests that many of the small grains in the localized area have almost the same orientation, which means that the small grain fragments (or subgrains) come from the same grain before loading. This finding implies

that significant grain rotation occurs during tensile and creep loading, and it is also consistent with previous creep experiment results in the literature [176].

It is clear in Figure 7.4(d) that the microstructure of Sample C at much higher stress (700 ℃/800 MPa) is significantly different from the microstructure of Sample B at lower stress and slightly higher temperature (750 ℃/400 MPa). Significant recrystallization occurs in Sample C and the grains are large and elongated in the loading direction during creep. Because it only takes 0.26h for Sample C compared to 35h for Sample B to get the same amount of creep deformation, a higher magnitude of stress not only dramatically increases the creep rate but also accelerates the recrystallization process. This finding is analogous to the results of dynamic recrystallization under the hot deformation or creep loading condition in face-centred cubic alloys [177-179]. Material processing parameters, such as strain rate, deformation temperature and strain level, are of significance to control the microstructural evolution during the recrystallization process. With the increase of deformation and strain rate, dislocation density within the sample becomes higher and leads to dislocation networks. Subgrains then form and eventually, grain recrystallization occurs. The apparent difference in grain morphologies for Sample B and C arises from the difference in deformation temperature and strain rate. It is assumed that Sample B was stopped at the subgrain stage while Sample C was interrupted at the recrystallization stage even though they had the same level of deformation. Additionally, the grains in the edge of Sample C are much smaller than those in the centre of the sample. It can be explained by the parabolic-shape temperature distribution profile developed across the width of the sample, as discussed in Appendix A. The sample centre had the highest temperature during

creep, and lead to fully recrystallization, as opposed to the edge of the sample.

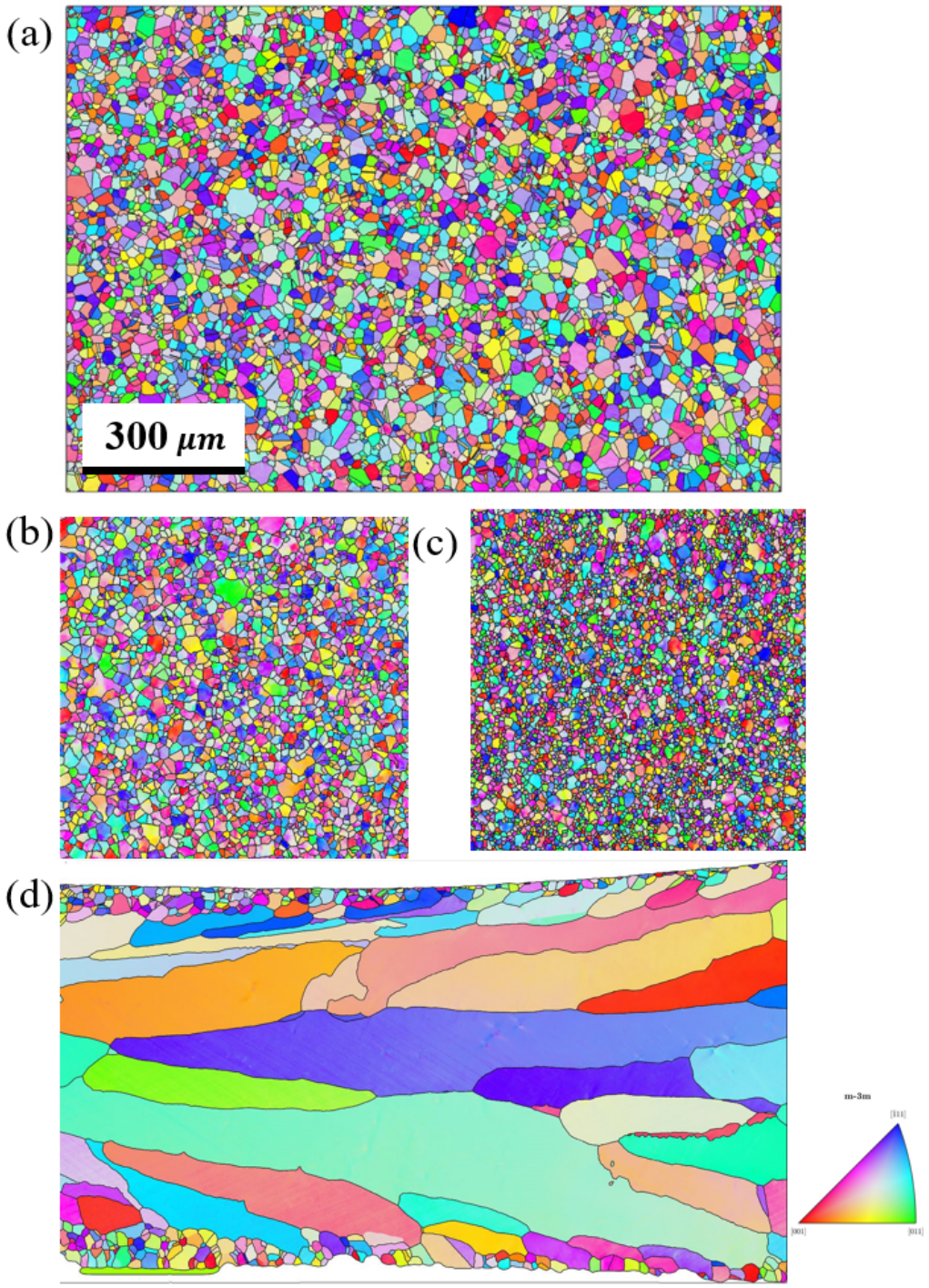


Figure 7.4. EBSD measurements of (a) reference Sample A, (b) the grip region of sample B crept at 750°C/400MPa, (c) the gauge region of Sample B crept at 750°C/400MPa (d) Sample C crept at 700°C/800MPa. The scale bar and inverse pole figure apply to all the EBSD mappings.

7.3.1.2 Deformation characterization using SEM and STEM

Scanning electron microscopy (SEM) and scanning transmission electron microscopy (STEM) characterization techniques were used to visualize the deformation mechanism of Sample B and Sample C that were crept to 0.6% plastic strain at different loading conditions. Several voids and inclusions were observed in the sample edge for both samples. Figure 7.5(a) reveals that both intergranular and intragranular cracks occurred on the edge of Sample B, while only intergranular cracks were found in Sample C as illustrated in Figure 7.5(c). Intergranular crack is a typical damage mode under creep loading, here we demonstrate that intragranular crack could also appear when there is a void in the crack path. Figure 7.5(b) and (d) show enlarged images of red rectangular areas A and B, respectively. Microvoids in the grain boundary and triple points were observed in Sample B, as shown in Figure 7.5(b). A close observation of the crack tip in sample C suggests that the crack stopped at the border of a primary γ' precipitate.

STEM images in Figure 7.6 reveal the microstructure and the deformation mechanisms for alloy 11 after creeping at 700℃/800MPa. Four kinds of deformation mechanisms were observed in the current study: (1) Dislocations in the γ matrix channel. (2) Shearing of γ' precipitate by APBs. (3) Continuous stacking faults cutting through both γ matrix and γ' precipitate. (4) isolated stacking faults shearing in the γ' precipitate. It is well known that the isolated stacking faults are formed by shearing of the γ' phase by a/3<112> dislocations. In the current research, a great number of transition elements, such as Co and W are added to alloy 11, which reduces the stacking fault energy (SFE) of γ matrix to some extent. According to Ref. [180], a reduction of SFE in γ phase

would facilitate the formation of continuous stacking fault. Therefore, both isolated stacking faults and continuous stacking faults were observed under the same crept alloy 11 samples.

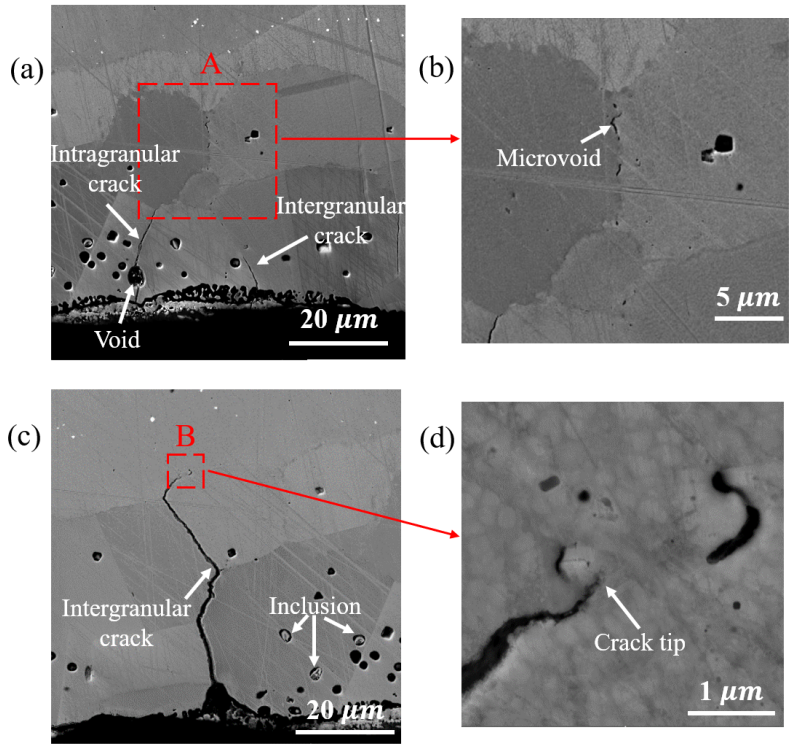


Figure 7.5. The microstructures and SEM images showing cracks, inclusions and microvoids in Sample B crept at 750°C/400MPa ((a) and (b)), and Sample C crept at 700°C/800MPa ((c) and (d)).

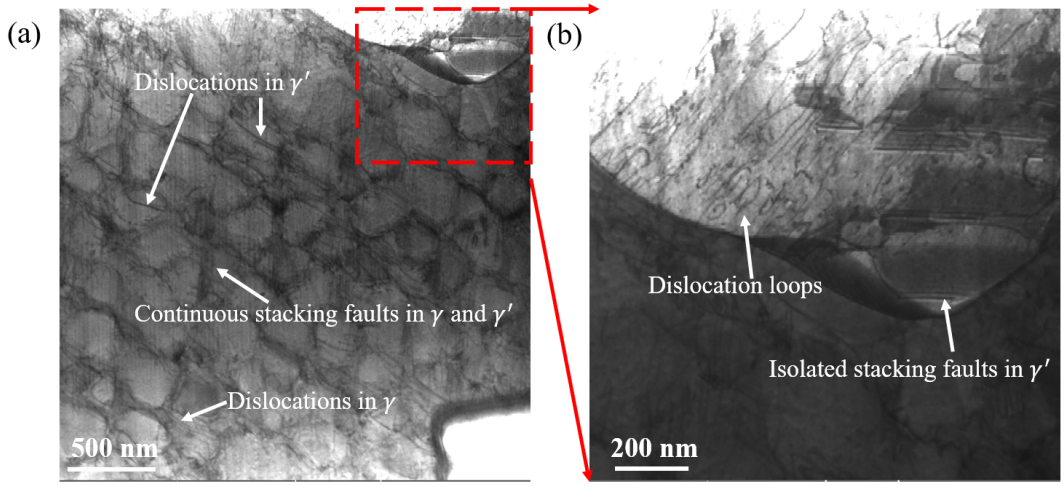


Figure 7.6. The microstructures and STEM images show the creep deformation mechanisms for alloy 11 after creeping at 700°C/800MPa for 0.26 hours.

7.3.2 Lattice misfit

For nickel-base superalloy, one important microstructural property is the γ/γ' lattice misfit, δ, which is defined as the relative difference of the lattice parameters in γ and γ' phase:

$$\delta = \frac{2(A_{\gamma'} - A_{\gamma})}{A_{\gamma'} + A_{\gamma}} \tag{7.1}$$

Where $A_{\gamma'}$ and A_{γ} are the lattice parameters of the γ' and γ phase, respectively. All the misfits calculated in this research are constrained misfits and are directly derived from the X-ray diffraction data. In the reference specimen, the constrained misfit arises from the stress-free states with coherent γ/γ' interfaces. In the pre-crept samples, the misfit represents a combination of stress-free constrained misfit and the residual strain contributions from the interfacial dislocation network.

Figure 7.7 (a) reports the contour map of lattice misfits in the three samples. Figure 7.7 (b) and (c) show the averaged lattice misfit in the horizontal and vertical direction, respectively. The lattice misfit in the reference sample is relatively uniform and ranges around -0.0031, while the lattice misfit in the two pre-crept samples shows a distinctly different spatial distribution. A much larger magnitude of negative misfit is observed in the middle region of crept Sample B and C. This particular distribution of misfit is due to the parabolic-shape temperature distribution profile. Creep deformation is dependent on the applied stress and the temperature. Here the applied stress was constant at each cross-section that perpendicular to the loading direction in the gauge length, while the temperature was non-uniform along the gauge length as discussed in Appendix A. Consequently, during the creep tests using ETMT system, the sample centre had the highest

temperature and is inclined to accumulate more deformation. In other words, creep deformation is localized, and the predominant deformation occurs in the sample centre. The above discussion reveals that there might exist a threshold temperature (see Figure B in Appendix A) above which more creep deformation accumulates or the dominant creep deformation mechanism changes. The differences between the minimum and maximum misfit are 1.6%, 9.3% and 37.1% for Sample A, B and C, respectively. The considerable spatial variation in terms of misfit suggests that it is crucial to perform measurements at different sample locations with space intervals instead of a single measurement point when investigating lattice-related parameters, such as strains and stresses. Since Sample C has the highest difference in spatial misfit and also the largest creep rate, it is then reasonable to assume that more localized deformation is expected to accumulate in samples with a larger creep rate.

The evolution of lattice mismatch is time-dependent, i.e. Its value varies at different stages of creep. The result in this chapter is comparable to an ex-situ neutron diffraction measurement of single crystal superalloy DD10 after creep [181] and an in-situ XRD measurement of superalloy AM1 during creep deformation [182], where the negative misfit ranges between -0.2% to -0.48% at different creep stages. The agreement suggests that the lattice misfit in superalloy developed during creep deformation is mostly retained after removing the external stress and thermal loading. In addition, the lattice misfit evaluated in pre-crept samples is also dependent on the magnitude of applied stress, as found in this study and other work in the literature [183].

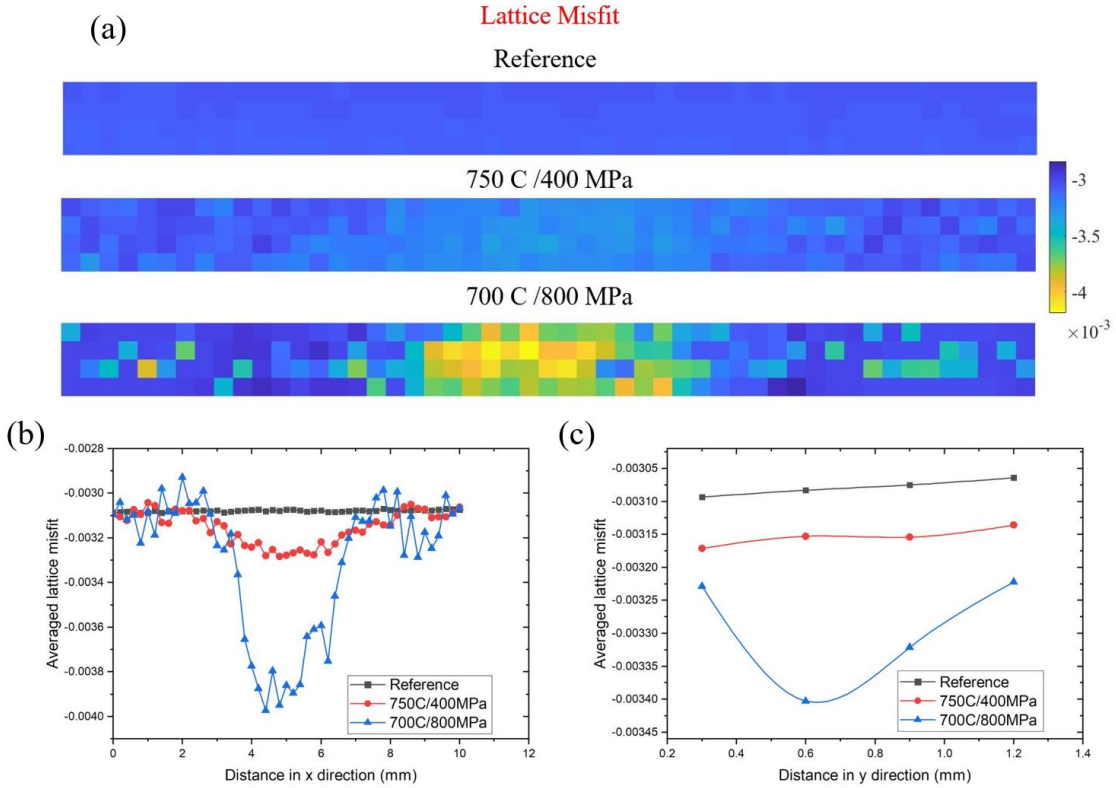


Figure 7.7. (a) The contour map of lattice misfits at different locations in the three samples. (b-c) The averaged lattice misfit along the x and y direction in the samples.

7.3.3 Phase fraction

Figure 7.8 (a) shows the contour map of the phase fraction of γ in the three samples, and Figure 7.8 (b), (c) illustrate the averaged γ phase fraction in the horizontal and vertical directions, respectively. Analogous to lattice misfit, the phase fraction in the reference sample is relatively uniform and ranges around 64%, while the phase fraction of γ in two pre-crept samples shows a slightly different spatial distribution and varies from 57% to 67%. The averaged γ phase fractions in Sample A, B and C are 64%, 62% and 61%, respectively. The γ' solvus temperature of this alloy is ~ 1100℃, which is much higher than the thermal condition in the creep test (750℃ for Sample B, and 700℃ for Sample C). The slight decrease in the γ phase fraction after creep deformation indicates that there

is a redistribution of alloying elements within the microstructure during creep even when the creep temperature is lower than the solvus temperature. Compared with Sample B, Sample C had a lower temperature, a much higher stress level and the lowest γ phase fraction. This finding implies that element diffusion is a thermal process and external stress is likely to accelerate the evolution of γ phase fraction.

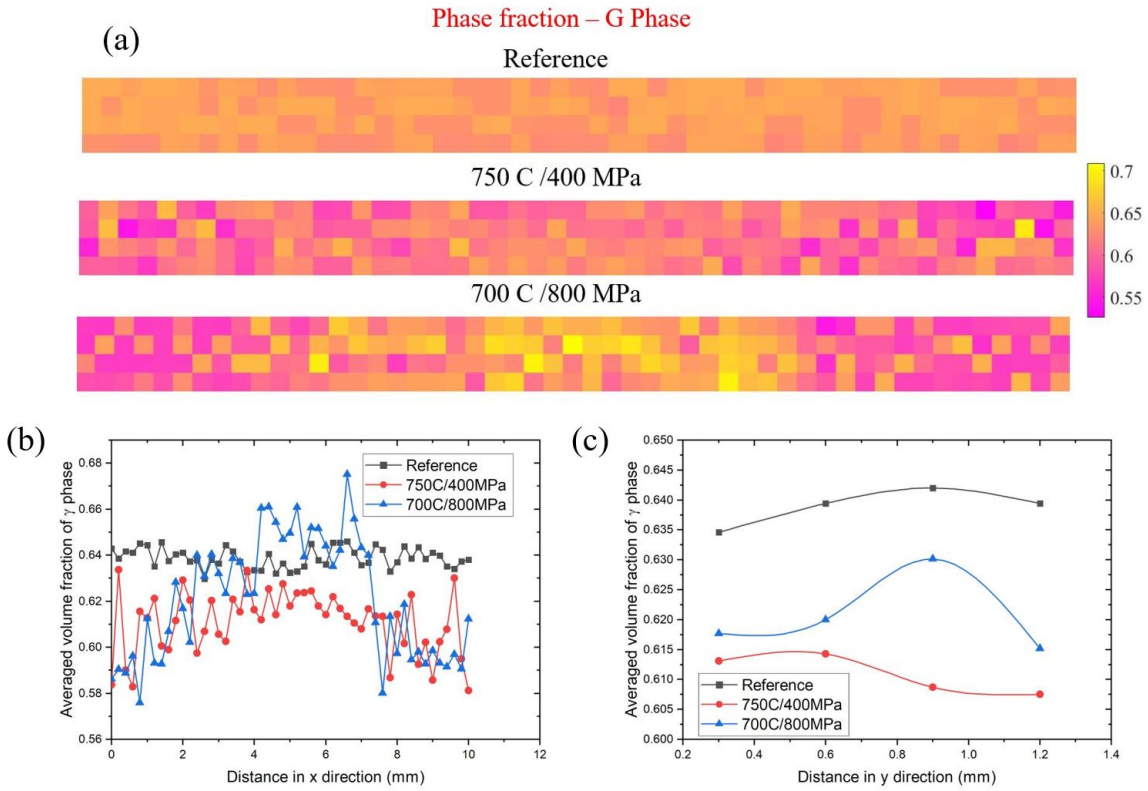


Figure 7.8. (a) The contour map of phase fraction of γ in the three samples. (b-c) The averaged volume fraction of γ phase along the x and y direction.

7.3.4 Microstrain

It is well known that microstrains could affect the broadness of the diffraction reflections and hence they were evaluated using the Scherer equation and strain function as implemented in GSAS-II. The microstrain in polycrystalline alloys reflects the lattice deformation and dislocation configuration within the alloys. Many publications suggest

that the microstrain evaluated from XRD can be directly related to dislocation density in the crystalline materials [184-186]. Figure 7.9 and 7.10 illustrate the microstrain in γ and γ' phase in the three samples, respectively. The averaged microstrain in γ phase in Sample A, B and C is 1465, 1598 and 2031, respectively, while the averaged microstrain in γ' phase is 590, 1195 and 1360 in the samples, respectively. Here we demonstrate that the microstrain in γ phase is much larger than the microstrain at the same location in γ' phase in all three samples, which means that the dislocation density in γ phase is much higher than that in γ' phase for both reference and pre-crept samples.

It is clear from Figure 7.9(c) and Figure 7.10(c) that the microstrain for both γ and γ' phase in Sample C with the largest creep rate is higher than that in Sample B and A. As can be seen from Figure 7.9(b) and Figure 7.10(b), the centre of Sample C was observed to have the highest value of microstrain compared to the other locations and the other samples. More dislocation networks were developed in both γ matrix and γ' precipitate in the centre of Sample C, which might indicate the main creep deformation mechanism in Sample B and Sample C are different. In a high temperature/low stress regime like the loading condition in Sample B, creep deformation is dominantly caused by dislocation loops or climbs moving in the γ matrix and forming interfacial dislocation networks at the γ/γ' interfaces. This mechanism is active until the back stress of the dislocations accumulated in the networks makes it impossible for new dislocations to enter the γ matrix channel. In low temperature/high stress regime like Sample C, the favourable deformation mechanism is the shearing of the microstructure (both γ matrix and γ' precipitate) by stacking faults. It is suggested that the dominant creep deformation

mechanism in Sample C is the stacking faults cutting through the γ and γ' phase (as illustrated in Figure 7.6), resulting in a higher dislocation density and microstrain in both phases as observed in this study.

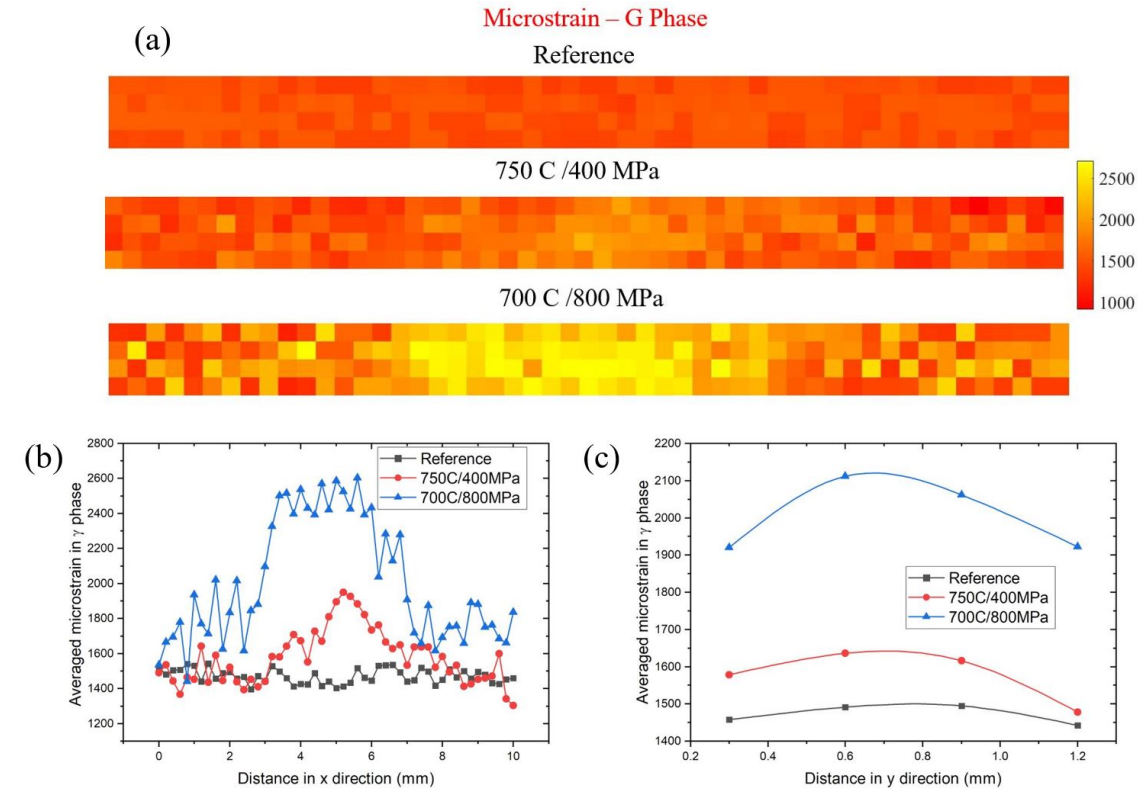


Figure 7.9. (a) The contour map of microstrain in γ phase in the three samples. (b-c) The averaged microstrain in γ phase along the x and y direction.

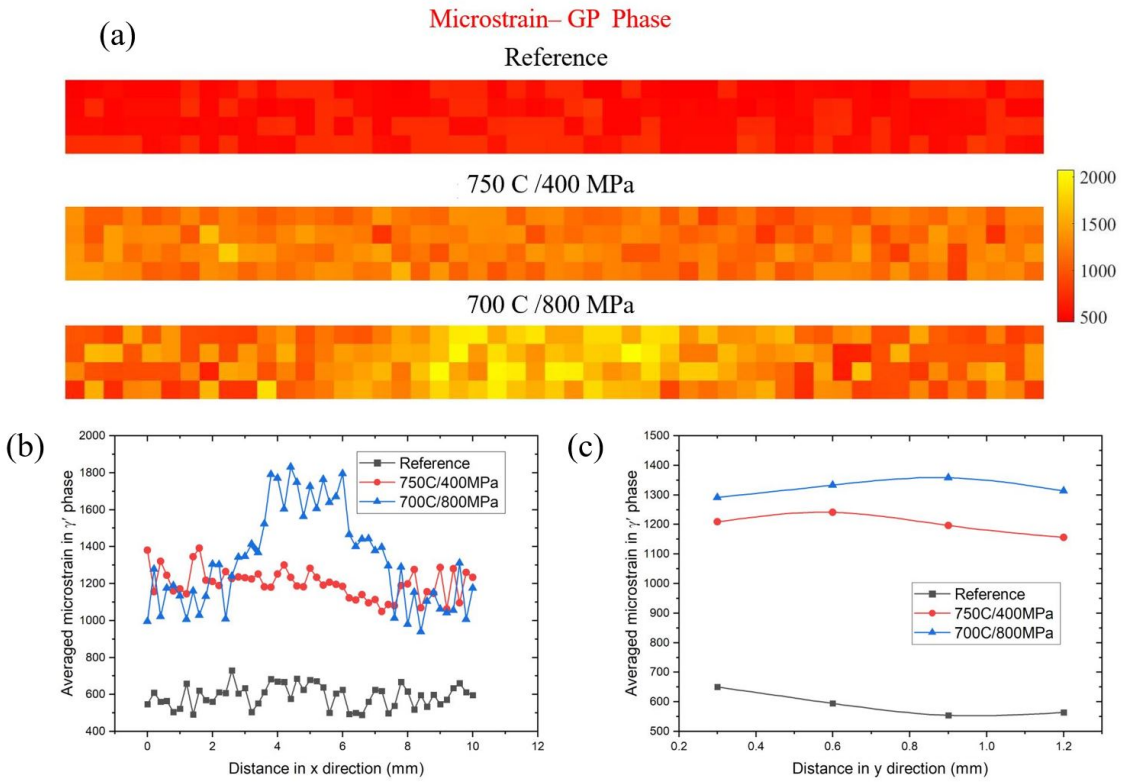


Figure 7.10. (a) The contour map of microstrain in γ' phase in the three samples. (b-c) The averaged microstrain in γ' phase along the x and y direction.

7.3.5 Lattice parameter distributions

7.3.5.1 Horizontal direction – lattice parameter

A quantitative determination of lattice parameters can be calculated from the relative change in X-ray diffraction peak position, which provides important information not only on the compositional change of matrix and precipitate phase but also on the developed strain field. As creep is a thermomechanical process, the changes in lattice parameters can be caused by both the occurrence of compositional changes in the phases and the internal stress/strain field. It is then inaccurate to evaluate internal stress from the changes in lattice parameters, as reported in the literature [181]. In this chapter, the XRD diffraction patterns were caked and integrated along a specified azimuth angle range to evaluate the lattice

parameters in both γ and γ' in horizontal and vertical directions.

Figure 7.11 and 7.12 illustrate the horizontal lattice parameters in γ and γ' phase in the three samples, respectively. The lattice parameters in both phases for the reference sample are relatively constant and do not vary with different locations. The averaged horizontal lattice parameters in γ phase in Sample A, B and C are 3.5981, 3.5971 and 3.5993, respectively, and the averaged horizontal lattice parameters in γ' phase are 3.5864, 3.5862 and 3.5882 in the samples, respectively. An apparent finding is that the lattice parameters of γ phase are all slightly larger than those of γ' phase, which provide a negative value of lattice misfit. In the sample centre, the lattice parameter in the γ phase in crept Sample C is larger than that in the reference sample, while the γ lattice parameter in crept Sample B is smaller compared to the reference sample. Significant deviations were observed in the γ' precipitate in the centre position of Sample C compared to the reference sample, while no apparent deviation was detected in the same region of Sample B, indicating the dominant creep deformation mechanism is different in this region for the two samples. The lattice parameter in Sample C varies significantly at different locations, this can be explained by the fact that the internal stresses and strains are orientation-dependent after creep loading. The orientation dependence will become more prominent when the grain is large and elongated (only a few grains in the region of interest) as for Sample C.

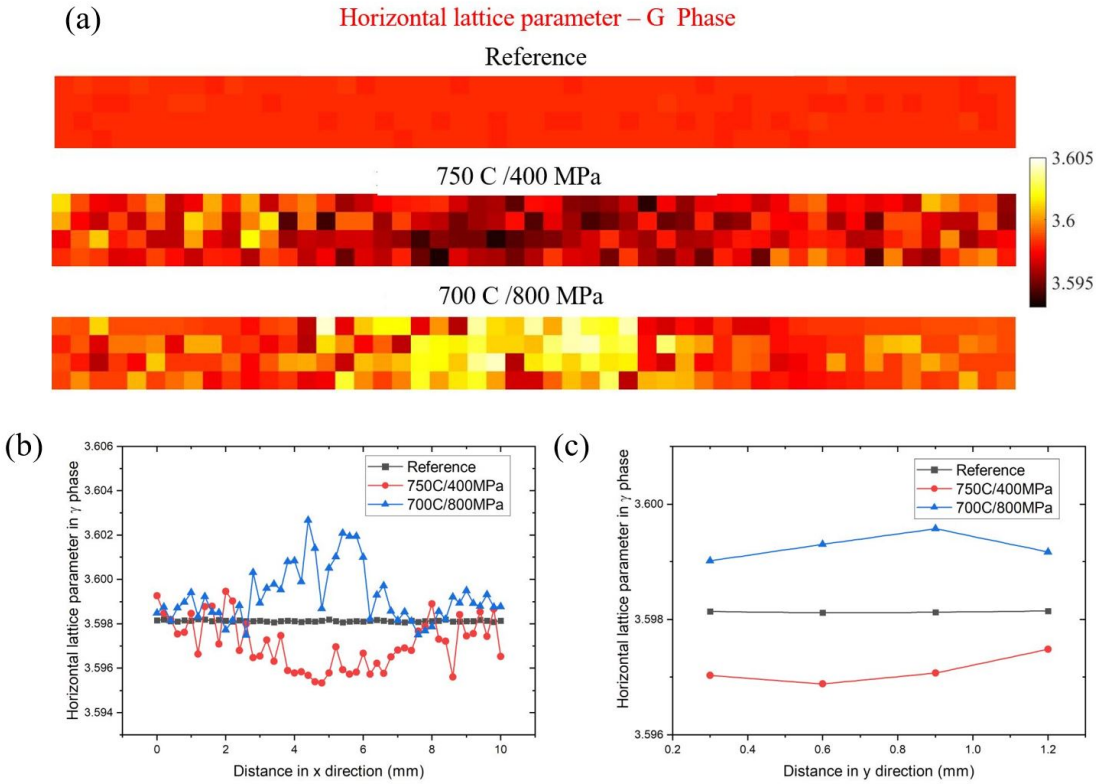


Figure 7.11. (a) The contour map of horizontal lattice parameter in γ phase in the three samples. (b-c) The averaged horizontal lattice parameter in γ phase along the x and y direction.

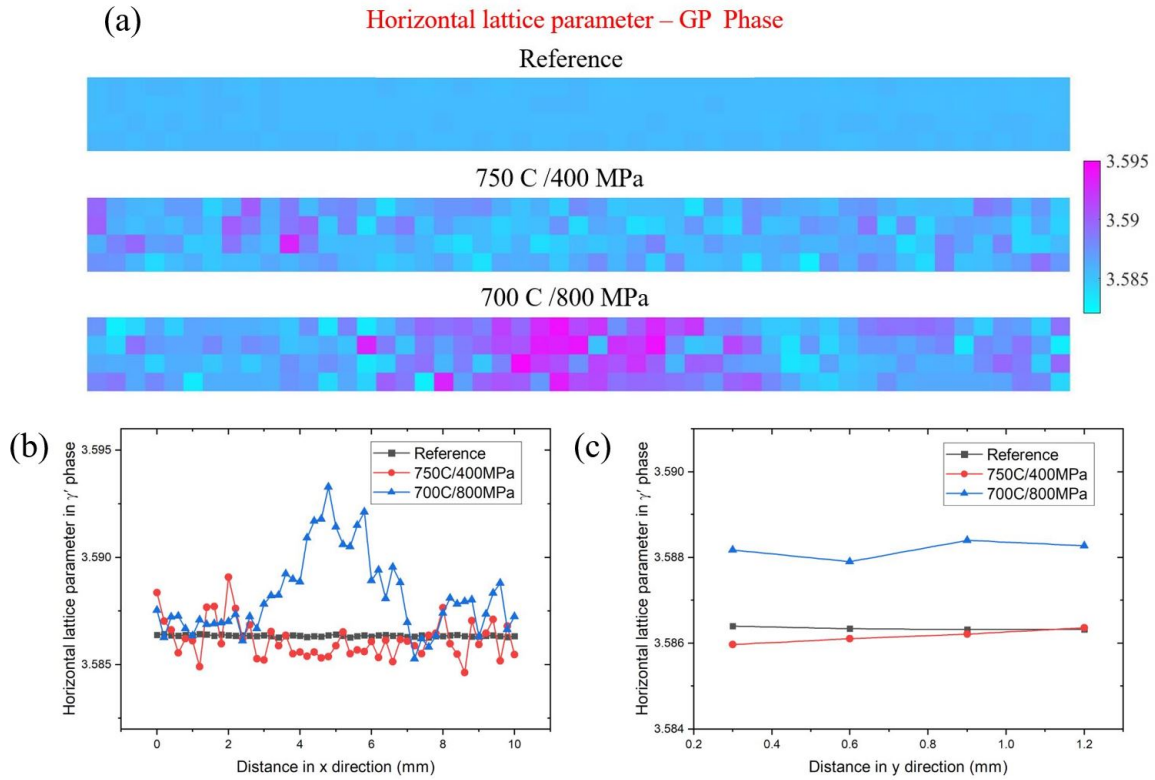


Figure 7.12. (a) The contour map of horizontal lattice parameter in γ' phase in the three samples. (b-c) The averaged horizontal lattice parameter in γ' phase along the x and y direction.

7.3.5.2 Vertical direction – lattice parameter

Figure 7.13 and 7.14 illustrate the vertical direction lattice parameter in γ and γ' phase in the three samples, respectively. There exists some extent of lattice parameter fluctuation in both phases for Sample B. A dramatic increase in lattice parameters of both phases is developed in the centre of Sample C. There is a prominent spatial variation of the lattice parameters in Sample C, suggesting that it is crucial to perform mapping measurement instead of a single measurement point when investigating the lattice-related parameters.

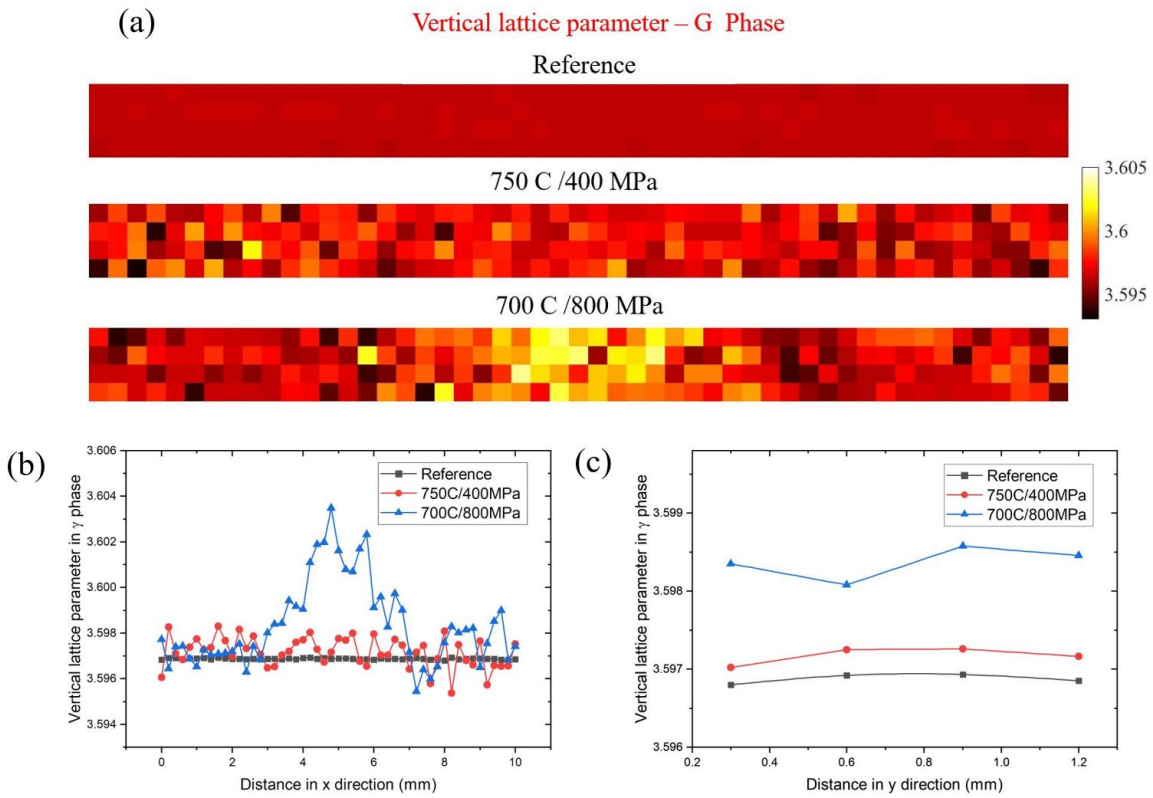


Figure 7.13. (a) The contour map of vertical lattice parameter in γ phase in the three samples. (b-c) The averaged vertical lattice parameter in γ phase along the x and y direction.

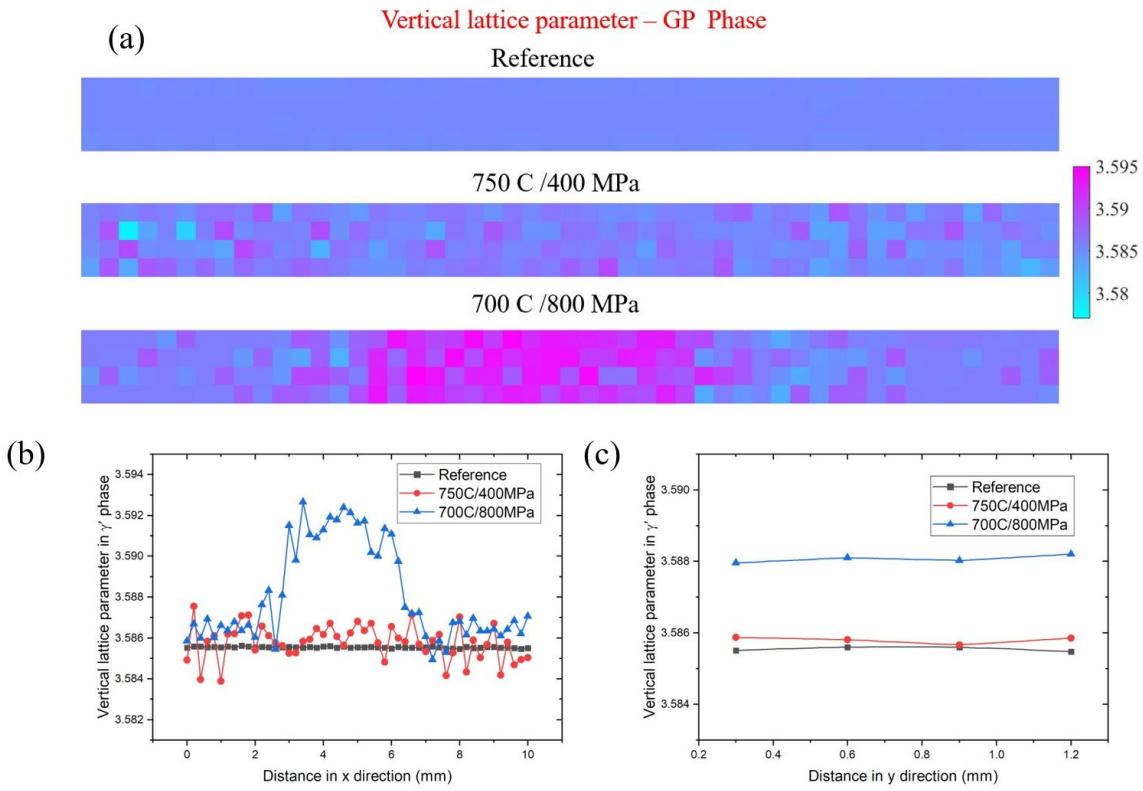


Figure 7.14. (a) The contour map of vertical lattice parameter in γ' phase in the three samples. (b-c) The averaged vertical lattice parameter in γ' phase along the x and y direction.

7.3.6 The statistical distribution of lattice parameter variation

In polycrystalline materials such as nickel-base superalloys, the elastic and plastic deformation are highly anisotropic, giving rise to strain spatial inhomogeneity that emerges within and between grains. The inhomogeneous nature of strain distribution has led to the concept of three types of strains that describe the spatial variation over different length scales: macroscale, mesoscale and microscale. On the macroscale, the whole sample can be regarded as a homogeneous medium with averaged material properties such as Young's modulus and yield stress. On the atomic scale (microscale), deformation is characterized by dislocation motion, dislocation-dislocation and dislocation-precipitate interactions. In this chapter, we are interested in the deformation behaviour at the mesoscale where the

controlling microstructural features are grain size, morphology and orientation, dislocation density, phase properties, and their spatial distribution. The investigation of the distribution of lattice-parameter change at the mesoscale can effectively provide further insights into the effect of mesoscopic microstructure on mechanical properties. The lattice-parameter change ε can be defined as follows:

$$\varepsilon = \frac{a-a_0}{a_0} \tag{7.2}$$

Where a and a_0 denote the lattice parameters at the loaded and stress-free state, respectively. Figure 7.15 illustrates the statistical distribution of horizontal lattice-parameter change in γ and γ' phase in Sample B. It is interesting to find that the lattice-parameter changes for both phases in the loading direction follow a normal distribution. The same type of statistical distribution of lattice-parameter change is observed in Sample C as shown in Figure 7.16. In this experiment, the sample thickness is 1.2mm and the X-ray beam size is $200\,\mu m \times 200\,\mu m$, leading to an illumination volume of $200\,\mu m \times 200\mu m \times 1200\mu m$ for a single diffraction pattern. Each measurement point provides averaged values of material properties and mechanical response within the illumination volume. Each illumination volume contains dozens to thousands of grains, and hence, it can be regarded as a representative volume element (RVE) for the material investigated in this study. The lattice-parameter change in the current study arises from a complex thermomechanical process that includes the effects of both strain filed and compositional change. The simulation results in Chapter 3 suggests that the flow stresses obtained from multiple RVEs with nominally identical microstructure conform to a normal distribution [187, 188]. The finding in this chapter further extends the applicability of our simulation

results from only mechanical loading conditions to thermomechanical processes in polycrystalline materials.

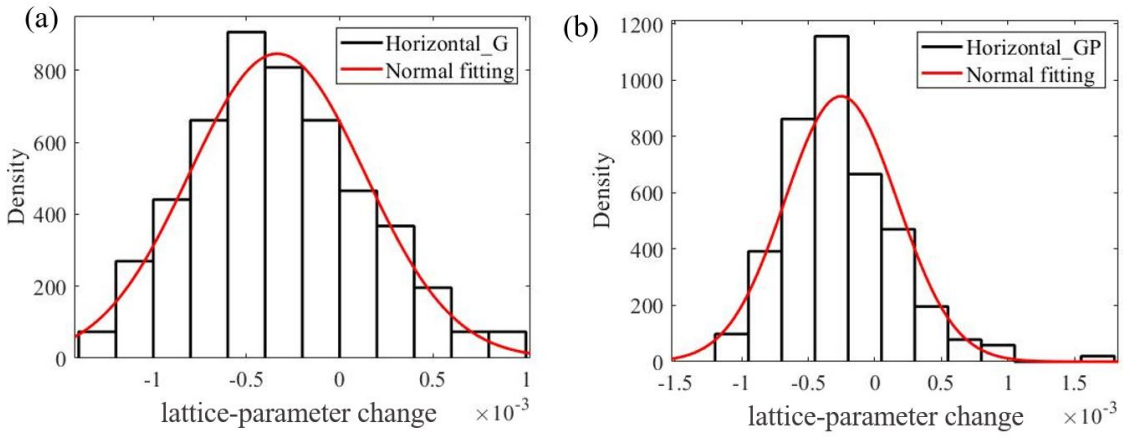


Figure 7.15. The statistical distribution of lattice-parameter changes in the loading direction within (a) γ and (b) γ' phase in Sample B crept at 750℃/400MPa.

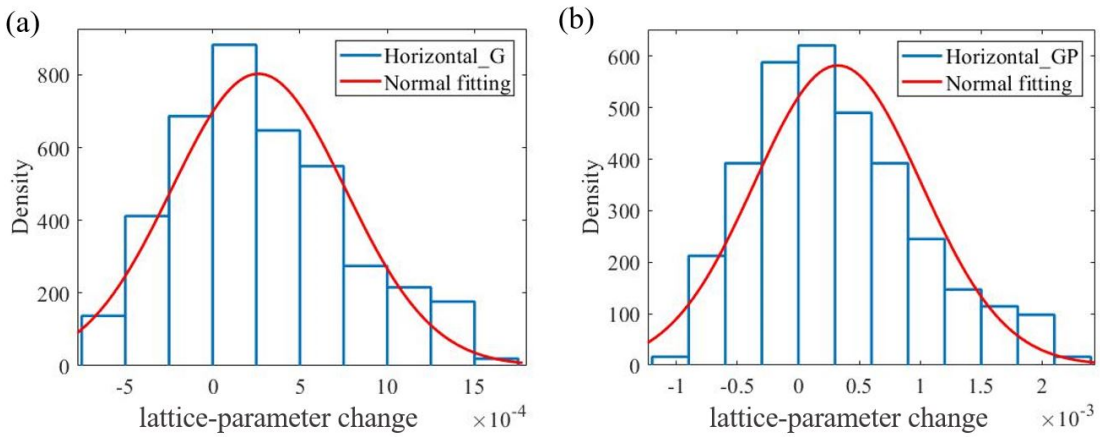


Figure 7.16. The statistical distribution of lattice-parameter changes in the loading direction within (a) γ and (b) γ' phase in Sample C crept at 700℃/800MPa.

7.4 Conclusion

In Chapter 7, the creep behaviours of a newly designed nickel-base superalloy at 750 ℃/400MPa and 700 ℃/800MPa have been systematically investigated using the scanning electron microscope, scanning transmission electron microscopy, electron backscatter diffraction and synchrotron X-ray diffraction. The experiment results from pre-

crept samples were compared with the results for the reference sample. Material properties and mechanical responses such as lattice misfit, phase fraction, lattice parameter and microstrain in the reference and crept samples have been analysed in detail. The main conclusions of this chapter can be listed as follows:

(1) The materials characterization of pre-crept samples reveals that creep loading conditions can introduce detwinning and recrystallization in nickel-base superalloy. A higher magnitude of external loading stress not only dramatically increases the creep rate but also accelerates the dynamic recrystallization process.

(2) Both intergranular and intragranular cracks were found in the pre-crept samples. Four types of creep deformation mechanisms, namely dislocations in the γ matrix channel, shearing of γ' precipitate by APBs, continuous and isolated stacking faults, were observed in the sample crept at high stress and low temperature.

(3) The highest values of lattice misfit and microstrain were observed at the centre of crept samples, which was caused by the parabolic-shape temperature distribution profile developed across the width of the sample during creep. The significant spatial variation in terms of misfit, microstrain and lattice parameters suggests that it is crucial to perform measurements at different sample locations instead of a single measurement point when investigating the lattice-related parameters.

(4) In both crept samples, the statistics of the lattice-parameter changes for γ and γ' phases in the loading direction were found to follow a normal distribution.

8. Conclusions and Future work

8.1 Conclusions

The focus of the thesis has been on evaluating macro-scale, intragranular and intergranular (Type I-II-III) residual stresses in aerospace nickel-base superalloys under thermo-mechanical loading conditions. Both FIB-DIC micro-ring-core milling and synchrotron XRD technique were used for experimental evaluation of local strains and stresses, which was interpreted with the help of continuum and crystal plasticity finite element modelling. The fundamental scientific contributions of this thesis are highlighted below:

1) Multiscale stress and strain statistics in the deformation of polycrystalline alloys.
2) The effect of discretization methods on CPFEM.
3) The statistical description of deformation process.
4) Residual stresses and internal strains evaluation at multiscale.

Here I concentrate on the scientific achievement in the research and the limitations that need further discussion.

8.1.1 Multiscale stress and strain statistics in the deformation of polycrystalline alloys

With the help of CPFEM, multiple RVE realizations with different grain morphologies and orientation permutations were generated to perform a multiscale analysis of the distributions of strain, stress and other mechanical responses. At macroscale, the overall stresses that correspond to 1.55% strain among different RVEs were found to follow a

normal distribution. The width and height of the normal distribution were affected by the parameters that described the lognormal grain size distribution. It is interesting to find that the morphology with a larger grain size dispersion will result in fewer overall stress discrepancies. The physical explanation of the phenomenon highlighted here is that broad grain size dispersions tend to reduce the grain size dependence whereas the individual grain behaviour is grain-size dependent according to the Hall–Petch like behaviour caused by discretization induced size effect. Microscopically, the elastic strain (and stress) accumulation is found to be additive leading to a normal distribution, whereas plastic strain can be well described by a lognormal distribution. Much more significant variation of stress magnitudes within one grain (Type III) and among different grains (Type II) is observed compared to the responses of whole RVEs (Type I). The above finding reveals the nature of stress and strain inhomogeneity at different scales and highlights the fact that the dispersion of local stress and strain distribution is much larger than the macroscopic average. The statistical analysis of stress and strain at the local and global level for multiple assembles of RVEs provides new insights into the relationship between microstructure and mechanical properties at multiscale.

8.1.2 The effect of discretization methods on CPFEM.

Chapter 4 employs a large number of simulations with static and grain-based mesh to investigate the discretization deviations in crystal plasticity finite element methods. Static mesh is integration point-based and the IPs in the same element can belong to one or multiple grains, while the minimum discretization unit for grain-based mesh is an element

and each element can only belong to one grain. The crystal plasticity constitutive law was programmed in the user material subroutine UMAT and the calculation was performed using commercial finite element software Abaqus. Multiple sets of RVEs were subjected to strain-controlled loading and periodic boundary conditions. The stress and strain contour maps obtained from RVEs with static mesh and grain-based mesh were compared. The simulation results reveal that the both discretization methods can well predict the stress-strain curves and the stress/strain localization points in polycrystalline alloys. Static mesh tends to smooth the stress/strain profile at the grain boundary, and more stress/strain discontinuities exist in grain-based mesh compared to static mesh. The above findings still remain valid when the number of grains within an RVE increases from 34 to 1250. A relative deviation is defined to quantitatively evaluate the difference caused by the static and grain-based mesh. The global deviations are relatively small and are all within 0.5%, while the local deviations are significant and range between 0-50%. Static mesh reduces both pre-processing procedure and computational time compared to grain-based mesh. It is suggested that static mesh is more desirable when investigating the *macroscopic* behaviour of the materials and grain-based mesh is recommended to study the *local* response using CPFEM.

8.1.3 The statistical description of deformation process

To explain the findings of strain statistics in Chapter 3, the origins of local strain and stress statistics were given fundamental consideration in the first part of Chapter 5. The evolution of strain distribution during tensile deformation was investigated using CPFEM. The simulation results were correlated with experimental observations of strain localization

and dislocation density distributions in the literature. The elastic strain (and stress) accumulation is found to be additive leading to a normal distribution, whereas plastic strain can be well described by a lognormal distribution and obeys a multiplicative accumulation process.

The second part of Chapter 5 focuses on the statistical description of the stress-strain behaviour using Yield Volume Fraction function. The relationship between stress-strain curves and the YVF function was derived based on a physically meaningful parameter that corresponds to the cumulative volume fraction of the polycrystal that undergoes yielding during monotonic deformation. The statistical nature of the polycrystal yield phenomenon is highlighted by the fact that the YVF model achieves good agreement with observations when the lognormal and extreme value distributions are employed to express the cumulative density function for the total yield volume fraction, and the probability density function for the incremental yield volume fraction, respectively. The accuracy of the proposed model was demonstrated by comparing its prediction with the Ramberg-Osgood model, CPFE simulation and experimental observations. Ramberg-Osgood equation tends to underestimate the incremental and cumulative YVF when the strain level is above 0.23% and hence overpredict the stress-strain curves in the immediate post-yield region. The results highlight the potential of more extensive use of statistical methods in the description of material deformation response for improved design.

8.1.4 Residual stresses and internal strains evaluation at multiscale.

The results reported here mainly focus on experimental evaluation of residual stresses

and internal strains in polycrystalline aggregates at both macroscopic and microscopic scales. Two case studies, i.e. the weldment in Chapter 6 and crept samples in Chapter 7, are presented in this part of the research. While the work and scientific findings are not limited to these two specific case studies, I believe the experimental and modelling techniques conducted here possess more applicability in scientific and industrial aspects.

To assess the residual stress state near manual welding surface along radial and hoop directions, FIB-DIC micro-ring-core technique and a sequentially coupled thermo-mechanical finite element model were employed in Chapter 6. The TIG fill-in weldments have a peculiar microstructure: a single crystal embedded with narrow and elongated grains. The diameter of the FIB milling rings was chosen to be smaller than the averaged grain size in filler metal, and consequently, the residual stresses evaluated by FIB-DIC represent the full grain level Type I+II+III residual stress. Good agreement was obtained between experimentally evaluated residual stresses and the refined numerically predictions. The highest hoop and radial tensile residual stresses were both observed at the boundary surface between the filler metal and base metal, a compressive region was found for hoop stress at the edge of base metal. The magnitude of maximum tensile stress is close to the yield point of filler metal, limiting the allowable service stress of engineering components in service. It is worth noting that there is still a minor mismatch between experiment measurements and FEM prediction. Relatively large uncertainty in the FIB-DIC measurements was observed, suggesting the importance of accounting for the elastic and plastic anisotropic behaviour (especially for single crystal) in FIB-DIC evaluations. Given the inherent variability in manual welding processes, it is not surprising that the residual stress

distribution is different in the two TIG welded samples. Another limitation of this research is that the thermal history during welding was not provided by the manufacturer. Local thermal history during welding needs to be measured in order to get a more accurate residual stress simulation.

The second case study systematically investigated the creep behaviour of a newly designed superalloy at 750℃/400MPa and 700℃/800MPa using SEM, STEM, EBSD and synchrotron X-ray diffraction. Spatially resolved measurements were performed to evaluate lattice parameters, misfit, phase volume fraction and microstrain in the reference and crept samples. EBSD characterization reveals that creep loading conditions can introduce detwinning and recrystallization in nickel-base superalloy. A higher magnitude of applied stress not only dramatically increases the creep rate but also accelerates the dynamic recrystallization process. Four types of creep deformation mechanisms, namely dislocations in the γ matrix channel, shearing of γ' precipitate by APBs, continuous and isolated stacking faults, were observed in the sample crept at high stress and low temperature. A parabolic-shape temperature distribution profile was developed across the width of the sample during creep, resulting in the highest values of lattice misfit and microstrain at the centre of crept samples. The significant spatial variation detected in terms of lattice-related parameters supports the conclusion that it is crucial to perform spatially resolved measurements instead of considering each sample as a single measurement point when investigating creep response. The experimental finding here validates and further extends the applicability of the simulation results for strain statistics in Chapter 3 from only mechanical loading conditions to thermomechanical processes.

8.2 Future work

This thesis mainly focuses on the experimental evaluation and modelling of stresses and strains at multiscale. In the future, a wider range of case studies, such as Elasto-Plastic Self-Consistent (EPSC) modelling, in-situ creep test and in-situ phase transformation, can be included in the project. I would like to highlight some ongoing and future work in the following areas:

1) CPFEM and EPSC are the two main simulation methods to model the thermo-mechanical behaviour of polycrystals. During the simulation process, it was found that the stress-strain curves obtained by CPFEM and EPSC are different even when both simulations use the same hardening law and material parameters. EPSC shows a consistent stress-strain curve, while CPFEM shows significant variation between the curves even for models with statistically nominally identical microstructure. a correlation between the CPFEM and EPSC simulation will be established. The implementation of EPSC model is based on a population of ellipsoidal grains chosen with a distribution of orientations and volume fractions that match the measured texture. It takes a significantly shorter computational time (~40 times faster) than CPFEM and hence provides a particularly elegant and efficient way to simulate mechanical properties and texture evolution during deformation. The principle of EPSC neglects the inhomogeneous nature of strain and stress distribution within one grain (group), i.e., Type II+III strains and stresses. In contrast, these are explicitly captured in a geometrically resolved manner by FEM simulation. In FEM the calculation is based on the local description of deformation at each integration point

(IP), while EPSC only captures the average of all the deformation within each grain (group) and thus describes the deformation in that grain (group) as a single value. According to the findings reported in Chapter 3, the strain and stress variation within one grain and one grain group is significant and follows certain statistical distributions. It is hypothesized that the main source of difference between the stress-strain curves obtained by EPSC and CPFEM comes from the Type II+III strains and stresses. An interesting challenge concerns finding a suitable means of representing the Type II+III variation of strain and stress within a grain (group) or identifying an alternative method to include statistical distribution of local strain in EPSC simulation.

2) Another promising work is to seek the ability to tailor the microstructure for optimum creep resistance by close control of the heat treatment procedure. To this end, the study will focus on the observation, quantification and prediction of the recrystallisation (grain morphology evolution) and the development of γ' precipitates in nickel-base superalloys during heat treatment at different cooling rates from solution heat treatment. The diffusion of solutes and the elemental partitioning have a profound effect on the lattice misfit between the γ matrix and γ' precipitate, which has a predominant role in impeding dislocations and therefore governs the creep strength of nickel-based superalloys. *In situ* observation of the recrystallisation process and the development of γ' precipitates in Alloy 11 and Haynes 282 were performed using X-ray diffraction in Diamond Light Source (MG25467-2). The experimental work and part of data analysis have now been completed, and the

remaining work mainly includes discussion and writing.

3) The project also requires further efforts focused on the evaluation of strain and stress at a microscopic scale with a different technique. White micro-beam Laue diffraction can be used to evaluate intragranular strains and stresses (Type III) in pure nickel samples under creep loading conditions. The *in-situ* micro-beam Laue diffraction experiment was conducted in Diamond Light Source (MM28775). The preliminary results suggest that there is a local stress redistribution during the creep test and the stress redistribution begins to occur at the secondary-tertiary creep transition region. Also, it is believed that the stress redistribution has a size effect and changes with different grain sizes. Bulk analysis of the data will be performed shortly after the submission of this thesis.

Appendix A

Evaluation of the temperature distribution during creep testing using ETMT

The temperature distribution within the sample during creep testing using ETMT is known to be non-uniform and requires evaluation for the purpose of result interpretation.

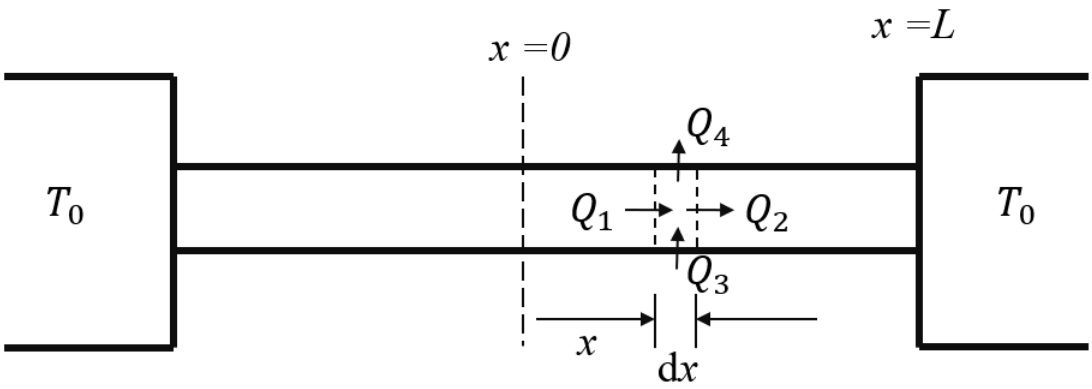


Figure A. The illustration of heat transfer process in an ETMT sample.

Considering the 1D representation of the sample as a wire of diameter $2R$ and length $2L$ illustrated in Figure A, assume that the cooled grips are maintained at a fixed ambient temperature T_0. Let the sample thermal conductivity be denoted by k, and let Joule heating per unit time and volume be given by G. Assuming that radiative and convective heat loss can be represented by the heat transfer coefficient h, the heat balance equation can be written as

$$k\pi R^2 \frac{\mathrm{d}T}{\mathrm{d}x} - k\pi R^2 \left[\frac{\mathrm{d}T}{\mathrm{d}x} + \frac{\mathrm{d}^2T}{\mathrm{d}x^2}\mathrm{d}x\right] + \pi R^2\, \mathrm{d}x\, G - 2\pi R\, \mathrm{d}x(T - T_0)h = 0 \qquad \text{(A.1)}$$

Introducing the temperature parameter $\theta = T - T_0$ the above equation is reduced to

$$\frac{\mathrm{d}^2\theta}{\mathrm{d}x^2} = \frac{G}{k} - \frac{2\theta h}{Rk} \qquad \text{(A.2)}$$

Equation (A.2) has the solution

$$\theta = A\sinh mx + B\cosh mx + \frac{GR}{2h}, \text{ where } m = \sqrt{\frac{2h}{Rk}} \quad \text{(A.3)}$$

To complete the solution, we determine the coefficients as follows: at $x = 0, \frac{d\theta}{dx} = 0$, hence $A = 0$. At $x = L, \theta = T - T_0 = 0$, and hence $B = -\frac{GR}{2h}\frac{1}{\cosh mL}$.

Therefore, the temperature T at location x can be calculated as

$$T = T_0 + \frac{GR}{2h}\left[1 - \frac{\cosh mx}{\cosh mL}\right] \quad \text{(A.4)}$$

Differentiating both sides with respect to x yields the following expression:

$$\frac{dT}{dx} = \frac{GR}{2h} m \frac{\sinh mx}{\cosh mL} \quad \text{(A.5)}$$

At $x = L$, $\left.\frac{dT}{dx}\right|_{x=L} = \frac{GR}{2h} m \tanh mL$.

The heat lost through one end is equal to

$$Q_{end} = k\pi R^2 \left.\frac{dT}{dx}\right|_{x=L} = \frac{k\pi R^3 Gm}{2h}\tanh mL \quad \text{(A.6)}$$

But $L = \sqrt{\frac{kR}{2h}}$, so $mL = 1$ and $\tanh mL = 0.7616$.

Hence,

$$Q_{end} = 0.7616\,\pi R^2 LG \quad \text{(A.7)}$$

The heat generated in half the wire is $\pi R^2 LG$, which means that 76% of the generated heat is lost through the ends. As illustrated in Figure B, the analytical solution discussed in Appendix A provides an excellent match to experimentally measured temperature in the creep test using ETMT system [189]. The fitting parameters are listed in Table A.1.

Table A.1. The fitting parameters for the analytical solution.

Parameters	T_0 (K)	L(m)	R(m)	m (m^{-1})	k (W/(m·K)	h (W/(m^2 ·K)	G (J/($s \cdot m^3$)
Value	293.15	1×10^{-2}	7.6×10^{-4}	0.19	9.8	1.3×10^{-4}	73.4

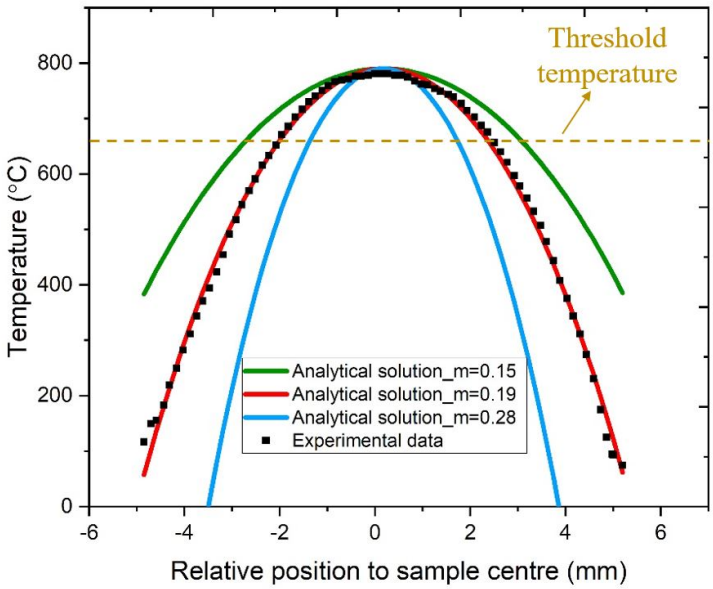


Figure B. The temperature profile along the sample obtained from experimental measurement during a creep test [189] and the best fit of the analytical solution is presented here.

As illustrated in Figure B using multiple curves, the key parameter m defines the steepness of the temperature profile variation in the middle of the sample. Parameter m depends on the sample geometry, namely, its effective wire radius R, and the sample thermal properties: conductivity k and the heat transfer coefficient between the sample and environment, h. Since parameter m does not depend on the maximum temperature of the experiment, nor the heat generation parameter G, the temperature variation curves for different experiments using identical samples can be obtained from the best fit 'master' curve shown above by scaling the temperature range.

References

[1] Ulutan, D. and Ozel, T., 2011. Machining induced surface integrity in titanium and nickel alloys: A review. *International Journal of Machine Tools and Manufacture*, 51(3), pp.250-280.

[2] Witek, L., 2009. Experimental crack propagation and failure analysis of the first stage compressor blade subjected to vibration. *Engineering Failure Analysis*, 16(7), pp.2163-2170.

[3] Evans, H.E. and Taylor, M.P., 2006. Oxidation of high-temperature coatings. Proceedings of the Institution of Mechanical Engineers, Part G: *Journal of Aerospace Engineering*, 220(1), pp.1-10.

[4] Bouchaud, B., Balmain, J. and Pedraza, F., 2008. Cyclic and isothermal oxidation at 1,100 C of a CVD aluminized directionally solidified Ni superalloy. *Oxidation of Metals*, 69(3-4), pp.193-210.

[5] Giamei, A.F., 2013. Development of single crystal superalloys: a brief history. *Adv. Mater. Process*, 171(9), pp.26-30.

[6] Raj, R. and Ashby, M.F., 1971. On grain boundary sliding and diffusional creep. *Metallurgical transactions*, 2(4), pp.1113-1127.

[7] Dai, H.J., Gebelin, J.C., Newell, M., Reed, R.C., D'Souza, N., Brown, P.D. and Dong, H.B., 2008. Grain selection during solidification in spiral grain selector. *Superalloys*, 2008, 367.

[8] Pelleg, J., 2012. Mechanical properties of materials (Vol. 190). Springer Science & Business Media.

[9] Courtney, T.H., 2005. Mechanical behavior of materials. Waveland Press.

[10] Kelly, A. (Anthony) & Nicholson, R.B & ScienceDirect (Online service) 1963, Precipitation hardening, Pergamon Press, Oxford.

[11] Callister, W.D. and Rethwisch, D.G., 2007. Materials science and engineering: an introduction (Vol. 7, pp. 665-715). New York: John wiley & sons.

[12] Totalmateria.com. (2019). Creep and Stress Rupture Properties: Total Materia Article. [online] Available at: https://www.totalmateria.com/page.aspx?ID=CheckArticle&site=kts&NM=296 [Accessed 15 Jul. 2019].

[13] Epishin, A., Link, T., Klingelhöffer, H., Fedelich, B. and Portella, P., 2010. Creep damage of single-crystal nickel base superalloys: mechanisms and effect on low cycle fatigue. *Materials at high temperatures*, 27(1), pp.53-59.

[14] Cui, L., Yu, J., Liu, J., Jin, T. and Sun, X., 2018. The creep deformation mechanisms of a newly designed nickel-base superalloy. *Materials Science and Engineering: A*, 710, pp.309-317.

[15] Larson, F.R. and Miller, J. (1952) Time-temperature relationship for rupture and creep stresses. *Transactions of ASME*, 74, pp.765-771.

[16] Withers, P.J. and Bhadeshia, H.K.D.H., 2001. Residual stress. Part 2–Nature and origins. *Materials science and technology*, 17(4), pp.366-375.

[17] Prime, M.B. and DeWald, A.T., 2013. The contour method. Practical residual stress measurement methods, pp.109-138.

[18] Macherauch E. , 1984. Residual Stresses. In: Sih G.C., Sommer E., Dahl W. (eds) Application of Fracture Mechanics to Materials and Structures. Springer, Dordrech

[19] Korsunsky, A.M., Sebastiani, M. and Bemporad, E., 2010. Residual stress evaluation at the micrometer scale: Analysis of thin coatings by FIB milling and digital image correlation. *Surface and Coatings Technology*, 205(7), pp.2393-2403.

[20] Stan, C.V., Beavers, C.M., Kunz, M. and Tamura, N., 2018. X-ray diffraction under extreme conditions at the Advanced Light Source. *Quantum Beam Science*, 2(1), p.4.

[21] Source, D., 2022. Powder Diffraction for industry | Diamond Light Source - - Diamond Light Source. [online] Diamond.ac.uk. Available at: <https://www.diamond.ac.uk/industry/Industry-News/Latest-News/Synchrotron-Industry-News-Powder-Diffraction.html> [Accessed 29 June 2022].

[22] Basham, M., Filik, J., Wharmby, M.T., Chang, P.C., El Kassaby, B., Gerring, M., Aishima, J., Levik, K., Pulford, B.C., Sikharulidze, I. and Sneddon, D., 2015. Data analysis workbench (DAWN). *Journal of synchrotron radiation*, 22(3), pp.853-858.

[23] Salvati, E. (2019). Residual Stress Evaluation and Modelling at the Micron Scale. PhD dissertation. University of Oxford.

[24] Salvati, E., Romano-Brandt, L., Mughal, M.Z., Sebastiani, M. and Korsunsky, A.M., 2019. Generalised residual stress depth profiling at the nanoscale using focused ion beam milling. *Journal of the Mechanics and Physics of Solids*, 125, pp.488-501.

[25] Sebastiani, M., Eberl, C., Bemporad, E. and Pharr, G.M., 2011. Depth-resolved residual stress analysis of thin coatings by a new FIB–DIC method. *Materials Science and Engineering: A*, 528(27), pp.7901-7908.

[26] Krottenthaler, M., Schmid, C., Schaufler, J., Durst, K. and Göken, M., 2013. A simple method for residual stress measurements in thin films by means of focused ion beam milling and digital image correlation. *Surface and Coatings Technology*, 215, pp.247-252.

[27] Zhu, R., Xie, H., Dai, X., Zhu, J. and Jin, A., 2014. Residual stress measurement in thin films using a slitting method with geometric phase analysis under a dual beam (FIB/SEM) system. *Measurement Science and Technology*, 25(9), p.095003.

[28] Winiarski, B., Benedetti, M., Fontanari, V., Allahkarami, M., Hanan, J.C. and Withers, P.J., 2016. High spatial resolution evaluation of residual stresses in shot peened specimens containing sharp and blunt notches by micro-hole drilling, micro-slot cutting and micro-x-ray diffraction methods. *Experimental Mechanics,* 56(8), pp.1449-1463.

[29] Korsunsky, A.M., Sebastiani, M. and Bemporad, E., 2009. Focused ion beam ring drilling for residual stress evaluation. *Materials Letters*, 63(22), pp.1961-1963.

[30] Lunt, A.J. and Korsunsky, A.M., 2015. A review of micro-scale focused ion beam milling and digital image correlation analysis for residual stress evaluation and error estimation. *Surface and Coatings Technology*, 283, pp.373-388.

[31] Lunt, A.J., Baimpas, N., Salvati, E., Dolbnya, I.P., Sui, T., Ying, S., Zhang, H., Kleppe, A.K., Dluhoš, J. and Korsunsky, A.M., 2015. A state-of-the-art review of micron-scale spatially resolved residual stress analysis by FIB-DIC ring-core milling and other techniques. The Journal of Strain Analysis for Engineering Design, 50(7), pp.426-444.

[32] Everaerts, J., Song, X., Nagarajan, B. and Korsunsky, A.M., 2018. Evaluation of macro-and microscopic residual stresses in laser shock-peened titanium alloy by FIB-DIC ring-core milling with different core diameters. *Surface and Coatings Technology*, 349, pp.719-724.

[33] Korsunsky, A.M., Salvati, E., Lunt, A.G.J., Sui, T., Mughal, M.Z., Daniel, R., Keckes, J., Bemporad, E. and Sebastiani, M., 2018. Nanoscale residual stress depth profiling by Focused Ion Beam milling and eigenstrain analysis. *Materials & Design*, 145, pp.55-64.

[34] Peirce, D., Asaro, R. J., & Needleman, A. (1982). An analysis of nonuniform and localized deformation in ductile single crystals. *Acta Metallurgica*, 30(6), 1087–1119.

[35] Peirce, D., Asaro, R. J., & Needleman, A. (1983). Material rate dependence and localized deformation in crystalline solids. *Acta Metallurgica*, 31(12), 1951–1976.

[36] Sarma, G. B., & Dawson, P. R. (1996). Effects of interactions among crystals on the inhomogeneous deformations of polycrystals. *Acta Materialia*, 44(5), 1937–1953.

[37] Sarma, G. B., & Dawson, P. R. (1996). Texture predictions using a polycrystal plasticity model incorporating neighbor interactions. *International Journal of Plasticity*, 12(8), 1023–1054.

[38] Anand, L., & Gurtin, M. E. (2003). Thermal effects in the superelasticity of crystalline shape-memory materials. *Journal of the Mechanics and Physics of Solids*, 51(6), 1015–1058.

[39] Barbe, F., Forest, S., Quilici, S., & Cailletaud, G. (2003). Numerical study of crystalline plasticity: measurements of the heterogeneities due to grain under small strains. *Revue de Métallurgie*, 100(9), 815-823.

[40] Diard, O., Leclercq, S., Rousselier, G., & Cailletaud, G. (2005). Evaluation of finite element based analysis of 3D multicrystalline aggregates plasticity Application to crystal plasticity model identification and the study of stress and strain fields near grain boundaries. *International Journal of Plasticity*, 21(4), 691–722.

[41] Hill, R. (1965). Continuum micro-mechanics of elastoplastic polycrystals. *Journal of the Mechanics and Physics of Solids*, 13(2), 89–101.

[42] Eshelby, J.D. (1957). The determination of the elastic field of an ellipsoidal inclusion, and related problems. *Proceedings of the royal society of London. Series A. Mathematical and physical sciences*, 241(1226), 376-396.

[43] Hutchinson J.W. (1970). Elastic- plastic behavior of polycrystalline metals and composites. *Proceedings of the Royal Society A: Mathematical, Physical and Engineering Sciences*, 319(1537), 247–272.

[44] Gloaguen, D., & François, M. (2006). Prediction of intragranular strains in metallic polycrystals with a two-level homogenisation approach: Influence of dislocation microstructure on the mechanical behaviour. *Physica Status Solidi (A) Applications and Materials Science*, 203(8), 1940–1953.

[45] Gloaguen, D., Berchi, T., Girard, E., & Guillén, R. (2007). Measurement and prediction of residual stresses and crystallographic texture development in rolled Zircaloy-4 plates: X-ray diffraction and the self-consistent model. *Acta Materialia*, 55(13), 4369–4379.

[46] Manonukul, A., & Dunne, F. P. E. (2004). High- and low-cycle fatigue crack initiation using polycrystal plasticity. *Proceedings of the Royal Society A: Mathematical, Physical and Engineering Sciences*, 460(2047), 1881–1903.

[47] Dini, D., Korsunsky, A. M., & Dunne, F. P. (2006). Diffraction post-processor for polycrystalline plasticity modelling. *Materials science forum*, 524, 427-432.

[48] Sinha V, Mills MJ, Williams JC, Spowart JE. Observations on the faceted initiation site in the dwell-fatigue tested Ti-6242 alloy: crystallographic orientation and size effects. *Metallurgical and Materials Transactions A*. 2006 May 1;37(5):1507-18.

[49] Nasri, M.A., Robert, C., Ammar, A., El Arem, S. and Morel, F., 2018. Proper Generalized Decomposition (PGD) for the numerical simulation of polycrystalline aggregates under cyclic loading. *Comptes Rendus Mécanique*, 346(2), pp.132-151.

[50] Farooq, H., Cailletaud, G., Forest, S., & Ryckelynck, D. (2020).Crystal plasticity modeling of the cyclic behavior of polycrystalline aggregates under non-symmetric uniaxial loading: Global and local analyses. *International Journal of Plasticity*, 126, 102619.

[51] Drugan, W. J., & Willis, J. R. (1996). A micromechanics-based nonlocal constitutive equation and estimates of representative volume element size for elastic composites. *Journal of the Mechanics and Physics of Solids*, *44*(4), 497–524.

[52] Kanit, T., Forest, S., Galliet, I., Mounoury, V., & Jeulin, D. (2003). Determination of the size of the representative volume element for random composites: Statistical and numerical approach. *International Journal of Solids and Structures*, 40(13–14), 3647–3679.

[53] Trias, D., Costa, J., Turon, A., & Hurtado, J. E. (2006). Determination of the critical size of a statistical representative volume element (SRVE) for carbon reinforced polymers. *Acta Materialia*, 54(13), 3471–3484.

[54] Gitman, I. M., Askes, H., & Sluys, L. J. (2007). Representative volume: Existence and size determination. *Engineering Fracture Mechanics*, 74(16), 2518–2534.

[55] Lim, H., Battaile, C. C., Bishop, J. E., & Foulk III, J. W. (2019). Investigating mesh sensitivity and polycrystalline RVEs in crystal plasticity finite element simulations. *International Journal of Plasticity*, 121, 101-115.

[56] Bilger, N., Auslender, F., Bornert, M., Michel, J. C., Moulinec, H., Suquet, P., & Zaoui, A. (2005). Effect of a nonuniform distribution of voids on the plastic response of voided materials: A computational and statistical analysis. *International Journal of Solids and Structures*, 42(2), 517–538.

[57] Dautriat, J., Bornert, M., Gland, N., Dimanov, A., & Raphanel, J. (2011). Localized deformation induced by heterogeneities in porous carbonate analysed by multi-scale digital image correlation. *Tectonophysics*, 503(1–2), 100–116.

[58] Jiang, J., Britton, T. B., & Wilkinson, A. J. (2013). Evolution of dislocation density distributions in copper during tensile deformation. *Acta Materialia*, 61(19), 7227-7239.

[59] Shimokawa, T., Oguro, T., Tanaka, M., Higashida, K., & Ohashi, T. (2014). A multiscale approach for the deformation mechanism in pearlite microstructure: Atomistic study of the role of the heterointerface on ductility. *Materials Science and Engineering: A*, 598, 68-76.

[60] Wang, Z., Chen, J., Besnard, C., Kuncicka, L., Kocich, R., & Korsunsky, A. M. (2020b). In situ neutron diffraction investigation of texture-dependent Shape Memory Effect in a near equiatomic NiTi alloy. *Acta Materialia*, 202, 135–148.

[61] Abd El-Aty, A., Xu, Y., Ha, S., & Zhang, S. H. (2018). Computational homogenization of tensile deformation behaviors of a third generation Al-Li alloy 2060-T8 using crystal plasticity finite element method. *Materials Science and Engineering: A*, 731, 583-594.

[62] Stopka, K. S., Gu, T., & McDowell, D. L. (2020). Effects of algorithmic simulation parameters on the prediction of extreme value fatigue indicator parameters in duplex Ti-6Al-4V. *International Journal of Fatigue*, 141, 105865.

[63] Li, Y., Wu, G., & Wang, G. (2020). Micro-plastic fatigue damage mechanism governing shape instability behavior. *International Journal of Fatigue*, 131, 105386.

[64] Min, K. M., Jeong, W., Hong, S. H., Lee, C. A., Cha, P. R., Han, H. N., & Lee, M. G. (2020). Integrated crystal plasticity and phase field model for prediction of recrystallization texture and anisotropic mechanical properties of cold-rolled ultra-low carbon steels. *International Journal of Plasticity*, 127, 102644.

[65] Moghaddam, M. G., Achuthan, A., Bednarcyk, B. A., Arnold, S. M., & Pineda, E. J. (2017). Grain size-dependent crystal plasticity constitutive model for polycrystal materials. *Materials Science and Engineering: A*, 703, 521-532.

[66] Zhang, K., Holmedal, B., Hopperstad, O. S., Dumoulin, S., Gawad, J., Van Bael, A., & Van Houtte, P. (2015). Multi-level modelling of mechanical anisotropy of commercial pure aluminium plate: crystal plasticity models, advanced yield functions and parameter identification. *International Journal of Plasticity*, 66, 3-30.

[67] Alleman, C. N., Foulk, J. W., Mota, A., Lim, H., & Littlewood, D. J. (2018). Concurrent multiscale modeling of microstructural effects on localization behavior in finite deformation solid mechanics. *Computational Mechanics*, 61(1), 207-218.

[68] Esmaeilpour, R., Kim, H., Park, T., Pourboghrat, F., Xu, Z., Mohammed, B., & Abu-Farha, F. (2018). Calibration of Barlat Yld2004-18P yield function using CPFEM and 3D RVE for

the simulation of single point incremental forming (SPIF) of 7075-O aluminum sheet. *International Journal of Mechanical Sciences*, 145, 24-41.

[69] Zhang, K., Holmedal, B., Manik, T., & Saai, A. (2019). Assessment of advanced Taylor models, the Taylor factor and yield-surface exponent for FCC metals. *International Journal of Plasticity*, 114, 144-160.

[70] Groeber, M. A., & Jackson, M. A. (2014). DREAM. 3D: a digital representation environment for the analysis of microstructure in 3D. *Integrating materials and manufacturing innovation*, 3(1), 56-72.

[71] Omairey, S. L., Dunning, P. D., & Sriramula, S. (2019). Development of an ABAQUS plugin tool for periodic RVE homogenisation. *Engineering with Computers*, 35(2), 567-577.

[72] Jaladurgam, N. R., Li, H., Kelleher, J., Persson, C., Steuwer, A., & Colliander, M. H. (2020). Microstructure-dependent deformation behaviour of a low γ′ volume fraction Ni-base superalloy studied by in-situ neutron diffraction. *Acta Materialia*, 183, 182–195.

[73] Quested, T. E., & Greer, A. L. (2004). The effect of the size distribution of inoculant particles on as-cast grain size in aluminium alloys. *Acta Materialia*, 52(13), 3859–3868.

[74] Berbenni, S., Favier, V., & Berveiller, M. (2007a). Impact of the grain size distribution on the yield stress of heterogeneous materials. *International Journal of Plasticity*, 23(1), 114–142.

[75] Tucker, J. C., Chan, L. H., Rohrer, G. S., Groeber, M. A., & Rollett, A. D. (2012). Tail departure of log-normal grain size distributions in synthetic three-dimensional microstructures. *Metallurgical and Materials Transactions A*, 43(8), 2810-2822.

[76] Xue, R., Wang, X., Yang, Q., Xu, D., Sun, Y., Zhang, J., & Krishnaswamy, S. (2021). Grain size distribution characterization of aluminum with a particle swarm optimization neural network using laser ultrasonics. *Applied Acoustics*, 180, 108125.

[77] Berbenni, S., Favier, V., & Berveiller, M. (2007b). Micro-macro modelling of the effects of the grain size distribution on the plastic flow stress of heterogeneous materials. *Computational Materials Science*, 39(1), 96–105.

[78] Kapetanou, O., Weygand, D., & Zaiser, M. (2015). Stress and strain fluctuations in plastic deformation of crystals with disordered microstructure. *Journal of Statistical Mechanics: Theory and Experiment*, 2015(8), P08009.

[79] Tang, A., Liu, H., Liu, G., Zhong, Y., Wang, L., Lu, Q., Wang, J., & Shen, Y. (2020). Lognormal Distribution of Local Strain: A Universal Law of Plastic Deformation in Material. *Physical Review Letters*, 124(15), 1–6.

[80] Groma, I. and Bakó, B., 1998. Probability distribution of internal stresses in parallel straight dislocation systems. *Physical Review B*, 58(6), p.2969.

[81] Dunne, F. P. E., & Rugg, D. (2008). On the mechanisms of fatigue facet nucleation in titanium alloys. *Fatigue & Fracture of Engineering Materials & Structures*, 31(11), 949-958.

[82] Chen, B., Jiang, J., & Dunne, F. P. (2018). Is stored energy density the primary meso-scale mechanistic driver for fatigue crack nucleation? *International Journal of Plasticity*, 101, 213-229.

[83] Dunne, F.P.E., Wilkinson, A.J. and Allen, R., 2007. Experimental and computational studies of low cycle fatigue crack nucleation in a polycrystal. *International Journal of Plasticity*, 23(2), pp.273-295.

[84] Skelton, R. P., Vilhelmsen, T., & Webster, G. A. (1998). Energy criteria and cumulative damage during fatigue crack growth. *International journal of fatigue*, 20(9), 641-649.

[85] Yuan, G. J., Zhang, X. C., Chen, B., Tu, S. T., & Zhang, C. C. (2020). Low-cycle fatigue life prediction of a polycrystalline nickel-base superalloy using crystal plasticity modelling approach. *Journal of Materials Science & Technology*, 38, 28-38.

[86] Roters, F., Eisenlohr, P., Hantcherli, L., Tjahjanto, D.D., Bieler, T.R. and Raabe, D., 2010. Overview of constitutive laws, kinematics, homogenization and multiscale methods in crystal plasticity finite-element modeling: Theory, experiments, applications. *Acta materialia*, 58(4), pp.1152-1211.

[87] Kanjarla, A.K., Van Houtte, P. and Delannay, L., 2010. Assessment of plastic heterogeneity in grain interaction models using crystal plasticity finite element method. *International Journal of Plasticity*, 26(8), pp.1220-1233.

[88] Choi, S.H., Kim, D.H., Park, S.S. and You, B.S., 2010. Simulation of stress concentration in Mg alloys using the crystal plasticity finite element method. *Acta Materialia*, 58(1), pp.320-329.

[89] Prakash, A., Weygand, S.M. and Riedel, H., 2009. Modeling the evolution of texture and grain shape in Mg alloy AZ31 using the crystal plasticity finite element method. *Computational Materials Science*, 45(3), pp.744-750.

[90] Hama, T. and Takuda, H., 2011. Crystal-plasticity finite-element analysis of inelastic behavior during unloading in a magnesium alloy sheet. *International Journal of Plasticity*, 27(7), pp.1072-1092.

[91] Choi, S.H., Kim, D.W., Seong, B.S. and Rollett, A.D., 2011. 3-D simulation of spatial stress distribution in an AZ31 Mg alloy sheet under in-plane compression. *International Journal of Plasticity*, 27(10), pp.1702-1720.

[92] Delaire, F., Raphanel, J.L. and Rey, C., 2000. Plastic heterogeneities of a copper multicrystal deformed in uniaxial tension: experimental study and finite element simulations. *Acta Materialia*, 48(5), pp.1075-1087.

[93] Erieau, P. and Rey, C., 2004. Modeling of deformation and rotation bands and of deformation induced grain boundaries in IF steel aggregate during large plane strain compression. *International Journal of Plasticity*, 20(10), pp.1763-1788.

[94] Raabe, D. and Roters, F., 2004. Using texture components in crystal plasticity finite element simulations. *International Journal of Plasticity*, 20(3), pp.339-361.

[95] Raabe, D., Wang, Y. and Roters, F., 2005. Crystal plasticity simulation study on the influence of texture on earing in steel. *Computational Materials Science*, 34(3), pp.221-234.

[96] Zhao, Z., Ramesh, M., Raabe, D., Cuitino, A.M. and Radovitzky, R., 2008. Investigation of three-dimensional aspects of grain-scale plastic surface deformation of an aluminum oligocrystal. *International Journal of Plasticity*, 24(12), pp.2278-2297.

[97] St-Pierre, L., Héripré, E., Dexet, M., Crépin, J., Bertolino, G. and Bilger, N., 2008. 3D simulations of microstructure and comparison with experimental microstructure coming from OIM analysis. *International Journal of Plasticity*, 24(9), pp.1516-1532.

[98] Kalidindi, S.R., Bronkhorst, C.A. and Anand, L., 1992. Crystallographic texture evolution in bulk deformation processing of FCC metals. *Journal of the Mechanics and Physics of Solids*, 40(3), pp.537-569.

[99] Choi, S.H., Kim, D.H., Lee, H.W. and Shin, E.J., 2010. Simulation of texture evolution and macroscopic properties in Mg alloys using the crystal plasticity finite element method. *Materials Science and Engineering: A*, 527(4-5), pp.1151-1159.

[100] Lee, M.G., Kim, S.J. and Han, H.N., 2010. Crystal plasticity finite element modeling of mechanically induced martensitic transformation (MIMT) in metastable austenite. *International journal of plasticity*, 26(5), pp.688-710.

[101] Lee, M.G., Wang, J. and Anderson, P.M., 2007. Texture evolution maps for upset deformation of body-centered cubic metals. *Materials Science and Engineering: A*, 463(1-2), pp.263-270.

[102] Sinha, S. and Ghosh, S., 2006. Modeling cyclic ratcheting based fatigue life of HSLA steels using crystal plasticity FEM simulations and experiments. *International Journal of Fatigue*, 28(12), pp.1690-1704.

[103] Zhang, J. and Ding, S., 2020. Mesoscale simulation research on the homogenized elasto-plastic behavior of FeCrAl alloys. *Materials Today Communications*, 22, p.100718.

[104] Phan, V.T., Nguyen, T.D., Bui, Q.H. and Dirras, G., 2015. Modelling of microstructural effects on the mechanical behavior of ultrafine-grained Nickel using crystal plasticity finite element model. *International Journal of Engineering Science*, 94, pp.212-225.

[105] Kim, D.K., Kim, J.M., Park, W.W., Lee, H.W., Im, Y.T. and Lee, Y.S., 2015. Three-dimensional crystal plasticity finite element analysis of microstructure and texture evolution during channel die compression of IF steel. *Computational Materials Science*, 100, pp.52-60.

[106] Liu, J., Huang, M., Li, Z., Zhao, L. and Zhu, Y., 2021. Microvoid growth mechanism in FCC polycrystals and a statistical damage model. *International Journal of Plasticity*, 137, p.102888.

[107] Quey, R., Dawson, P.R. and Barbe, F., 2011. Large-scale 3D random polycrystals for the finite element method: Generation, meshing and remeshing. *Computer Methods in Applied Mechanics and Engineering*, 200(17-20), pp.1729-1745.

[108] Musienko, A., Tatschl, A., Schmidegg, K., Kolednik, O., Pippan, R. and Cailletaud, G., 2007. Three-dimensional finite element simulation of a polycrystalline copper specimen. *Acta materialia*, 55(12), pp.4121-4136.

[109] Kamaya, M., Kawamura, Y. and Kitamura, T., 2007. Three-dimensional local stress analysis on grain boundaries in polycrystalline material. *International Journal of Solids and Structures*, 44(10), pp.3267-3277.

[110] Tanaka, M., Yoshimi, Y., Higashida, K., Shimokawa, T. and Ohashi, T., 2014. A multiscale approach for the deformation mechanism in pearlite microstructure: Experimental measurements of strain distribution using a novel technique of precision markers. *Materials Science and Engineering: A*, 590, pp.37-43.

[111] Korsunsky, A.M., Kim, K. and Botvina, L.R., 2004. An analysis of defect size evolution. *International journal of fracture*, 128(1), pp.139-145.

[112] GraphPad, Origin of the Gaussian distribution. https://www.graphpad.com/guides/prism/7/statistics/origin_of_the_gaussian_distribution.htm, 2020 (accessed 6 October 2020).

[113] Oddershede, J., Schmidt, S., Poulsen, H.F., Margulies, L., Wright, J., Moscicki, M., Reimers, W. and Winther, G., 2011. Grain-resolved elastic strains in deformed copper measured by three-dimensional X-ray diffraction. *Materials characterization*, 62(7), pp.651-660.

[114] Ramberg, W. and Osgood, W.R., 1943. Description of stress-strain curves by three parameters (No. NACA-TN-902).

[115] Hill, H.N., 1944. Determination of stress-strain relations from" offset" yield strength values. Aluminum Co of America Pittsburgh Pa.

[116] Fernando, D., Teng, J.G., Quach, W.M. and De Waal, L., 2020. Full-range stress-strain model for stainless steel alloys. *Journal of Constructional Steel Research*, 173, p.106266.

[117] Macdonald, M., Rhodes, J. and Taylor, G.T., 2000. Mechanical properties of stainless steel lipped channels.

[118] Mirambell, E. and Real, E., 2000. On the calculation of deflections in structural stainless steel beams: an experimental and numerical investigation. *Journal of Constructional Steel Research*, 54(1), pp.109-133.

[119] Mirambell, E. and Real, E., 2000. On the calculation of deflections in structural stainless steel beams: an experimental and numerical investigation. *Journal of Constructional Steel Research*, 54(1), pp.109-133.

[120] Quach, W.M., Teng, J.G. and Chung, K.F., 2008. Three-stage full-range stress-strain model for stainless steels. *Journal of Structural Engineering*, 134(9), pp.1518-1527.

[121] Hradil, P., Talja, A., Real, E., Mirambell, E. and Rossi, B., 2013. Generalized multistage mechanical model for nonlinear metallic materials. *Thin-walled structures*, 63, pp.63-69.

[122] Dundu, M., 2018. Evolution of stress–strain models of stainless steel in structural engineering applications. *Construction and Building Materials*, 165, pp.413-423.

[123] Everaerts, J., Papadaki, C., Li, W. and Korsunsky, A.M., 2019. Evaluation of single crystal elastic stiffness coefficients of a nickel-based superalloy by electron backscatter diffraction and nanoindentation. *Journal of the Mechanics and Physics of Solids*, 131, pp.303-312.

[124] Ying, S., Ma, L., Sui, T., Papadaki, C., Salvati, E., Romano Brandt, L., Zhang, H. and Korsunsky, A.M., 2018. Nanoscale origins of the size effect in the compression response of single crystal Ni-base superalloy micro-pillars. *Materials*, 11(4), p.561.

[125] Korsunsky, A., 2017. A teaching essay on residual stresses and eigenstrains. Butterworth-Heinemann.

[126] Vacchieri, E., Holdsworth, S.R., Costa, A., Poggio, E., Riva, A. and Villari, P., 2014. Creep–fatigue interaction in two gas turbine Ni based superalloys subjected to service-like conditions. *Materials at High Temperatures,* 31(4), pp.348-356.

[127] Al-Jarba, K.A. and Fuchs, G.E., 2004. Effect of carbon additions on the as-cast microstructure and defect formation of a single crystal Ni-based superalloy. *Materials Science and Engineering: A*, 373(1-2), pp.255-267.

[128] Furtado, H.C. and May, I.L., 2004. High temperature degradation in power plants and refineries. *Materials research*, 7, pp.103-110.

[129] Radaj, D., 2012. Heat effects of welding: temperature field, residual stress, distortion. Springer Science & Business Media.

[130] Woo, W., Em, V., Hubbard, C.R., Lee, H.J. and Park, K.S., 2011. Residual stress determination in a dissimilar weld overlay pipe by neutron diffraction. *Materials Science and Engineering: A*, 528(27), pp.8021-8027.

[131] Abadias, G., Chason, E., Keckes, J., Sebastiani, M., Thompson, G.B., Barthel, E., Doll, G.L., Murray, C.E., Stoessel, C.H. and Martinu, L., 2018. Stress in thin films and coatings: Current status, challenges, and prospects. *Journal of Vacuum Science & Technology A: Vacuum, Surfaces, and Films*, 36(2), p.020801.

[132] Guo, Y., Abdolvand, H., Britton, T.B. and Wilkinson, A.J., 2017. Growth of {112 2} twins in titanium: A combined experimental and modelling investigation of the local state of deformation. *Acta Materialia*, 126, pp.221-235.

[133] Kartal, M.E., Kiwanuka, R. and Dunne, F.P.E., 2015. Determination of sub-surface stresses at inclusions in single crystal superalloy using HR-EBSD, crystal plasticity and inverse eigenstrain analysis. *International Journal of Solids and Structures*, 67, pp.27-39.

[134] Jiang, J., Britton, T.B. and Wilkinson, A.J., 2015. The orientation and strain dependence of dislocation structure evolution in monotonically deformed polycrystalline copper. *International Journal of Plasticity*, 69, pp.102-117.

[135] Wan, V.V.C., Cuddihy, M.A., Jiang, J., MacLachlan, D.W. and Dunne, F.P.E., 2016. An HR-EBSD and computational crystal plasticity investigation of microstructural stress distributions and fatigue hotspots in polycrystalline copper. *Acta Materialia*, 115, pp.45-57.

[136] Belnoue, J.P., Jun, T.S., Hofmann, F., Abbey, B. and Korsunsky, A.M., 2010. Evaluation of the overload effect on fatigue crack growth with the help of synchrotron XRD strain mapping. *Engineering Fracture Mechanics*, 77(16), pp.3216-3226.

[137] Everaerts, J., Salvati, E., Uzun, F., Brandt, L.R., Zhang, H. and Korsunsky, A.M., 2018. Separating macro-(Type I) and micro-(Type II+ III) residual stresses by ring-core FIB-DIC milling and eigenstrain modelling of a plastically bent titanium alloy bar. *Acta Materialia*, 156, pp.43-51.

[138] Frasier, D.J., Whetstone, J.R., Harris, K., Erickson, G.L. and Schwer, R.E., 1990. Process and alloy optimization for CMSX-4 superalloy single crystal airfoils. *High temperature materials for power engineering*, pp.1281-1300.

[139] Sengupta, A., Putatunda, S.K., Bartosiewicz, L., Hangas, J., Nailos, P.J., Peputapeck, M. and Alberts, F.E., 1994. Tensile behavior of a new single-crystal nickel-based superalloy (CMSX-4) at room and elevated temperatures. *Journal of materials engineering and performance*, 3(1), pp.73-81.

[140] Baicheng, Z., Xiaohua, L., Jiaming, B., Junfeng, G., Pan, W., Chen-nan, S., Muiling, N., Guojun, Q. and Jun, W., 2017. Study of selective laser melting (SLM) Inconel 718 part surface improvement by electrochemical polishing. *Materials & Design*, 116, pp.531-537.

[141] Everaerts, J., Salvati, E. and Korsunsky, A.M., 2019. Nanoscale depth profiling of residual stresses due to fine surface finishing. *Advanced Materials Interfaces*, 6(21), p.1900947.

[142] Salvati, E., O'connor, S., Sui, T., Nowell, D. and Korsunsky, A.M., 2016. A study of overload effect on fatigue crack propagation using EBSD, FIB–DIC and FEM methods. *Engineering Fracture Mechanics*, 167, pp.210-223.

[143] Salvati, E., Sui, T. and Korsunsky, A.M., 2016. Uncertainty quantification of residual stress evaluation by the FIB–DIC ring-core method due to elastic anisotropy effects. *International Journal of Solids and Structures*, 87, pp.61-69.

[144] Salvati, E. and Korsunsky, A.M., 2020. Micro-scale measurement & FEM modelling of residual stresses in AA6082-T6 Al alloy generated by wire EDM cutting. *Journal of Materials Processing Technology*, 275, p.116373.

[145] Lu, M. and Kou, S., 1988. Power and current distributions in gas tungsten arcs. Weld. J.(Miami);(United States), 67(2).

[146] Mousavi, S.A. and Miresmaeili, R., 2008. Experimental and numerical analyses of residual stress distributions in TIG welding process for 304L stainless steel. *Journal of materials processing technology*, 208(1-3), pp.383-394.

[147] ABAQUS, V. (2007). ABAQUS standard user's manual: Version 6.7.

[148] Siebörger, D., Knake, H. and Glatzel, U., 2001. Temperature dependence of the elastic moduli of the nickel-base superalloy CMSX-4 and its isolated phases. *Materials Science and Engineering: A*, 298(1-2), pp.26-33.

[149] Hightechalloys.de. Elgiloy® The Co-Cr-Ni Alloy. [online] Available at: http://hightechalloys.de/pdf/Elgiloy_Flyer.pdf. [Accessed 4 July. 2019].

[150] Matweb.com. Elgiloy® Co-Cr-Ni Alloy, Wire. [online] Available at: http://www.matweb.com/search/datasheet.aspx?MatGUID=9bd90091755740648e2afa5cdb9fb09b. [Accessed 4 July. 2019].

[151] Webster, G.A. and Ezeilo, A.N., 2001. Residual stress distributions and their influence on fatigue lifetimes. *International Journal of Fatigue*, 23, pp.375-383.

[152] James, M.N., Hughes, D.J., Chen, Z., Lombard, H., Hattingh, D.G., Asquith, D., Yates, J.R. and Webster, P.J., 2007. Residual stresses and fatigue performance. *Engineering Failure Analysis*, 14(2), pp.384-395.

[153] Chen, J., Salvati, E., Uzun, F., Papadaki, C., Wang, Z., Everaerts, J. and Korsunsky, A.M., 2020. An experimental and numerical analysis of residual stresses in a TIG weldment of a single crystal nickel-base superalloy. *Journal of Manufacturing Processes*, 53, pp.190-200.

[154] Le Graverend, J.B., Jacques, A., Cormier, J., Ferry, O., Schenk, T. and Mendez, J., 2015. Creep of a nickel-based single-crystal superalloy during very high-temperature jumps followed by synchrotron X-ray diffraction. *Acta Materialia*, 84, pp.65-79.

[155] Smith, T.M., Good, B.S., Gabb, T.P., Esser, B.D., Egan, A.J., Evans, L.J., McComb, D.W. and Mills, M.J., 2019. Effect of stacking fault segregation and local phase transformations on creep strength in Ni-base superalloys. *Acta Materialia*, 172, pp.55-65.

[156] Tian, C., Han, G., Cui, C. And Sun, X., 2014. Effects of stacking fault energy on the creep be-haviors of Ni-base superalloy. *Materials & Design*, 64, pp.316-323.

[157] Ma, A., Dye, D. And Reed, R.C., 2008. A model for the creep deformation behaviour of single-crystal superalloy CMSX-4. *Acta Materialia*, 56(8), pp.1657-1670.

[158] Yuan, Y., Kawagishi, K., Koizumi, Y., Kobayashi, T., Yokokawa, T. And Harada, H., 2014. Creep deformation of a sixth generation Ni-base single crystal superalloy at 800 C. *Materials Science and Engineering: A*, 608, pp.95-100.

[159] Smith, T.M., Unocic, R.R., Deutchman, H. And Mills, M.J., 2016. Creep deformation mechanism mapping in nickel base disk superalloys. *Materials at High Temperatures*, 33(4-5), pp.372-383.

[160] Qi, D., Wang, D., Du, K., Qi, Y., Lou, L., Zhang, J. And Ye, H., 2018. Creep deformation of a nickel-based single crystal superalloy under high stress at 1033 K. *Journal of Alloys and Compounds*, 735, pp.813-820.

[161] Zhu, Z., Basoalto, H., Warnken, N. And Reed, R.C., 2012. A model for the creep deformation behaviour of nickel-based single crystal superalloys. *Acta Materialia*, 60(12), pp.4888-4900.

[162] Wang, X.G., Liu, J.L., Jin, T., Sun, X.F., Zhou, Y.Z., Hu, Z.Q., Do, J.H., Choi, B.G., Kim, I.S. and Jo, C.Y., 2015. Creep deformation related to dislocations cutting the γ′ phase of a Ni-base single crystal superalloy. *Materials Science and Engineering: A*, 626, pp.406-414.

[163] Xu, K., Wang, G., Liu, J., Li, J., Liu, J., Wang, X., Yang, Y., Ye, L., Zhou, Y. And Sun, X., 2020. Creep behavior and a deformation mechanism based creep rate model under high temperature and low stress condition for single crystal superalloy DD5. *Materials Science and Engineering: A*, 786, p.139414.

[164] Chu, Z., Yu, J., Sun, X., Guan, H. And Hu, Z., 2009. High-temperature creep deformation and fracture behavior of a directionally solidified Ni-base superalloy DZ951. *Metallurgical and Materials Transactions A*, 40(12), pp.2927-2937.

[165] Unocic, R.R., Viswanathan, G.B., Sarosi, P.M., Karthikeyan, S., Li, J. And Mills, M.J., 2008. Mechanisms of creep deformation in polycrystalline Ni-base disk superalloys. *Materials Science and Engineering: A*, 483, pp.25-32.

[166] Unocic, R.R., Zhou, N., Kovarik, L., Shen, C., Wang, Y. And Mills, M.J., 2011. Dislocation decorrelation and relationship to deformation microtwins during creep of a γ′ precipitate strengthened Ni-based superalloy. *Acta Materialia*, 59(19), pp.7325-7339.

[167] Barba, D., Alabort, E., Pedrazzini, S., Collins, D.M., Wilkinson, A.J., Bagot, P.A.J., Moody, M.P., Atkinson, C., Jérusalem, A. And Reed, R.C., 2017. On the microtwinning mechanism in a single crystal superalloy. *Acta Materialia*, 135, pp.314-329.

[168] Viswanathan, G.B., Sarosi, P.M., Henry, M.F., Whitis, D.D., Milligan, W.W. and Mills, M.J., 2005. Investigation of creep deformation mechanisms at intermediate temperatures in René 88 DT. *Acta Materialia*, 53(10), pp.3041-3057.

[169] He, J., Zenk, C.H., Zhou, X., Neumeier, S., Raabe, D., Gault, B. And Makineni, S.K., 2020. On the atomic solute diffusional mechanisms during compressive creep deformation of a Co-Al-W-Ta single crystal superalloy. *Acta Materialia*, 184, pp.86-99.

[170] Wang, Z., Chen, J., Besnard, C. And Korsunsky, A.M., 2020. Microstructure evolution in a se-verely cold-worked niti wire during ageing treatment: an in situ neutron diffraction study. *Materials Letters*, 281, p.128676.

[171] Barhli, S.M., Saucedo-Mora, L., Jordan, M.S.L., Cinar, A.F., Reinhard, C., Mostafavi, M. And Marrow, T.J., 2017. Synchrotron X-ray characterization of crack strain fields in polygranular graphite. *Carbon*, 124, pp.357-371.

[172] Young, M.L., Gollerthan, S., Baruj, A., Frenzel, J., Schmahl, W.W. and Eggeler, G., 2013. Strain mapping of crack extension in pseudoelastic niti shape memory alloys during static loading. *Acta materialia*, 61(15), pp.5800-5806.

[173] Reed, R.; Crudden, D.; Raeisinia, B.; Hardy, M. European Patent Specification. Patent EP2894234B1, 19 October 2016.

[174] Toby, B.H. and Von Dreele, R.B., 2013. GSAS-II: the genesis of a modern open-source all pur-pose crystallography software package. *Journal of Applied Crystallography*, 46(2), pp.544-549.

[175] Toby, B.H., 2006. R factors in Rietveld analysis: How good is good enough?. Powder diffraction, 21(1), pp.67-70.

[176] Yadav, S.D., El-Tahawy, M., Kalácska, S., Dománková, M., Yubero, D.C. and Poletti, C., 2017. Characterizing dislocation configurations and their evolution during creep of a new 12% Cr steel. *Materials characterization*, 134, pp.387-397.

[177] Cao, Y., Di, H., Zhang, J., Zhang, J., Ma, T. And Misra, R.D.K., 2013. An electron backscattered diffraction study on the dynamic recrystallization behavior of a nickel–chromium alloy (800H) during hot deformation. *Materials Science and Engineering: A*, 585, pp.71-85.

[178] Dudova, N., Belyakov, A., Sakai, T. And Kaibyshev, R., 2010. Dynamic recrystallization mecha-nisms operating in a Ni–20% Cr alloy under hot-to-warm working. *Acta Materialia*, 58(10), pp.3624-3632.

[179] Chen, X.M., Lin, Y.C., Chen, M.S., Li, H.B., Wen, D.X., Zhang, J.L. and He, M., 2015. Micro-structural evolution of a nickel-based superalloy during hot deformation. *Materials & Design*, 77, pp.41-49.

[180] Decamps, B., Raujol, S., Coujou, A., Pettinari-Sturmel, F., Clement, N., Locq, D. and Caron, P., 2004. On the shearing mechanism of γ′ precipitates by a single (a/6)⟨ 112⟩ Shockley partial in Ni-based superalloys. *Philosophical Magazine*, 84(1), pp.91-107.

[181] Wu, E., Sun, G., Chen, B.O., Zhang, J., Ji, V., Klosek, V. And Mathon, M.H., 2014. Neutron dif-fraction study of strain/stress states and subgrain defects in a creep-deformed, single-crystal superalloy. *Metallurgical and Materials Transactions A*, 45(1), pp.139-146.

[182] Royer, A., Jacques, A., Bastie, P. And Veron, M., 2001. The evolution of the lattice parameter mismatch of nickel based superalloy: an in situ study during creep deformation. *Materials Science and Engineering: A*, 319, pp.800-804.

[183] Pyczak, F., Neumeier, S. and Göken, M., 2009. Influence of lattice misfit on the internal stress and strain states before and after creep investigated in nickel-base superalloys containing rhenium and ruthenium. *Materials Science and Engineering: A*, 510, pp.295-300.

[184] Williamson, G.K. and Smallman, R.E., 1956. III. Dislocation densities in some annealed and cold-worked metals from measurements on the X-ray debye-scherrer spectrum. *Philosophical magazine*, 1(1), pp.34-46.

[185] Zhao, Y.H., Liao, X.Z., Jin, Z., Valiev, R.Z. and Zhu, Y.T., 2004. Microstructures and mechanical properties of ultrafine grained 7075 Al alloy processed by ECAP and their evolutions during annealing. *Acta Materialia*, 52(15), pp.4589-4599.

[186] Zhao, Y.H., Horita, Z., Langdon, T.G. and Zhu, Y.T., 2008. Evolution of defect structures during cold rolling of ultrafine-grained Cu and Cu–Zn alloys: Influence of stacking fault energy. *Materials Science and Engineering: A*, 474(1-2), pp.342-347.

[187] Chen, J., Wang, Z. and Korsunsky, A.M., 2022. Multiscale stress and strain statistics in the deformation of polycrystalline alloys. *International Journal of Plasticity*, p.103260.

[188] Chen, J. and Korsunsky, A.M., 2021. Why is local stress statistics normal, and strain lognormal?. *Materials & Design*, 198, p.109319.

[189] Barba, D., Reed, R.C. and Alabort, E., 2019. Ultrafast miniaturised assessment of high-temperature creep properties of metals. *Materials Letters*, 240, pp.287-290.